Development of Aluminium Nitride (AlN) Based Materials for RF-Window and Microwave Applications

A THESIS

Submitted to

Indian Institute of Technology Guwahati

In Partial Fulfillment of the Requirements for the Award of the Degree of

DOCTOR OF PHILOSOPHY

By

Ethireddy Radhika

Under the supervision of

Prof. Pamu Dobbidi

Centre for Nanotechnology

Indian Institute of Technology Guwahati

Guwahati – 781039

INDIAN INSTITUTE OF TECHNOLOGY GUWAHATI

Centre for Nanotechnology

Guwahati - 781039

STATEMENT

The present thesis entitled, "**Development of Aluminium Nitride (AlN) Based Materials for RF-Window and Microwave Applications**" has been carried out by me under the supervision of Prof. D. Pamu, Centre for Nanotechnology, Indian Institute of Technology Guwahati. This work has not been submitted elsewhere for the award of any degree.

April, 2024

(Ethireddy Radhika)

Centre for Nanotechnology,

Indian Institute of Technology Guwahati,

Guwahati – 781039.

INDIAN INSTITUTE OF TECHNOLOGY GUWAHATI

Centre for Nanotechnology

Guwahati - 781039

CERTIFICATE

It is certified that the work described in this thesis, entitled "**Development of Aluminium Nitride (AlN) Based Materials for RF-Window and Microwave Applications**" done by Mrs. Ethireddy Radhika, a Ph. D. student of Centre for Nanotechnology, Indian Institute of Technology Guwahati, for the award of degree of Doctor of Philosophy has been carried out under my supervision. This work has not been submitted elsewhere for the award of any degree.

April, 2024

Prof. D. Pamu

Professor,

Centre for Nanotechnology,

Indian Institute of Technology Guwahati,

Guwahati – 781039.

Dedicated to the Almighty God and my Family

ACKNOWLEDGEMENTS

The work reported in this thesis is the most significant scientific accomplishment and a milestone in my life. Without innumerable help and support from all the people around me, both inside and outside my department and institute, it would have been impossible. I owe a debt of gratitude to all of you!

With profound appreciation, I sincerely thank my research supervisor, Prof. D. Pamu, centre for nanotechnology, for his encouragement, guidance, consistent support, and valuable discussions. It provides me with many learning opportunities that help me improve my understanding of the subject along with the skills and successful culmination of the present endeavor of my thesis work. I must acknowledge him for providing absolute freedom to think, plan, execute, and express what I have done in every step of my research work by keeping trust and assuredness in my competencies. You helped me by spending your valuable time even when the water was too deep or shallow for the matter – Thank you!

I sincerely thank my doctoral committee members, Prof. P. K. Giri, Prof. Nageswara Rao Peela, Dr. T. Tiwari, and Dr. T. Malleswara Rao. During my research work, their continuous academic guidance and evaluation of my annual progress reports and seminars with valuable discussions, suggestions, and words of encouragement inspired me and improved the quality of my research work.

I am highly thankful to Dr. Akshai Kumar A. S. head of the centre for nanotechnology, and former head of the centre for nanotechnology, Dr. Dipankar Bandyopadhyay for allowing me to work in the centre for nanotechnology and to use the centre for nanotechnology facilities. I am also thankful to all the faculty members of the centre for nanotechnology. Special thanks to all scientific officers and faculty members in the Centre for Nanotechnology, Department of Physics, Sameer Institute, and Central Instruments Facility.

My sincere thanks to collaborator Dr. T. Tiwari, for providing vacuum furnace, spark plasma sintering furnace and valuable suggestions for research work. I am highly thankful to Narugopal nayak,

Manoj in SAMEER centre for high power microwave tube and component technology for assisting in simulations for RF-window design and experimental help in operating vacuum furnaces.

I am also grateful to my seniors Dr. Srinivas Pattipaka, Dr. Susmita Rabha, Dr. Apurba Das, Prajna Paromita Mahapatra, Sunil Gone, for sharing their knowledge, providing useful counsel and help. I would like to thank my research team members and colleagues Shashi Priya Balamuchu, Patibandla Anilkumar, Subingya Pande, Jaharlal Patil, Hodom karnajit, Somanath Sahu, Motupalli Ganesh, Naphisabiang sun for their suggestions, time, cooperation, help, and company throughout my project. I sincerely thank my lecturer, Dr. T. Samuel, for his continuous guidance and support from my M. Sc. and throughout Ph. D.

I take this opportunity to thank all my friends at IIT Guwahati, especially Ravi kiran, Shaona, Sampreeth, Mithali Bask, Konika Choudhury, Chintak Kamalesh parashar, Vinod, Prathu for creating a friendly and homely atmosphere.

From bottom of my heart, I thank my parents (Mrs. E. Kumari, Ethireddy Venugopala Reddy), my husband (Sk. Karimulla), my son (Sk. Arsalan Zane), brother-in-law (Sk. Azaruddin), sisters (Mrs. Shanthi, Mrs. Gowthami), and all other family members for being near to my heart and provide continuous moral support as well as encouragement. This work would not have been possible to complete successfully without my family's love and support.

I am sincerely thankful to the Almighty "GOD," whose blessings have enabled me to proceed in difficult situations, pursue higher studies, and get the strength to take up challenges and complete the task successfully.

Ethireddy Radhika

IIT Guwahati, Guwahati,

Assam, India, 781039.

Abstract

The rapid evolution in communication systems, satellite technology, navigation, data processing systems, and personal computers with the demand for higher speeds and larger bandwidths necessitates the synthesis of novel functional materials for the fabrication of devices with excellent performance and high quality at reduced manufacturing costs. The development of 5G technologies, targeted at increasing data rate on a wireless communication network by a factor of 100, will impose on the radio frequency (RF) electronics some specifications such as large band width, high gain, temperature-independent performance, and small size. Monopoles, dipoles, and patch antennas provide solutions to various front-end antennas for millimeter-wave applications. These antennas can easily be integrated on a chip, characterized by small size, low cost, and low weight. However, lensing structures or integration of suitable dielectric superstrates are adopted for advanced design solutions; these antennas mainly suffer from narrow impedance band width and reduced radiation frequency by the effect of lossy silicon substrate materials. In millimeter-wave applications, especially dielectric resonator antennas (DRAs) are promising candidates to replace traditional radiating elements at high frequencies. This replacement is because the DRAs do not suffer conduction losses and are characterized by high radiation efficiency when appropriately excited.

The present thesis focused on developing pure and composite AlN ceramics for RF-window applications. RF window is an essential component of microwave tubes' output section like klystron, magnetron, and gyrotron. This RF window is a barrier between the vacuum side of the gyrotron and the transmission line output. Thus, the RF window should withstand hard conditions such as high power thermal and mechanical stresses, be leak-tight (~10^{-10} Torr), and have low RF transmission losses. In high-power RF windows, basic problems are selecting window material, managing thermal and mechanical stresses, power

handling capability, window flashing/ arcing, and physical damage. The desired properties for an ideal window are minimum return loss, minimum insertion loss, high power handling capability, and wide band width. Thus, the material for the RF window needs to be chosen carefully with high thermal conductivity, low dissipation factor, low thermal expansion coefficient, suitable mechanical strength, and perfect design for better transmission with minimization of power absorption and reflections. The commercial development of light-emitting diodes and semiconductor lasers is attracting more interest in the materials of wider band gap semiconductor III-V mononitrides. Optoelectronic devices contain specifical bandgaps of energies from the visible to UV region, which are theoretically possible by materials such as AlN, BN, GaN, and InN. These materials' wide band gap and strong atomic bonding make them suitable candidates for high-temperature and high-power devices.

The pure and composite AlN ceramics are prepared using a solid-state reaction method by adopting a powder bed in conventional sintering at 1700 ℃. The structural properties are studied from XRD and Raman spectra. All pure and composite AlN ceramics exhibited pure wurtzite AlN phase without any secondary phase as oxides or alumina. The vibrational modes of all sintered pure and composite AlN ceramics confirm the wurtzite structure. Temperature-dependent dielectric properties are also measured. Sintered AlN ceramics exhibited good microwave dielectric properties as $\varepsilon_r = 8.83$ and $\tan\delta = 2.69 \times 10^{-4}$ are suitable for RF-window applications.

AlN-ZnO composite ceramics are studied by optimizing the amount of additive and its effect on structural and dielectric properties. The microwave dielectric properties of AlN-ZnO composite ceramics are as $\varepsilon_r = 7.20$ and $\tan\delta = 4.90 \times 10^{-3}$ for the best composite AlN-15ZnO ceramic. AlN-Er_2O_3 composite ceramics are prepared using a powder bed with pure wurtzite AlN phase in the conventional sintering method in nitrogen's presence. The AlN-Er_2O_3

composite ceramics exhibited microwave dielectric properties as $\varepsilon_r = 7.81$ and $\tan\delta = 5\text{x}10^{-4}$. The dielectric window is designed in CST by using experimentally derived dielectric properties. The theoretical value of the window's insertion and return loss is better than 61.25 dB and 0.009 dB, respectively, at 3.7 GHz.

AlN-BN composite ceramics shows pure nitride phase sintered in conventional sintering at 1700 ℃, using powder bed. The Cole-Cole plots of impedance spectra of all AlN-BN composite ceramics show non-Debye type relaxations and are fitted with RCRCRC circuits corresponding to three parallelly with R and C circuits connected in series belonging to grain, grain boundary, and electrode. The best microwave dielectric properties at 12 GHz, ($\varepsilon_r = 7.38$ and $\tan\delta = 2.60 \times 10^{-3}$) is achieved for AlN-15BN composite ceramics with pure nitride phase without any alumina or intermediate phases are appropriate for electronic applications.

The comparison study on sintering methods of AlN ceramics is discussed, and the effect of the sintering technique on structural, dielectric properties and hardness of the pure and composite AlN ceramics are investigated systematically. The composite ACZ2Y (AlN + Wt% $CaZrO_3$ + 2 Y_2O_3) composite ceramics sintered in microwave sintering method, shows best microwave dielectric properties ($\varepsilon_r = 9.02$ and $\tan\delta = 7.34 \text{ x } 10^{-4}$) at 12 GHz resonant frequency, with maximum hardness (1079.51 HV30) are appropriately suited for RF window and electronic applications.

List of Publications

Patents:

1. Filed a patent with the title "**Low temperature microwave sintered phase pure AlN ceramics comprising rare earth oxide additives**" by Pamu Dobbidi, **Ethireddy Radhika,** and Dr. T. Tiwari. dated 08/07/2020, Indian patent with reference number: 202031028984.

Journals:

2. **Ethireddy Radhika,** Nayek, N., Tiwari, T., & Pamu, D. (2021). Development and design of aluminium nitride disc for high power S-band dielectric window. *Open Ceramics*, *8*, 100172. https://doi.org/10.1016/j.oceram.2021.100172
3. **Radhika, E.,** Samuel, T., & Dobbidi, P. (2022). A modified sintering method to prepare phase pure AlN ceramics: Structural and dielectric studies for microwave applications. Ceramics International, 48(19), 29372-29385. https://doi.org/10.1016/j.ceramint.2022.06.001
4. **Radhika, E.,** & Dobbidi, P. (2023). XPS and dielectric studies of phase pure AlN-BN composite ceramics using powder bed. Materials Science and Engineering: B, 297, 116783. https://doi.org/10.1016/j.mseb.2023.116783
5. **Radhika, E.,** Balmuchu, S. P., Sridhar, V., & Dobbidi, P. (2023). Effect of ZnO on structural and dielectric properties of AlN ceramics. Journal of Materials Science: Materials in Electronics, 34(26), 1799. https://doi.org/10.1007/s10854-023-11226-8

Publications outside the thesis work:

1. Rabha, S., Das, A., Gonne, S., Mohapatra, P. P., Balmuchu, S. P., **Radhika, E.**, & Dobiddi, P. (2022). Dielectric and leakage characteristics of MTO/STO bilayer films

deposited by RF magnetron sputtering technique for optical and electronic applications. *Materials Science and Engineering: B*, *282*, 115790. https://doi.org/10.1016/j.mseb.2022.115790

2. Balmuchu, S. P., **Radhika, E.,** & Dobbidi, P. (2023). The impact of oxygen partial pressure in modifying energy storage property of lanthanum doped multiferroic bismuth ferrite thin films deposited via pulsed laser deposition. Journal of Energy Storage, 71, 108179. https://doi.org/10.1016/j.est.2023.108179
3. **Radhika, E.,** & Dobbidi, P. (2024, January). Structural and dielectric properties of cubic AlN thin films deposited by RF-magnetron sputtering technique for electronic applications. In *AIP Conference Proceedings* (Vol. 2995, No. 1). AIP Publishing.

Conferences and Workshops attended:

1. "Structural and Dielectric Properties of Cubic AlN Thin Films Deposited by RF-magnetron Sputtering Technique for Electronic Applications" **Radhika, E.**, & Dobiddi, P. presented poster in the 66th DAE Solid State Physics Symposium (DAE-SSPS-2022) during 18-22 December 20222, held at Birla Institute of Technology Mesra, Ranchi, India.
2. "A Modified Sintering Method to Prepare Phase Pure AlN Ceramics: Structural and Dielectric Studies for Electronic Applications". **Radhika, E.,** Samuel, T., & Dobbidi, P. presented poster in the International Conference on Advanced Materials and Mechanical Characterization (ICAMMC-2021) (virtual mode) during 2- 4 December 2021, SRM Institute of Science and Technology, India.
3. "Dielectric and Mechanical Properties of AlN Ceramics for Ballistic Armour Applications" **Radhika, E.,** & Dobbidi, P. presented oral presentation in the International Conference on Advanced Materials and Processes for Defence Applications (ADMAT-2019) during 23-25 September 2019 at Hyderabad, India.

4. "Microwave Dielectric Studies on AlN Ceramics for RF Window Applications" **Radhika, E.,** & Dobbidi, P. presented a paper in National Symposium on Vacuum Electronic Devices and Applications VEDA-2018, 22-24th November, 2018, at Indian Institute of Technology, Guwahati, India.

CONTENTS

List of Figures

Figure no.	Figure description	Page no.

Chapter 1

Chapter 2

Chapter 3

Chapter 4

Chapter 5

Chapter 6

List of Tables

Chapter 1

Chapter 3

Chapter 4

Chapter 5

Chapter 6

Chapter 7

List of Symbols and Abbreviations

Units of measurement

m	Meter
cm	Centimetre
μm	Micrometre
nm	Nanometre
Å	Angstrom
℃	Centigrade (degree)
h	Hour
F	Farad
pC	Pico Coulomb
μC	Micro Coulomb
N	Newton
V	Volt
eV	Electron-volt
GPa	Giga Pascal
kHz	Kilo Hertz
MHz	Mega Hertz
GHz	Giga Hertz
g	Gram
W	Watt
A	Ampere

Electrical measurements

ε_r	Relative dielectric permittivity
tanδ	Dissipation factor
C	Capacitance
d	thickness
A	Area of the electrodes
ε'	Real part of permittivity
ε''	Imaginary part of permitivity

ε_0	Permitivity of free space
σ_{ac}	AC-conductivity
E	Electric field
P	polarization
p	dipole moment
V	unit cell volume
Z	Impedance
Z'	Real part of impedance
Z''	Imaginary part of impedance
R	Resistance
X	Reactance
DC	Direct current
AC	Alternating current
χ	Electric susceptibility
τ	Relaxation time
Q	Quality factor
Q_l	Loaded quality factor
Q_{ul}	Unloaded quality factor
k_B	Boltzman constant
ω	Angular frequency

Optical measurements

λ	wave length
n	Refractive index
$h\boldsymbol{\nu}$	photon energy
c	velocity of light
E_g	Optical bandgap

Other Parameters

$\boldsymbol{\theta}$	Angle
D	crystallite size
wt.	weight
$\boldsymbol{\rho}$	density

O_2	Oxygen
N_2	Nitrogen
FWHM	Full width at half maximum
a, b, c	Lattice parameters
χ^2	Chi-square
R_{Bragg}	Bragg factor
R_f	Profile factor
RT	Room temperature
CSSR	Conventional solid-state reaction
rms	Root mean square
SPDR	Split post dielectric resonator
MIM	Metal-Insulator-Metal
XRD	X-Ray diffraction
EDS	Energy dispersive X-ray spectrometer
SEM	Scanning electron microscopy
VNA	Vector network analyzer
AFM	Atomic force microscopy
XPS	X-Ray photoelectron spectroscopy
SAED	selected area electron diffraction
RF	Radio frequency
MIC	Microwave integrated circuits
DBS	Direct broadcasting satellite
GPS	Global positioning system
IoT	Internet of things
ITS	Intelligent transport systems
RFID	Radio frequency identification
f	frequency
$\boldsymbol{\kappa}$	thermal conductivity
C_p	specific heat
Y	Young's modulus

σ_b	bending strength
TE	Transverse Electric modes
TM	Transverse Magnetic modes
HEM	hybrid electromagnetic modes
EM	Electromagnetic radiation
DR	Dielectric resonator
μ_r	Relative permeability
MCP	Mechanochemical processing
$\boldsymbol{\rho}_e$	electrical resistivity

Chapter 1

Introduction to Microwave Ceramics

1.1 Introduction

Microwave dielectric materials are occupying an essential role in the present world due to dielectric resonators improved performance at microwave frequencies in different areas in terrestrial and satellite communications, Internet of things (IoT), radio technology, global positioning systems (GPS) for environmental monitoring via satellite, cellular phones, direct broadcasting satellite (DBS). These materials are mainly used as resonators, substrates, coaxial resonators, and ceramic filters in microwave integrated circuits (MIC). Nowadays, all business, education, medical treatment, medicine preparation, and research depend on the internet. In the future, the IoT posed to make rapid growth. In this paradigm, most everyday objects will be networked through sensor network technologies, radio frequency identification (RFID), and printed electronics. The research on low-loss dielectric materials is increasing daily due to rapid progress in microwave telecommunications, intelligent transport systems (ITS), IoT, and satellite broadcasting. The constant demand for miniaturization leads to the research, discovery, and development of smaller/lighter dielectric materials that outperform existing materials.

A dielectric resonator is an electromagnetic component that provides resonance for a narrow range of frequencies. The requirements of a ceramic puck for a dielectric resonator are high relative permittivity, high-quality factor, low loss tangent, and near-zero temperature coefficients at the resonance frequency. Low permittivity ceramics are used as a substrate in microwave integrated circuits and microwave communication systems. Low permittivity ceramics must be stable at various temperatures. The Ceramics should contain a high Q (quality factor)-value, with low permittivity for substrate and MIC applications to transmit high-speed

signal with minimum attenuation. Suppose the relative permittivity is decreasing, then the signal transmission speed increases. A high Q-value minimizes the insertion loss of the circuit, suppresses the electrical noise in oscillator devices, and helps in high-speed signal transmission. Medium permittivity ceramics in the 25-50 are applied in satellite communications and mobile phone base stations. Higher permittivity ceramics are used in mobile phone handsets where miniaturization plays a key role.

1.2 History and applications of dielectric materials

The materials that are poor conductors of electric current, that exhibit the property of polarization and modify the vacuum's dielectric function, are called dielectrics. In 1745, Cunaeus and Mussachenbroek constructed the first capacitor called the Leyden jar. The first numerical measurements were published on dielectric material by Faraday called dielectrics. It was found that the material placed between the conducting material alters the capacity of the condenser. This experiment leads to further empirical studies on dielectric materials to maximize the amount of charge the capacitor stores.

Mossotti and Clausius did a systematic investigation of the dielectric properties of materials. A macroscopic characteristic of the insulator introduced by Faraday correlated with the specific inductive capacity by Mossotti and Clausius is known as dielectric permittivity with the material's microscopic structure. Clausius and Mossotti derived a relation between the real part of dielectric permittivity and the polarizability in the dielectric by considering that the dielectrics are composed of conducting spheres in a non-conducting medium. At the beginning of the 20th century, Debye extends the Clausius-Mossotti theory by considering the molecule's permanent moments, which allows for calculating molecular dipole moment from measuring dielectric permittivity. Later, Onsager and Kirkwood extended Debye's theory and agreed with the experimental results of most polar liquids.

Debye's theory is in excellent agreement with the dielectric experimental results of polar liquids while deviating considerably from the experimental results of solids. Several modifications and extensions to Debye's theory have been proposed to correct this deviation. The proposal by Cole, Davidson, and William interprets non-Debye relaxation of the material as the first approach. Jonscher made the second approach that proposes that molecular-level relaxation behavior is intrinsically non-Debye-like relaxation due to the cooperative molecular motions.

1.3 Physics of dielectrics

Revolution comes in the digital world through the recent advances in ceramic science and technology—new inventions day by day, attracting interest in research and development in the field of dielectrics. The most famous application of dielectric material is observed in capacitors (conducting plates are separated by the insulating material (dielectric material)). A brief introduction to dielectrics and their applications are addressed in the following sections.

1.3.1 Dielectrics

Dielectrics are insulators or poor in conducting electricity but are efficient supporters of an electrostatic field. Dielectrics do not have free charge carriers and are tightly bound to the nucleus/atoms. If dielectric materials are placed in an external electric field, the electric charge carriers do not flow through it (unlike conductors). However, the charge carriers in dielectric material placed in an electric field will shift away from their average equilibrium position in the sample, causing polarization results in a net dipole moment. In dielectric material, the net dipole moment ($\vec{\mu}$) per unit volume (V) of material is known as polarization $\left(\vec{P} = \sum\left(\frac{\vec{\mu}}{V}\right)\right)$. The amount of polarization is a dimensionless quantity called a dielectric constant. Dielectrics are classified into two types: active dielectrics and passive dielectrics. If the dielectric material

is placed in an active external electric field and then dielectric material allows the electric flow and stores electrical energy, it is termed active dielectric material examples are ferroelectric, piezoelectric and pyroelectric materials. These active dielectrics are useful for energy storage applications. If the dielectric material restricts the flow of charge through it, it is termed passive dielectric material. Dielectric materials are further classified into three types depending on the state of the material, such as solids, liquids, and gases. Examples of solid dielectrics are paper, mica, ceramic, glass, etc. Liquid dielectrics are distilled water, an oil used in transformers, etc. Gas dielectrics are metal oxides, nitrogen, helium, etc. According to the type of molecules in the dielectric material, dielectrics are further classified into polar and non-polar. If the dielectric material contains polar molecules, then when we place it in an external electric field in such a case, the charge molecules assemble in a direction similar to the electric field due to the non-center of symmetry. The possibility of coinciding with the positive and negative types of molecules is zero. Thus, they exhibit permanent dipoles. In non-polar molecules, both positive and negative charges coincide due to the center of symmetry, and there is no condition of a permanent dipole moment among all. Dry air is treated as an excellent dielectric material used in transmission lines and variable types of capacitors.

1.3.2 Basic aspect of RF-window

RF-window is a critical component used at the output section of the device for extracting RF power from a vacuum to the high-pressurized atmospheric environment in the gyrotron. Thus, careful design is needed for this component RF-window, which is essential to the successful operation of the device. In designing an RF window, consider the window as minimum power reflection and maximum power handling capability and optimize the window disc dimensions. In the RF window, the RF loss directly depends on the dielectric properties of the materials used for the RF window. Incontestably, in a wide range of temperatures, the

dielectric properties of the material should be stable so that the window performance remains stable during heating. RF-window should be fabricated with a low dissipation factor for low absorption and suitable for ultra-high vacuum applications. There is a high-power limit for all RF windows due to the absorbed RF power by the window resulting in heating the window. Even though the absorbed energy by the RF window is relatively small, the fraction of energy is 0.1% for typical materials of interest. Even this relatively small fraction of absorbed energy leading to significant heating of the RF-window causes thermal stress produced in the RF-window. The absorbed energy initiates the thermal energy in the RF window. In steady-state operation, this thermal energy is removed by thermal conduction and forced convection. The temperature gradients formed in the RF window necessarily drive thermal energy out of the window, which is essential since it ultimately leads to the failure of the window when power is high. The thickness of the RF-window (d) is chosen such that the RF power reflection should be minimal, and it may be estimated from the following relations;

$$d = \frac{N_i \lambda_i}{2(\varepsilon_r)^{1/2}} \tag{1.1}$$

where suffix i signifies various integers, N is constant, λ is the wavelength, ε_r is the dielectric permittivity of the window material, respectively. For $i = 0$, the thickness of the window is as follows;

$$d = \frac{N_0 \lambda_0}{2(\varepsilon_r)^{1/2}} \tag{1.2}$$

where, λ_0 is free space wavelength. The Brewster window is the possible solution for a broadband window. This Brewster window is used in multi-frequency Gyrotron. The main problem in the design of the Brewster window is the window reflections. In the Brewster window, the transmission band is large, and the window is tilted at a specific angle ($\theta_B =$

$\theta_{Brewster}$). The angle between a normal to the Brewster window and the propagation axis of RF is as follows;

$$\theta_B = arc\ \tan(\varepsilon_r)^{1/2} \tag{1.3}$$

In the case of TE_{mn} mode, the value of the thickness of the window (d′) for low power window can be obtained from the following relation;

$$d' = \frac{N\pi}{\left[\left(2\pi f\left(\frac{\varepsilon_r}{c}\right)^{1/2}\right)^2 - \left(\frac{x'_{mn}}{R_{win}}\right)^2\right]^{1/2}} \tag{1.4}$$

where f is the frequency, c is the velocity of light, x'_{mn} the n^{th} root of the derivative of m^{th} order first kind Bessel function, and R_{win} is the window radius. The two empirical parameters, namely failure resistance (R'), and power transmission capacity (P_T) for edge-cooled windows are obtained from the following relations;

$$R'Y\alpha = \kappa\sigma_{\boldsymbol{b}}(1-\nu) \tag{1.5}$$

where Y is Young's modulus, α is the thermal expansion coefficient, κ is the thermal conductivity, $\sigma_{\boldsymbol{b}}$ is the bending strength, and ν is the poison number.

$$P_T \tan\delta = \frac{R'\rho c_p}{(1+\varepsilon_r)} \tag{1.6}$$

ρ is density, and c_p is the specific heat of the material, respectively.

1.3.3 Material requirements for RF-window

RF windows transmit microwave power by placing it as a penetrable barrier between the vacuum and transmission line and separating the ultra-high vacuum environment inside the tube against the air. RF windows are the most valuable and critical components in microwave tubes. RF-window separates vacuum and high pressurized environment; hence, the material

used for RF-window should exhibit the following properties: low dielectric permittivity, low dissipation factor, high thermal conductivity, high mechanical strength, low thermal expansion coefficient, and excellent capability of metallization. The important dielectric properties of the RF-window as a low dissipation factor help to avoid a high amount of power dissipation in the window, a low secondary electron emission coefficient of RF-window is to suppress the multipacting, low dielectric permittivity is to make matching the RF-window easier. Also, the RF window's high dielectric strength helps withstand breakdown. High thermal conductivity of RF-window utilized to conduct/away the dissipated heat. RF-window should contain high mechanical strength to withstand structural loads and suppress the fracture. The materials used for the RF window are listed in Table 1.1 with their properties. The other important property of the RF window is the good metallization capability to maintain the vacuum seal between the ceramic window and metal flange. Metallization of the ceramic window will be formed by using metal alloy and brazing it with ceramic window.

1.3.4 Current status of materials developed for RF-window applications

The most commonly used material for most of the RF-window is high-purity polycrystalline alumina (Al_2O_3) ceramic, with other materials including AlN (aluminium nitride), BeO (beryllium oxide), BN (boron nitride), and sapphire. However, due to its toxicity, BeO is limited to being used as an RF window for environmental safety. Alumina as an RF window for high-power klystrons was studied and compared at KEK (Kō Enerugī Kasokuki Kenkyū Kikō) national laboratory [22]. The HA997 (99.7% alumina) and UHA99 (99% alumina) performed best in high-power tests. To reduce RF losses, 99.7% of alumina has very special sintering additives, and 99% of alumina has tiny size grains with good density. 99.9% alumina (XKP999) shows degraded RF performance due to high porosity since the lack of additives. The sapphire window can transmit one-fourth of RF power through 99.7% and 99% alumina. Sapphire window has a low dissipation factor even though it shows a significant

luminescence due to the large amount of F centres caused by a high secondary electron emission coefficient. AlN has better dielectric and thermal properties than all other samples appropriate for RF-window applications.

1.3.5 Well-known materials for RF-window

Table 1. 1: The list of materials used for RF windows with their specifications.

S. No.	Material	Dielectric permittivity at 10 GHz	Dissipation factor at 10 GHz (10^{-4})	Dielectric strength (kV/cm)	Thermal conductivity (W/mK)	Reference
1	Al_2O_3	12	8-10	4000	40	[1]
2	AlN	9	5-9	150	170-300	[2–4]
3	BeO	6.6	1	100-140	250-370	[5–7]
4	BN	5	4.6-5	67	140-300	[8,9]
5	GaAs	12.85	6	350	30	[10]
6	GaN	10.4	-	4000	66-225	[11]
7	Glass	4-7	1	350	0.8-1.2	[12–14]
8	Ferrite/ Garnet	13-16	1-2	120	3	[15]
9	InP	12.4	10	350	40	[16]
10	Quartz	308	1	200-400	2	[17,18]
11	Saphire	11.6	0.4-0.7	4000	23-25	[19]
12	SiC	10.8	20	2500	120-200	[20]
13	TiO_2	90/170	2-50	40-80	10.4	[21]

1.3.6 Future requirements of the RF-window

For RF-window applications, the material should have high thermal conductivity, low dielectric constant, low dissipation factor, low thermal expansion coefficient, and low cost [23]. Since all these requirements are filled by AlN ceramics, AlN ceramic window fabrication has

some challenges to fabricating at a low price. AlN has high stability, high mechanical strength, and a high rate of radiation resistance to several types of influences externally; hence, it will be applicable for fusion reactor [24] RF windows [25] applications [26, 27]. AlN has high thermal conductivity and a low thermal expansion coefficient; therefore, it is a heat sink in nuclear reactor applications and electronic packages [28].

AlN is difficult to sinter at low temperatures due to the covalent bond present and to maintain a pure phase with good density. While sintering AlN ceramics, oxidation is possible since oxidation will quickly occur at high temperatures. AlN exists in several crystal structures. AlN's highly stable crystal structure is a hexagonal wurtzite-type lattice (w-AlN) [29, 30]. Other structures are cubic zinc blende (zb-AlN) [31–34] and rock salt type AlN structure (rs-AlN) [35]. AlN ceramics should be prepared in a cost-effective method with pure phase for RF windows with the improvement of dielectric and structural properties of AlN at a wide range of temperatures for RF-window stability [36].

1.4 Physics of dielectric resonator materials

The dielectric material (AlN) used for RF window acts as a dielectric resonator (DR) in presence of electromagnetic field. Dielectric resonators are widely used in modern microwave communication systems due to their compactness, superior temperature stability, and Q-factor performance. A dielectric resonator is a component of electromagnetic that functions as a resonator by reflections at the high dielectric (ε_r) – air interface. The dielectric object with free space boundaries can resonate in different modes. Thus, the resonant modes are classified as follows;

i Transverse Electric Modes (TE)

ii Transverse Magnetic modes (TM)

iii Hybrid Electromagnetic Modes (HEM)

The constituent resonant modes in the dielectric resonator can be classified with azimuthal variation, such as $\cos(m\varphi)$ or $\sin(m\varphi)$, where $m = 0, 1, 2, 3, etc$. For axial symmetric modes (i.e., $m = 0$), the set of modes can be divided into TE_{mnp} and TM_{mnp}. In these modes, the first subscript m denotes the azimuthal dependence of resonant modes in φ. The second subscript refers to the radial mode, and the third subscript (p) refers to the axial mode. The subscript p is replaced by $\ell + \delta$, where $\ell = 0, 1, 2, 3, etc$, and $0 < \delta < \ell$ due to the effect of the evanescent field in a DR, which refers that variations in the DR along the axial direction such as a fraction of a period of field variations and ℓ number of half period variations [37].

$HEM_{11\delta}$ is the lowest hybrid mode. The resonant frequency of the $HEM_{11\delta}$ mode can be lower than that of $TE_{01\delta}$ mode. Its proximity to $TE_{01\delta}$ mode, governed by the aspect ratio of DR and the proximity of perturbing metallic surfaces to the DR. low Q (quality factor) value is not preferred by the proximity of $HEM_{11\delta}$ mode to $TE_{01\delta}$ mode. In between $TE_{01\delta}$ and $TM_{01\delta}$ modes, there will be $HEM_{21\delta}$ mode; this also has a lower resonant frequency. Thus, $HEM_{21\delta}$ mode can cause difficulties while operating in either of these modes. A different arrangement is required while coupling TM modes than TE modes; HEM modes contain both components and can be coupled to both TE and TM coupling arrangements. HEM modes use TE and TM modes, cause difficulties by their inherent Q values, and are highly radiative (i.e., leaky). The HEM modes' complexity increases with the higher integer values of m and n takes. $TE_{01\delta}$ mode is separated from all neighbouring modes by the aspect ratio (ratio D/L; D is DR's diameter; L is DR's height) of 2.5. This $TE_{01\delta}$ mode is the most commonly used in dielectric resonators [38].

Communication through mobile phones from one place to another is by antennas placed on masts and base stations associated with them. The average base station coverage is a diameter of 35 and 18 km at 900 and 1800 MHz, respectively, within a cellular network.

Microwave resonators carry specific frequency signals and remove (filter) side bands and spurious signals that interfere with transmitted/received frequency band quality in each base station. In narrow bandwidth applications, the selectivity of a particular frequency is necessary; low loss, temperature stable ceramics are used in preference cheaper metal cavities. In single-mode resonator applications, cylindrical ceramics are used based on the original concepts of the Richtmyer. In the ceramic, the interaction of electric and magnetic fields of electromagnetic radiation (EM) is shown in Figure 1.1.

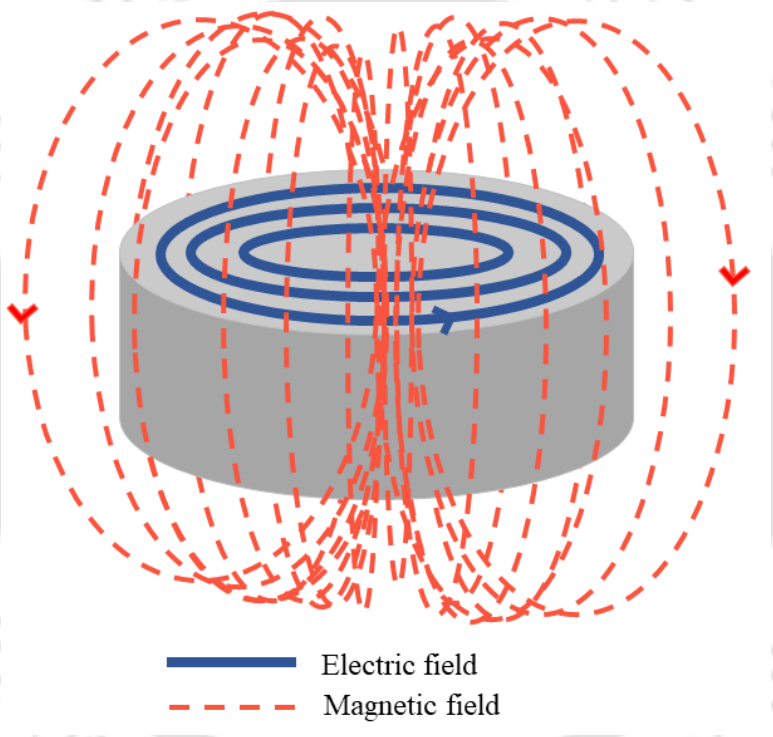

***Figure 1. 1*: The electric and magnetic fields formed in a dielectric resonator**

The ceramic is used as a filter or a transmitting resonator; hence, such ceramic has to be designed to sustain standing waves within its body of a specific resonant frequency. The prime motive of the research and development section in designing dielectric resonators are their dimensions, maintaining dielectric properties, and precise phase assemblage during processing that affects the resonant frequency and temperature stability. The ceramic is made in different geometries according to the applications, such as single-mode resonators and multi-mode

resonators. Ceramics for different modes, such as TE / TM / HE, are shown in Figure 1.2 [38]. Multi-mode resonators are used to induce several resonant microwave modes within their body at any one time, made in unusual geometries.

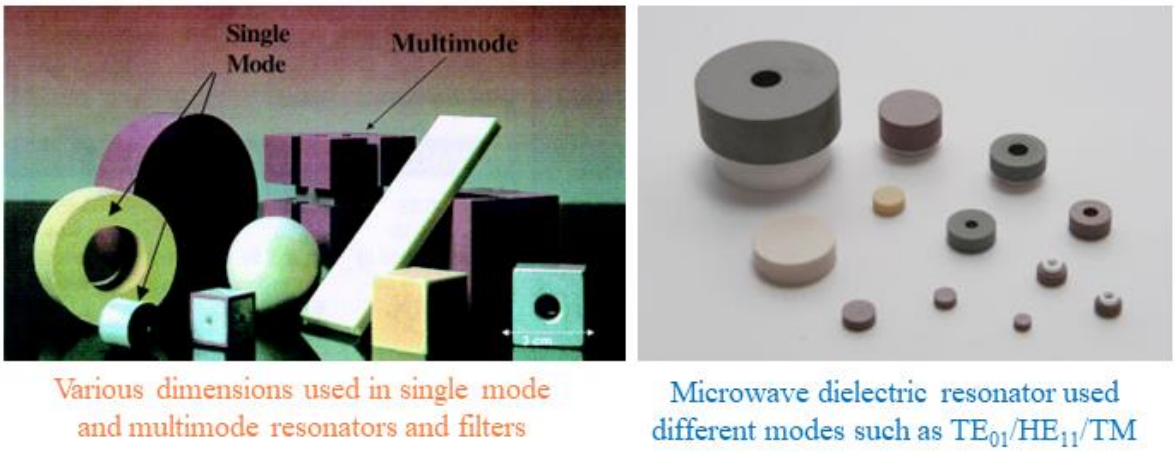

***Figure 1. 2*: The various geometries of dielectric resonators used for different modes in resonators and filters.**

The ceramic sintered for dielectric resonator/ filter applications needs to optimize or check the three parameters, mainly such as dielectric permittivity, temperature coefficient of resonant frequency, and dissipation factor rather than its inverse (quality factor).

1.4.1 Polarization mechanisms in dielectrics

Electrically charged units are aligned in an order under the influence of an external electric field in space. A dielectric material is an electrical insulator that can be polarized in each separate polarizing unit (atom, ion, or molecule); thus, it forms an electric moment in DR. Electric charges in a dielectric do not move as in a conductor by applying an external electric field, but slightly shifting from their average equilibrium position causes dielectric polarization. The positive charge in the dielectric shifts towards the direction of the external electric field, and the negative charge displaces in the opposite direction, as shown in Figure 1.3. Thus, the displacement of charges causes polarization, which creates an internal electric field in a dielectric material, reducing the overall electric field within the dielectric itself. Suppose a

weakly bonded molecule presents in the dielectric material, then those molecules become polarized and reorient themselves such that their symmetry axis aligns in the direction of the external electric field. The term dielectric refers to the material's energy-storing capacity by means of polarization. In a capacitor, the dielectric material is placed between the capacitor's metal plates—the capacitor surface charge increases by the polarization produced in dielectric material due to the applied electric field. A dielectric sample acquires a nonzero macroscopic dipole moment in an external electric field, indicating that the dielectric sample is polarized under the external electric field. The polarization (P) or dipole density of the dielectric material is defined as follows;

$$P = {\langle M \rangle}/{V} \tag{1.7}$$

where $\langle M \rangle$ is the macroscopic dipole moment of the whole dielectric material having the volume V, that have permanent micro dipoles (coupled pair of opposite charges) and not coupled pair of micro charges within the dielectric sample. $\langle M \rangle$ The brackets refer to the ensemble average. The macroscopic polarization is directly proportional to the applied external field strength E in the linear approximation as follows;

$$P \propto E_k \tag{1.8}$$

$$P = \varepsilon_0 \chi_{ik} E_k \tag{1.9}$$

where χ_{ik} is the susceptibility tensor of the dielectric material, and $\varepsilon_0 = 8.85 \times 10^{-12}$ the permittivity of free space. χ is dielectric susceptibility and is a scalar; if the dielectric is isotropic and uniform, then the polarization is as follows;

$$P = \varepsilon_0 \chi E \tag{1.10}$$

The electric field is the result of the electric displacement vector D according to the macroscopic maxwell approach then the polarization is as follows;

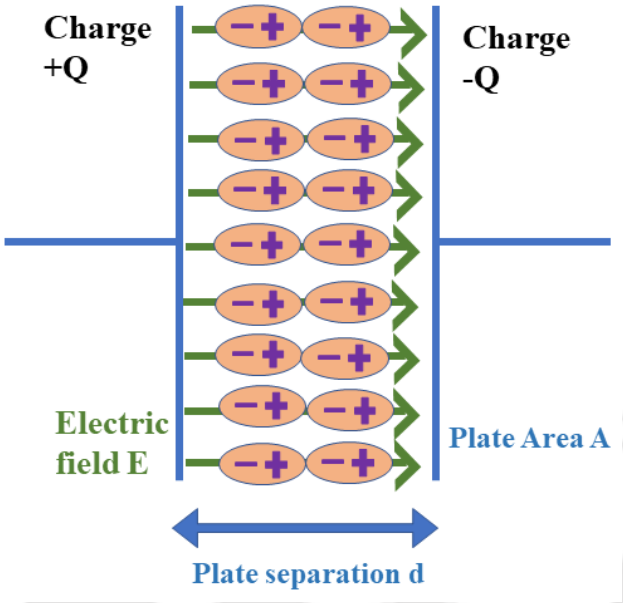

***Figure 1. 3*: Polarization inside the dielectric material under the influence of an electric field**

$$P = D - \varepsilon_0 E \tag{1.11}$$

For isotropic dielectric medium, the vector D, E, and P is independent of coordinate, therefore;

$$D = \varepsilon_0(1 + \chi)E = \varepsilon_0\varepsilon_r E \tag{1.12}$$

$$\varepsilon_r = 1 + \chi \tag{1.13}$$

where, ε_r is the relative dielectric permittivity. Generally, it is independent of field strength in the linear region and is called a dielectric constant. However, it will depend upon sample temperature, density, chemical composition, and the frequency of the applied electric field for the time variable field. In the presence of an external electric field, the dipole density is created in the dielectric sample due to polarization. The different types of polarization are as follows;

Electronic polarization: In dielectric material, the nuclei and electrons in the atom are displaced

under the influence of an external electric field known as electronic polarization. The schematic diagram of the displacement of nuclei is shown in Figure 1.4(a).

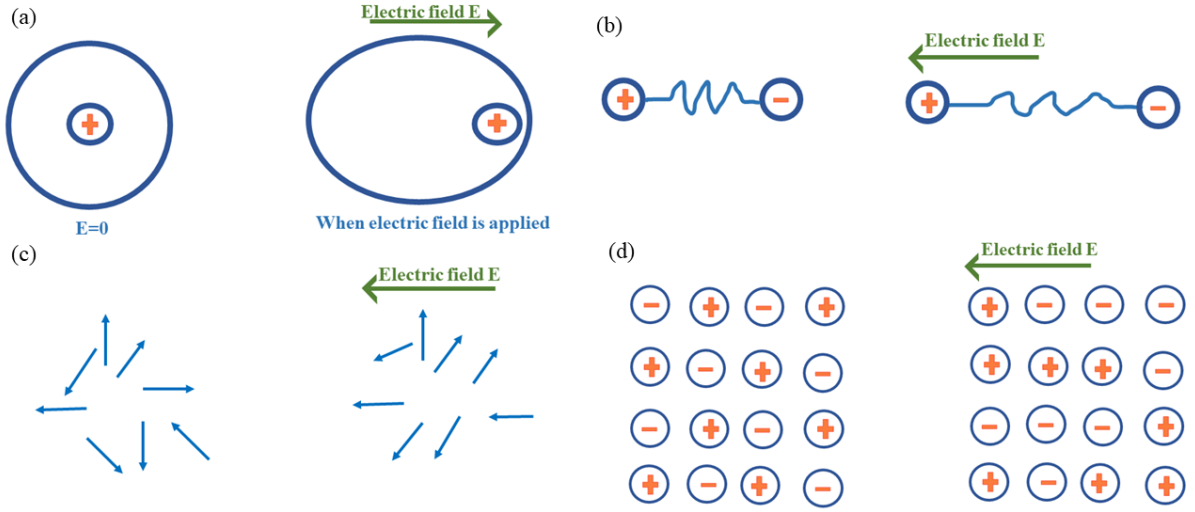

Figure 1. 4: Schematic diagram of (a) electronic polarization, (b) ionic polarization, (c) dipolar polarization, and (d) space charge polarization.

In the dielectric material, there is a displacement of atoms or a group of atoms in the molecule under the influence of electric field called atomic polarization. The separation of the positive and negative ion air molecules held together by ionic bonds results from ionic polarization. In such a molecule, the negative ion displaces in the opposite direction of the applied electric field. Their interionic separation increases up to the bounding force to step the process causes, increasing the dipole moment under the influence of the external electric field and schematic diagram shown in Figure 1.4(b). Ionic polarization is determined due to the nature of the interface, where ions can accumulate and demonstrate weak temperature dependence.

The randomly distributed dipole moments in the polar molecule orient themselves with the applied electric field. The phenomenon of the orientation of dipole moment in the field direction is called orientation or dipolar polarization and is shown in Figure 1.4(c). The

permanent dipole moments tend to be directed by an external field. The rotation depends on the counteraction of the thermal motion of the molecule. Thus, the orientation polarization is temperature and frequency-dependent. The dipoles take a long time to align along the direction of the applied field.

The space charge polarization occurs due to the accumulation of charge at the interface of multi-phase material or the interface of the electrode; the ion diffuses over an appreciable distance due to the application of an external electric field, resulting in the redistribution of charge in the dielectric material shown in Figure 1.4(d). This space charge polarization is also known as interfacial polarization.

The dielectric permittivity and dissipation factor are dependent on the frequency. Dielectric permittivity for the polar molecule is due to the contribution of multi-component polarization such as electronic (P_e), ionic (P_i), dipolar or orientation (P_d), and space charge polarization (P_s) [39]. The displacement of electrons relative to the positive nucleus under the influence of an electric field leads to electronic polarization. This polarization forms at frequencies up to 10^{17} Hz. Ionic polarization arises due to the displacement of positive and negative ions with respect to each other. The maximum frequency of ionic polarization is approximately 10^{14} Hz. Ions are heavier than electrons; hence, ionic polarization cannot occur rapidly. Dipolar polarization occurs up to 10^{11} Hz. Finally, the space charge polarization occurs between 1 to 10^4 Hz [40]. Thus, the total polarization (P) in dielectric material can be represented as follows;

$$P = (P_e) + (P_i) + (P_d) + (P_s) \tag{1.14}$$

Deformation polarization is the sum of electronic and atomic polarization, and the contribution of space charge polarization is less.

1.4.2 Dielectric losses

The dielectric material can store energy when the external electric field is applied. In a parallel plate capacitor, DC voltage is applied. More energy is stored in a dielectric material placed between the parallel plates (electrodes) than in a vacuum, or no material is placed between the plates (electrodes). The storage capacity of the capacitor increases due to dielectric material by neutralizing charges at the electrodes that generally contribute to the external electric field. The capacitance of dielectric material related to the dielectric permittivity of the dielectric material is as follows;

$$C_0 = \varepsilon_0 \frac{A}{t} \tag{1.15}$$

$$C = kC_0 = \varepsilon_r \varepsilon_0 \frac{A}{t} \tag{1.16}$$

where C and C_0 are the capacitance with and without dielectric material, ε_0 is the permittivity of the free space, A is the area of the plate or electrode, t is the thickness of the dielectric material, k is the proportionality constant, and ε_r is the relative permittivity of dielectric material accordingly. The DC voltage-connected circuit is shown in Figure 1.5(a).

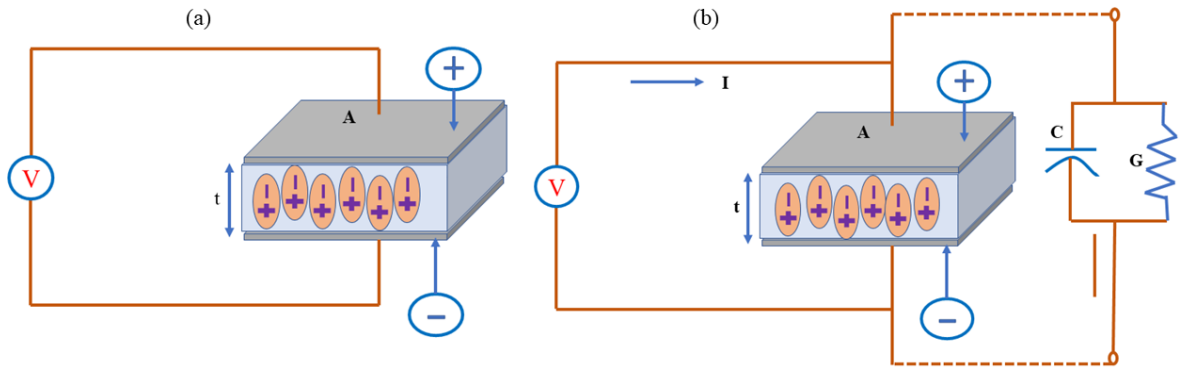

Figure 1. 5: (a) DC and (b) AC voltage source connected to a parallel plate capacitor

If the AC voltage source is connected to the same capacitor as shown in Figure 1.5(b)., the resultant current in the circuit will be made up of charging current (I_c) and lossy current (I_l) as follows;

$$I = I_c + I_l = V(J\omega C_0 + G) \tag{1.17}$$

$$G = \omega C_0 \varepsilon_r'' \tag{1.18}$$

$$I = VJ\omega C_0(\varepsilon_r' - j\varepsilon_r'') = VJ\omega C_0 \varepsilon_r \tag{1.19}$$

where G is the conductance, ε_r' the real part of dielectric permittivity, ε_r'' The imaginary part of dielectric permittivity, $\omega = 2\pi f$ angular frequency, J is current density and j complex number. The dissipation factor or dielectric loss measures how dissipative or lossy the dielectric material is to the applied external electric field. The dissipation factor is the ratio of the imaginary part to the real part of the dielectric permittivity of the sample and is also defined as the inverse of the quality factor (Q) as follows;

$$\tan\delta = \frac{\varepsilon_r''}{\varepsilon_r'} = \frac{1}{Q} \tag{1.20}$$

1.5 Electronic applications of low dielectric permittivity and dissipation factor dielectric materials

New applications of low-loss microwave ceramics are constantly emerging, such as LTCC (low-temperature co-fired ceramics) for embedded microwave circuitry applications, tunable filters, global positioning systems, and applications in advanced radar technology [38]. Some of the AlN applications are shown in Figure 1.6. AlN has unique properties such as high thermal conductivity, low dissipation factor, non-toxic nature, excellent electrical insulation properties, and low thermal expansion coefficient matching silicon, making it an essential material for the electronic industry. Due to its unique properties, AlN is used for LED / Laser

applications in high-power circuits, ultra-low temperature electronics, power management applications, and microelectronics. The best-performing circuit solutions today for high-current and high-temperature electronics are AlN PCB (printed circuit boards) due to their excellent thermal conductivity and dielectric properties with low thermal expansion coefficient. AlN is used in ultra-low temperature vacuum chamber electronics (for example, quantum computing). AlN exhibits high-temperature stability, high acoustic velocity, and a large electromechanical coupling factor. Hence, it can be used as dielectric resonators [41–44], filters [45–47], sensors (ammonia, hydrogen, and humidity sensors), and actuators [48–52].

AlN has other unique qualities compared with other ceramics, such as rigidity, resistance against environments, and 0% water absorption. In the semiconductor industry, AlN is widely used due to its non-toxic nature and does not produce dangerous vapors when ground and machined. AlN is a semiconductor circuit carrier (substrate) and heat sink in LED light technologies or high-power electronics. AlN is widely used in electronic packages in the place of light-emitting diodes and electronic substrates, photodetectors, high power, and high voltage units [53–55]. AlN is resistant to molten aluminium, gallium, iron, nickel, molybdenum, silicon, and boron. AlN can be brazed, metalized, and plated easily and is also an excellent electrical insulator; hence, this AlN is used as a heat sink in many electronic devices. Dielectric materials are mainly used in the microelectronic industry for many essential functions. Substrate requirements in new packaging technology are low dielectric permittivity, high conductivity metals to make interconnections, high wiring density, and embedded passive circuit elements. Thin films, low-temperature co-fired ceramics (LTCC), printed writing boards, and thinner are required to use fine line signal conductors. The need is increasing for the measurements of dielectric properties of thin material due to increasing demand daily for the miniaturization of electrical components [56]. Ceramic substrates are used in printed writing boards (PWB), central processing units, and thin films. Low dissipation factor, high

thermal conductivity, high interfacial adhesion to metal surfaces or other films, and low thermal expansion coefficient are essential properties of LTCC, PWB, and other substrate materials.

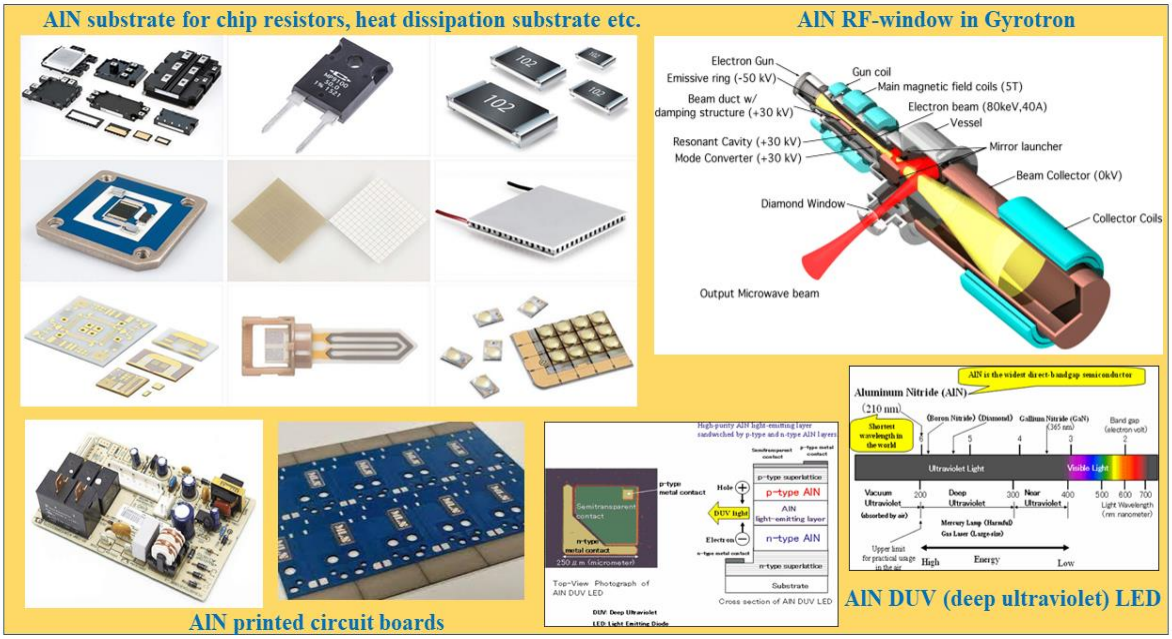

***Figure 1. 6*: Applications of aluminium nitride (AlN) in different fields.**

A low dissipation factor helps decrease heating and signal attenuation in the circuit, high thermal conductivity rapidly dissipates heat, and the material's thermal conductivity promotes the circuit's durability. The speed of signal propagation is essential in high-frequency circuits. The dielectric permittivity and the transmission line structure will affect the signal propagation delay. Thus, the dependence of propagation delay on dielectric permittivity manifests in the equation for the transverse electromagnetic (TEM) propagation modes in a lossless line as follows;

$$t_d = \frac{l(\varepsilon_r \mu_r)^{1/2}}{c} \tag{1.21}$$

where, t_d is the propagation delay time, c is the speed of light in vacuum, l is the line length, ε_r is the dielectric permittivity, μ_r is permeability. High permittivity ($\varepsilon_r \approx 8 - 500$) materials

also have a niche in microelectronic applications at low frequencies to keep the dimensions of the circuit small. The following relation can explain this dependence;

$$\lambda = \frac{c}{f(\varepsilon_r \mu_r)^{1/2}} \tag{1.22}$$

where λ is the TEM mode wavelength in material, f is the frequency. Compact antenna arrays use high permittivity material substrates to maintain phase shifts between elements. AlN is appropriate for electronic applications since AlN has moderate dielectric permittivity to transmit signals rapidly, a non-zero temperature coefficient of resonant frequency for frequency stability against temperature change, and a high-quality factor in enhancing frequency selectivity [57–59].

The thick film, plated copper, photo-patterned thick film, high-temperature co-fired ceramics (HTCC), and LTCC are ceramic substrate designs. Ceramic substrates have an advantage over polymer substrates in durability, relatively high thermal conductivity, and low thermal expansion coefficient. High permittivity helps to slower propagation speed and larger crosstalk in circuits. The propagation speed varies as the square root of permittivity. LTCCs are used in circuitry for cable-free interconnections between devices (Bluetooth technology).

1.6 Brief literature survey

Technical ceramics:

- AlN ceramics were prepared in conventional sintering method with the composition AlN + CaO / BaO / SrO + C after compacted under the pressure of 2 tonn/cm^2 being packed with AlN powder as a padding material was sintered at 1800 ℃, in N_2 atmosphere for 30 min. The obtained sintered AlN ceramics have 98.5% relative density and achieved 71.17 $W/m\text{-}°K$ [60].

- Manufacturing of AlN substrate by sintering the compact pulverized mixture of AlN with one of the additives BN / at least one oxide of Ca, Cr, Mn, Al, Ti, Zr, Si, and rare earth metals at temperatures ranging from 1300 ℃ -1900 ℃ in the presence of N_2 atmosphere and the chamber pressure 140 mbar-190 mbar with 2 h holding time. These AlN ceramics achieved 90-98% theoretical density with 184 $W/m\text{-}°K$ [61].
- AlN ceramics were prepared by combustion reaction method; then ball milled using ZrO_2 balls with Y_2O_3 additive using acetone as milling medi, and compacted into cylindrical disks; this compacted material sintered from 1600 ℃-2000 ℃ with different soaking times 15, 30 and 60 min in a microwave furnace. The compact of AlN with an initial size of 0.9 μm with 3-5 wt % of Y_2O_3 sintered at 1800 ℃ shows 99% relative density and thermal conductivity 122-132 $W/m\text{-}°K$ [62].
- Starting Sample of AlN (1.5 µm particle size) blended with 2 wt% of PVA pressed at 30 MPa followed by cold isostatic pressing at 280 MPa into cylindrical compacts. These compacted disks were preheated at 110 ℃ for 2 hours in the presence of 1atm. Flowing nitrogen atmosphere 50 wt% AlN+ 50 wt% BN powder used as a powder bed to separate the pellets and reduce evaporation and degradation of AlN at high temperatures using a BN crucible and a small hole made on BN crucible for temperature sensing. The microwave sintering temperature range is 1500 ℃ – 1850 ℃. The sample sintered at 1850 ℃ with 0.5 h soaking time achieved a density of 3.22 g/cc. This sample exhibits 38% transmittance at 5.8 μm and thermal conductivity 98-104 $W/m\text{-}°K$[63].
- In previous literature, 70 % of ultrafine aluminum powder of average size 0.1-0.2 µm mixed was compression moulded under a pressure of 100 kg/cm^2 was heated at 600 ℃-800 ℃ and continued up to 1400 ℃ in the presence of nitrogen with 5-15 ℃/*min.* This process will be possible with different additives of ultrafine powders of metal oxides, metal carbides, and metal

nitrides—achieved hardness 320 HV. In this process the sintered sample contains AlN and Al_2O_3 are both phases [64].

- AlN with 0-10 wt% of tungsten (W) milled by using high energy ball milling, and the powdered samples were dried in a vacuum furnace for 2 h at 75 ℃ and this dried powder filled in a graphite crucible and sintered at 1400 ℃ - 1700 ℃ with 20 min holding time, with 100 ℃/*min* in spark plasma sintering method, dielectric properties measured in the range from (1 kHz -1 MHz). Obtained ceramics had a relative density of 84.4%, with dielectric permittivity of 10-60 and a dissipation factor of $10\text{-}10^{-4}$. [65]
- AlN with 0-3 wt% of CaF_2 was planetary ball milled for 8 h using ethanol as a grinding media, then dried in vacuum, sintered in spark plasma sintering method at 1800 ℃ at a heating rate of 100 ℃/*min*, in a nitrogen atmosphere with 15 *min* holding time, 30 MPa pressure was applied from the beginning of the sintering. Achieved 99.8% with a transmittance of 54.7% [66].
- Additives and AlN initial powders were dispersed in alcohol by sonication and mechanical agitation. This slurry was dried in the oven and sintered in spark plasma sintering method at 1700 ℃-1850 ℃ with 5 min dwelling time in nitrogen gas of 0.07 MPa; sample pressure kept constant 25 MPa while sintering.

AlN ceramics sintered at 1850 ℃ with 5 min dwelling time reached 95% relative density and obtained thermal conductivity 66 $W/m\text{-}°K$.

AlN – (1.5 wt%) (Sm_2O_3 – Y_2O_3) composite sintered at 1750 ℃ for 5 min reached 98.6% relative density, shows 113 $W/m\text{-}°K$thermal conductivity.

AlN + (1.5 wt%) Sm_2O_3 + 1 wt% Li_2O composition sintered at 1750 ℃ for 5 min reached 98.5% relative density with 93 $W/m\text{-}°K$thermal conductivity.

AlN + (2 wt%) Sm_2O_3 composite sintered at 1780 ℃ for 5 min reached 99.4% relative density and achieved thermal conductivity 131 $W/m\text{-}°K$.[67]

- Nitride (AlN, BN) ceramics were fabricated in different methods, i.e., conventional sintering, spark plasma sintering (SPS), and microwave sintering. These have their limitations. Conventional sintering requires more time, plasma sintering is costly and rare, and microwave sintering is risky to operate. Even by sintering in these methods, there are few literatures on the pure phase of the resultant product [38, 68–70].
- Adding additives can enhance the thermal conductivity of nitride ceramics. The thermal conductivity of AlN ceramics is enhanced by adding a $CaZrO_3$ additive. The density of the product reached theoretical density due to a decrease in porosity and formed microstructure with clear boundaries by replacing Al, N vacancies with additive elements [68].
- However, the synthesis of pure AlN is complicated because of its low chemical stability [71–74]. Achieving 100% density is challenging due to its covalent bond nature. While sintering, oxygen can settle on the grain boundaries and in the AlN lattice. This oxygen scatters the primary heat carrier (phonon), decreasing thermal conductivity [75].
- Most of the used additives were rare earth oxides and alkaline earth oxides for AlN ceramic's densification. While sintering, these additives form a liquid phase, resulting in the ceramics' densification at lower temperatures [76, 77]. The most used rare earth oxide additives for fabricating AlN ceramics were Sm_2O_3 and Y_2O_3. These additives help to densify AlN by forming the liquid phase, but the formation of secondary phases was inevitable. Hence, the chemical inertness of AlN would be lost. These additives helped to densify the ceramics but could not eliminate the secondary phase [77–79].
- However, AlN with ZnO and Er_2O_3 additives has not been studied intensively. The pressure-less sintering method easily creates a problem of aluminum vacancies in AlN since oxygen can easily replace nitrogen to form aluminum vacancies while sintering at high temperatures. Oxygen in AlN is in the form of Al_2O_3 [80, 81]. The oxide additives react with

Al_2O_3-covered AlN particles and help remove Al_2O_3 by reacting, avoiding Al^{3+} vacancies, and reducing pores by forming a liquid phase [82].

1.7 Literature gap and motivation of the present work

- Based on the literature survey, it is found that most of the studies are focused on densifying AlN ceramics by sintering at high temperatures. Even though very few studies achieved pure phase by sintering at high temperatures with special sintering techniques such as spark plasma sintering and hot press. To use AlN for practical applications, there is a need to fabricate AlN ceramics in a cost-effective method with pure phase and to reduce sintering temperature.
- There is no literature on preparing AlN composite ceramics with oxides and nitrides as additives obtained pure phase with low sintering temperature. It is necessary to reduce the sintering temperature for fabricating AlN ceramics with pure phase to modify the sintering method to make it abundant.
- However, the ideal phase pure AlN ceramics with high density, good dielectric properties at different temperatures, and structural properties are necessary for RF window applications. Since RF windows must be used in different environments to separate high-pressurized environments from standard atmospheres, studying AlN ceramics' temperature-dependent properties and mechanical properties is essential. The literature reveals no complete study on pure and composite AlN ceramics' temperature-dependent structural and dielectric properties.
- No literature exists on the temperature-dependent dielectric permittivity, dissipation factor, and impedance analysis of AlN ceramics in the frequency range from 1 kHz to 100 MHz. These broadband frequency studies with temperature stability and pure phase AlN ceramics studies are necessary for electronic and RF window applications.

This literature survey reveals that preparing nitride materials (AlN, BN) in bulk mode was unsuccessful. There is much scope to reduce the processing temperature and improve their properties. The AlN ceramics prepared in different methods lag pure phase, i.e., products with some secondary phases as their respective oxides or additive composites.

It is very challenging to fabricate nitride materials with high purity at low temperatures. Thus, this motivated us to study AlN ceramics to prepare with pure phase as follows;

1.8 Objectives of the thesis:

The present thesis aims to prepare pure AlN and composite AlN ceramics with oxides and nitride additives in a new method. It also aims to reduce sintering temperature, improve density, and study the dielectric properties of pure and composite AlN ceramics. This thesis focuses on the effect of oxide and nitride additives on AlN ceramics' structural and dielectric properties, as shown in the schematic diagram in Figure 1.7.

- The primary objective of the present thesis work is to provide pure-phase AlN ceramics with maximum relative density at low sintering temperatures.
- To achieve maximum relative density, good mechanical and microwave dielectric properties.
- To suppress the formation of Al_2O_3 (oxidation reduction) during the high-temperature sintering process and to get phase pure AlN ceramics.
- To provide a method to obtain phase pure and densified AlN ceramics, which would be environmentally friendly.

In addition to the above points, the objectives of the thesis are extended as follows;

- To investigate the modified sintering method to prepare phase pure AlN ceramics.

- Study the effect of oxide additives (ZnO and Er_2O_3) on the structural and dielectric properties of AlN ceramics sintered in conventional sintering using a powder bed.
- To study the effect of nitride additives such as BN on the structural and dielectric properties of AlN ceramics.
- To compare the effect of the sintering method on structural and dielectric properties of AlN ceramics.

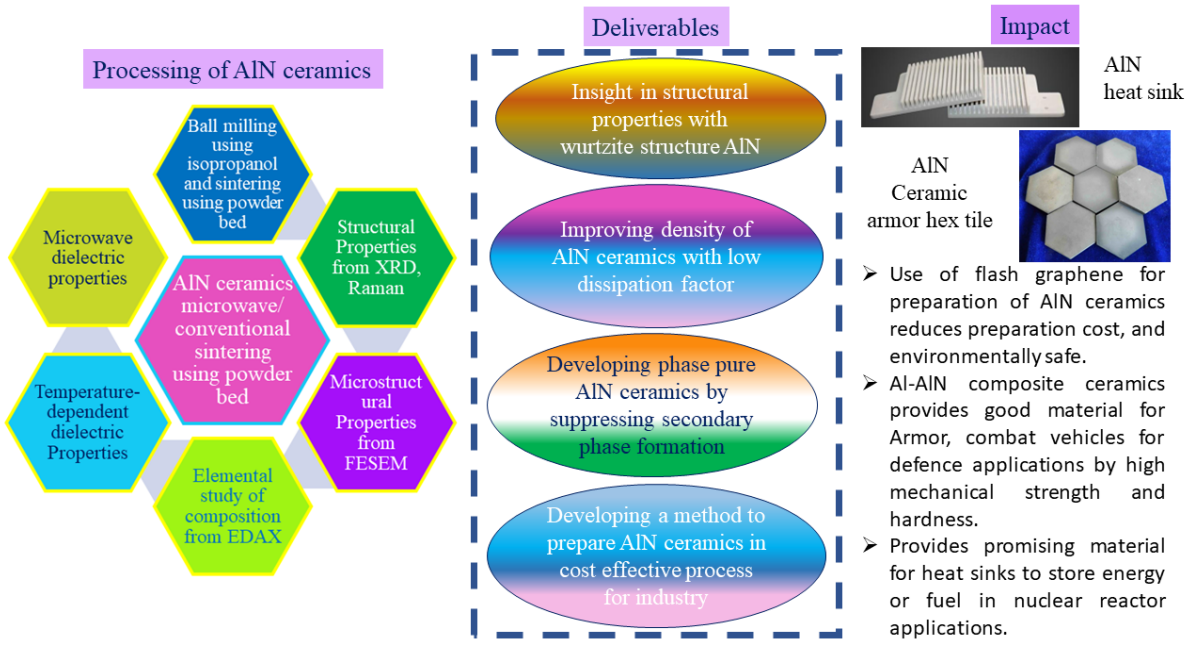

***Figure 1. 7*: Schematic diagram of processing of AlN ceramics with its impact on applications.**

1.9 Outline of the thesis

This thesis investigates the process for preparing phase pure AlN ceramics and sintering conditions, and appropriate additives to densify AlN ceramics at low sintering temperatures are studied. The physical properties such as structural and dielectric properties for pure and composite AlN ceramics are explored for the suitability of the material to be used for RF windows in microwave devices and electronic applications such as heat dissipators, substrate material, PCB (printed circuit board), etc., (low permittivity, low dissipation factor, and temperature stability). This thesis explains the effect of oxide and nitride additives on

structural, microstructural, dielectric permittivity, and dissipation factors. Temperature (RT to 400 ℃) - frequency (1 kHz to 1 MHz) dependent dielectric, microwave dielectric properties, and structural properties of pure and composite AlN ceramics are studied systematically. This thesis uses conventional and microwave sintering techniques to compare the effect of the sintering method on density, structural, and dielectric properties investigated by sintering pure and additive AlN ceramics.

Chapter 1 briefly introduces dielectric materials, RF windows, and related areas. This chapter discusses dielectrics' theory and fundamental concepts, various applications, especially RF-window and electronic applications. Also, RF-window's essential aspects and requirements with the current status of materials developed for RF-window applications. The importance of dielectric resonators with polarization mechanisms inside them is discussed. The low-loss nitride materials applications in electronic applications, a literature survey of aluminium nitride (AlN) ceramics with a literature gap are also discussed, including the research problem. The motivation behind the selection of AlN with objectives is presented at the end of chapter 1.

Chapter 2 describes the various methods used for preparing pure AlN and composite AlN ceramics. AlN ceramics have been synthesized using solid-state reaction and microwave sintering methods. The conventional and the microwave sintering mechanisms are discussed briefly. It also describes the characterization techniques of nitride ceramics such as XRD (X-Ray Diffraction), Raman, FESEM (Field Emission Scanning Electron Microscope), dielectric measurements (LCR meter, Impedance analyzer), microwave dielectric measurement (VNA), and AFM with their basic working principle and arrangement.

Chapter 3 describes the new method to prepare phase pure AlN ceramics using the conventional sintering method. Densifying AlN ceramics requires high sintering temperatures >1900 °C in a special environment (presence of nitrogen). Different sintering techniques are

used to increase the density of AlN ceramics, such as microwave, spark plasma, and conventional sintering techniques. Microwave sintering of AlN ceramics processing at high temperatures is a high-risk rate, spark plasma sintering furnace is rarely available and extravagant, and conventional sintering is inexpensive but time-intensive. Synthesizing phase pure AlN ceramics is challenging because of its oxidizing nature at high sintering temperatures during sintering. This study focuses on preparing phase pure AlN ceramics with temperature-dependent dielectric and structural properties. In this survey, AlN ceramics are synthesized at a low temperature of 1700 °C for 30 h by applying the powder bed (70% AlN powder and 30% carbon (C) powder) method in the presence of nitrogen. These obtained ceramics exhibited a high relative density of ~95% with pure AlN phase belonging to space group $P6_3mc$, confirmed from XRD refinement. It is conspicuous to note that the formation of Al_2O_3 is prevented using a powder bed, proven by the XRD and Raman spectra. The smaller initial particle sizes of the AlN powder lead to improved density at the lower sintering temperatures. The Raman spectra of AlN ceramics confirm the wurtzite structure by exhibiting six standard vibrational modes. The average grain size obtained for the sintered AlN ceramic is ~1.45 μm. The Raman spectrum of AlN ceramics recorded at various temperatures confirms the structure stability with stable wurtzite structure phonon modes. Good microwave dielectric properties as $\varepsilon_r = 8.83$ and $\tan\delta = 2.69 \times 10^{-4}$ achieved by the sintered AlN ceramics. AlN ceramic exhibited the best dielectric properties from 1 MHz to 100 MHz at temperatures from -140 °C to 200 °C. Thus, the obtained properties of AlN ceramics with pure phase are essential and best suited for RF-window and electronic applications.

Chapter 4 presents a systematic study of the effect of oxide additives on AlN ceramics by considering zinc oxide (ZnO) and rare earth oxide Er_2O_3 as additives—the composite AlN ceramics with oxide additives (ZnO) prepared by optimizing the ball milling time and sintering temperature. The prepared composite ceramics' structural and dielectric properties are studied

systematically. AlN (pure and composite) ceramics are sintered in the conventional sintering method at 1700 ℃ in the presence of nitrogen. AlN-ZnO composite powder is prepared by high-energy ball milling. ZnO helps reduce the sintering temperature to 1700 ℃ and densifies AlN at lower temperatures by forming the eutectic phase at around 1400 ℃. The ZnO-added AlN ceramics revealed that the sintered composite ceramics are of pure wurtzite AlN phase by their refined XRD pattern. The powder bed prevents the formation of Al_2O_3 and enhances densification. The frequency and temperature variation dielectric properties of AlN-ZnO composite ceramics are studied. The powder bed helps reduce pores, implying a low dissipation factor with a good dielectric response. The microwave dielectric properties of AlN-ZnO composite ceramics show the best dielectric permittivity ($\varepsilon_r = 7.20$) and dissipation factor ($\tan\delta = 4.90 \times 10^{-3}$) for the best composite AlN-15ZnO ceramic.

The aluminum nitride (AlN) disc of negligible reflection and transmission loss is developed to handle average and peak power of 6 kW and 6 MW, respectively, for pillbox-type S-band dielectric windows. Pure and Er_2O_3 doped AlN ceramics of dimension 10 mm x 5 mm (diameter x thicknesses) are synthesized at 1700^{o}C using the solid-state reaction method with the sintering bed (the combination of AlN and carbon powders). Engrossing, this process helps prevent the formation of Al_2O_3 completely while sintering at high temperatures. The diffractometry of pure and Er_2O_3-added AlN ceramics exhibited the wurtzite AlN structure of space group $P6_3mc$. The AlN ceramics with Er_2O_3 additive exhibited microwave dielectric properties ($\varepsilon_r = 7.81$ and $\tan\delta = 5\text{x}10^{-4}$) at 12 GHz. The dielectric window is designed using CST (Computer Simulation Technology) with the experimentally obtained dielectric properties as input. The theoretical value of the window's insertion loss and return loss is better than 61.25 dB and 0.009 dB, respectively, at 3.7 GHz.

In **Chapter 5**, the effect of nitride additives on the structural and dielectric properties of AlN ceramics is studied. AlN-BN composite ceramics are prepared with pure AlN

(aluminium nitride) phase using a powder bed in the conventional sintering method. The powder bed comprises 80% AlN powder and 20% Carbon (C) powder as layers. The effect of adding BN (boron nitride) on the structural and dielectric properties of AlN ceramics is studied by sintering in the conventional sintering method in the presence of nitrogen using a powder bed. The additive for synthesizing AlN-BN composite ceramics was chosen from 0-20 wt%. The AlN-BN composite ceramics sintered at 1700 ℃ for 20 h in the presence of nitrogen. The obtained composites exhibit pure AlN phase without any oxide phases (secondary phases). The XRD pattern and Raman spectrum of all obtained composites confirm the structure as wurtzite AlN with $P6_3mc$ space group with a small peak corresponding to BN with no other oxide phases. The Raman spectrum shows six vibrational modes of wurtzite structure at every temperature and confirms the stability of the composite with temperature variation. The dielectric properties of AlN-BN composite ceramics are studied by varying temperatures from 30-500 ℃, with frequency variation from 1 kHz to 1 MHz systematically.

Chapter 6: This investigation demonstrates the comparative studies of conventional and microwave sintering of AlN ceramics with $CaZrO_3$ and Y_2O_3 as additives. Additives are considered the same for conventional and microwave sintering methods and studied the properties of obtained ceramics. In the conventional sintering method, the samples are sintered at 1700 ℃ for 20 h dwelling time, while in the microwave sintering method, the samples are sintered at 1400 ℃ for 30 min. A powder bed is adopted in the conventional sintering method, while in the microwave sintering method, the susceptor bed is adopted to sinter at low temperatures. The powder bed and susceptor bed both contain AlN and carbon powder as a combination layer to prevent oxidation while sintering. High relative density above 95% is obtained through both methods for additive ACZ2Y sample; in microwave sintering, 97.68% and 98.87% relative density is achieved in conventional sintering. In both sintering ways, pure wurtzite structure without any secondary phase with space group $P6_3mc$ is obtained for all pure

and additive ceramics. The Raman spectrum of all sintered samples confirms the wurtzite structure by exhibiting six vibrational modes in both sintering methods. Dielectric properties are studied at temperatures ranging from -140 to 250 ℃ for higher frequencies (1 MHz to 100 MHz). The best composite ACZ2Y ceramic sintered in conventional sintering shows dielectric permittivity $7.99 \leq \varepsilon_r \leq 8.61$ and $0.12 \times 10^{-2} \leq \tan\delta \leq 5.21 \times 10^{-2}$ and for the composite sintered in microwave sintering exhibited as $7.20 \leq \varepsilon_r \leq 7.96$ and $0.31 \times 10^{-2} \leq \tan\delta \leq 1.37 \times 10^{-2}$. The microwave sintered composite ceramics show low dissipation factor and low dielectric permittivity with minimal variation with temperature in the higher frequency range of 1 MHz to 100 MHz due to highly densified and compacted small grains compared with conventional sintered samples. The microwave dielectric properties of the best composite ACZ2Y ceramic sintered in the conventional sintering method achieved a dielectric permittivity of 9.94 and a low dissipation factor of 11.05 x 10^{-4}. The composite ceramic is sintered in the microwave sintering method, obtaining a dielectric permittivity of 9.00 and a low dissipation factor of 7.34 x 10^{-4}. Conventional sintered composite ceramics achieve good dielectric properties with higher relative density than the sample sintered in the microwave sintering method, but a time-consuming process. Microwave sintered composite ceramics also exhibit good dielectric permittivity with a lower dissipation factor than that obtained in the conventional sintering method with appropriate relative density and achieved in less time duration at lower sintering temperature.

Chapter 7: Summarizes the process of preparing pure aluminium nitride (AlN) ceramics, with other oxide and nitride composite ceramics. This chapter summarizes the best results obtained in this research work for RF-window and electronic applications in the present world. It also contains the future scope of the work to improve properties and for the complete study of AlN ceramics for expanding applications. Thin film bilayer and multilayer can be

deposited for sensor applications and to improve thermal conductivity, piezoelectric and dielectric properties.

Chapter 2

Preparation Methods, and Characterization Techniques

This chapter describes the preparation methods of nitride ceramics with various experimental techniques implemented to characterize the nitride ceramics. Section 2.1 and its sub-sections describe nitride ceramics' preparation by solid-state reaction method and sintering mechanisms. Section 2.2 explains various characterization techniques for studying structural, microstructural, dielectric, microwave dielectric, and optical properties of nitride ceramics.

2.1 Preparation techniques of ceramics

This section deals with the preparation techniques used to prepare nitride ceramics. Since these nitride materials must be characterized for RF-window applications in the microwave range, they must be prepared with the highest density and in regular geometry. The required material, a nitride material, must face many challenges while sintering to avoid oxidation and in densifying nitride ceramics. Several methods have been developed to synthesize pure nitride and composite ceramics with good purity and homogeneity, such as the solid-state reaction [1-2], sol-gel process [3-4], microwave sintering [5–7], spark plasma sintering [8–10], etc. In this thesis, a conventional solid-state reaction method with a powder bed and a microwave sintering with a susceptor bed is used to prepare phase pure nitride ceramics.

2.1.1 The conventional solid-state reaction method

Ceramics are polycrystalline materials with fine grains with imperfections like grain boundaries, pores, and impurities incorporated in the grains. Generally, ceramics are brittle refractories; hence, carving and densifying them without cracks and deformation is

challenging. The conventional solid-state reaction method forms pure AlN and additive AlN composites from the initial reagents.

In this work, the conventional solid-state reaction method involves the synthesis of an additive selected for preparing AlN composites. This method combines initial reagents by milling to satisfy the chemical reaction to form a specific composite. Then, calcination at high temperatures allows interdiffusion of cations for oxide additives. In this process, re-milling reduces composite particle size, then milling with nitrides to make composites.

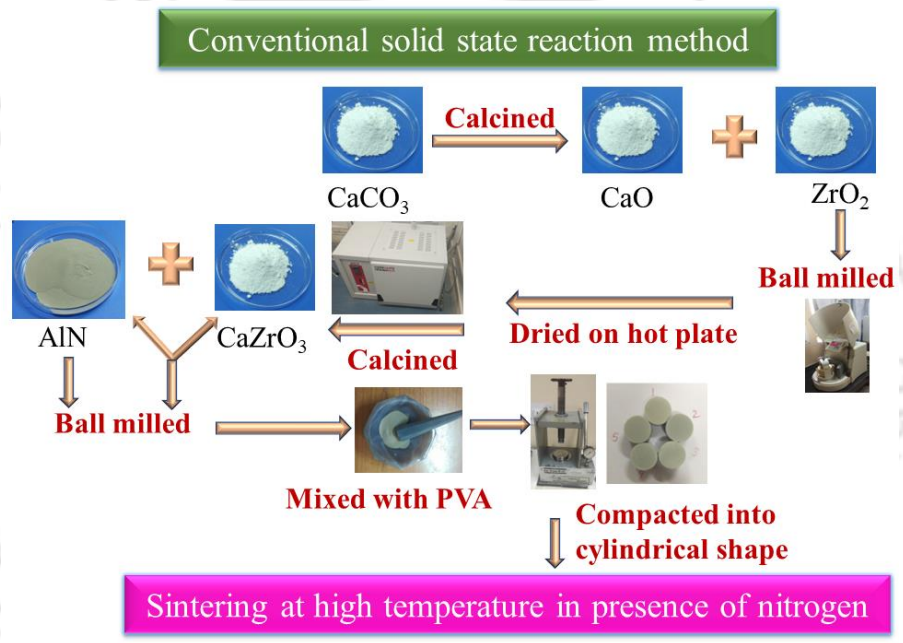

Figure 2. 1: The schematic diagram of the synthesis procedure in a conventional solid-state reaction method.

This method produces complex oxides from simple oxides, carbonates, nitrates, oxalates, hydroxides, alkoxides, and other metal salts. Usually, this method includes annealing steps with several intermediate milling steps to increase the composite's homogeneity and reduce particle size. This reduction of particle size helps to increase the active nature of powder particles to form densified ceramics in further subsequent heat treatment steps (sintering). The schematic diagram of various stages of the synthesis of composite in the CSSR method is

shown in Figure 2. 1. The conventional solid-state reaction method requires simple apparatus and is inexpensive. This method is thermodynamically stable, eco-friendly, and simple and produces a stoichiometric stable and pure final product.

2.1.2 Mechanochemical processing

Mechanochemical processing (MCP) is the combined process of both mechanical process and chemical reactions. This mechanochemical processing name itself reveals that in MCP, the chemical reaction takes place, phase transformations occur and make the material with fine particles by the application of mechanical energy. Different types of high-energy ball mills are available with high enough mechanical energy output to induce many chemical reactions due to advancements in modern technology [90, 91]. There are three different types of mechanochemical processes: 1) Mechanical milling (MM), 2) Mechanical alloying, and 3) Reaction milling (RM). Mechanical milling (MM) is needed to reduce the particle size of the pure metal or compound in a state of thermodynamic equilibrium at the start of the ball milling process. Mechanical alloying (MA) is needed to form an alloy or compound by milling elemental or some chemicals as precursors. Reaction milling (RM) is used to prepare compounds where there is a need to induce chemical reactions by the milling process of reactants. In mechanically activated chemical reactions, mechanical energy is considered input, which is supplied repeatedly. It leads to shifts of atoms from the equilibrium positions due to inducing changes in the bond lengths and angles and, in some cases, by exciting electron subsystems.

Mechanical milling exists in three effective methods depending on their milling mechanisms. These methods are tumbler milling, vibratory milling, and planetary milling. These milling process schematic diagrams are shown in Figure 2.2 with rotating directions. The particle size of a resultant compound due to these milling types depends upon machine

type, milling time, speed, milling media, kind of vial used, temperature effects, and milling atmosphere, etc., as shown in Figure 2.3.

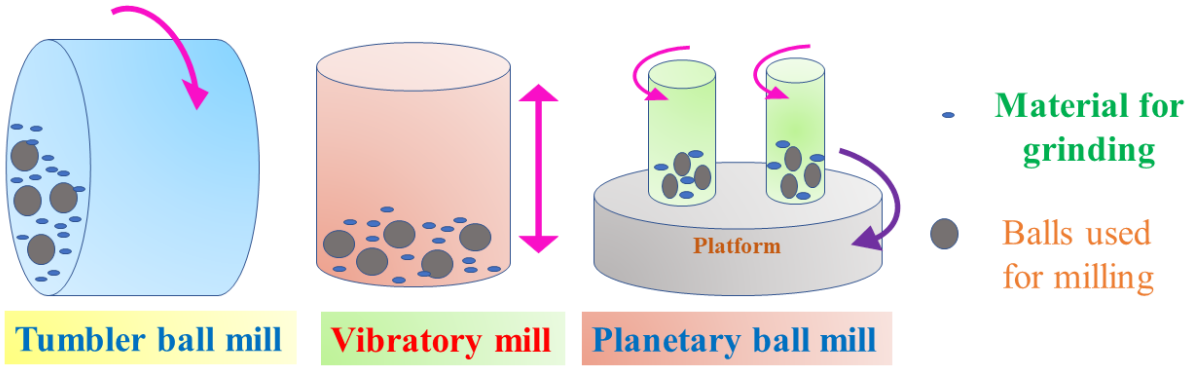

Figure 2. 2: Schematic diagram of different types of milling processes.

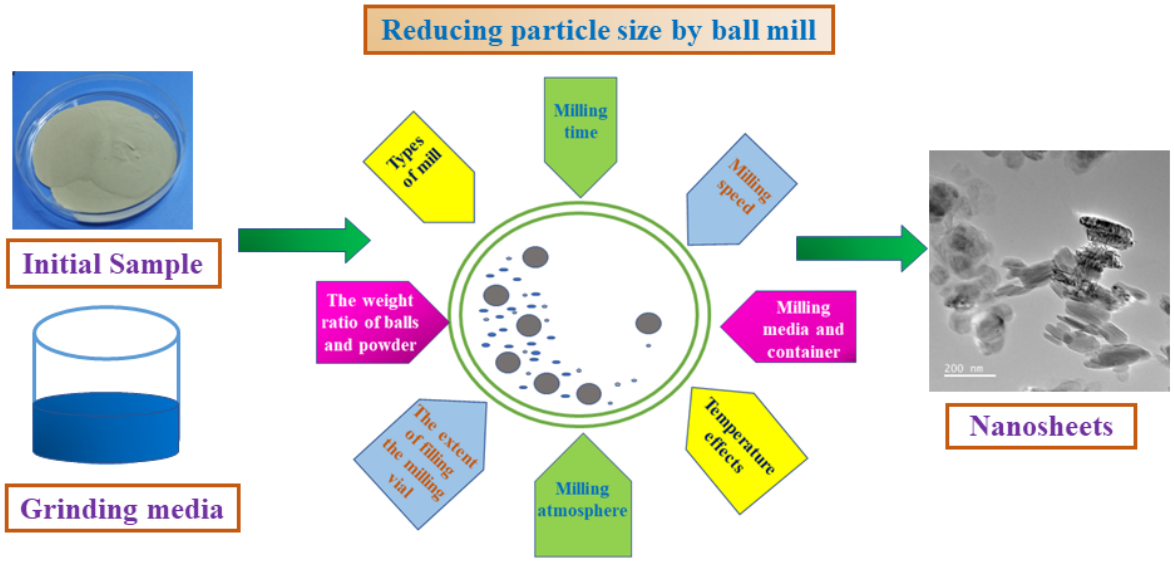

Figure 2. 3: The parameters affecting particle size reduction by the ball mill method.

The material to reduce particle size using a ball mill (planetary ball mill (M/s Fritsch, Pulverisette 6)) is taken in a suitable vial with a powder-to-ball ratio of 1:10. Figure 2.4(a) shows the planetary ball mill. Primarily, grinding balls will have a high energy impact on the material. For this impact, the grinding vial and balls rotate around their axis on a supporting disk rotating in the opposite direction, as shown in Figure 2.4(b). Ground material and grinding balls will separate the inner wall of the vial at a certain speed due to the centrifugal force. Hence, grinding balls cross the vial at high speed and further grind the material by impact against the opposite vail wall. In addition to the effects of a

ball on material against the vial wall, the impact between the balls on the material helps reduce particle size or mix initial reactants to form the compound.

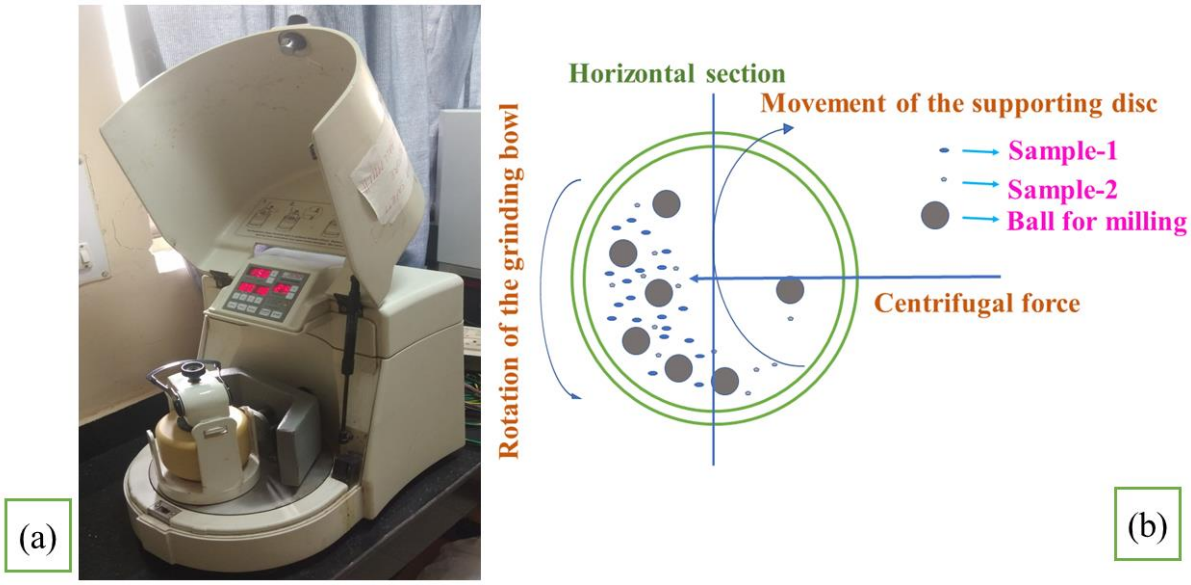

***Figure 2. 4*: (a) Photographic view of the planetary ball mill used to mix the initial powders and to reduce particle size and (b) Schematic view of the milling process.**

2.1.3 Particle size reduction

Particle size reduction is crucial for manufacturing ceramics. The particle size of the initial raw powders used to make ceramics will directly affect the physical and mechanical properties. It is a well-known fact that the sintering temperature of the ceramics reduces, and density is enhanced due to the reduction in particle size of the initial raw material. Hence, minimizing the initial raw material's particle size is essential to reduce nitride ceramics' sintering temperature to enhance the density and thermal conductivity. This study uses a planetary ball mill to mix the additive with AlN for uniform mixing and the second for particle size reduction. Zirconia/ tungsten vials with 5 & 10 mm diameter spherical balls mill the raw materials. The processing parameters of the ball mill are milling speed (rotations per minute), milling time (number of repetitions per cycle, time per one cycle, pass the time between consequent repetitions), and the ratio of ball weight to raw chemical weight. Ball mill processing parameters are optimized to reduce particle size without any secondary phase formation.

2.1.4 Uniaxial pressing

The fine powder (pure and composites) obtained after ball milling, mixed with organic binder polyvinyl alcohol, and compacted into cylindrical specimens (green discs) by uniaxial pressing using Kbr hydraulic press (M-20, Techno search Instruments, India) shown in Figure 2.5. These cylindrical-shaped discs are dimension 10 mm in diameter and 1 mm or 5 mm thick. Slow compaction of powder facilitates the escape of the entrapped air in the powder.

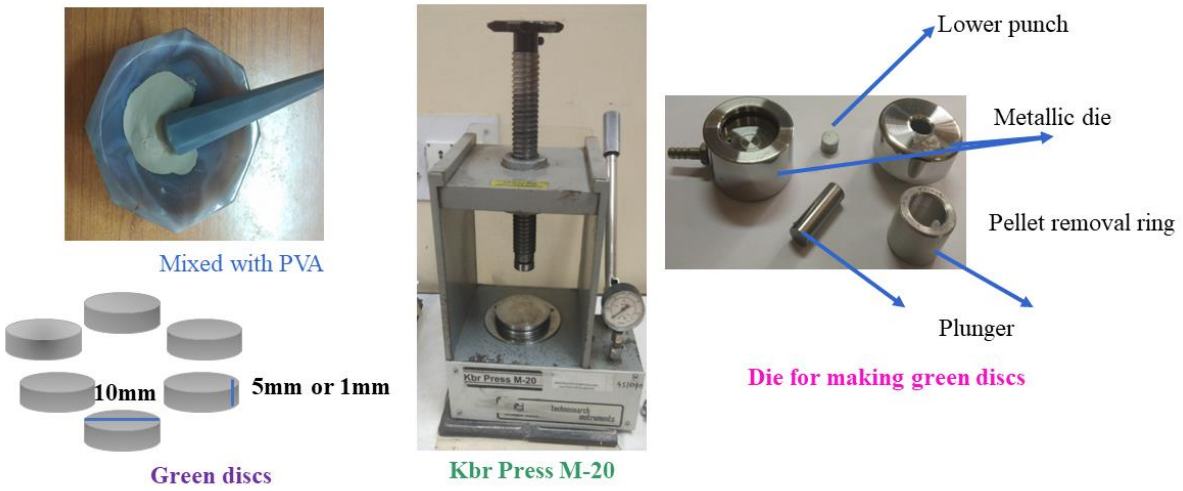

Figure 2. 5: The green compacted discs of aluminium nitride using a die by Kbr press M-20.

The high-pressure unit supplies hydraulic fluid to the up-stroking ram of the cylinder and helps raise the ram steadily and positively in the upward direction. Thus, the pressure is applied and produces a green compacted pellet. The ratio of pressure gradient on the die (P_x) and applied pressure (P_a) is given by the following equation

$$\frac{P_x}{P_a} = e^{\frac{-4\mu KL}{D}} \tag{2.1}$$

Where μ is the coefficient of friction, L is the length, D is the diameter of the die, and K is a constant [92].

2.1.5 Conventional sintering

Sintering is a process of thermal treatment for bonding particles into a predominantly solid structure via mass transport that often occurs on the atomic scale. In this process, the surface energy consumed in bonding particles enhances the compact strength and is often a dimensional change. Sintering involves transforming a powder-compact (pellet) into a strongly bonded monolithic mass by removing interparticulate pores. The tiny particles or clusters of particles with uniform composition change in shape and size by heating at a sufficiently high temperature is also considered sintering. According to ISO definition, the heat treatment performed on the powder compact at a temperature below its melting point to bond particles by atomic forces, thus producing strength and hardness of compacted sample, is termed as sintering. The sintering temperature is optimized between 0.7 and 0.9 of the compound's melting point. At this elevated temperature selected for sintering, atoms are free to diffuse. The sintering furnace used in this study (M/s Carbolite Gero, HTF 18/4 220-240V 1PH, 21-801839) is shown in Figure 2.6. Thus, in this sintering, the compound is not melting since the sintering temperature selected is below its melting temperature.

***Figure 2. 6*: Photograph of the conventional sintering furnace.**

Hence, this conventional sintering is also termed solid-state sintering or solid-phase sintering. The heat treatment consists mainly of three steps: 1) preheat, 2) sintering, and 3) cooling process, as shown in Figure 2.7. The binder or lubricants used to make compacts such as PVA are burned off or evaporated in the first process termed preheat. In sintering, the compact strengthens by densification and reduction in pores, as shown in Figure 2.8, and bonded particles by diffusion due to atomic forces. The final step in the sintering process involves the cooling process. The cooling process can be done in two ways: standard cooling or by setting a program for cooling fast.

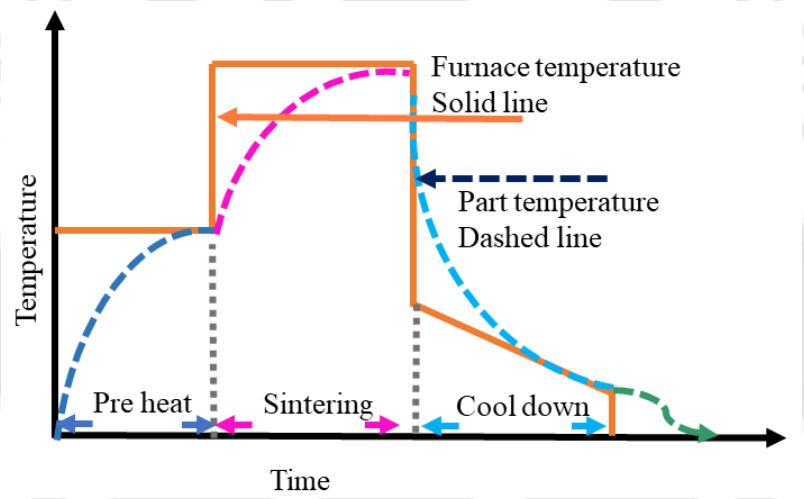

Figure 2. 7: Schematic diagram of heat treatment in sintering.

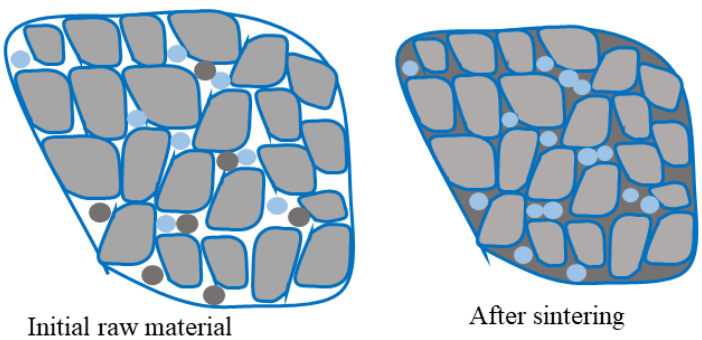

Figure 2. 8: schematic diagram of densification of a compound in sintering by reducing pores.

The cooling process from high temperature to some minimum of 200 ℃ can be done by programming with a low cooling rate; a lower than 200 ℃ normal cooling process is preferable. The key parameters that play a role while sintering is atmosphere, dwelling time, and heating or cooling rate. A specific inert gas atmosphere must be maintained to avoid the undesirable surface layer formation on the compound surface (oxidized layer). The heating and cooling rate will affect the formation of grains and reduce pores significantly [93].

2.1.6 Microwave sintering

Microwave energy is an electromagnetic wave with a frequency range of 300 MHz to 300 GHz with a corresponding wavelength between 1 mm and 1 m. Microwaves are extensively used in communication applications such as radar, television, and satellite [94]. The other application of microwaves is the heating of different materials. 2.45 GHz frequency is the most commonly used home microwave oven invented by Percy L. Spencer [95]. Heat is generated by heating elements and transformed into samples via radiation, conduction, and convection in conventional sintering. In microwave sintering, the material gets heat within its body by absorbing microwaves [96]. The heating of the material in microwave sintering depends upon the penetration depth of microwaves into it. The penetration depth of the microwave field inside the material is defined as *1/e* time of the depth from the material's surface at which the microwave field's magnitude drops. The penetration depth or skin depth (*D*) mathematically can be expressed as follows [97];

$$D = \frac{1}{\sqrt{(\pi f \sigma \mu)}} = 0.029(\rho_e \lambda_0)^{1/2} \quad (2.2)$$

where f is the microwave frequency, σ is the electrical conductivity of the material (S/m), μ is the magnetic permeability of the material H/m, ρ_e is the electrical resistivity of the material, and λ_0 is the incident wavelength of the microwave. This equation reveals the material's high

conductivity results in a low penetration depth. Thus, the penetration depth of metals is very low since the metals are good conductors of heat. However, the penetration depth of metals increases by increasing the metals' processing temperature [98].

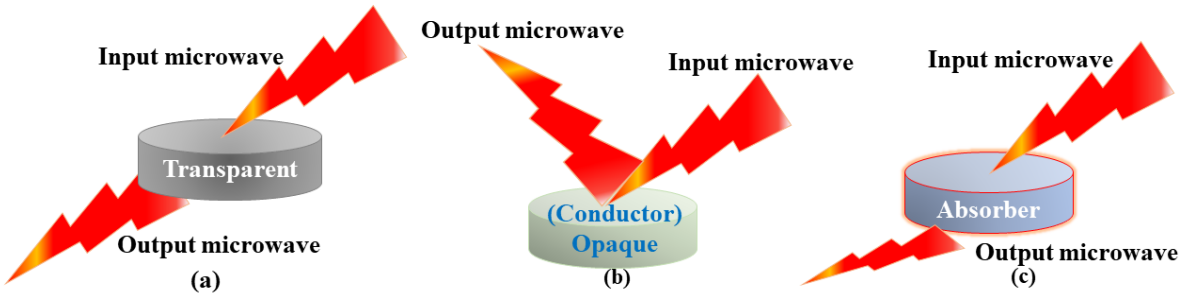

***Figure 2. 9*: The interaction of microwaves with different materials.**

The materials are classified into three types depending upon the interaction of microwaves with them, as shown in Figure 2.9. (a) transparent materials are materials with low dielectric loss (dissipation factor) materials.

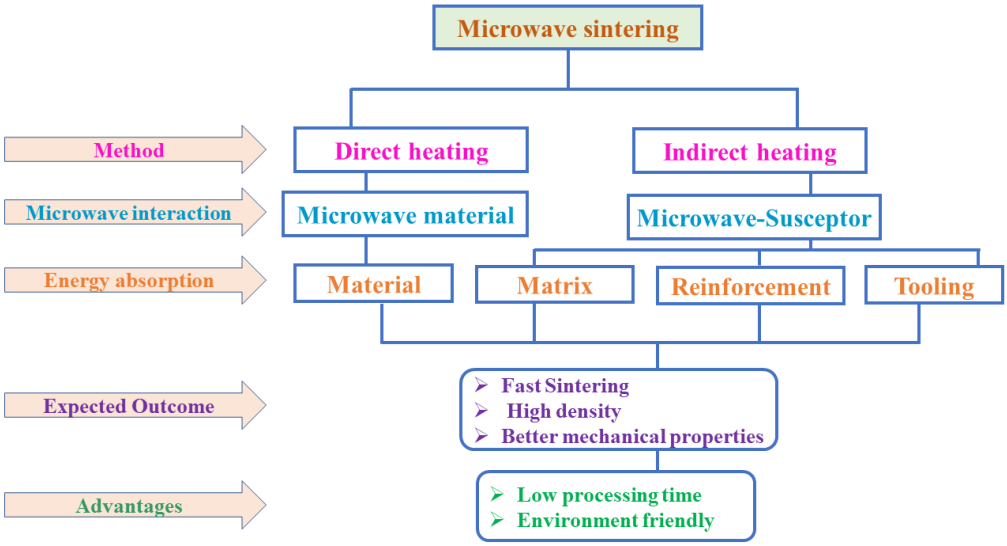

***Figure 2. 10*: The steps involved in the microwave sintering process in sintering material.**

In transparent materials, microwaves transmit without any losses. Figure 2.9(b) opaque (conductors) materials are materials with high conductivity. Microwaves reflect and cannot penetrate through opaque materials (opaque materials used in radar detection). And Figure 2.9(c) absorber materials are the materials with high dielectric loss. The absorber materials

absorb microwaves depending on their dissipation factor value. The steps involved in microwave sintering are shown in Figure 2.10. The material which absorbs microwaves transforms into heat according to the following equation [97];

$$\frac{\Delta T}{\Delta t} = \frac{2\pi f \tan\delta |E|^2}{\rho C_P} \tag{2.3}$$

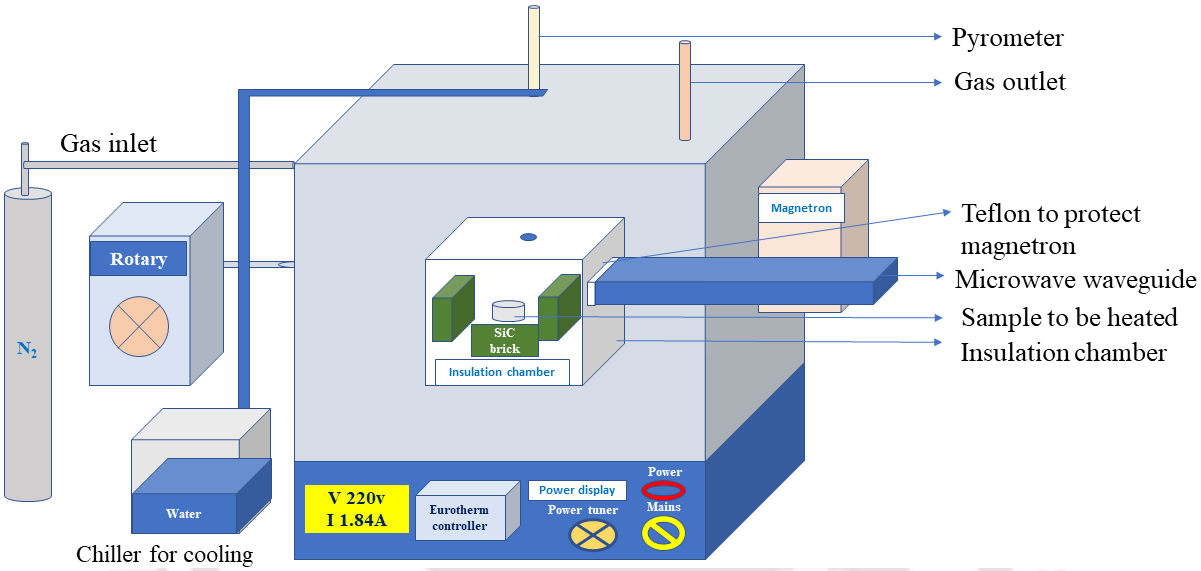

***Figure 2. 11*: The schematic diagram illustrating the microwave furnace and sintering process.**

where T is the temperature, t is time, ρ is the density, C_P is the heat capacity, $\tan\delta$ is the dissipation factor, and E is the magnitude of an internal electric field. The average absorbed power is a volumetric absorption of microwave energy in material expressed as follows;

$$P = \frac{1}{2}\omega \tan\delta\, E^2 V e^{-2\alpha z} = \frac{1}{2} 2\pi f \tan\delta\, E^2 V e^{-2\alpha z} \tag{2.4}$$

where, V is volume, z is the distance into the specimen, ω is $2\,\pi f$, and α is attenuation constant. Two methods are available in microwave sintering, such as direct and indirect heating (see Figure 2.10). This indirect heating method is used to prepare phase pure AlN ceramics without any secondary phase. This microwave susceptor used in this method helps to reduce the sintering temperature and time. The schematic diagram for the microwave sintering furnace

is shown in Figure 2.11. the photograph of the microwave sintering furnace is shown in Figure 2.12. The critical parameters of microwave sintering are atmosphere, microwave susceptor bed material, sintering temperature, and dwelling time.

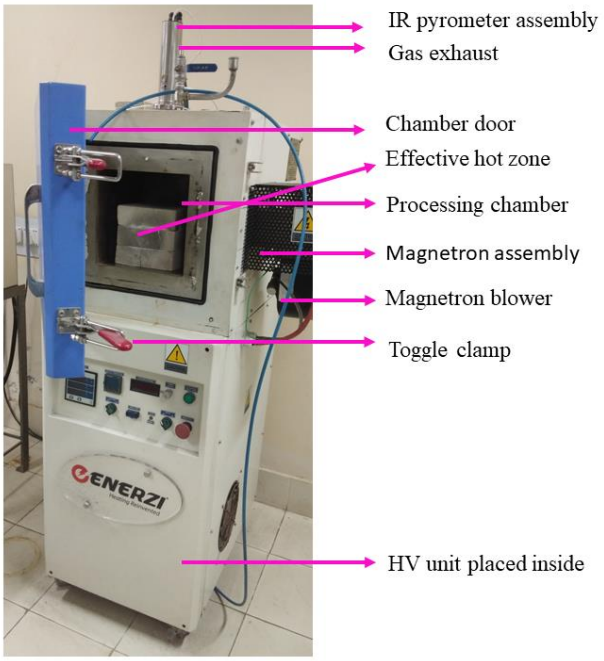

***Figure 2. 12*: Photograph image of the microwave sintering furnace.**

2.1.7 Liquid phase sintering

During the sintering process, if the liquid phase coexists with solid particles for a certain period at a high temperature, then that sintering is termed liquid phase sintering. Diffusion and mass transformation of particles or atoms mechanisms occur much faster in the liquid phase than in the solid phase. Hence, this method significantly enhances the density of the sintered composite ceramic. The liquid phase sintering requires at least two chemical elements. Generally, a mix of powders related to different chemical compositions with a significant component remains solid, and one or more minor components that form a liquid phase act as additives and promote densification below the sintering temperature of the major component. In this method, the liquid phase can be formed in two ways such as by the melting of the

additive (the melting point of the additive should be less than the sintering temperature) or by the formation of low-melting eutectic phase between the solid phase and additive at the end of contacts between them [99]. The liquid phase formed in the liquid phase sintering method can be present during the whole or only for a certain sintering period, depending on the solubility ratio of liquid and solid phases [100]. Volume shrinkage in the sintered ceramic occurs due to the presence of wetting liquid by bulk viscous flow. Each grain in the sintered ceramic is joined with liquid and coated with it; then, the material can often achieve higher density at lower sintering with less tendency of excessive grain growth. In this method, particles will rearrange rapidly due to the transformation of higher density configuration—the liquid in the composite concentrates at particle contacts, causing an adequate compressive pressure on the compact. Particle contacts flatten due to compressive stress by capillary pressure resulting in further enhancement in the densification of the composite after the initial rearrangements of particles [101].

2.2 Characterization techniques

2.2.1 X-Ray diffraction

X-ray diffraction (XRD) is a non-destructive technique for analyzing the material's crystallographic structure, physical properties, and chemical composition. The schematic diagram of the X-ray diffractometer is shown in Figure 2.13. The essential elements of a Bragg Brentano diffractometer are as follows: X-ray tube, flat specimen (labeled sample in Figure 2.13), and goniometer circle (labeled measuring circle in Figure 2.13). The goniometer circle remains constant through analysis defined by the Cu (copper) target's position in the X-ray tube, the position of the receiving slit on the detector side (labeled as detector slit in Figure 2.13), and the center of the specimen (sample). The focusing circle also contains an X-ray tube, the center of the specimen, receiving slit. The focusing circle radius is a function of $\boldsymbol{\theta}$-$2\boldsymbol{\theta}$,

unlike the goniometer circle, which remains constant, with the decreasing radius as $\boldsymbol{\theta}$ increases. $\boldsymbol{\theta}$ is the angle between the incident beam and sample, and $2\boldsymbol{\theta}$ is the angle between the incident and diffracted beams [102]. The slit (labeled as aperture slit) on the incident beam side is used to make it narrow so that it is confined to the area of the specimen.

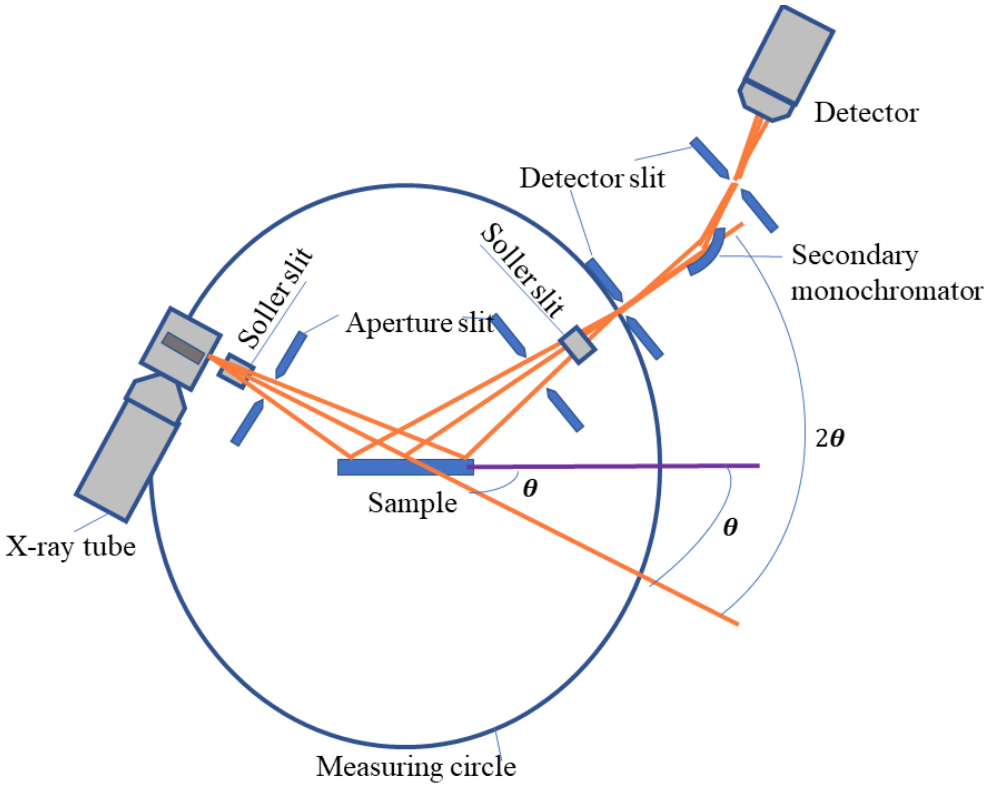

***Figure 2. 13*: Schematic diagram of the X-ray diffractometer.**

Two soller slits are in the XRD diffractometer on both the tube and detector sides. A graphite monochromator is present in this system on the detector side to eliminate the need for a filter. Filter used to remove all except K$\boldsymbol{\alpha}$ radiation from the diffracted beam before entering the detector. When the X-rays interact with the sample, it creates a diffracted beam of X-rays depending upon the interplanar spacing of crystal planes (shown in Figure 2.14) according to a mathematic relation called Bragg's law as follows;

$$n\lambda = 2d \sin\theta \tag{2.5}$$

where *n* is an integer, λ is the wavelength of X-rays, *d* is the interplanar spacing due to which diffraction occurs, and $\boldsymbol{\theta}$ is the diffraction angle. Diffractometer works mainly in two ways, such as $\boldsymbol{\theta}$-$\boldsymbol{\theta}$ scan $\boldsymbol{\theta}$-2$\boldsymbol{\theta}$ scan. In $\boldsymbol{\theta}$-$\boldsymbol{\theta}$ scan, both the detector and X-ray tube move simultaneously; in $\boldsymbol{\theta}$-2$\boldsymbol{\theta}$ scan, the X-ray tube is fixed, and the specimen moves at ½ the rate of the detector to maintain the $\boldsymbol{\theta}$-2$\boldsymbol{\theta}$ geometry. The detector records the angles and intensities of diffractions electronically, using electronics and special software, resulting in a plot of 2$\boldsymbol{\theta}$ versus intensity for the specimen. XRD is useful for studying the structure of materials such as minerals, chemical compounds, ceramics, or other new composites.

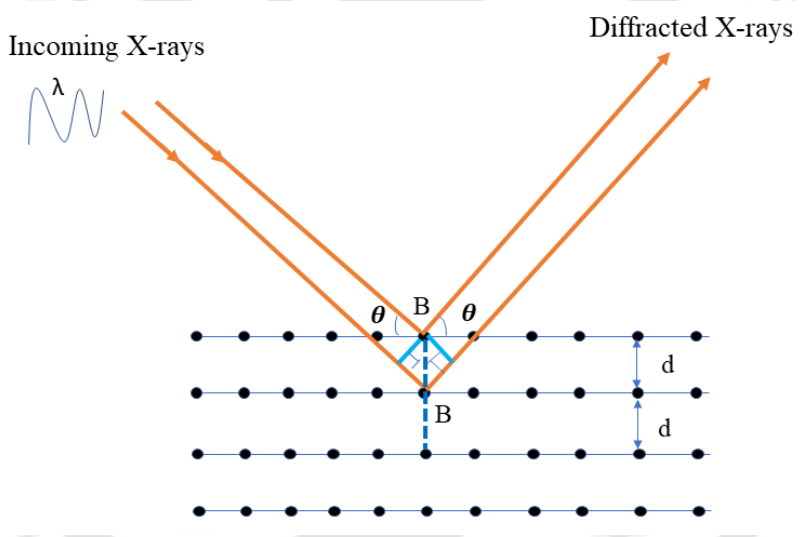

***Figure 2. 14*: Schematic representation of Bragg's law for diffraction in the lattice.**

It also identifies the multi-phases in microcrystalline mixtures and the amorphous phase in partially crystalline mixtures. Crystallographic structural analysis and unit cell calculations can be done using the XRD spectrum. In the present thesis, the Rigaku X-ray diffractometer (TTRAX-III 18 kW) with CuK$\boldsymbol{\alpha}$ (λ = 1.5406 Å) radiation was used to characterize the pure and composite AlN ceramics. The XRD patterns were analyzed using Rietveld refinement [103] with Ful Prof software using the pseudo-Voigt function.

2.2.2 Raman spectroscopy

Raman spectroscopy is a non-destructive analytical technique that provides detailed molecular information about the sample. This spectroscopy measures the transition between vibrational levels of the molecules. Raman spectroscopy is similar to IR spectroscopy, but the principles differ entirely. Raman spectroscopy is based on the inelastic scattering of incident radiation by the molecules present in the sample [104], while IR is based on the absorption of electromagnetic radiation. The Raman spectrum is obtained as follows: the sample is illuminated with a monochromatic laser beam that interacts with the sample's molecules and is scattered.

The scattered light constructs the Raman spectra with a frequency different from the incident light (inelastic scattering). If the frequency of scattered radiation is lower than incident radiation, the Stokes line appears in the Raman spectrum. If the scattered radiation frequency is higher than the incident radiation, the anti-stokes line appears in the Raman spectrum. The energy transfer diagram for a material illuminated with electromagnetic radiation is shown in Figure 2.15. The transitions from lower to higher energy vibrational levels induce stokes shifted Raman bands. These Stokes bands are more intense than anti-stokes bands. Hence, these bands are measured in conventional Raman spectroscopy, while anti-stokes are measured in fluorescing samples since this fluorescence causes interference with stroke lines. Raman shift magnitude does not depend on the wavelength of incident radiation used to illuminate the sample, but Raman scattering depends on it. The essential requirement to obtain the Raman spectra of the sample is a change in polarizability during molecular vibration [105].

There are two Raman spectrophotometers: dispersive and non-dispersive. Prism or grating, A combination of the notch filter and high-quality grating monochromator, is frequently used in the dispersive Raman spectrophotometer.

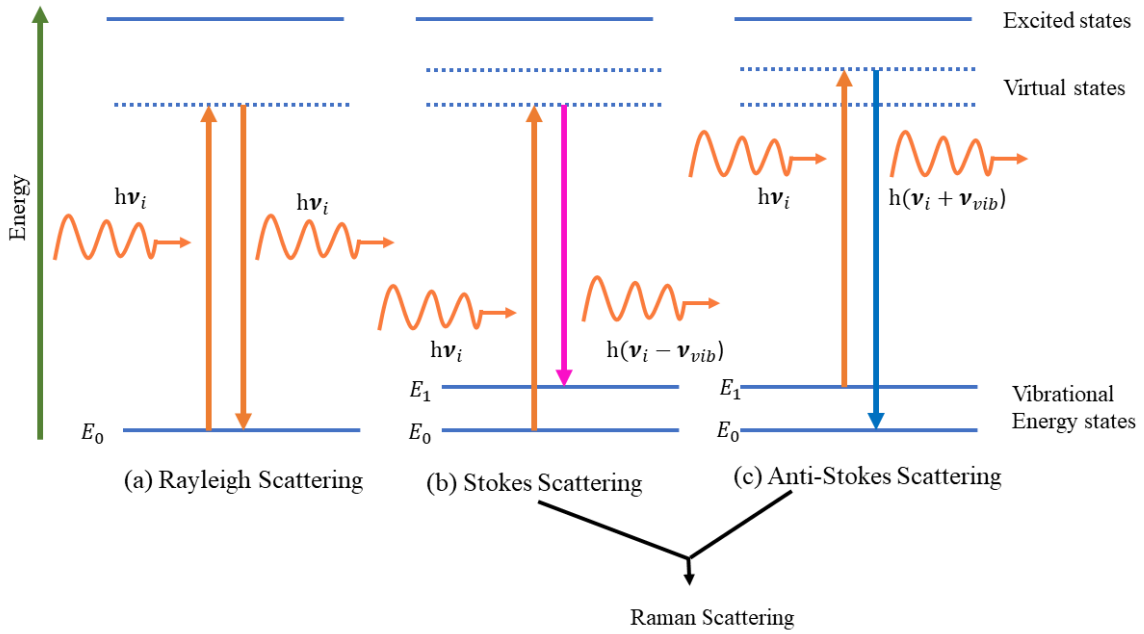

***Figure 2. 15*: Energy level diagram of different scattering processes that can occur by interacting electromagnetic radiation with material.**

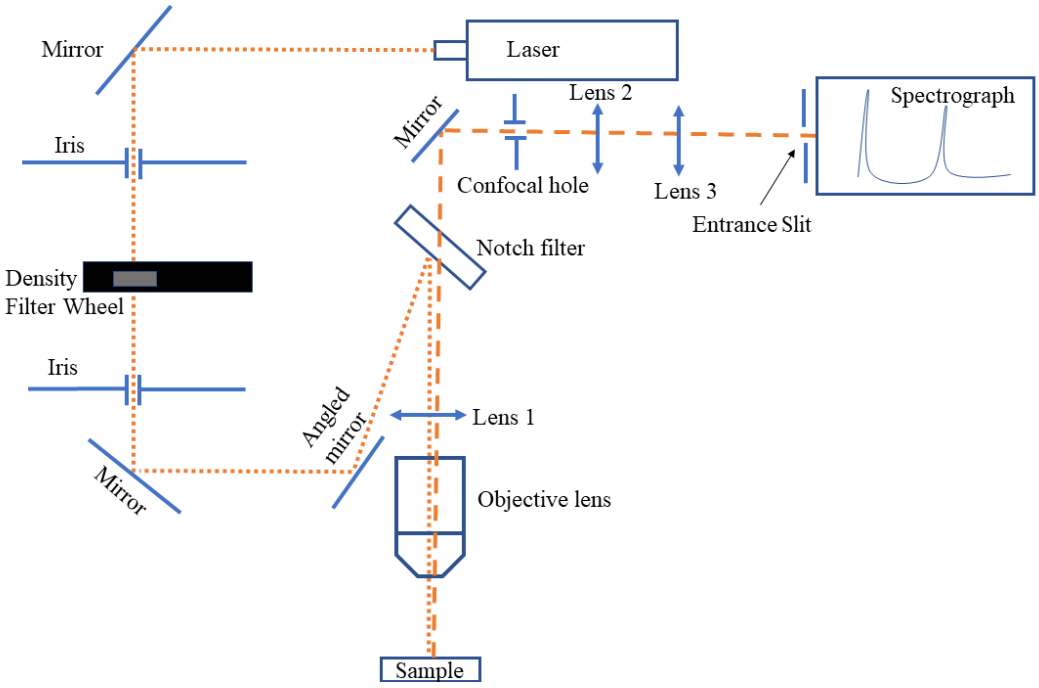

***Figure 2. 16*: Lab Ram HR 800 spectrophotometer schematic diagram.**

A non-dispersive spectrophotometer uses an interferometer such as a Michelson interferometer in a Fourier Transform Raman spectrophotometer. Bandpass filters are used to isolate a single laser beam. Most scattered radiation contains a frequency similar to the incident

frequency (Rayleigh scattering), but only a small fraction of scattered radiation has a frequency different from incident radiation (Raman scattering). Separating weak Raman lines from intense Rayleigh scattered radiation is done using double or triple-grating monochromators, super notch filters, holographic notch or edge filters, and rejection filters.

The Lab Ram HR spectrophotometer manufactured by Horiba Jobin Yvon is used for observing the vibrational modes in the Raman spectrum of the sample. The schematic diagram of the Lab Ram HR 800 spectrophotometer is shown in Figure 2.16. It consists of the internal He-Ne Laser with 20 mW at 633 nm wavelength. The key components of the system are the density Filer wheel with D0.3, D0.6, D1, D2, D3, and D4 filters, asymmetric Czerny Turner spectrograph with two gratings 1800, and 600 1/mm, three objective lenses such as (10 X, 50 X, and 100 X). It has a high-quality microscope, an adjustable confocal hole between 0 and 1108 μm, and a notch filter to filter out excitation wavelength <120 cm^{-1} stokes edge.

2.2.3 Density measurements

In the present work, the experimental densities of the sintered samples are measured using Archimedes' principle. Archimedes' principle states that the body experiences an upward force (buoyant force) if it is immersed partially or entirely in a fluid, and that force is equal to the weight of the liquid it displaces. The apparent density of the sintered composite ceramics is calculated using the following relation:

$$\rho_a = \frac{w_a}{w_b - w_c} \times \rho_w \; g/cm^3 \tag{2.6}$$

where, ρ_a is the apparent density of the sintered sample, w_a is the weight of the sintered sample in air, w_b is the weight of the sintered sample immersed in a liquid medium (in this study, distilled water), w_c is the weight of the sintered sample after removing it from liquid media

(distilled water), and ρ_w is the density of the liquid medium (for water $\rho_w = 1\ g/cm^3$). The relative densities of the sintered samples are calculated using the following equation;

$$\text{Relative density} = \frac{\rho_a}{\rho_0} = \frac{\text{apparent density of the sample}}{\text{the theoretical density of the sample}} \tag{2.7}$$

2.2.4 Field emission scanning electron microscope

The field emission scanning electron microscope (FESEM) is used to survey the surface morphology of the sintered ceramics. The attraction between the electron beam accelerated by the electromagnetic fields of the same energies and the same path with the material's atoms plays a vital role in detecting material morphology. In the present work, the microstructure and composition of pure and additive AlN ceramics have been investigated by the scanning electron microscopy (SEM) (1430 VP, M/s LEO) equipped with field emission scanning electron microscope (FESEM) (Sigma, Zeiss) and energy dispersive X-ray spectrometer (EDS). The schematic diagram of the SEM is shown in Figure 2.17. In SEM, the morphology of a material is scanned by high-energy electrons. It is generated by heating a tungsten filament, a lanthanum hexaboride (LaB_6) crystal, and a field emission source accelerated towards an anode by electromagnetic lenses with sufficient kinetic energy. The wavelength of the electron beam (λ) depends on the operating excitation voltage as follows;

$$\lambda^2 = \frac{h^2}{2m_0 eV} \tag{2.8}$$

where, *h* is plank's constant, m_0 is a mass of the electron at rest, *e* is the electron's charge, and *V* is the excitation voltage. If the excitation voltage is high, then the wavelength of the electron beam will be shorter. When this electron beam interacts with the specimen, it generates various signals to obtain information about its microstructure. These signals are classified as secondary electrons, backscattered electrons, and characteristic X-rays.

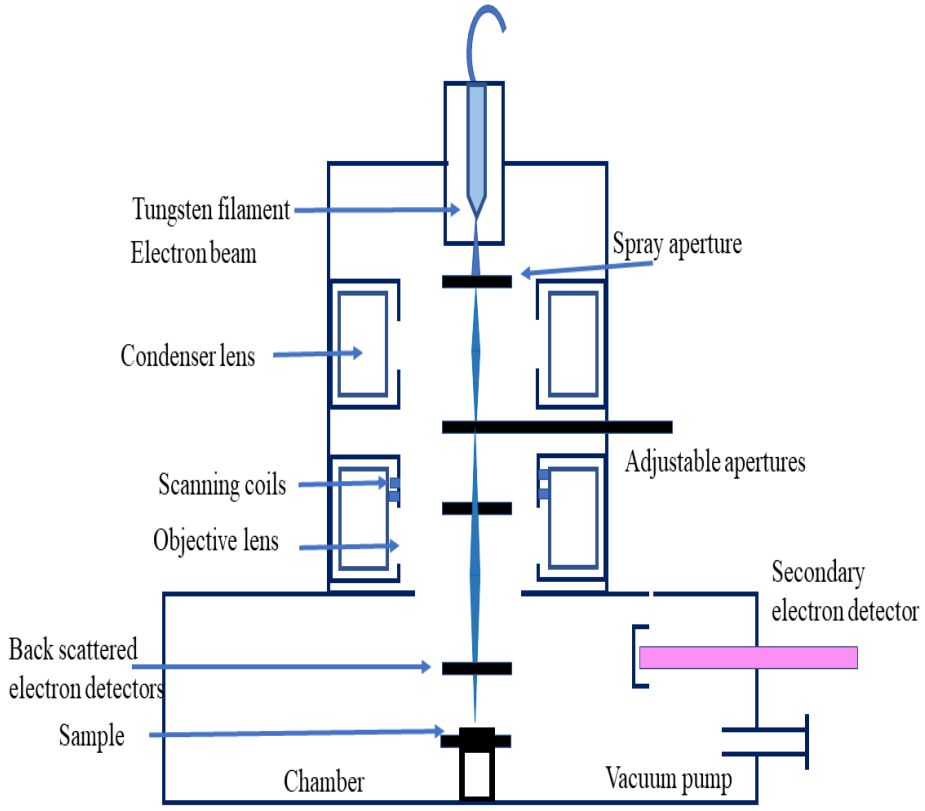

***Figure 2. 17*: The schematic diagram of a scanning electron microscope.**

If the primary electron in the electron beam interacts with the loosely bound electrons (on the specimen's surface), the specimen's atoms produce secondary electrons. These secondary electrons have energies in the range of 10-50 eV and are generally used to examine the specimen's microstructure as a secondary electron imaging technique. The angle between the incident beam and the specimen surface affects the yield of secondary electrons. Backscattered electrons are produced from the single large angle or multiple small angles scattering process, and their proportion is affected by the atomic number of elements that consist in the specimen's microstructure. These backscattered electrons usually originated from the surface layer of the specimen depth of 0.1-1 μm. This depth increases with increasing excitation voltage and decreasing atomic number. The bright portion in the image is due to the phases and particles of higher atomic number since many primary electrons are backscattered. Thus, the backscattered electron imaging technique can identify phases and particles with different

atomic numbers. If the primary electrons have sufficient energy to knock out electrons from the atoms, it produces the characteristic X-rays. These X-rays generated from the specimen are utilized to determine the specimen's chemistry by energy dispersive spectroscopy (EDS) or wavelength dispersive spectroscopy (WDS) and to create an X-ray dot image or elemental map that conveys the distribution of different elements in the specimen.

2.2.5 Dielectric measurements and impedance spectroscopy

The dielectric measurements of the pure and additive AlN composite ceramics are measured using LCR (Wayne Kerr Electronics Pvt. Ltd.) at lower frequencies from 1 kHz to 1 MHz as a function of temperature ranging from 40 ℃ to 500 ℃ for dielectric measurements. After sintering, the pure and additive AlN ceramics are polished smoothly on both sides and coated with conducting silver paste to make it a metal insulator metal (MIM) type test structure and collected the capacitance (C), dissipation factor (D), resistance (R), and reactance (X) with frequency and temperature variation. This data is used in the dielectric permittivity and impedance of the sintered sample calculation.

2.2.6 Microwave dielectric measurements

Microwave dielectric properties of ceramics using the Krupka cavity resonator

Measuring the dielectric permittivity and dissipation factor of the dielectric material at microwave frequencies is essential for the application of microwave passive devices such as resonators or filters [27, 28]. There are several methods for measuring the dielectric permittivity of the material, among them the transmission mode cavity resonator method, which is very useful for measuring dielectric properties at microwave frequencies. Hakki and Coleman’s modified Courtney technique is the most widely used technique for measuring the dielectric properties of resonator materials. The dielectric properties of low-loss materials at

microwave frequencies can be measured accurately by resonance methods employing cavity, dielectric, or open resonators [108]. The presence of air gaps limits the accuracy of permittivity measurement unless the electric field does not have a component perpendicular to the surface of the dielectric material. Therefore, TE_{onp} modes are considered the most accurate for permittivity measurements [109]. The manufacturers of dielectric materials use the quasi-$TE_{01\delta}$ (often referred to as TE_{011} mode) mode of operation commonly for measuring their dielectric properties. The dielectric resonator's essential characteristics are appropriate dielectric permittivity and low dissipation factor at particular resonant frequency.

The theory behind the dielectric measurements of DRs:

The structure consists of a shorted dielectric waveguide, essentially i. e., the cylindrical dielectric rod of finite length waveguide is shorted by placing conducting plates at each end of the rod and turning the transmission line into a resonator. The characteristic equation for the resonant structure operating in TE_{011} mode is as follows;

$$\frac{\alpha_m J_0(\alpha_m)}{J_1(\alpha_m)} = -\mu_r \beta_m \frac{K_0(\beta_m)}{K_1(\beta_m)} \tag{2.10}$$

$J_0(\alpha_m), J_1(\alpha_m)$ are the Bessel functions of the first kind of orders zero and one, respectively, $K_0(\beta_m), K_1(\beta_m)$ are the modified Bessel functions of the second kind of orders zero and one, respectively. μ_r is the relative permeability. The parameters α_m, and β_m are the first roots of the characteristic equation depends on the geometry, the resonant wavelength and dielectric properties. Thus

$$\alpha_m = \frac{\pi D f_m}{c}\sqrt{\varepsilon_r \mu_r - \left(\frac{c}{2L f_m}\right)^2} \tag{2.11}$$

$$\beta_m = \frac{\pi D f_m}{c}\sqrt{\left(\frac{c}{2L f_m}\right)^2 - 1} \tag{2.12}$$

where, f_m is the resonant frequency of TE_{011} mode, α_m and β_m are the first roots of the characteristic equation, D is the diameter, and L is the length of the dielectric specimen, c is the velocity of light.

The permittivity of the dielectric specimen can be found by knowing the dimensions of the specimen and measuring the resonant frequency of the TE_{011} mode using the following relation;

$$\varepsilon_r = 1 + \left(\frac{c}{\pi D f_1}\right)^2 (\alpha_1^2 + \beta_1^2) \quad (2.13)$$

where, α_1, β_1 are the first roots of the characteristic equation with m=0, f_1 is resonant frequency.

Measurement of dielectric permittivity:

The unloaded quality factor Q_{ul} of the cavity is defined as follows;

$$Q_{ul} = 2\pi \frac{maximum\ energy\ stored}{energy\ lost\ in\ one\ cycle} \quad (2.14)$$

***Figure 2. 18*: QWED Krupka cavity resonator used for analyzing microwave dielectric properties of pure and composite AlN ceramics.**

This measurement uses a cylindrical cavity of 10 mm in height and 24 mm in diameter (inner dimensions). The cavity contains the rigid coaxial cable at the center of the cavity, as

shown in Figure 2.18 for electromagnetic field coupling. It can be adjusted by moving in and out to form weak and strong coupling.

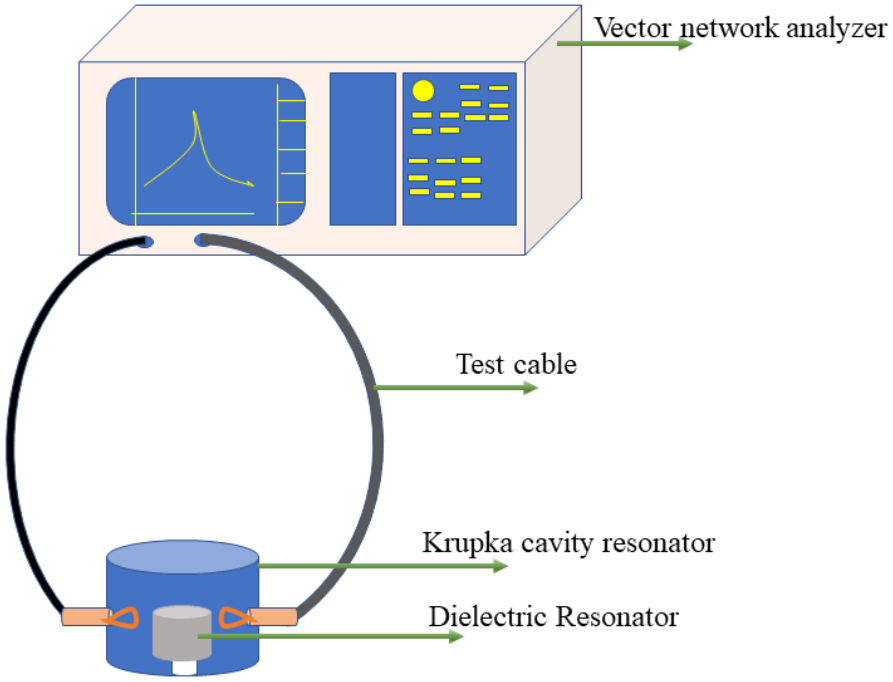

Figure 2. 19: Schematic diagram of the microwave dielectric measurements using VNA.

The cavity is connected to the vector network analyzer (VNA, M/s PNA-L Network Analyzer N5232A) by rigid coaxial cable using connectors on both ends (THRU), as shown in Figure 2.19. The network analyzer was calibrated by setting in S_{21} mode. Weak coupling exists between the rigid coaxial cable and DR (dielectric resonator) by adjusting the coaxial cable. The spectrum's resonant frequency and -3 dB width were calculated for measuring loaded quality factor and dielectric properties by identifying $TE_{01\delta}$ mode. Q_l is the loaded quality factor measured as the ratio of resonant frequency and the difference between left and right frequencies 3 dB down to resonant frequency. The dissipation factor ($\tan\delta$) of the dielectric material can be measured using the following relations.

$$Q_{ul} = \frac{Q_l}{1-\beta} \tag{2.15}$$

$$\tan\delta = \frac{1}{Q_{ul}} \tag{2.16}$$

$$\beta = 10^{\frac{-S_{21}}{20}} \tag{2.17}$$

Chapter 3

Structural and Dielectric Properties of Phase Pure AlN Ceramics

3.1 Graphical abstract:

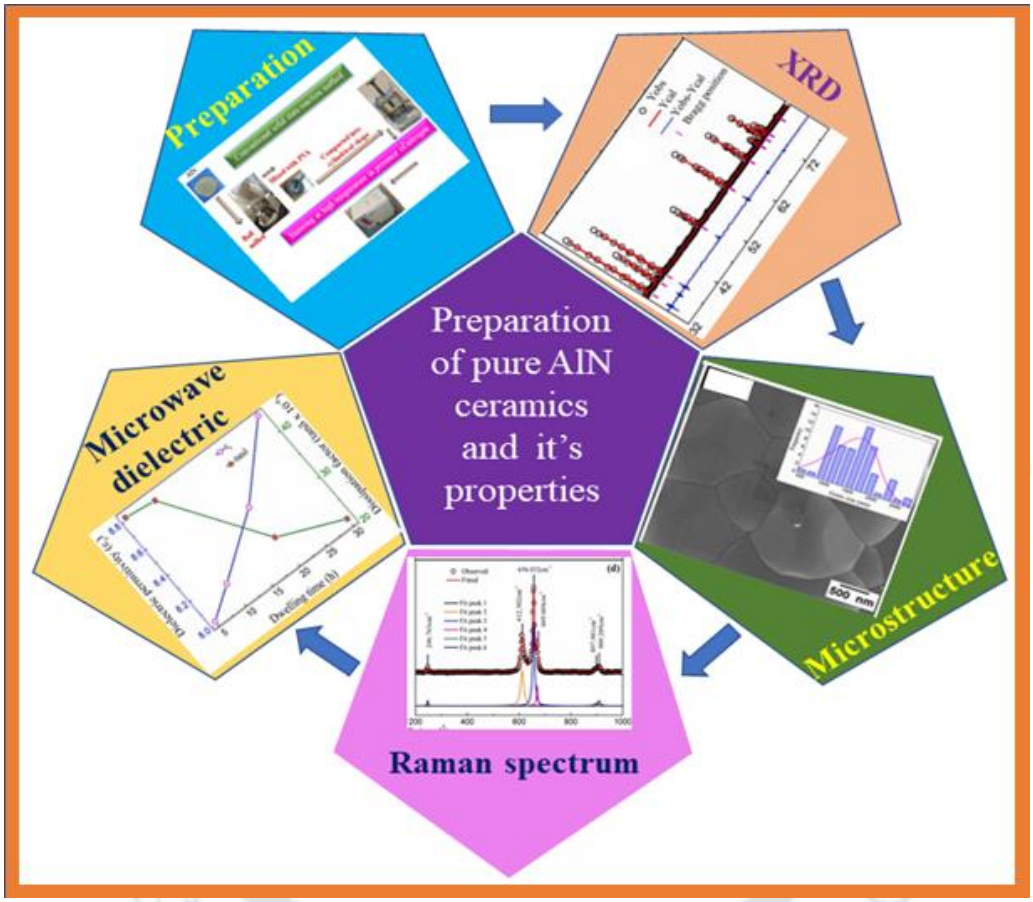

3.2 Abstract

In this study, AlN ceramics are prepared at a low-sintering temperature of ~1700 ℃ by adopting the powder bed method in the presence of nitrogen, achieving maximum relative density ~ 95% with wurtzite structure of space group $P6_3mc$ confirmed from XRD refinement. The average grain size of sintered AlN ceramic is 1.45 μm. The temperature-dependent Raman spectrum exhibits structure stability at various temperatures with stable wurtzite structure phonon modes. These sintered AlN ceramics exhibited good microwave dielectric properties

as dielectric permittivity ($\varepsilon_r = 8.83$) and dissipation factor ($\tan\delta = 2.69 \times 10^{-4}$). In this study, the AlN ceramic exhibits the best dielectric properties in the broad frequency range 1 MHz to 100 MHz at different temperatures from -140 °C to 200 °C. The obtained properties of AlN ceramics are essential and appropriate for RF-window and electronic applications.

3.3 Introduction

AlN is widely used in electronic packages in the place of light-emitting diodes and electronic substrates, photodetectors, high power, and high voltage units [53–55]. AlN ceramic is chemically inert up to ~ 1500 ℃, highly stable, and nontoxic [110]. Cheng-Yu Hsiesh et al. [62] used microwave sintering to prepare densified AlN ceramics. In this study, AlN ceramics were sintered at high temperatures of 1900 ℃ or above, and additive Y_2O_3 was used to densify AlN ceramics. Jiping Cheng et al., [63] pure AlN ceramics sintered at 1850 ℃ for 30-60 min dwelling time using microwave sintering method. Bin Feng et al. used the vibration-assisted hot press sintering method. Here, AlN ceramics sintered at 1750 ℃ and 1800 ℃ for 2 h and applied pressure while heating up from 5 MPa with 20 Hz vibration [111]. M. J. Li et al. prepared AlN ceramics with pure AlN at 1850 ℃ and Y_2O_3, Sm_2O_3 additives at 1750 ℃-1780 ℃ for 5 min using spark plasma sintering [67]. In all these sintering techniques, AlN was sintered at a high temperature above 1800 ℃. Hence, many researchers are trying to reduce its sintering temperature and enhance density at lower temperatures by adding additives and reducing particle size. In adding additives with AlN, secondary phase formation is a major problem.

Most researchers studied the thermal conductivity of pure and additive AlN ceramics [112–114]. He. Xiulan et al. studied the thermal conductivity of AlN ceramics with the addition of rare earth oxides and CaF_2 as an additive by ball mill for 24 h and sintered using spark plasma sintering technique at 1800 ℃. These samples with spark plasma sintering achieved thermal

conductivity from 93 to 130 $Wm^{-1}K^{-1}$ with secondary phases [115]. Only a few studies are available on temperature-dependent dielectric properties of AlN ceramics at low and high frequencies and the formation of pure AlN at lower sintering temperatures with maximum relative density. In addition, the microwave dielectric properties of AlN are also crucial for microwave applications [116, 117]. Using the powder bed method motivated us to study the temperature-dependent phonon modes and dielectric properties of pure AlN ceramics sintered at low temperatures.

3.4 Preparation of AlN ceramics using powder bed

AlN ceramics are sintered using a powder bed in a conventional method. Initially, the AlN powders (Thruttek Applied Materials Co., Ltd. Global Top Technology Inc.) are milled at 300 rpm for 10 hours in the dry ball milling method using a ball mill. The ball-milled powders were collected and ground to get a fine powder. Further, 5 mol% polyvinyl alcohol (PVA) is added to fine powdered AlN as a binder. Then, this PVA added AlN powder compacted into a cylindrical shape using a hydraulic press by applying 2.5 MPa with dimensions 10 mm (diameter), 5 mm, and 1 mm (thickness). The compacted samples are immersed in a powder bed. This powder bed consists of AlN (70%) and C (Carbon) (30%) powder. Then, this arrangement is kept in a crucible and sintered in a furnace in the presence of nitrogen at 1700 ℃ for different sintering durations.

By using Archimedes' principle, the density of the samples is measured. The crystalline structure and phase were identified by X-ray diffraction spectrum using an X-ray diffractometer (M/s Rigaku, TTRAX III 18 kW) employing Cu-Kα radiation (λ = 1.5406 Å). The microstructure of the sintered AlN ceramics is studied by a field emission scanning electron microscope (FESEM) (M/s Zeiss, Sigma). The vibration modes of AlN ceramics are studied by Raman spectrum recorded by the Raman spectrometer (M/s Horiba Jobin Vyon,

LabRam HR800). The microwave dielectric properties of AlN ceramics sintered using a powder bed are studied by vector network analyzer (VNA) (M/s PNA-L Network Analyzer N5232A). The temperature-dependent dielectric properties at low frequencies are measured by the LCR meter (M/s Wayne Kerr Pvt. Ltd., 4300) and at high frequencies, are measured by RF-an impedance analyzer attached with the automatic temperature controller (M/s Agilent Technologies, 4991 A and M/s Novocontrol Technologies Pvt. Ltd., BDS 2200).

3.5 Results and discussion of AlN ceramics sintered using powder bed

3.5.1 Sintering and density of AlN ceramics:

The pure AlN ceramics are sintered using a powder bed of AlN and carbon powders conventional sintering method at 1700 ℃ with a 15 ℃/min the heating rate and for different dwelling times 5 h, 10 h, 20 h, and 30 h. The relative density of sintered ceramics increased from 79.5% to 95% by increasing the dwelling time from 5 h to 30 h, as is shown in Figure 3.1(a). The relative density of the AlN ceramics enhanced with the dwelling time and reduced pores and uniform grain growth, observed in FESEM images. The maximum ~ 95% relative density achieved by this powder bed sintering for the AlN ceramic sintered for 30 h at 1700 ℃. The obtained maximum density at a lower sintering temperature can be attributed to the smaller initial particle sizes. The smaller particles enhance the densification at lower sintering temperatures. The lower densities for their smaller sintering duration may not be sufficient to enhance the nucleation process, as the driving force for sintering is very minimal.

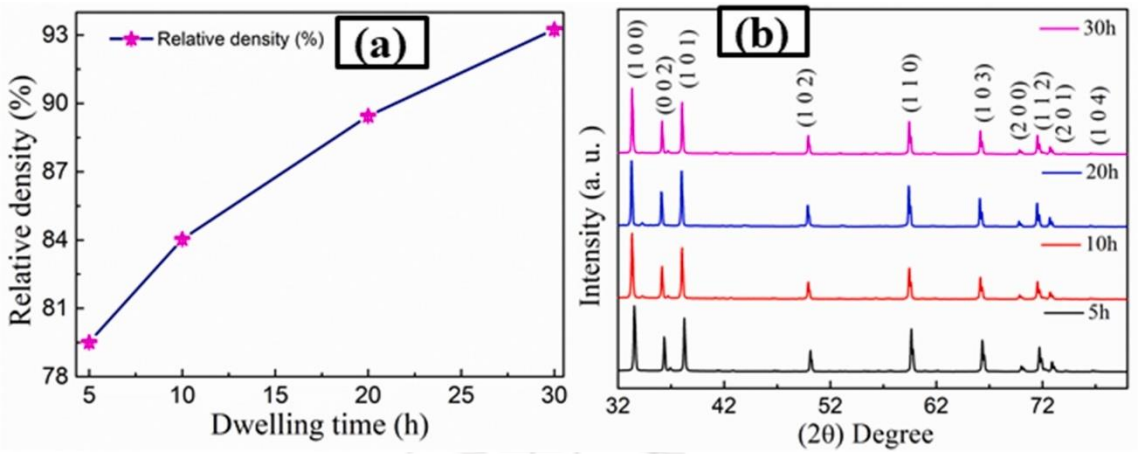

***Figure 3. 1**: (a) Variation of relative density of AlN ceramics with different dwelling times (sintered at 1700 ℃) (b) XRD pattern of AlN ceramics sintered at 1700 ℃ using a powder bed with different dwelling times.*

3.5.2 Structural analysis:

The XRD pattern of AlN ceramics, sintered using a powder bed at 1700 ℃ for different dwelling times for the pure AlN phase is shown in Figure 3.1(b). The obtained XRD pattern of AlN ceramics is appropriately matched with (JCPDS card No: 01-075-1620). The lattice strain and crystallite size are calculated from the modified Williamson-Hall equation [118] as follows;

$$\beta \cos\theta = \frac{k\lambda}{D} + 4\varepsilon \sin\theta \tag{3.1}$$

where β is the full-width half maxima (FWHM) of the diffraction peak, θ is the Bragg angle, k is the shape factor, λ is the incident X-ray wavelength, D is the crystallite size, and ε is the strain in the lattice.

***Table 3. 1**: The list of Rietveld refined parameters of AlN ceramics.*

Sample	χ^2	Bragg Rf factor	Rf factor	a=b (Å)	c (Å)	Volume (Å^3)	The crystallite size (nm)
AlN-5h	3.11	3.62	2.53	3.112(3)	4.980(12)	41.761(11)	103.8
AlN-10h	2.98	3.20	2.28	3.112(4)	4.981(10)	41.771(10)	117.8
AlN-20h	2.43	3.83	2.82	3.112(2)	4.981(5)	41.776(7)	136.2
AlN-30h	2.32	2.13	1.61	3.113(2)	4.982(9)	41.807(8)	168.8

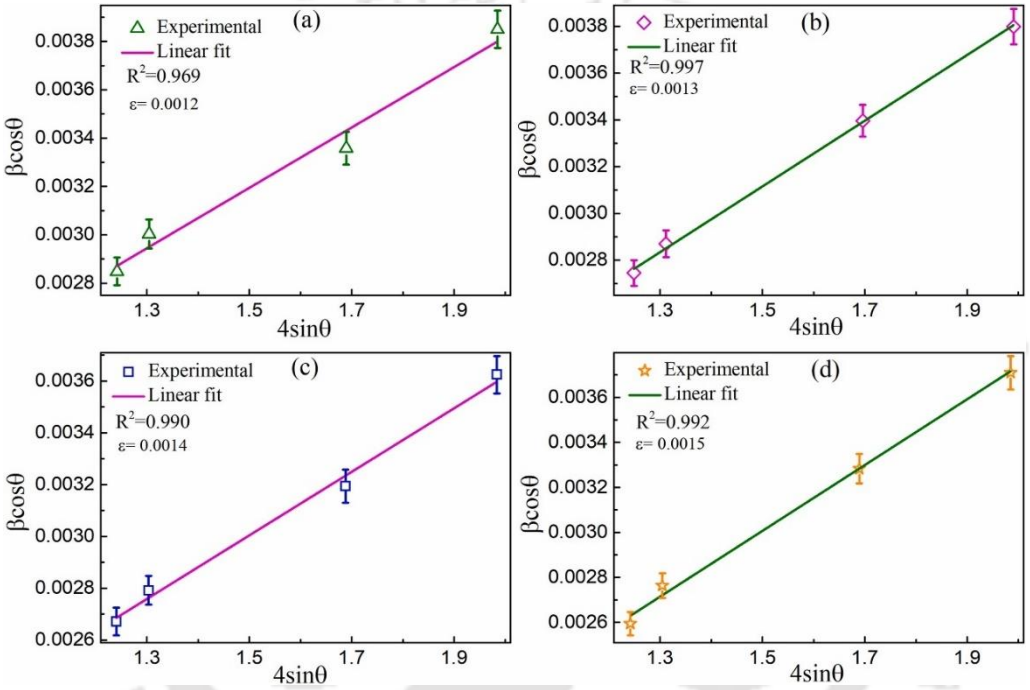

***Figure 3. 2**: The W-H plot of AlN ceramics sintered, at 1700 ℃ using a powder bed for (a) 5 h, (b) 10 h, (C) 20 h, (d) 30 h.*

This equation 3.1 is known as the uniform deformation model (UDM), one of the modified forms of the W-H plot equation. The plot between $\beta\cos\theta$ (along Y-axis) and $4\sin\theta$ (along X-axis) for AlN ceramics sintered for different dwelling times are shown in Figure 3.2. This line corresponding to all the samples fitted well as shown by correlation coefficient R^2 for each sample fit ~ 0.9. The crystallite size is calculated from the intercept of the W-H plot. Strain is the slope of the W-H plot. The crystallite size of AlN ceramics increases from 103.8

nm to 168.8 nm by increasing the dwelling time from 5 h to 20 h (see Table 3.1). The strain in the lattice and crystallite size is enhanced with an increase in the dwelling time of sintering.

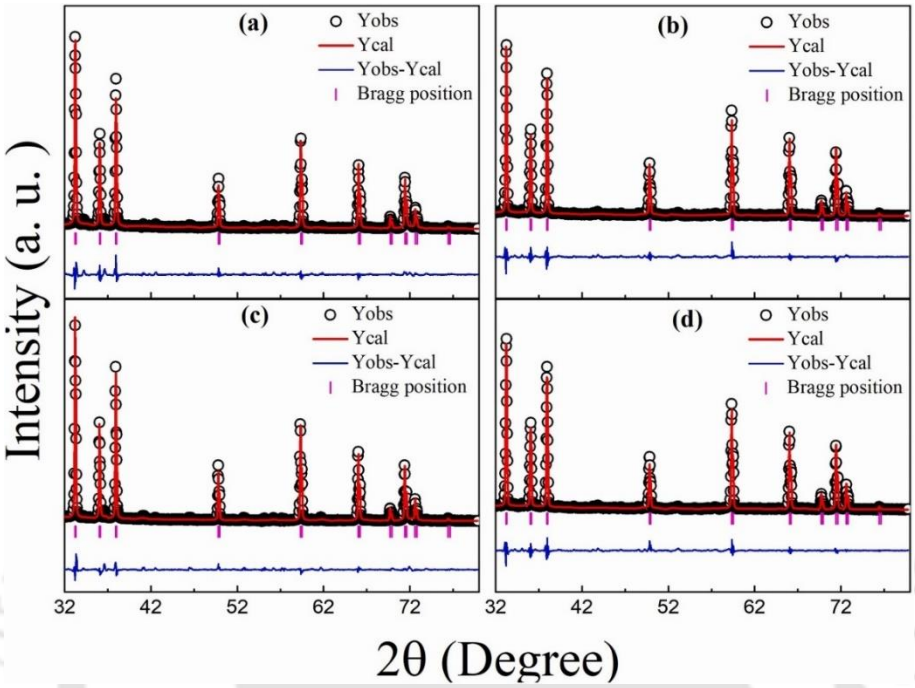

***Figure 3. 3**: Rietveld refinement of XRD pattern of AlN ceramics having a wurtzite crystal structure with $P6_3mc$ space group of space group number 186.*

It proves that all sintered AlN ceramics at 1700 ℃ with various dwelling timings are of wurtzite crystal structure, confirming the space group $P6_3mc$ with space group number 186. It is interesting to note that there is no signature of Al_2O_3, as it is difficult to eliminate its formation. The powder bed method aided in suppressing the formation of Al_2O_3. This suppression is confirmed by the Rietveld refinement shown in Figure 3.3.

The Rietveld refinement of the XRD patterns of AlN ceramics sintered at different durations is carried out and shown in Figure 3.3. It is observed that the AlN ceramics crystallized in the wurtzite phase, and the χ^2 values are in the minimal range, showing the goodness of fit. Also, a small variation in the unit cell parameters prove that these samples are

not oxidized, and the formation of Al_2O_3 is eliminated by using the powder bed method (see Table 3.1). The refined parameters are listed in Table 3.1.

3.5.3 Microstructure analysis:

The surface morphology of AlN ceramics is observed by a field emission scanning electron microscope (FESEM), shown in Figure 3.4, along with their histograms. This observation reveals that the microstructure of AlN ceramics is well compacted with uniform grains. The microstructure and grain size are noticeably affected by increasing the dwelling time from 5 h to 30 h while sintering. The density of AlN ceramics is found to improve by increasing dwelling time.

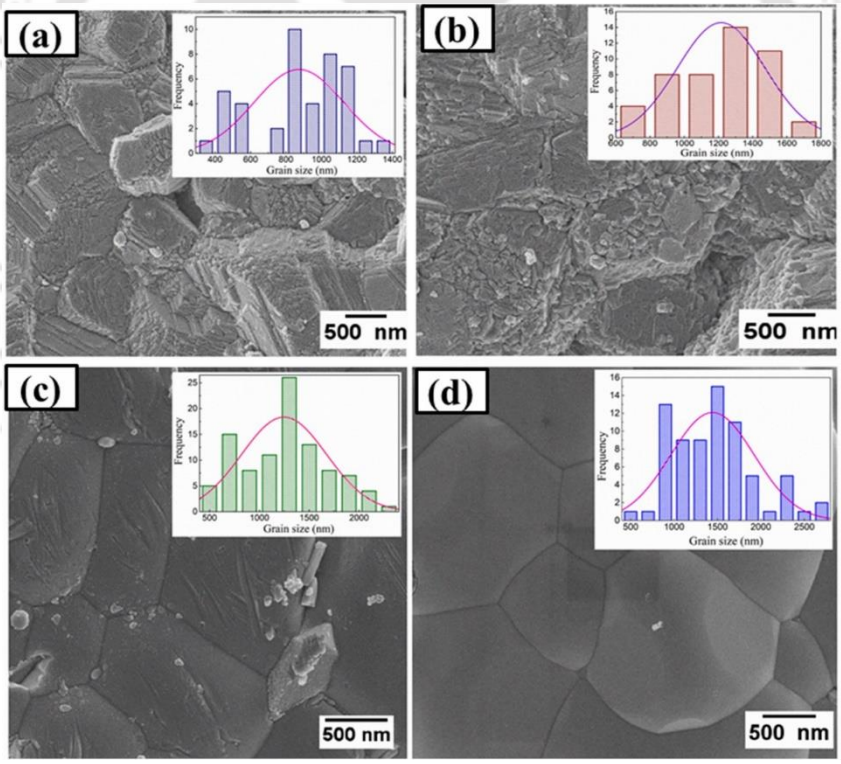

***Figure 3. 4*: Surface morphologies of AlN ceramics, sintered at (a) 5 h (b) 10 h (c) 20 h (d) 30 h.**

The average grain size is measured by Image J software and is verified by the linear intercept method. The obtained grain sizes are in the range 0.87 μm to 1.45 μm. The reason for the increment in grain size by the increase in dwelling time is due to the influence of domain wall contributions and the diffusion coefficient of Al^{3+} and N^{3-} ions. Grain growth and crystallization occur because of the mobility of grain boundaries [119]. In addition, the smaller initial particle sizes also play an essential role in nucleation and uniform grain growth. The improvement in the relative density and the formation of uniform microstructure is attributed to the smaller initial particle sizes. The small particle sizes enhance the sintering energy and help densification at a lower temperature. The smaller particles have a higher surface reactivity that aids densification.

Further, the sintering bed enabled the formation of Al_2O_3 and led to pure phase formation. Additionally, the sintering of these ceramics in a nitrogen environment is another critical factor in suppressing the Al_2O_3. This study shows that the smaller initial particle sizes and the sintering bed helped obtain phase pure AlN ceramics with maximum density and uniform grain growth.

3.5.4 Raman spectroscopy

The vibrational modes of AlN ceramics recorded at room temperature by exciting with a 514 nm laser with 30 mW power are shown in Figure 3.5. This result reveals that the sintered AlN ceramics using a powder bed contain 6 vibrational modes—the number of vibrational modes calculated from the following formula.

$$\text{Number of vibrational modes} = 3N - 3 \tag{3.2}$$

where *N* represents the number of atoms in the molecule, the AlN ceramics show 6 vibrational modes (see Figure 3.5 and Table 3.2). According to group theory, 8 sets of phonon modes exist

for q = 0. Those phonon modes are two E_2, two E_1, two A_1, and two B_1 modes. Among these, B_1 modes are silent [120, 121]. A and E modes are Raman and Infrared active modes. Both A_1 and E_1 modes are split into transversal (TO) and longitudinal (LO) optical modes because of the long-range electrostatic field formed due to lattice vibrations. These vibrations polarize the unit cell and create a long-range electrostatic field [121, 122]. The Raman mode E_2 is usually denoted as E_2 (High) and E_2 (Low) symmetries. The phonon symmetries and the allowed configuration for the Raman backscattering of the wurtzite crystal structure are shown in Table 3.2. Q (LO) phonon mode is commonly visible in backscattering geometry. This mixture of E_1 (LO) and a small A_1 component. E_1 (LO) frequency approximates the frequency of Q (LO) phonon mode. In this study, z (x, y) $\bar{z}$ Scattering geometry is considered to record Raman spectra. Where z indicates the propagation of the incident laser beam parallel to the c-axis of wurtzite AlN ceramics, x denotes the polarization of the incident, and y indicates the polarization of scattered light.

Table 3. 2: The list of phonon modes presents in AlN ceramics.

Scattering configuration	Allowed mode
x (zx)z	Q (TO), Q (LO)
x(yy)z	E_2, Q (TO), Q (LO)
x(yz)y	E_1 (TO), E_1 (LO)
z(xy)$\bar{z}$	E_2
z(yy)$\bar{z}$	E_2, A_1 (LO)
x(zz)$\bar{x}$	A_1 (TO)
x(yz)$\bar{x}$	E_1 (TO)
x(yy)$\bar{x}$	A_1 (TO), E_2

The Raman spectra of AlN ceramics sintered at 1700 ℃ by varying dwelling time from 5 h to 30 h, fitted using the Lorentz function, are shown in Figure 3.5. The fitted result is shown in Table 3.3. This result reveals that all samples contain six phonon modes near each other.

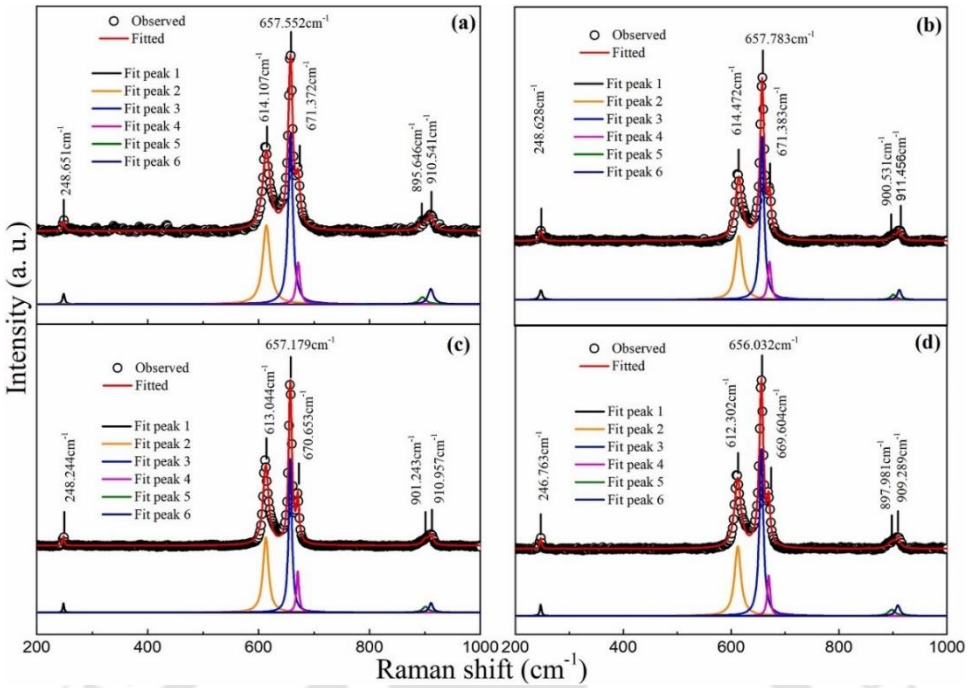

***Figure 3. 5**: The Raman spectra of AlN ceramics sintered at 1700 ℃ for (a) 5 h, (b) 10 h, (c) 2 0h, (d) 30 h recorded at room temperature by exiting with 514 nm laser, with 30 mW power.*

***Table 3. 3**: The phonon modes of AlN ceramics, sintered at 1700 ℃ for different sintering durations.*

Sample	AlN-5h		AlN-10h		AlN-20h		AlN-30h	
	γ(cm^{-1})	β(cm^{-1})	γ (cm^{-1})	β(cm^{-1})	γ (cm^{-1})	β(cm^{-1})	γ (cm^{-1})	β(cm^{-1})
E_2(Low)	248.65	4.881	248.63	6.628	248.24	3.003	246.76	3.808
A_1(TO)	614.11	15.942	614.47	14.842	613.04	11.813	612.30	14.234
E_2(High)	657.55	9.715	657.78	8.914	657.18	6.889	656.03	8.862
E_1(TO)	671.37	7.947	671.38	7.268	670.65	5.447	669.60	6.299
A_1(LO)	895.65	14.926	900.53	12.205	901.24	13.242	897.98	15.314
E_1(LO)	910.54	11.850	911.46	8.645	910.96	8.475	909.29	10.115

The shift in vibrational modes was observed from the fitting result of the Raman spectra of AlN ceramics. The E_2 (Low) vibrational mode shows the redshift from 5 h to 30 h. A_1 (TO), E_2 (High), E_1 (TO), and E_1 (LO) modes show a blue shift from 6 h to 10 h and a red shift from

10 h to 30 h. E_2 (High) mode and A_1 (LO) mode show a blue shift from 6 h to 20 h and a redshift from 20 h to 30 h.

3.5.5 Temperature-dependent Raman studies:

In addition, the temperature variation (123 K to 423 K) Raman spectra of AlN ceramic sintered at 1700 ℃ for 30 h are obtained. The Raman spectrum of AlN ceramic at various temperatures exhibits six phonon modes of wurtzite structure (see Figures 3.6(a) and (c)), confirming the stability and structure of AlN ceramic by increasing the temperature. Lorentz function is used to fit the Raman spectrum at various temperatures. The fitted result of the phonon mode E_2 (High) is studied by increasing temperature; this mode exhibits the redshift (see Figures 3.6(b) and (d)).

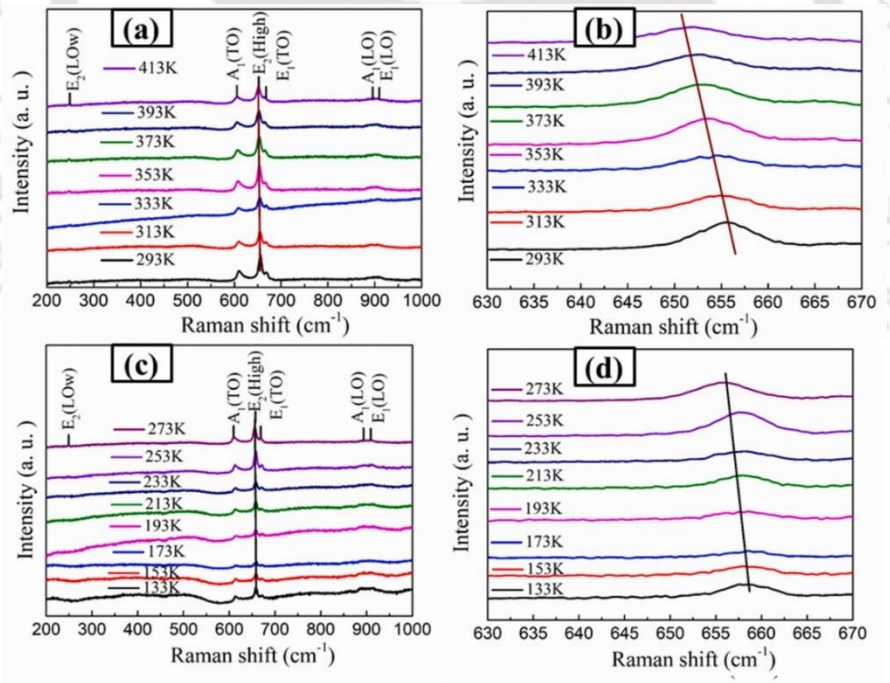

***Figure 3. 6**: The Raman spectra of AlN ceramic sintered at 1700 ℃ for 30 h by varying temperatures (a) and (c) The Raman spectra (b) and (d) shift in E_2 (High) peak by varying temperatures from 293 K to 413 K and from 133 K to 273 K, respectively.*

The relation of Raman shift with temperature is linear, increasing the temperature from 123 K to 273 K and 283 K to 423 K, shown in Figures 3.7(a) and (b), respectively. This result confirms the relationship between the Raman shift and temperature as follows:

$$\omega = \omega_0 + \alpha T \tag{3.3}$$

where ω is the Raman shift, T is the temperature, and α is the first-order temperature coefficient [123]. The Raman spectra of AlN ceramic are recorded by varying the power of the laser from 20 mW to 36 mW, shown in Figure 3.7 (c).

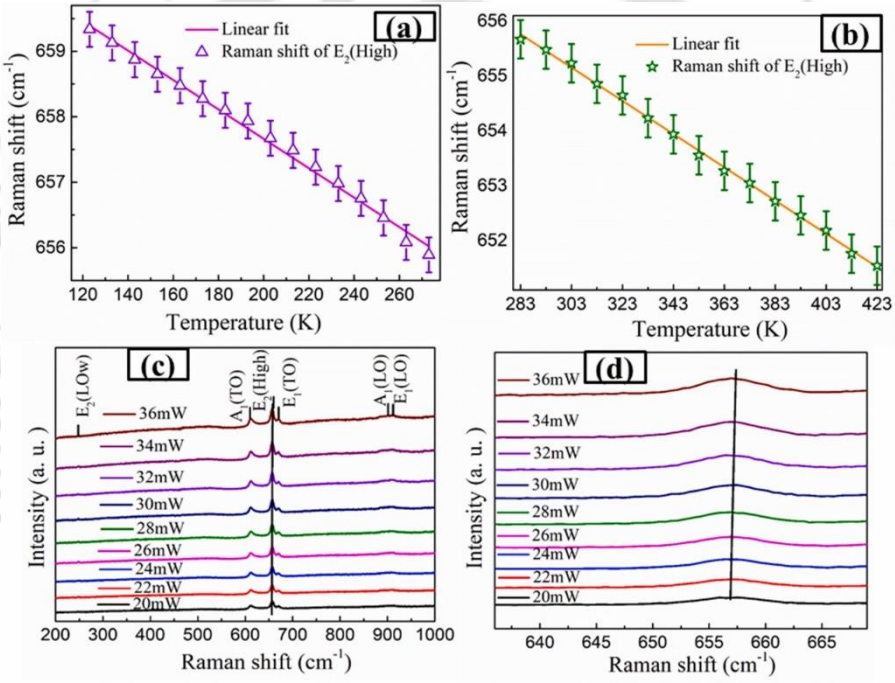

***Figure 3. 7*: The variation in Raman shifts of E_2(High) mode by varying temperature (a) from 123 K to 273 K, (b) from 283 K to 423 K, and (c) the Raman spectrum (d) shift in E_2 (High) mode, recorded at room temperature by varying power of the laser from 20 mW to 36 mW.**

This result reveals that the AlN ceramic exhibits six phonon modes of wurtzite structure at each laser power. Increasing the laser power enhances the intensity counts of the Raman spectrum. The increment in intensity counts is more photon incidents, resulting in more phonons participation in scattering from the sample [124], and the localized generated heat on

the sample due to more photon incidents. The high-intensity E_2 (High) mode shows a redshift (see Figure 3.7 (d)). The Raman shift value of phonon mode in one spectrum is less when compared with the Raman shift value of the same particular phonon mode in another spectrum. That displacement is called redshift and can be observed in Figures 3.7 (b) and (d). The Raman spectra of the AlN ceramics revealed no signatures of Al_2O_3. This result shows that the powder bed method can obtain phase pure AlN ceramics at lower sintering temperatures.

3.5.6 Dielectric studies:

3.5.6.1 Low-frequency dielectric properties:

The frequency-dependent dielectric properties of AlN ceramics sintered at 1700 ℃ by varying the dwelling time from 5 h to 30 h are calculated, and the obtained results are shown in Figure 3.8.

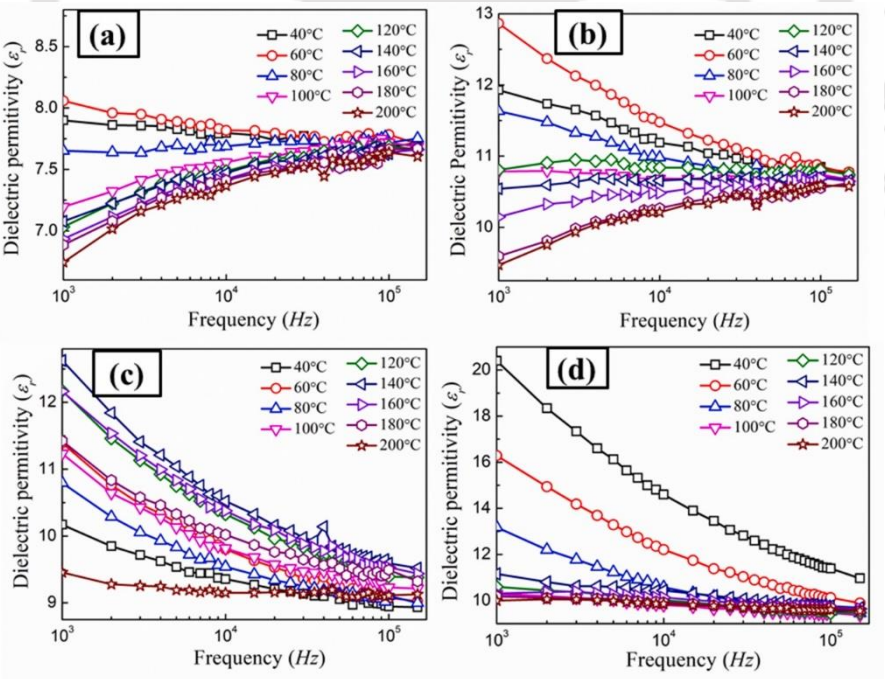

Figure 3. 8: The variation of dielectric permittivity as a function of frequency for AlN ceramics in powder bed method sintered at 1700 ℃ for (a) 5 h, (b) 10 h, (c) 20 h, and (d) 30 h.

The dielectric permittivity is calculated from the capacitance of AlN ceramics. This result (see Figure 3.8) reveals that the permittivity range of the samples increased as follows 8.1- 6.5 for 5 h, 13 - 9.1 for 10 h sample, 12.9 - 9 for 20 h, 20 - 9 for 30 h with an increase in the dwelling time while sintering from 5 h to 30 h. The dielectric permittivity decreases by increasing the frequency from 1 KHz to 100 KHz for 20 h and 30 h samples. The samples sintered for 5 h and 10 h dielectric permittivity show slight increment above 100 ℃ for 5 h, and 140 ℃ for 10 h by increasing the frequency from 1 KHz to 100 KHz. The reason may be the porosity and lower density of the samples. The dielectric permittivity and dissipation factor by varying the temperature is constant, but slight variation is observed at low temperatures and is shown in Figure 3.9 and Figure 3.10.

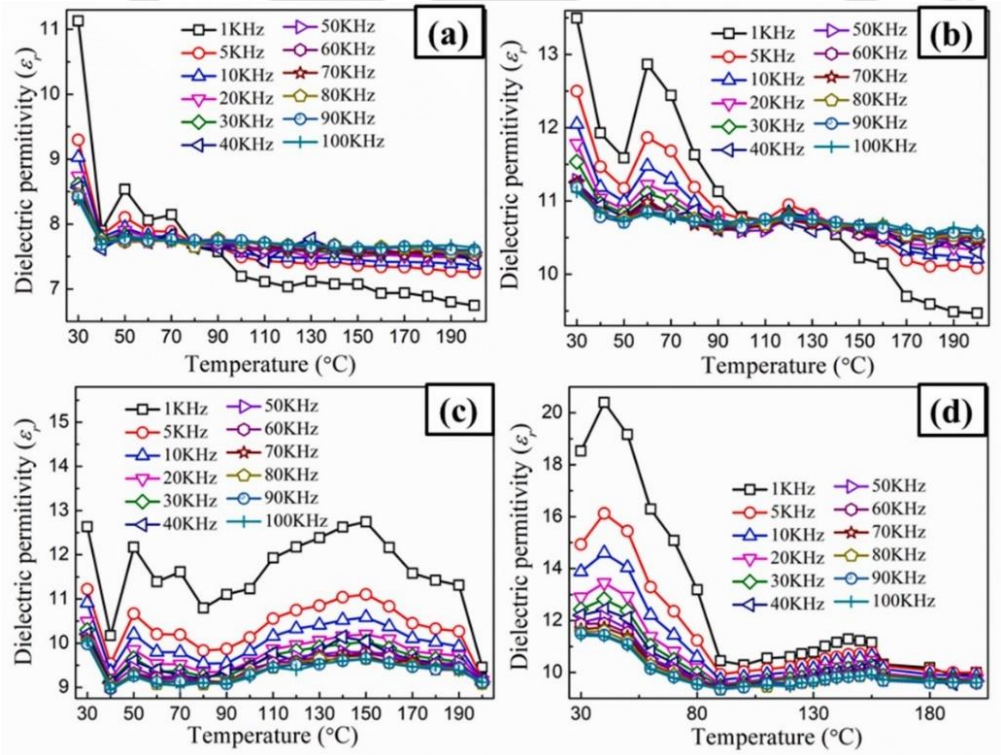

Figure 3. 9: The variation (from 25 ℃ to 200 ℃) of dielectric permittivity as a function of temperature for AlN ceramics in powder bed method sintered at 1700 ℃ for (a) 5 h (b) 10 h (c) 20 h and (d) 30 h.

The dielectric permittivity of the sample depends on the temperature, radii, volume, and polarizability of the atom/ion. The applied electric field (E_a) does not affect the atom/ ion consisting in the material, but the local field (E_L) will affect it. The difference between the applied electric and depolarization field (E_{dp}) is called the macroscopic field. The local field may equal or less than the applied field. The local field (E_L) is the sum of the macroscopic field (E_m), the electric field due to dipoles within the boundary (E_d), and the field due to charges at the surface (E_p). The relation between dielectric permittivity(ε_r) and polarization is as follows:

$$\frac{\varepsilon_r - 1}{\varepsilon_r + 2} = \frac{N\alpha}{3\varepsilon_0} \tag{3.4}$$

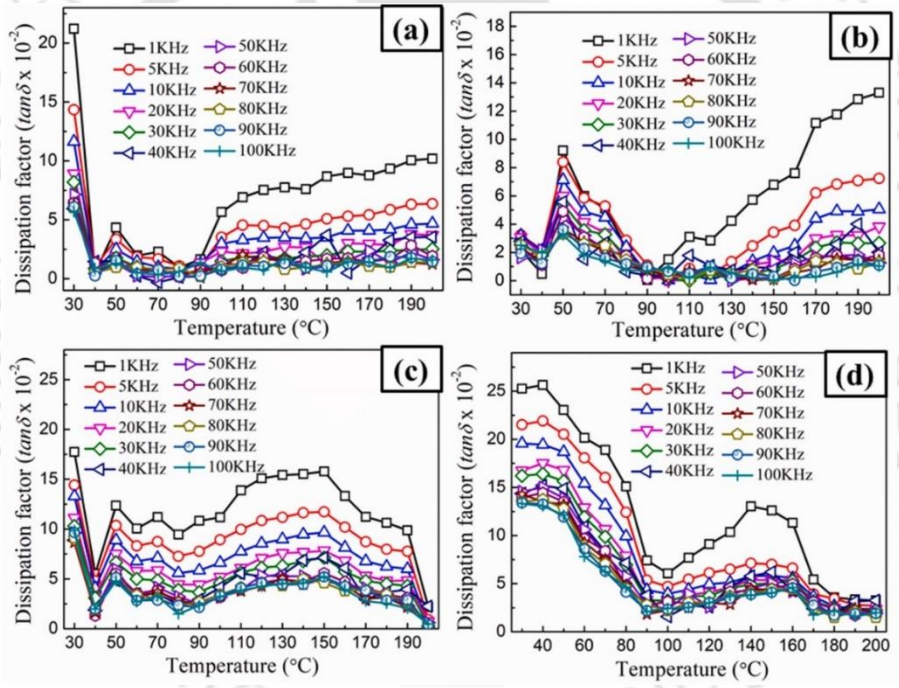

***Figure 3. 10*: The variation of dissipation factor as a function of temperature for AlN ceramics in powder bed method sintered at 1700℃ for (a) 5 h, (b) 10 h, (c) 2 0h, and (d) 30 h.**

which is known as the Clausius Mossotti relation [125]. Here, α is polarizability or dipole moment (p) induced in the area of interest per unit local field (E_L), ε_0 is the permittivity of free space, and N is derived from the total dipole moment (P) as follows:

$$P = Np = N\alpha\left(E_m + \frac{P}{3\varepsilon_0}\right) \quad (3.5)$$

The polarization induced in the dielectric material is the result of four mechanisms. (1) space charge polarization, (2) dipole polarization, (3) ionic polarization, and (4) atomic polarization. The maximum frequency (f_{max}) that induces polarizability can be measured by equating the quantum mechanical energy related to the frequency with the classical kinetic energy of the particle and by setting the speed of light as the maximum speed of the particle as follows [126]:

$$f_{max}h < \frac{mc^2}{2} \quad (3.6)$$

where m is the particle's mass, c is the speed of light, and h is the Plank's constant.

For electron $f_{max} = (10^{18} - 10^{19})\ Hz$, in the case of ions $f_{max} = (10^{15} - 10^{16})\ Hz$. Here, we have studied the broadband dielectric properties from 1 MHz to 100 MHz. Space charge polarization will affect dielectric permittivity at $\leq 10^4\ Hz$, dipole polarization effect is at $\leq 10^8\ Hz$, ionic and dipole polarization affects broadband frequency range 1 MHz to 100 MHz.

3.5.6.2 Broadband dielectric properties

The AlN ceramics sintered for 20 h and 30 h exhibit good dielectric properties at lower frequencies selected to study high-frequency behaviour. The dielectric permittivity and dissipation factor variation with frequency at different temperatures (-140 ℃ to 200 ℃) were studied. The dielectric permittivity of the sample sintered for 20 h is constant with the interpretation of frequencies from 1 MHz to 100 MHz at lower temperatures, and the sample sintered for 30 h shows a slightly increasing nature but is higher than the sample sintered for 20 h (see Figure 3.11 (a) and Figure 3.11 (b). The dissipation factor of the AlN ceramic sintered

for 20 h shows more fluctuations from 1 MHz to 10 MHz, further slightly increasing nature, and that of the AlN ceramics sintered for 30 h shows constantly decreasing nature without many fluctuations. The dielectric properties as ε_r (6.65-7.0) and $\tan\delta$ ((1-50) x 10^{-3}) for the frequency region 1 MHz to 100 MHz obtained for the AlN ceramic sintered for 20 h.

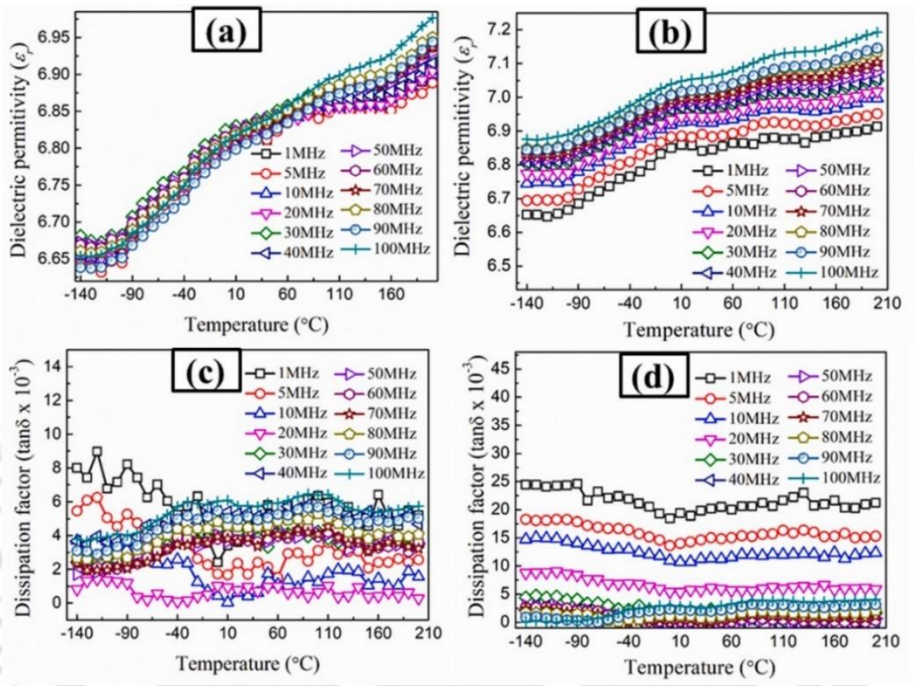

Figure 3. 11: The dielectric permittivity of AlN ceramics sintered for (a) 20 h (b) 30 h and dissipation factor of AlN ceramics sintered for (c) 20 h (d) 30 h with a function of temperature.

The dielectric properties of AlN ceramics at higher temperature (see Figure 3.11) reveal that the AlN ceramic sintered for 30h shows the best dielectric permittivity (6.72-7.15) and dissipation factor ((1-50) x 10^{-3}). the dielectric response obtained for AlN ceramics sintered for 30 h is consistent with the previously reported values [127]. The dielectric permittivity of pure AlN ceramics (see Figure 3.11) reveals that the dielectric permittivity (6.60-7.15) of the AlN ceramic sintered for 30 h is higher than that of AlN ceramic sintered for 20 h. The dissipation factor of AlN ceramic sintered for 30 h is constant by varying temperatures, while AlN ceramic sintered for 20 h shows small variation at negative temperatures since porosity. The electrical

conductivity of AlN ceramics varies with applied frequency and temperature due to charge transport mechanisms.

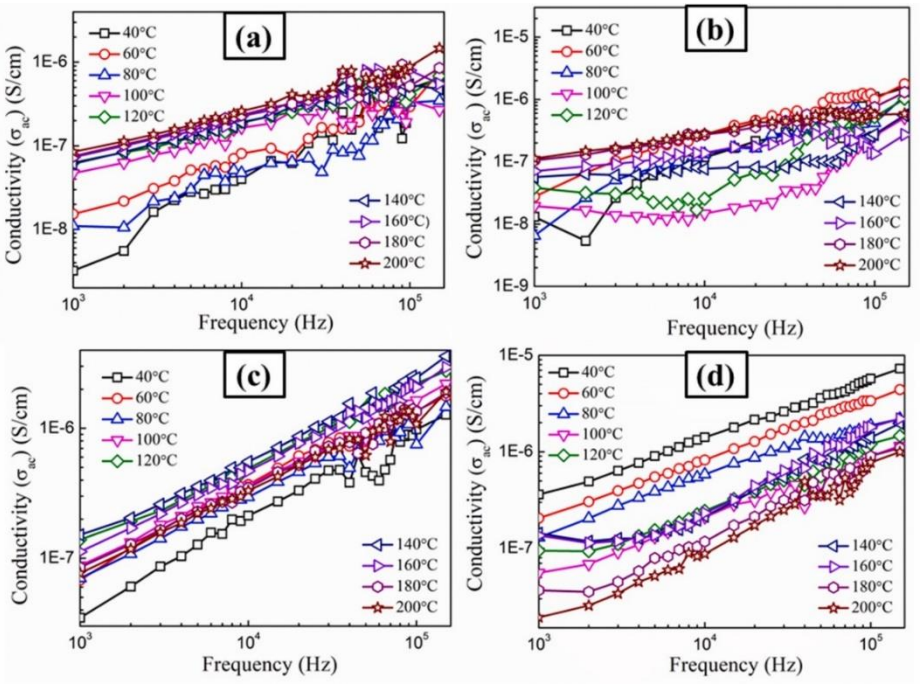

***Figure 3. 12*: The variation of conductivity as a function of frequency for AlN ceramics sintered at 1700 ℃ for (a) 5 h, (b) 10 h, (c) 20 h, and (d) 30 h.**

To understand the frequency and temperature effect on the electrical conductivity of AlN ceramics, the alternate current (AC) conductivity of AlN ceramics sintered at various dwelling times from 5 h to 30 h are studied and are shown in Figure 3.12 by varying frequency from 1 KHz to 100 KHz at different temperatures 40 ℃ to 200 ℃. The ac conductivity (σ_{ac})of the AlN ceramics are calculated from the following relation:

$$\sigma_{ac} = \omega \varepsilon_r \varepsilon_0 \tan\delta \tag{3.7}$$

where $\omega = 2\pi f$, f is frequency, ε_r is relative permittivity, ε_0 is the permittivity of free space, $\tan\delta$ is the dissipation factor. The variation of ac conductivity with frequency at different temperatures is shown in Figure 3.12. This result reveals that the electrical conductivity (σ_{ac}) vs. frequency curve contains two regions—one region at a lower frequency (1 KHz to 10 KHz).

The conductivity is less in this lower frequency region due to the grain boundary. The grain boundaries act as a barrier to charge conduction [128].

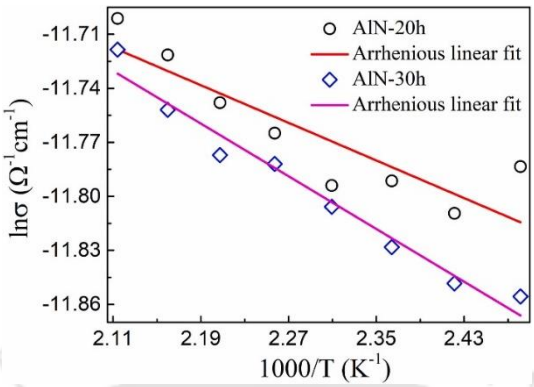

***Figure 3. 13*: Logarithmic variation of σ_{ac} as a function of 1000/T of AlN ceramics sintered for 20 h and 30 h.**

The other is in the high-frequency region (10 KHz to 100 KHz). In this high-frequency region, the conductivity increases due to the hoping process. The best sample shows electrical conductivity in 2.1 x 10^{-8} S/cm to 1.2 x 10^{-5} S/cm. The activation energy of AlN ceramic sintered for 20 h and 30 h are calculated from the Arrhenius relation [129]:

$$\sigma_{ac} = \sigma_0 exp\left(\frac{E_A}{k_B T}\right) \tag{3.8}$$

where σ_{ac} is the conductivity, σ_0 is the pre-exponential factor, E_A is the activation energy, k_B is the Boltzmann constant, and T is the temperature. The plot between σ_{ac}, and 1000/T is shown in Figure 3.13 for the AlN ceramic sintered for 20 h and 30 h. These results revealed that the activation energy of AlN ceramic sintered for 20 h is 0.02 eV, and that of AlN ceramic sintered for 30 h is 0.03 eV at 0.19 GHz. The minimum amount of energy required to undergo the transformation of molecules or atoms for the AlN ceramics sintered at 1700 ℃ for 30 h is 0.03 eV.

3.5.7 Microwave dielectric properties

Microwave dielectric properties of AlN ceramics are measured by a vector network analyzer using Hakki- the Coleman method. Using the Krupka cavity resonator, this vector network analyzer will give the spectrum of signal S_{21} versus frequency. This spectrum reveals the resonant frequency and transmittance signal at that resonant frequency and FWHM (full-width half maximum) of the peak at a resonant frequency. The material's dielectric permittivity and dissipation factor are calculated using the Hakki Colemon method [130]. We have prepared AlN ceramics of dimensions 10 mm (diameter) and 5 mm (thickness) to measure microwave dielectric properties. The obtained dielectric permittivity and dissipation factor of sintered AlN ceramics is shown in Figure 3.14. These results reveal that the sample's dielectric permittivity increases from 8.02 to 8.83 by increasing the dwelling time while sintering from 5 h to 30 h. The dissipation factor of the sample decreased from 43.81 to 21.69 in the order of 10^{-4}. The dielectric permittivity increment and dissipation factor reduction are attributed to porosity reduction. Fractional density increases with the dwelling time from 5 h to 30 h; hence, porosity decreases. The relation between fractional density and porosity is as follows

$$P = 1 - D \tag{3.9}$$

where P is the porosity, and D is the fractional density of the material density to theoretical density. The dielectric permittivity is calculated from the following relations:

$$\varepsilon_r = \frac{c^2}{f_0^2 \lambda_d^2} \tag{3.10}$$

where ε_r is dielectric permittivity, c is the speed of light, f_o is the resonant frequency, λ_d is the wavelength in a dielectric equal to the diameter (size) D of the cylindrical dielectric resonator. Dissipation factor $(\tan\delta)$ is the inverse of the unloaded quality factor $\left[1/Q_{ul}\right]$. This unloaded

quality factor can be calculated using loaded quality (Q_l) factor and coupling coefficient β from the following relations:

$$\frac{1}{Q_{ul}} = \frac{1-\beta}{Q_l} \tag{3.11}$$

$$S_{21} = -20 \log \beta \tag{3.12}$$

The loaded quality factor (Q_l) is the ratio of resonant frequency (f_0) to the modulus value for the difference of frequencies right(f_2) and left (f_1) 3 dB down to the resonant frequency. The high dielectric permittivity ($\varepsilon_r = 8.83$) and low dissipation factor (21.69 x 10^{-4}) are obtained for the AlN ceramics, sintered at 1700 ℃ for a 30 h sample. The obtained dielectric results agree with previously reported values [131]. These obtained results are appropriate for RF-window and electronic applications of AlN ceramics. The obtained dielectric response is enhanced as compared with the earlier studies [132].

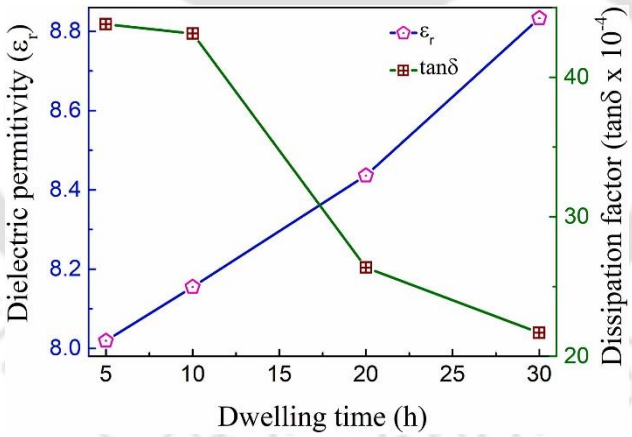

***Figure 3. 14*: Microwave dielectric properties of AlN ceramics by varying dwelling time from 5 h to 30 h.**

3.6 Conclusions

- In this study, pure AlN ceramics are prepared at a low sintering temperature of 1700 ℃ using a powder bed. The obtained densified AlN ceramic sintered at 1700 ℃ for 30 h, with a compacted grain size of an average grain size 1.45 μm.
- The Rietveld refined XRD studies revealed that AlN ceramics' crystal structure exhibits Wurtzite structure, with the $P6_3mc$ space group. XRD pattern matched with JCPDS card number 01-075-1620 conforming wurtzite structure and correlated these structural properties with temperature-dependent phonon modes from Raman spectrum and electrical properties.
- This study demonstrates the densification of AlN ceramics at lower sintering temperatures and the elimination of the Al_2O_3 phase by the powder bed method. The improvement in density, uniform microstructure, and good electrical properties are also attributed to consistent grain growth due to smaller initial particle sizes.
- The dielectric permittivity (6.72-7.15) and dissipation factor ((1-50) x 10^{-3}) were obtained for the range of frequencies 1 MHz to 100 MHz in the temperature range -140 ℃ to 200 ℃. The best microwave dielectric properties with low loss tangent ($\tan\delta =$ 21.69 x 10^{-4}) and high dielectric permittivity ($\varepsilon_r = 8.83$)) obtained are promising for microwave applications.

Chapter 4

Effect of Additives on Structural and Dielectric Properties of AlN Ceramics

4.1 Graphical abstract:

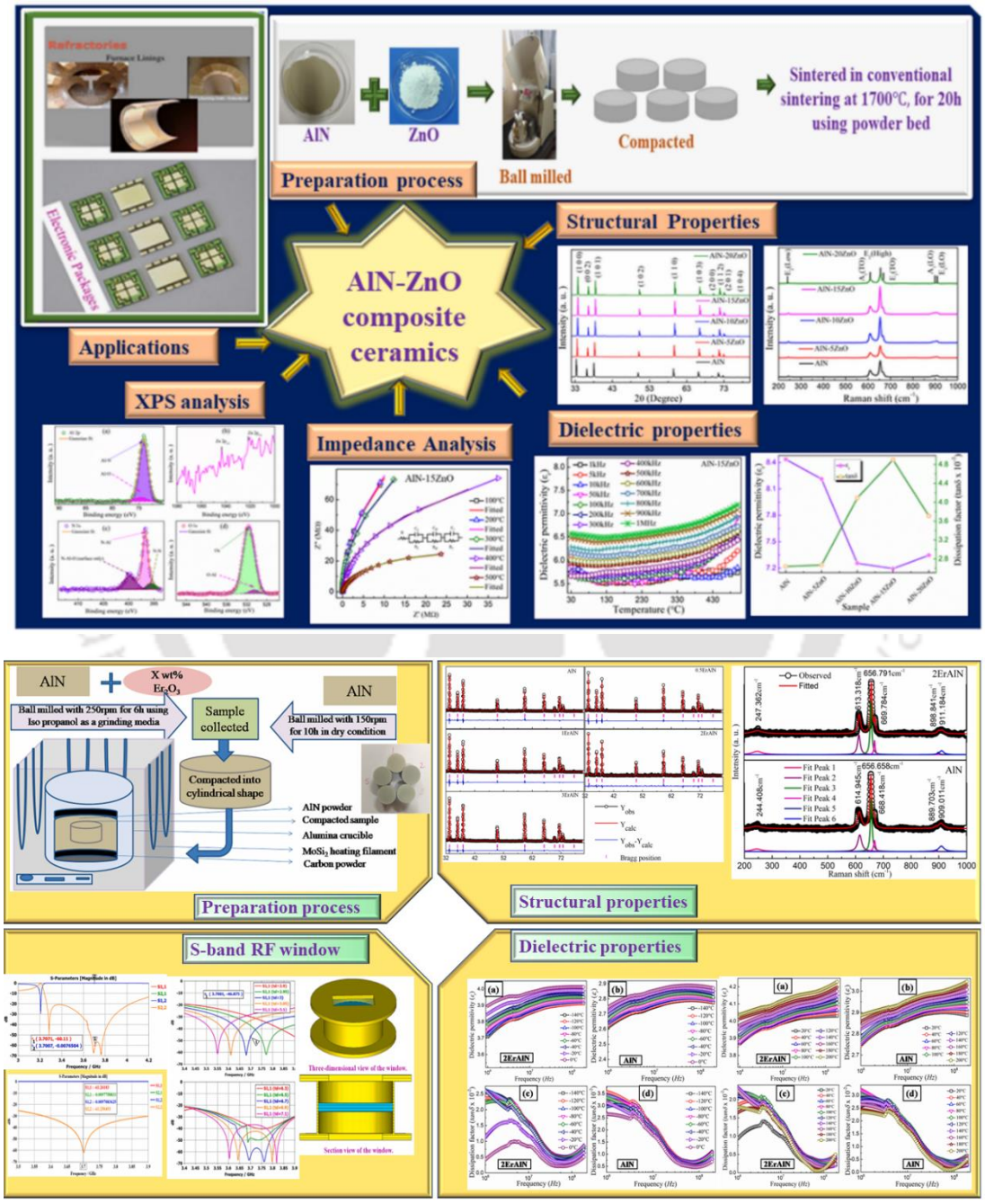

4.2 Abstract

This chapter is divided into two parts. In the first part, the effect of ZnO on structural, dielectric, and electrical properties is investigated systematically. In addition, the small initial particle sizes and ZnO also help decrease the sintering temperature to 1700 ℃ and densify AlN at lower temperatures due to the formation of the eutectic phase around 1400 ℃. The XRD pattern of ZnO-added AlN ceramics revealed that the sintered ceramics have pure AlN phase. The Raman spectrum of all sintered AlN-ZnO composites confirms wurtzite AlN structure. The XPS results confirm Al 2p, Zn 2p, N 1s, and O 1s presented in the AlN-15ZnO composite ceramic. O1s deconvoluted into Os and O-Al and this deconvoluted peaks fit reveals that the percentage of Os is higher than the percentage O-Al present in the sample. This result proves that the oxygen in the AlN-15ZnO composite ceramics is on the surface, not in grains. The powder bed prevents the formation of Al_2O_3 and enhances densification. The best additive AlN-15ZnO composite obtained dielectric permittivity is 5.50 to 7.41 in the variation of temperature 30 to 500 ℃. The impedance spectroscopy revealed that the AlN-ZnO composite ceramics contain non-Debye type relaxations. The best microwave dielectric properties ($\varepsilon_r =$ 7.20 and $\tan\delta = 4.90 \times 10^{-3}$) for the best composite AlN-15ZnO ceramic for transmission of signals with high speed in electronic applications.

In the second part, pure and Er_2O_3 doped AlN ceramics are prepared by solid-state reaction method and sintered using the sintering bed at 1700 ℃. Interestingly, it prevented the formation of Al_2O_3 completely. X-ray diffraction patterns of pure and Er_2O_3 added samples show wurtzite crystal structure with $P6_3mc$ space group. Er-AlN composite ceramics exhibited good microwave dielectric properties ($\varepsilon_r = 7.81$ and $\tan\delta = 5 \times 10^{-4}$) compared to the pure samples. The dielectric window is designed in computer simulation technology (CST) using

experimentally derived dielectric properties. The theoretical value of the window's insertion and return loss is better than 61.25 dB and 0.009 dB, respectively, at 3.7 GHz.

4.3 Introduction

AlN (aluminium nitride) contains a covalent bond with a wurtzite structure, making it challenging to sinter and densify at low temperatures [133]. Many researchers followed different sintering methods and used different oxide or fluoride additives to reduce the sintering temperature and densify AlN ceramics [17, 18]. Various sintering methods used for densifying AlN ceramics are spark plasma sintering [136-137], microwave sintering [138, 62], Hot isostatic pressing, etc., and Honma. T et al. [139] sintered AlN ceramics using $Ca_3Al_2O_6$ as an additive at 1880 ℃, studied (cathodoluminescence properties) transmittance spectra and said that in the range 260-550 nm increase in transmittance, intensity is due to the oxygen-induced defect caused by the additive. Yao. Y. et al. [79] sintered AlN ceramics using Er_2O_3 and Y_2O_3 as additives at 1800 ℃-1950 ℃ for 2 h in a graphite furnace, achieved 106 W/mK.

However, the synthesis of pure AlN is complicated because of its low chemical stability [71–74]. Achieving 100% density is challenging due to its covalent bond nature. While sintering, oxygen can settle on the grain boundaries and in the AlN lattice. This oxygen scatters the primary heat carrier (phonon), decreasing thermal conductivity [75]. Most of the used additives were rare earth oxides and alkaline earth oxides for AlN ceramic's densification. While sintering, these additives form a liquid phase, resulting in the ceramics' densification at lower temperatures [76, 77]. The most used rare earth oxide additives for fabricating AlN ceramics were Sm_2O_3 and Y_2O_3. These additives help to densify AlN by forming the liquid phase, but the formation of secondary phases was inevitable. Hence, the chemical inertness of AlN would be lost. These additives helped to densify the ceramics but could not eliminate the secondary phase [77–79]. However, AlN with ZnO and Er_2O_3 additives has not been studied

intensively. The pressure-less sintering method easily creates a problem of aluminum vacancies in AlN since oxygen can easily replace nitrogen to form aluminum vacancies while sintering at high temperatures. Oxygen in AlN is in the form of Al_2O_3 [80, 81]. The oxide additives react with Al_2O_3-covered AlN particles and helps in avoiding Al^{3+} vacancies, and reducing pores by forming a liquid phase. Thus theses oxide additives prevent formation of Al_2O_3 by reacting with Al^{3+} vacancies [82].

The dielectric window is a critical component and hermetically sealed barrier between the external and ultra-high vacuum regions through which microwave power can pass with negligible absorption. Although a lot of work on the dielectric window is available in the literature [5, 140–147], not much work has been carried out on the study of demountable type dielectric window along with the dielectric materials for S-band frequency at spot frequency 3.7 GHz. In this regard, both preliminary experiments and simulations are carried out. In the simulations, to feed the input parameters, it's necessary to give actual values obtained from the experiments to get the exact dimensions and understanding of the window parameters, which are crucial in developing the window.

Most researchers studied the thermal conductivity of AlN ceramics [76, 78, 148, 149]. Some researchers studied the fluorescence effect of Er-doped AlN ceramics, which were sintered in hot isostatic pressing with a 6-ton load for 24 h and sintered at 2000 ℃ [149]**.** However, most of these studies on AlN aim at improving thermal conductivity and densification. Also, there were no reports on the theoretical simulations to identify a suitable diameter and thickness of AlN for the window design at 3.7 GHz. This literature gap motivated us to carry out this study—the phase pure AlN and AlN ceramics with ZnO and Er_2O_3 as additives. AlN- Er_2O_3 composite ceramics' microwave dielectric properties were obtained to provide the input for dielectric window design and simulations.

4.4 Experimental procedure

Preparation of AlN – x ZnO composite ceramics: In this study, the pure and ZnO-added AlN ceramics are sintered using a two-step sintering process. Initially, powders are prepared using the solid-state reaction method. Pure AlN powder is ball milled in dry ball milling for 10 h with 300 rpm using a ball mill. ZnO-added AlN composites are prepared using isopropanol as a liquid media using the wet ball milling method. The additive AlN-ZnO composition is prepared by ball milling at 150 rpm for 12 h. Here, the additive is added in different wt% from 5 wt% to 20 wt%, and these samples are named as shown in Table 4.1. The ball-milled sample is collected and dried on a hot plate. Then, the dried sample is ground to make a fine powder.

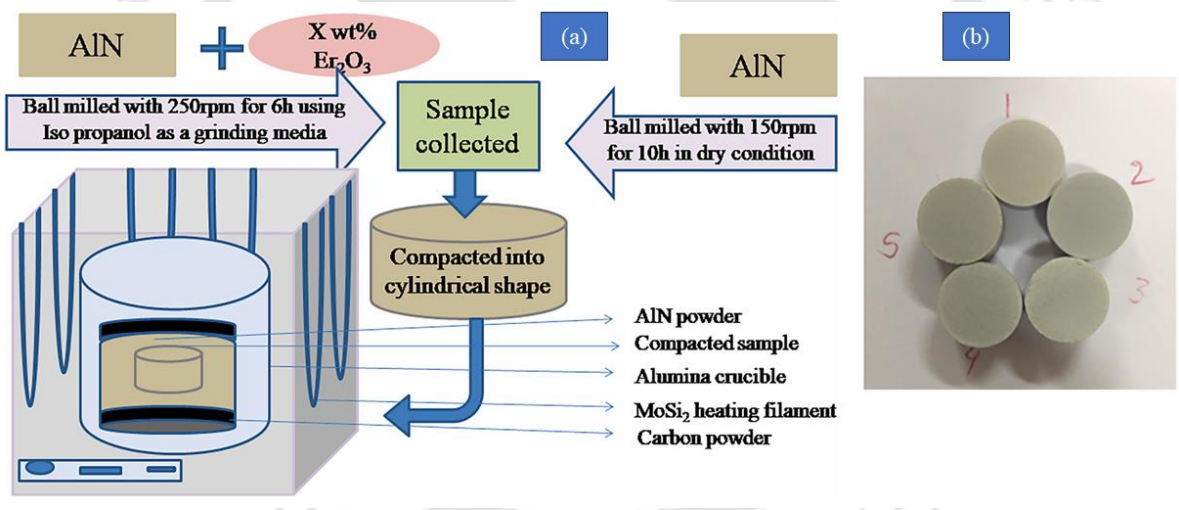

***Figure 4. 1*: (a) The process of preparing AlN ceramics in the solid-state reaction method and (b) Sintered samples at 1700 ℃ with 3 h 1) Pure AlN 2) 0.5ErAlN 3) 1ErAlN 4)2ErAlN 5) 3ErAlN.**

These powder samples are compacted into a cylindrical shape using a hydraulic press by applying a 2.5 MPa pressure. The compacted sample is of dimensions 10 mm (diameter), ~5 mm, and 1 mm (thickness). The compacted samples are sintered using the powder bed method in a sintering furnace. A two-step sintering process is used to densify the AlN ceramics. The

sintering process is as follows: first from 20-800 ℃ with 17 ℃/min with 1 h dwelling time, and the second step involves 800-1700 ℃ with 15 ℃/min with 20 h dwelling time.

***Table 4. 1*: Specification of the AlN-ZnO composites.**

Sample	AlN (wt%)	ZnO (wt%)	Relative density (%)
AlN	100	0	94.67
AlN-5ZnO	95	5	94.63
AlN-10ZnO	90	10	94.51
AlN-15ZnO	85	15	94.43
AlN-20ZnO	80	20	94.32

Preparation of AlN – x Er_2O_3 composite ceramics: Rare earth oxide (Er_2O_3) additive AlN ceramics are prepared using conventional sintering by solid-state reaction method, as shown in Figure 4.1(a). Pristine AlN and Er_2O_3 powders are added to make the required composition and mixed by employing a ball mill using isopropanol as a liquid media at 250 rpm for six h. Additive Er_2O_3 was added (0.5-2 wt%) to study the additive AlN ceramics' effect. Then, the slurry collected in a beaker dried on a hot plate ground to get a fine powder. This fine mixture of AlN + *x* wt% Er_2O_3 compacted cylindrical shape with KBr press of size 10 mm diameter and 1 mm and 5 mm thicknesses according to the requirement. The Compacted samples are sintered in two stages: initially at 1600 ℃ for 3 h and then at 1700 ℃ for 3 h in the presence of nitrogen with a powder bed, as shown in Figure 4.1(b). The powder bed consists of 80% AlN powder and 20% C (carbon) powder to arrest the formation of Al_2O_3, which forms by oxidation during the sintering at high temperatures.

4.5 Results and discussions of AlN-ZnO composite ceramics

4.5.1 Structural analysis:

The density of the sintered samples is measured using Archimedes' principle using distilled water as a liquid media. The calculated relative densities of all AlN-ZnO composites are listed in Table 4.1. XRD pattern of all sintered AlN-ZnO composites is observed in the 2θ range 32° to 80° with a step size of 0.02°, as shown in Figure 4.2. This XRD pattern reveals that all sintered AlN-ZnO composites exhibit the desired wurtzite crystal structure with the $P6_3mc$ space group. Pure and additive AlN ceramics XRD pattern indexed with the standard XRD pattern using JCPDS of card number 01-077-9871 of space group 186.

Table 4. 2: The Rietveld refined parameters for the XRD pattern of AlN-ZnO composites.

Composite	χ^2	Rf-factor	Bragg Rf-factor	a (Å)	c (Å)	Volume $(Å)^3$
AlN	1.12	3.08	3.59	3.113 (28)	4.981 (76)	41.793 (1)
AlN-5ZnO	1.53	2.32	3.64	3.115 (31)	4.985 (58)	41.894 (1)
AlN-10ZnO	1.42	2.57	4.16	3.116 (38)	4.987 (69)	41.936 (1)
AlN-15ZnO	1.28	2.39	4.08	3.115 (23)	4.986 (65)	41.907 (1)
AlN-20ZnO	1.89	2.71	3.93	3.116 (77)	4.987 (84)	41.938 (2)

Further, the XRD pattern of pure AlN and AlN-15ZnO composites are refined by Rietveld refinement using full prof suit software for determining lattice parameters and volume. The Rietveld refined patterns of pure AlN and AlN-15ZnO are shown in Figure 4.3. the diffraction peaks of pure AlN and AlN-15ZnO are fitted using the pseudo-Voigt function. The powder bed helps in preventing oxidation. It is well known that avoiding the formation of Al_2O_3

is challenging. However, the sintering bed suppressed the formation of Al_2O_3. The Rietveld refined parameters of all sintered samples are shown in Table 4.2.

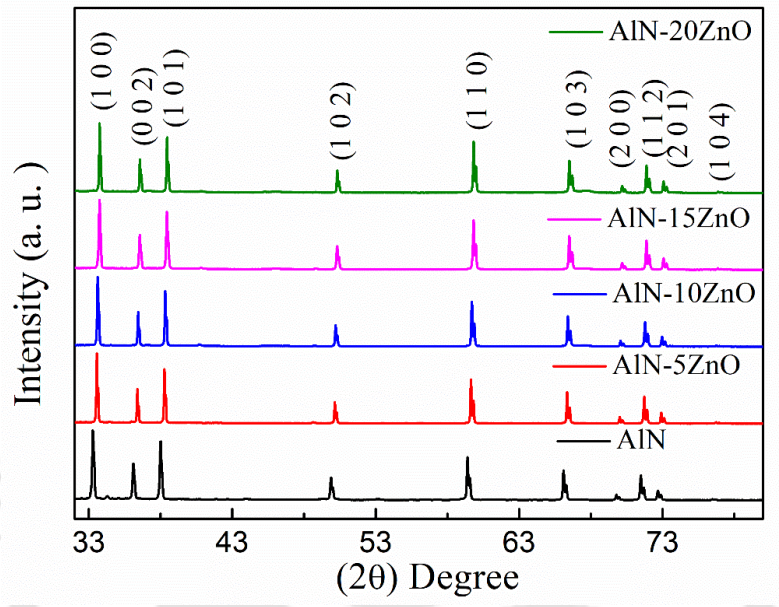

***Figure 4. 2*: The XRD pattern of all samples of AlN-ZnO composites sintered at 1700 ℃ for 20 h.**

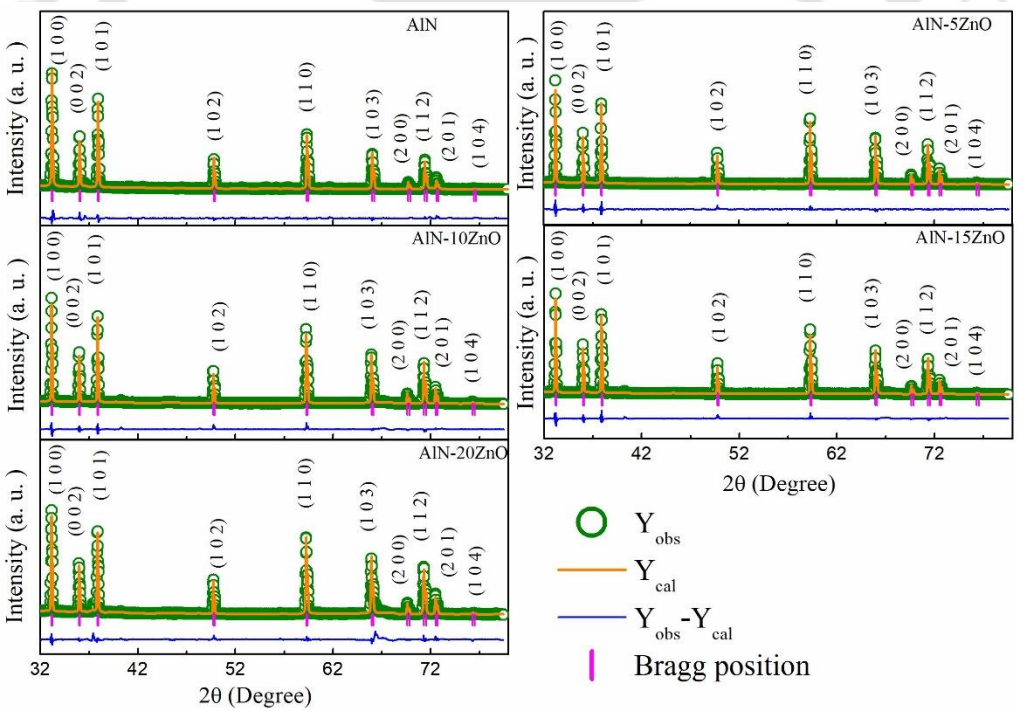

***Figure 4. 3*: The Rietveld refinement XRD pattern of pure AlN and AlN-15ZnO composite.**

The Rietveld refined parameters of AlN-15ZnO ceramic are $\chi^2 = 1.28$, Bragg Rf-factor 4.08, volume 41.907 $Å^3$, with lattice parameters $a = b = 3.115$ Å, $c = 4.986$ Å. The Rietveld refinement parameters for pure AlN ceramics are $\chi^2 = 1.12$, Bragg Rf-factor 3.59, volume 41.793 $Å^3$, with lattice parameters $a = b = 3.113$ Å, $c = 4.981$ Å. The lattice volume of additive AlN ceramics is higher than that of pure AlN ceramics; this might be due to the occupation of vacancies or the replacement of Aluminum vacancies with Zn^{2+}. The lattice parameters of all sintered AlN-ZnO composites agree with previously reported values [150].

4.5.2 Raman analysis:

The Raman spectrum of all sintered pure and AlN-ZnO composites is obtained using a 532 nm laser by exiting with 30 mW power and shown in Figure 4.4. This result reveals that each composition has six vibrational modes of the wurtzite AlN phase. One of all vibrational modes, the most vital mode is E_2 (High), representing nonpolar vibrations of Al and N atoms. The Raman spectra of all sintered samples are fitted using the Lorentzian function.

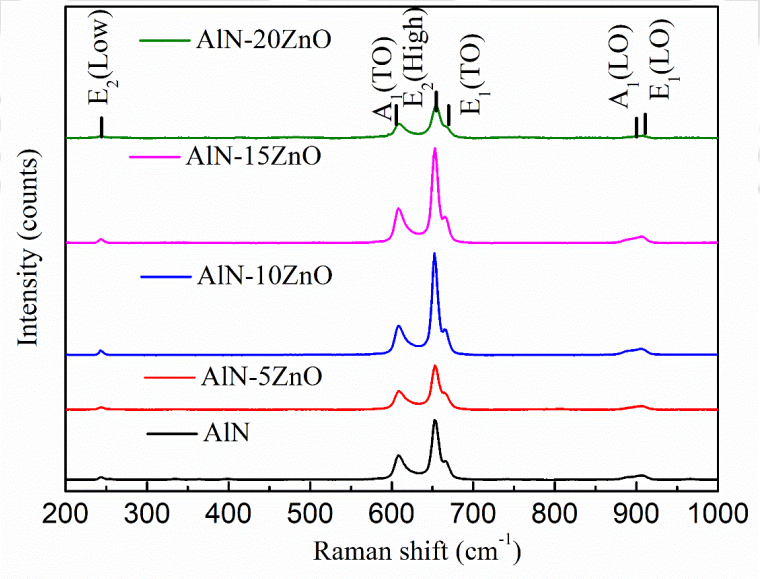

Figure 4. 4: The Raman spectrum is obtained using a 532 nm laser with 30 mW power for pure AlN, and AlN-ZnO composite ceramics sintered at 1700 °C for 20 h.

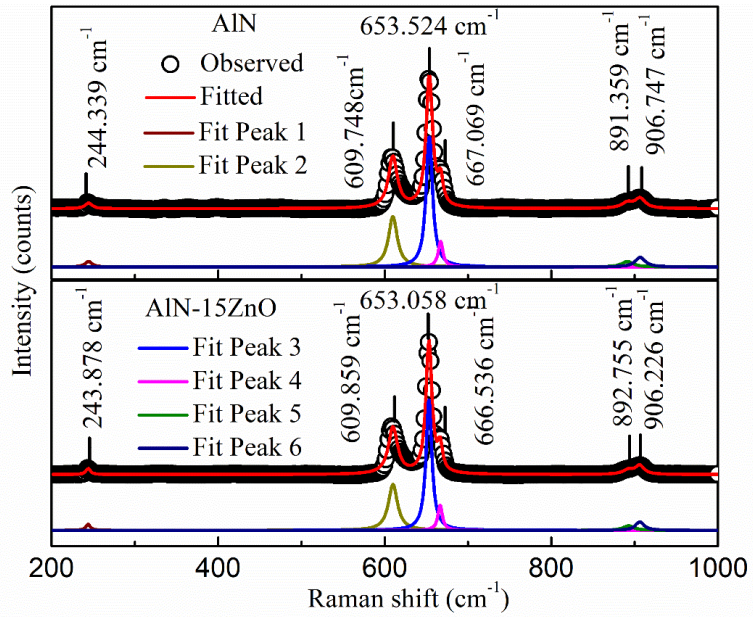

***Figure 4. 5*: The Raman spectrum fitting of pure AlN and AlN-15ZnO composite are recorded using a 532 nm laser with 30 mW power and fitted using the Lorentz function.**

***Table 4. 3*: The fitted parameters for the Raman spectra of AlN-ZnO composites.**

Sample/	AlN		AlN-5ZnO		AlN-10ZnO		AlN-15ZnO		AlN-20ZnO	
Phonon mode	γ (Cm^{-1})	β (Cm^{-1})	γ (Cm^{-1})	β (Cm^{-1})	γ (Cm^{-1})	β (Cm^{-1})	γ (Cm^{-1})	β (Cm^{-1})	γ (Cm^{-1})	B (Cm^{-1})
E_2(Low)	244.00	9.371	243.51	11.673	243.41	17.353	242.92	19.787	243.45	24.304
A_1(TO)	609.81	13.952	609.73	15.841	610.00	15.417	610.32	16.282	610.37	15.890
E_2(High)	653.49	9.312	653.18	9.803	653.05	8.608	652.88	8.096	654.48	11.886
E_1(TO)	666.85	7.237	665.58	10.726	665.60	7.218	666.45	7.535	667.84	9.800
A_1(LO)	891.87	17.080	896.98	25.372	894.74	23.021	895.40	55.265	896.64	32.630
E_1(LO)	906.57	12.583	905.47	14.147	906.31	11.242	905.60	23.111	907.88	19.447

The fitted spectrum of pure AlN and the best composition AlN-15ZnO are shown in Figure 4.5. The fitted results of all spectrums as Raman shift and full width half maximum values of all modes are shown in Table 4.3. The Raman modes corresponding AlN-5ZnO, AlN-10ZnO, AlN-15ZnO composites, E_2 (Low), E_2 (High), E_1 (TO), and E_1 (LO) show redshift

(shifting towards lower frequency) and other modes shows blue shift (shifting towards higher frequency) in comparison with the Raman modes of pure AlN ceramic.

AlN-20ZnO composition E_2 (High), E_1 (LO) modes also show blue shift with other A_1 (TO), A_1 (LO) modes as common with other composites. Oxygen-related defects in the AlN lattice are implied in the broadening of the E_2 (high) mode. Al vacancy in AlN lattice created due to the substitution of oxygen atom in place of *N* atoms by the charge neutrality constraint broadens the Raman line width.

4.5.3 XPS analysis:

The XPS high-resolution spectra of Al 2p, Zn 2p, N 1s, and O 1s for AlN-15ZnO ceramic are shown in Figure 4.6 (a)-(d), respectively, with corresponding deconvoluted peaks.

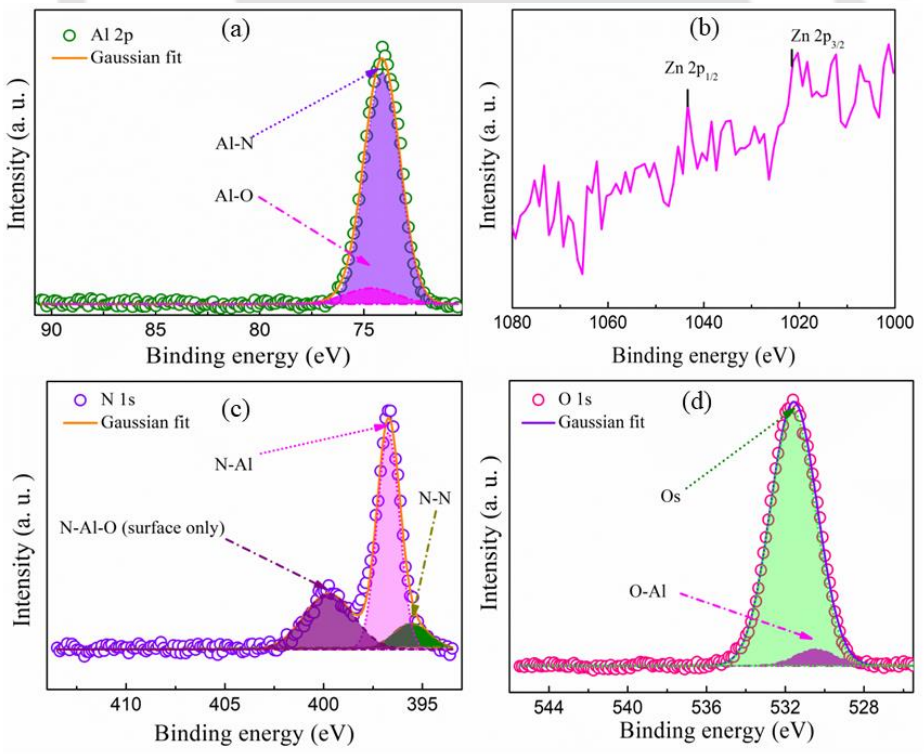

Figure 4. 6: The High-resolution spectra of AlN-15ZnO ceramics fitted using the Gaussian function with their deconvoluted peaks (a) Al 2p (b) Zn 2p (c) N 1s and (d) O 1s.

The XPS investigation of sintered composite AlN-15ZnO ceramics confirms the existence of aluminium vacancies and oxygen. The primary C 1s peak at 284.83 eV for adventitious surface carbon is set as a reference binding energy. All deconvoluted peaks are fitted using the Gaussian function. All deconvoluted peaks of AlN-15ZnO composite binding energies with their corresponding proposed chemical bond descriptions are summarized and listed in Table 4.4. The high-resolution XPS scan of the Al 2p peak reveals the nature of aluminium bonding. Figure 4.6 (a) indicates that only small intensity Al-O at 74.66 eV is detected besides the primary bond Al-N at 74.11 eV assigned for aluminium bound to nitrogen in wurtzite AlN.

Table 4. 4: XPS high-resolution spectra results and their deconvoluted peaks with related chemical bonds.

Sub shell	Chemical bond	Binding energy (eV)
C 1s	C-C	284.83
Al 2p	Al-N	74.11
	Al-O	74.66
Zn 2p	Zn $2p_{3/2}$	1021.57
	Zn $2p_{1/2}$	1043.35
N 1s	N-N	395.57
	N-Al	396.72
	N-Al-O (surface only)	399.73
O 1s	O-Al (grain boundaries)	530.47
	Os (surface only)	531.61

The Zn 2p, high-resolution spectrum, shows doublet (see Figure 4.6 (b)) with binding energies 1021.57 eV and 1043.35 eV identified as a corresponding line to Zn $2p_{3/2}$ and Zn $2p_{1/2}$ respectively, with very low intensities compared to other elements. The binding energy difference between the two lines is 21.78 eV, in good agreement with previously reported

values [151]. The analysis of Figure 4.6 (c) indicates that the nitrogen mainly bonded with aluminium indicated by the deconvoluted peak by N-Al at 396.72 eV.

The deconvoluted peaks of N 1s with N-Al are as little intensity at 395.57 eV and 399.73 eV, corresponding to the chemical bonds N-N and N-Al-O, respectively. This N-Al-O is located at the surface only, not in grain boundaries, and matches with previously assigned values [152]. The oxygen high-resolution peak is fitted with two deconvoluted peaks corresponding to O-Al at grain boundaries and Os at the surface only, with binding energies at 530.47 eV and 531.61 eV, respectively (see Figure 4.6 (d)). The O-Al at grain boundaries deconvoluted peak is with low intensity compared with surface oxygen, and this oxygen might be additive. This surface oxygen is due to the adsorbed gas and powder bed oxidation. This XPS result of the AlN-15ZnO composite shows that the Zinc (Zn) present in the sample is much less, and oxygen is present in the composite ceramics on the surface, not in grains. The other elements of wurtzite AlN obtained appropriately, such as Al 2p the significant contribution of 90.77% is of Al-N chemical bond, N 1s high-resolution spectra contain 56.79% contribution is of N-Al, significantly less amount as 10.90% as N-N chemical bond contribution.

4.5.4 Dielectric properties:

Semiconductor devices and multi-chip modules in the micro-electronics industry require high density and frequency to meet high-speed signal processing. The dielectric permittivity and dissipation factor of dielectric material for electronic applications is significant since the low dissipation factor of insulating material used in electronic packages helps reduce signal loss by resisting absorption or desorption of electrical signals passing throughout the electronic package. The dielectric permittivity should be low for high-speed digital circuitry. Since the transmission speed of a pulse is inversely proportional to the square root of that

dielectric permittivity in a circuit in contact with the dielectric material. Hence, the lower the dielectric permittivity, the higher the transmission speed. High-quality signal delay in the substrate also needs to be reduced to improve the performance of high-speed IC systems. The signal propagation delay time depends upon the dielectric permittivity of the substrate as follows.

$$T_d = lx\frac{\sqrt{\varepsilon_r}}{c} \tag{4.1}$$

where, T_d = Delay time, l = Signal transmission length, ε_r = Dielectric permittivity of the substrate, c = Speed of light. Hence, the reduction of delay time is possible by lowering dielectric permittivity. The length of the resonator is inversely proportional to the square root of dielectric permittivity. The RF-components size can increase inconveniently if the dielectric permittivity is low.

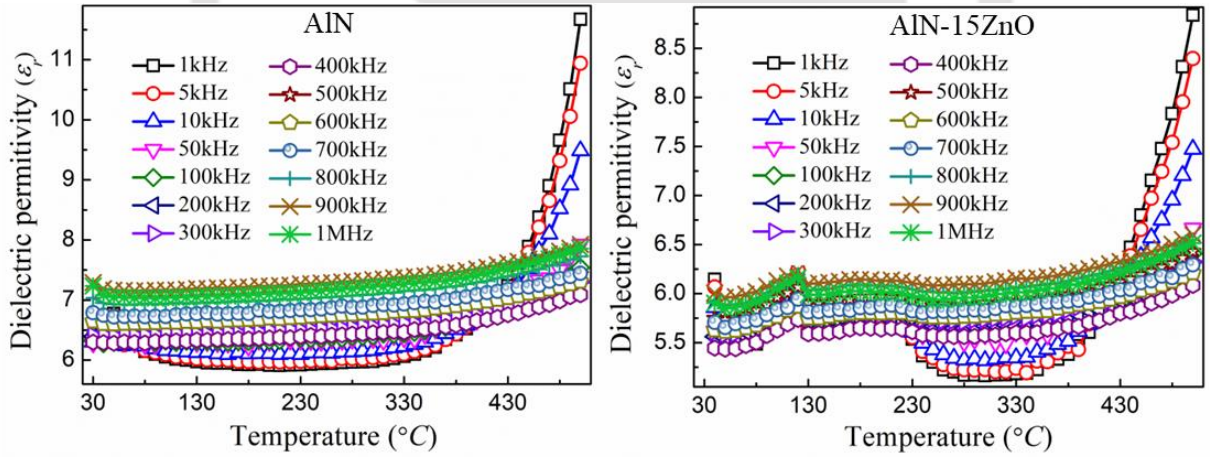

Figure 4. 7: The variation of dielectric permittivity with temperature for pure AlN and AlN-15ZnO composite measured at frequencies ranging from 1 kHz to 1 MHz.

The case of materials with high permittivity also causes problems since they require narrow lines to match impedance properly. Dielectric permittivity is essential in controlling the impedance of microwave and RF circuits to reduce the energy reflections at the interface of circuit tracks and components. The dielectric properties of AlN and best composition AlN-

15ZnO are studied using a sample of 10 mm diameter and 1 mm thickness, sintered at 1700 ℃. After sintering, the sample is polished and coated with silver paint on both sides for measuring capacitance. The dielectric permittivity is calculated from capacitance obtained for pure and composite AlN ceramics using the following relation:

$$\varepsilon_r = \frac{Ct}{A\varepsilon_0} \tag{4.2}$$

The variation of dielectric permittivity with temperature increment from 30 to 500 ℃ at various frequencies is shown in Figure 4.7. The dielectric permittivity of pure AlN ceramic ranges from 5.6 to 8.0, and the best additive AlN-15ZnO composite ranges from 5.5 to 7.4 in temperatures ranging from 30 to 500 ℃. The dielectric permittivity of AlN-15ZnO is lower than that of pure AlN ceramics. The dielectric permittivity of pure AlN and AlN-15ZnO composite is enhanced with an increase of temperature from 30-500 ℃, attributed to the alignment of dipoles due to the thermal energy.

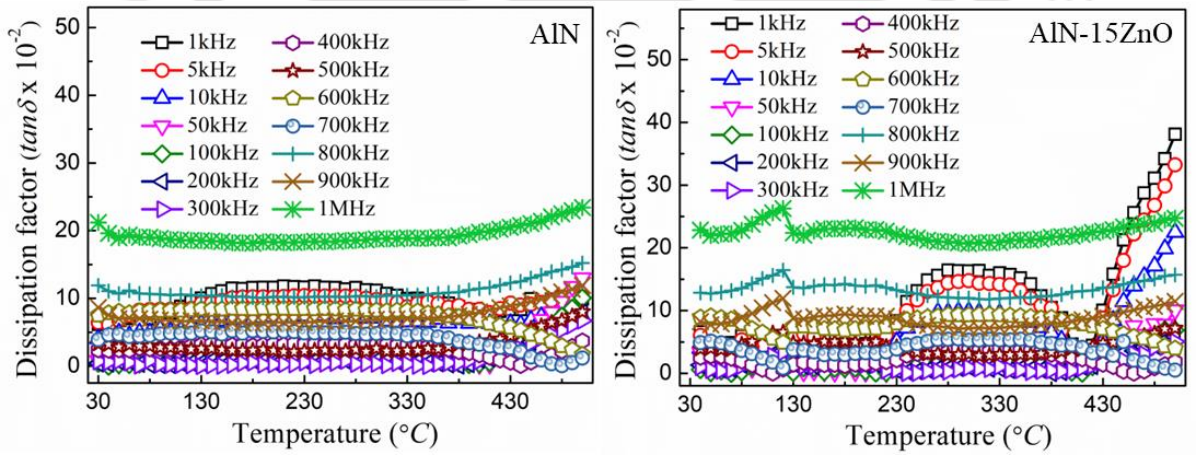

Figure 4. 8: The variation of dissipation factor with temperature for pure AlN and AlN-15ZnO composite at various frequencies ranging from 1 kHz to 1 MHz.

The Dissipation factor of pure and best additive AlN-15ZnO ceramics as a function of temperatures at various frequencies are shown in Figure 4.8. This result reveals that the dissipation factor of pure AlN and AlN-15ZnO ceramics is almost constant by the varying

temperature at a particular frequency. The dissipation factor of pure AlN ceramic shows a slightly increasing nature of 380 ℃ at higher frequencies 300 kHz onwards. For the best additive, AlN-15ZnO ceramic shows a slightly decreasing nature at 80 ℃, continues almost constant up to 420 ℃, and then slightly increasing nature from 420-500 ℃. The increment at higher temperatures in pure AlN ceramic above 380 ℃ and additive above 420 ℃ may be higher phonon scattering due to thermal activation. The slightly enhancing dissipation factor behavior of AlN-15ZnO composite at 80 ℃ attributed to the addition of ZnO. The dissipation factor of pure AlN ceramics shows a minor increasing nature by increasing frequency from 1 kHz to 1 MHz due to the dipolar polarization. Impedance spectroscopy is an effective technique to characterize the electrical properties of sintered ceramics. The impedance spectroscopy is obtained over a frequency range of 1 kHz to 1 MHz at various temperatures of 100 ℃ to 500 ℃ for the samples pure AlN and best composite AlN-15ZnO sintered using a two-step sintering process, which is shown in Figure 4.9. This result reveals that the impedance spectrum at each temperature for pure AlN and composite AlN-15ZnO ceramics is well-fitted with the circuit corresponding to three RC (resistor-capacitor) units. The equivalent circuit consists three number of RC circuits.

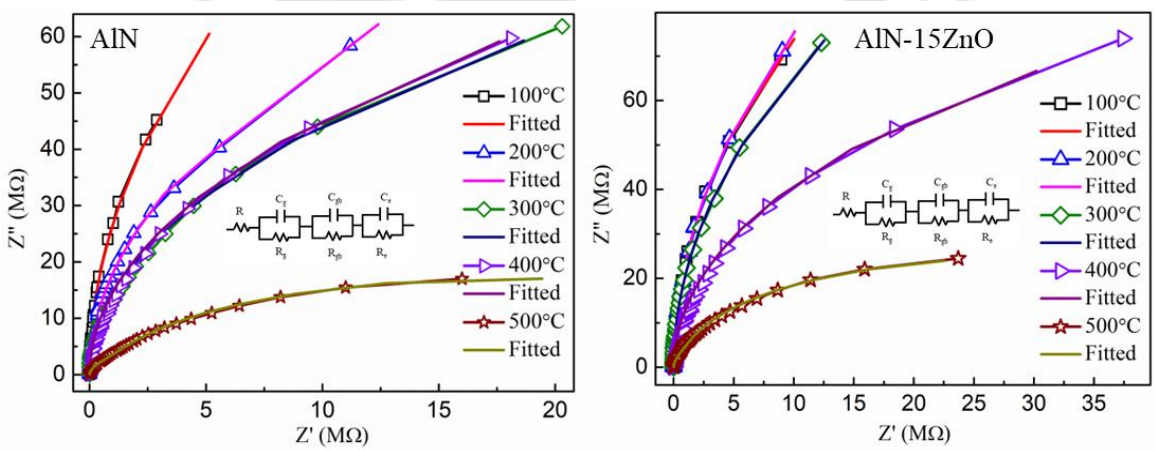

***Figure 4. 9*: The Cole-Cole plot for pure AlN and AlN-15ZnO composite at various temperatures from 100-500 ℃.**

The number of RC units in the equivalent circuit is related to the number of different microstructural components of ceramic causes for impedance spectroscopy. Those microstructural components affecting impedance spectroscopy are grains, grain boundaries, electrodes, residues, or pores. In the present study, the impedance spectroscopy of pure and best composite AlN-15ZnO ceramics, fitted with the equivalent circuit containing three RC components in series, as shown in Figure 4.9. One RC circuit representing grain resistance(R_g) and grain capacitance (C_g), second RC circuit representing grain boundary resistance (R_{gb}) and grain boundary capacitance (C_{gb}), the third RC unit corresponding to electrode resistance (R_e) and electrode capacitance (C_e).

***Table 4. 5*: The numerical values are evaluated from the Cole-Cole fitting for the AlN-15ZnO composite.**

Temperature (℃)	Capacitance (*pF*)	Resistance (*MΩ*)	Relaxation time (*msec*)
100	2.076	575.7	1.19515
200	2.07	576	1.19232
300	2.104	443.8	0.93376
400	9.259	13.13	0.12157
500	1.981	17.73	0.03512

Precipitates are unaffected since fewer pores in the sintered sample in the two-step sintering process result in high density. The Cole-Cole plot of pure and AlN-15ZnO composite ceramics is fitted well with an equivalent circuit containing three RC circuits, as shown in Figure 4.9. The fitted parameters of grain resistance and grain capacitance of the best composite AlN-15ZnO ceramic are shown in Table 4.5. The impedance spectra of pure AlN and the best composite AlN-15ZnO ceramics of sintered samples prove that the non-Debye conduction process is contained in the samples. The frequency-dependent real part of impedance for pure AlN and the best AlN-15ZnO composite is shown in Figure 4.10. This result reveals that the

impedance of the best composite AlN-15ZnO is more than pure AlN ceramic in the frequency range of 1 kHz to 1 MHz.

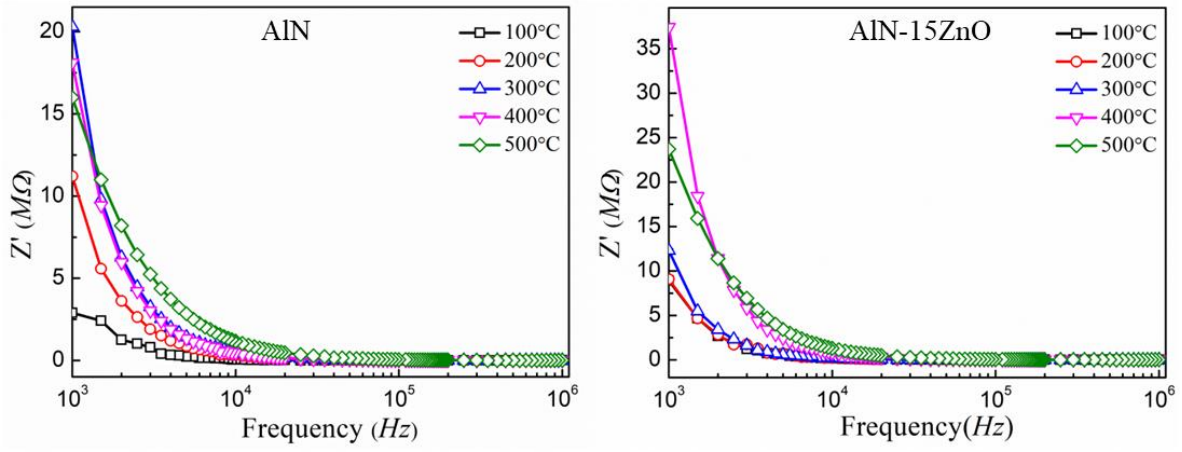

***Figure 4. 10**: The variation of the real part of impedance for AlN and AlN-15ZnO composite as a function of frequency from 1 kHz to 1 MHz measured at various temperatures from 100-500* ℃.

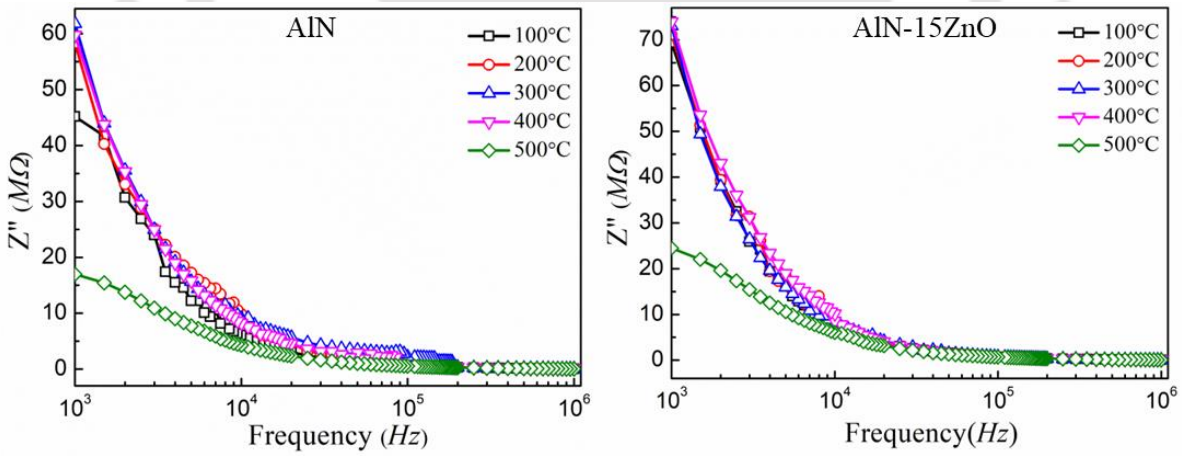

***Figure 4. 11**: The variation of the imaginary part of impedance for AlN and AlN-15ZnO composite with frequency variation from 1 kHz to 1 MHz, at various temperatures from 100-500* ℃.

The impedance of pure and additive AlN ceramics decreases with frequency increasing from 1 kHz to 1 MHz. The impedance increases if the temperature rises from 100-500 ℃ for pure AlN and AlN-15ZnO composite. This response indicates that the conductivity will increase with frequency from 1 kHz to 1 MHz, as a typical semiconductor behavior. The

impedance of pure and additive AlN ceramics at higher frequencies above 20 kHz merged. The merging at higher frequencies might be due to space charge polarization relaxation.

There are two types of dielectric relaxation processes: one is the Debye type, and the other is the non-Debye type of relaxation. The Debye type of dielectric relaxation is for a non-interacting system (one body). i. e., the system containing non-interacting dipoles considering dipoles separated by a viscous medium. In the Debye type of relaxations, the dipoles are aligned along the field direction by applying the electric field and return to their original position by removing the applied electric field. Impedance spectra will be a perfect semi-circle originating from the real axis in the case of the Debye type of relaxation. However, generally, many systems exhibit non-Debye-type relaxations. This non-Debye type system contains a distorted semi-circle since interactions present in the dipoles present in the system. The imaginary part of impedance for pure AlN and AlN-15ZnO composite as a function of frequency at various temperatures ranging from 100-500 ℃ are measured and shown in Figure 4.11. This result indicates the imaginary part of impedance for both pure and composite AlN ceramics are high value and decreases with temperature; this response is due to thermally activated charges relaxation.

4.5.5 Microwave dielectric properties

The microwave dielectric properties of sintered AlN-ZnO composite ceramics are measured using Hakki Colemann's method. The measured values are shown in Table 4.6. This result reveals that the pure AlN dielectric permittivity (ε_r) 8.44, dissipation factor ($\tan\delta \times 10^{-3}$) 2.64 at 12 GHz. The dielectric permittivity decreases by increasing the amount of additive ZnO. The best additive composition AlN-15ZnO composite dielectric permittivity (ε_r) = 7.20 is lower than all composites with dissipation factor ($\tan\delta$) = 4.90 × 10^{-3}. The dissipation factor results are one order of magnitude lesser than the previously reported values [127] and

in good agreement with the previously reported values by Gonzalez M. et al. [131]. These results are appropriate for transmitting a signal with low signal loss and high speed.

Table 4. 6: The microwave dielectric properties of pure AlN and AlN-ZnO composites.

Sample	Dielectric Permittivity	Loss tangent ($\tan\delta \times 10^{-3}$)
AlN	8.44	2.64
AlN-5ZnO	8.21	2.67
AlN-10ZnO	7.26	4.09
AlN-15ZnO	7.20	4.90
AlN-20ZnO	7.35	3.71

4.6 Results and discussions of AlN-Er_2O_3 composite ceramics

4.6.1 Density analysis

The AlN ceramics added with different concentrations of Er_2O_3 and their codes are given in Table 4.7. The relative densities of pure and additive ceramics are as follows: (1) AlN - 90.53%, (2) 0.5ErAlN – 91.65%, (2) ErAlN - 92.21%, (3) 2ErAlN – 94.16%, and (3) 3ErAlN – 93.11%. Archimedes' principle is used to measure density.

Table 4. 7: Specification of the prepared compositions.

Composition name	Er_2O_3 (x wt%)
AlN	0
0.5ErAlN	0.5
1ErAlN	1
2ErAlN	2
3ErAlN	3

The density of additive ceramics increases by increasing additive concentration and showing decreasing nature at 3 wt% additive; the reason for this increasing density is replacing

vacancies in AlN by the additive. The ceramics with 3 wt% additive show less density due to the formation of pores by replacing Al^{3+} or N^{3-} with additive ions. The maximum density (~ 94%) is obtained for 2ErAlN.

4.6.2 XRD analysis

The X-ray diffraction (XRD) patterns of pure and additive (Er_2O_3) AlN ceramics are shown in Figure 4.12. Interestingly, all the sintered samples showed a wurtzite crystal structure with a $P6_3mc$ space group without any secondary phase at a lower temperature than in previous studies [153]. Carbon in the powder bed avoids entering oxygen into grains, and AlN powder prevents oxide layer formation. Thus, the powder bed avoids secondary phase formation even at high temperatures. The sintered samples ' XRD pattern (see Figure 4.12) showed the pure AlN phase. Further, it is noteworthy that the samples exhibited better densities at lower sintering temperatures without any secondary phases.

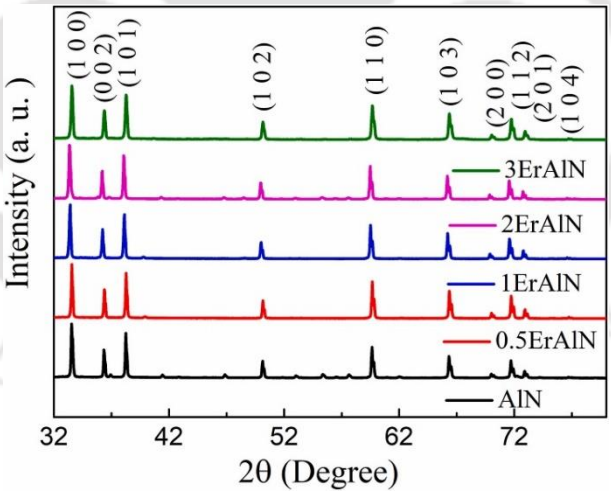

Figure 4. 12: The XRD pattern of pure and Er_2O_3-added AlN ceramics.

The Rietveld refinement of pure and Er_2O_3-added AlN ceramics is shown in Figure 4.13. This result reveals that the sintered samples had pure AlN phase with space group $P6_3mc$ and space group number 186 in the wurtzite structure. The Rietveld refinement parameters of

pure and Er_2O_3-added AlN ceramics are shown in Table 4.8. It reveals that the formed crystal structure after sintering is a wurtzite crystal structure with $\alpha = \beta = 90°, \gamma = 120°$.

Table 4. 8: The Rietveld refinement parameters of pure and Er_2O_3 added AlN ceramics, sintered at 1700 ℃ for 3h.

Sample	χ^2	Brag Rf-factor	Rf - factor	*a* = *b* (Å)	*c* (Å)	Volume (Å^3)
AlN	3.88	3.20	2.28	3.112	4.981	41.777
0.5ErAlN	3.18	2.51	1.27	3.113	4.981	41.806
1ErAlN	2.84	2.28	1.35	3.115	4.983	41.869
2ErAlN	2.52	2.62	1.60	3.113	4.983	41.826
3ErAlN	2.85	4.41	5.35	3.113	4.982	41.824

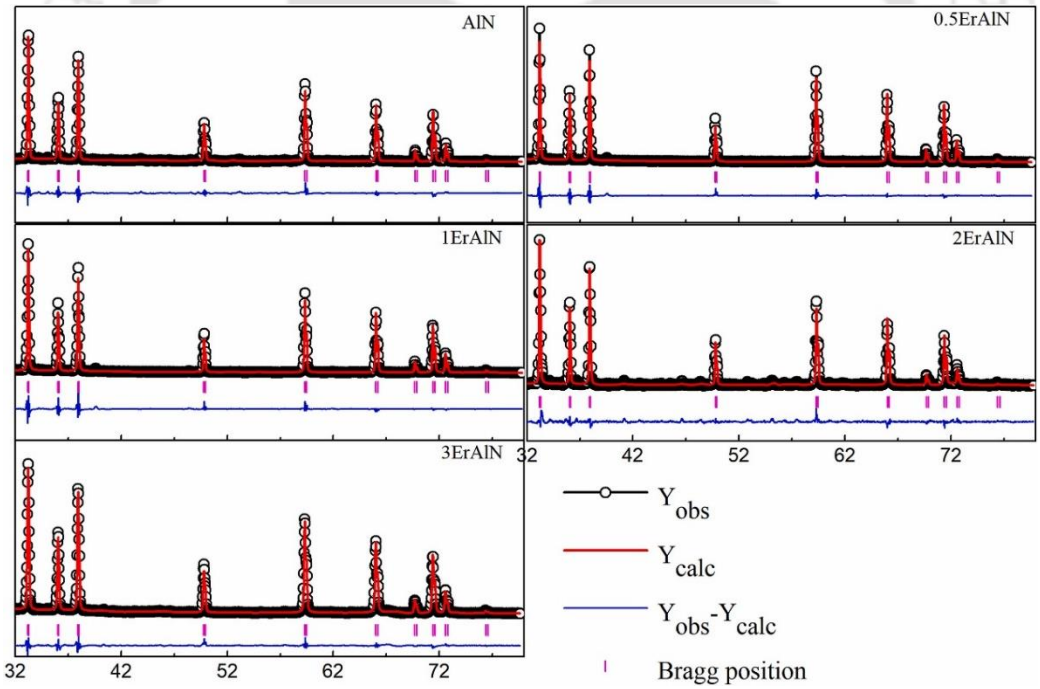

Figure 4. 13: The Rietveld refinement of Er_2O_3 added AlN ceramics.

4.6.3 Raman analysis

Raman spectroscopy is a sensitive tool for detecting impurities and studying crystalline structures. The Raman spectra of sintered samples recorded at room temperature for the pure

and 2ErAlN and shown in Figure 4.14. These spectra are obtained by exciting the sample with laser light of wavelength 514 nm with 30 mW power and 30 sec acquisition time. The Raman spectrum result revealed that prepared samples pure and additive (2ErAlN) consist of 6 phonon modes of AlN and confirmed that the obtained sample's structures are wurtzite.

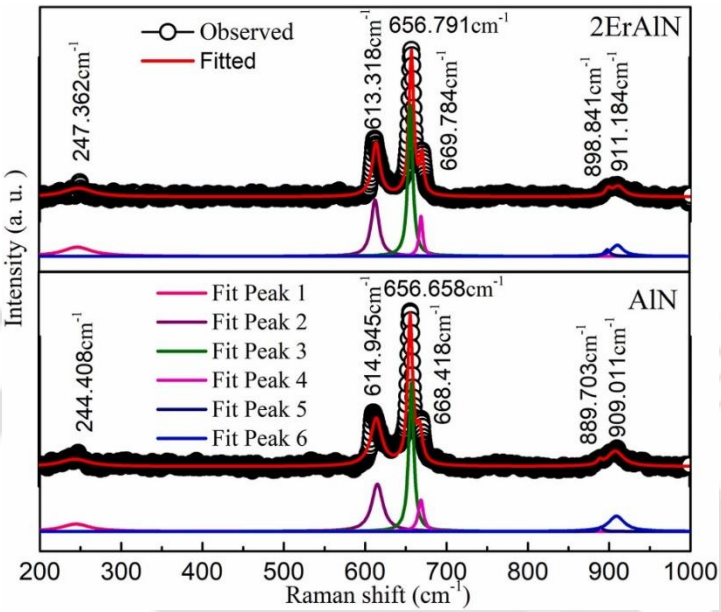

Figure 4. 14: The Raman spectra of the pure and 2ErAlN ceramics.

Table 4. 9: Phonon modes observed for pure AlN and additive 2ErAlN ceramics.

Sample/Phono n mode	AlN		2ErAlN	
	γ (Cm^{-1})	β (Cm^{-1})	γ (Cm^{-1})	β (Cm^{-1})
E_2 (Low)	244.41	42.181	247.36	43.597
A_1 (TO)	614.94	16.708	613.32	11.499
E_2 (High)	656.66	7.289	656.791	6.977
E_1 (TO)	668.42	7.901	669.78	5.394
A_1 (LO)	889.70	5.966	898.84	8.139
E_1 (LO)	909.01	23.209	911.18	18.004

The Lorentz function fits the Raman spectrum (see Figure 4.14). This result shows that the synthesized samples' pure and additive (2ErAlN) ceramics exhibited a wurtzite structure with pure phase AlN. The fitted result conveys us exact FWHM (β) values, and the phonon modes (γ) for pure AlN and additive 2ErAlN samples are in good agreement with the pure AlN wurtzite structure with $P6_3mc$ space group, which are tabulated in Table 4.9. All phonon modes except A_1 (TO) exhibited a blue shift (shifted towards the high frequency) due to the addition of Er_2O_3. A_1 (TO) mode shows a redshift (shifted towards the lower frequency). This blue and red shift in the Raman spectrum of 2ErAlN with pure AlN is attributed to the strain formed due to the additive Er^{3+} ions [154]. From XRD and Raman studies, phase pure AlN ceramics are obtained using a two-stage sintering process along with the sintering bed.

4.6.4 Broad band dielectric analysis

Few studies are available on AlN ceramics' dielectric properties [155, 156]. The dissipation factor of sintered samples is calculated in the following equation.

$$\tan\delta = {\varepsilon_r''}/{\varepsilon_r'} \tag{4.3}$$

The dielectric properties of pure and Er_2O_3-added AlN ceramics are measured using an RF-impedance analyzer from 1 MHz to 1 GHZ by varying the temperature from -140 ℃ to 200 ℃. The variation in dielectric permittivity and dissipation factor measured as a function of frequency is shown in Figure 4.15: a & b, respectively. It is observed that with an increase in the measurement frequency, the dielectric response of all the samples is stable. In contrast, the dissipation factor diminished with frequency and is a typical dielectric response. 2ErAlN shows the best result as compared to pure and other compositions.

The previous studies show that AlN added with 2 wt % exhibited the best structural and frequency-dependant properties; hence, for further studies, pure AlN and AlN doped with 2 wt

% Er_2O_3 are chosen. Further, it is vital to understand the temperature stability of these ceramics' dielectric behavior over a range of temperatures (-140 ℃ to 200 ℃) at a wide range of frequencies. To the author's knowledge, this study is unavailable in the literature. The variation of dielectric permittivity and dissipation factor as a function of temperature at different frequencies for pure AlN and 2ErAlN ceramics are shown in Figure 4.16. (a-d), respectively.

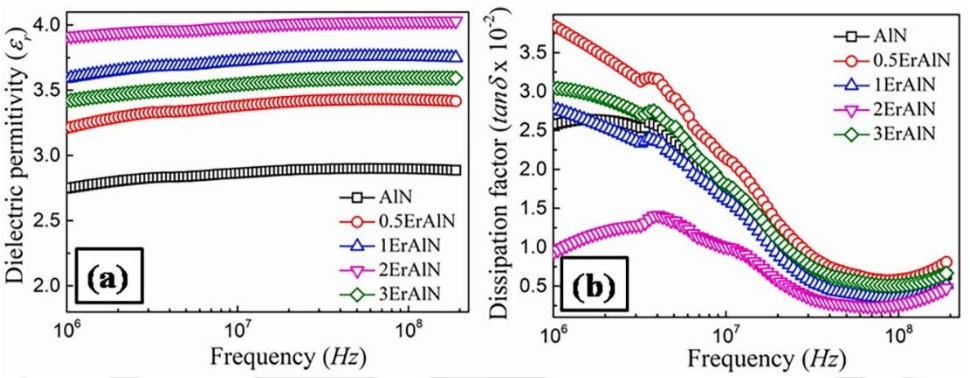

***Figure 4. 15*: (a) Dielectric permittivity & (b) dissipation factor of pure and Er_2O_3addedAlN ceramics, measured as a function of frequency.**

It is perceived that with a rise in the temperature, both samples' dielectric permittivity increased gradually and decreased with an increase in frequency. At low temperatures, all the thermal vibrations die out; thus, the dipoles are frozen. As the temperature increases, the dipoles align in the field direction with the available thermal energy, which improves the dielectric permittivity. Dissipation factor ($\tan\delta$) of these samples displayed a static response with temperature and fluctuated slightly with frequency. This result can be attributed to the higher relative densities, uniform grain growth, and the second phase's suppression. Besides, the sample with 2ErAlN ($\varepsilon_r = 4.11$ and $\tan\delta = 1.5 \times 10^{-2}$) exhibited a better dielectric response than the pristine AlN ceramics. This result states that the dielectric permittivity and dissipation factor are stable by increasing the temperature. The variation of dielectric properties of pure and 2ErAlN as a function of frequency (1 MHz to 10 MHz) measured at low temperatures -140 ℃ to 0 ℃ are shown in Figures 4.17: (a-d), respectively. Also, the variation

of dielectric properties of pure and 2ErAlN as a function of frequency (1 MHz to 10 MHz) measured at higher temperatures 20 ℃ to 200 ℃are shown in Figure 4.18 (a-d), respectively.

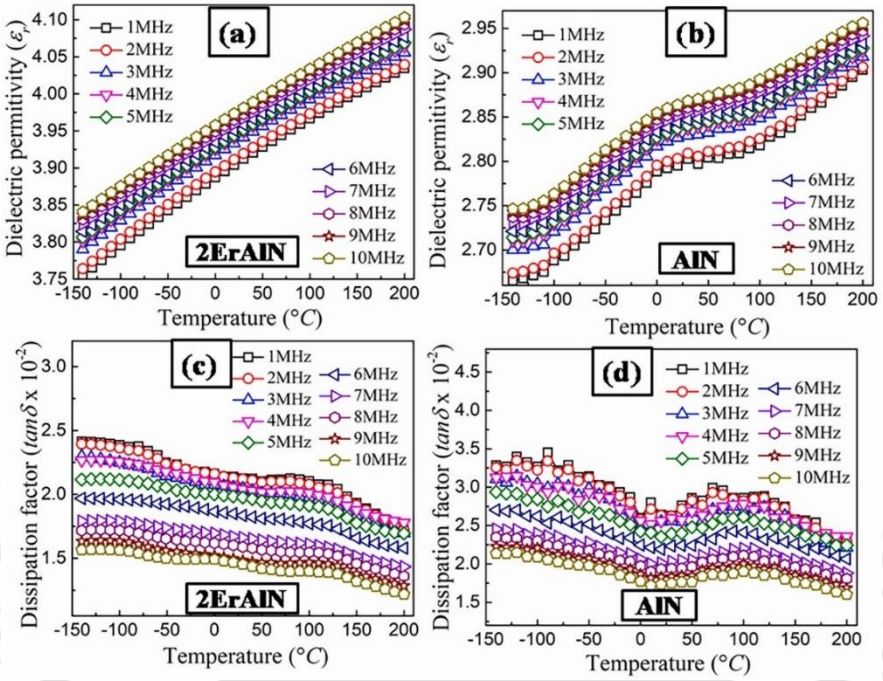

***Figure 4. 16*: Variation of dielectric permittivity (a) 2ErAlN; (b)AlN; and dissipation factor (c) 2ErAlN and (d) AlN ceramics as a function of temperature.**

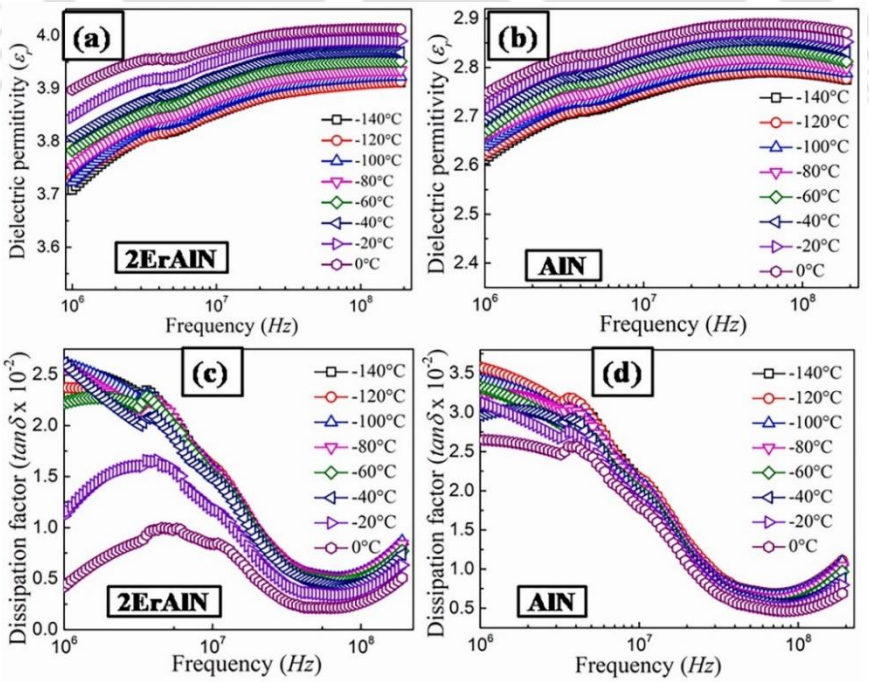

***Figure 4. 17*: Variation of dielectric properties as a function of frequency measured at -140 ℃ to 0 ℃: dielectric permittivity (a) 2ErAlN; (b)AlN; and dissipation factor (c) 2ErAlN and (d) AlN ceramics.**

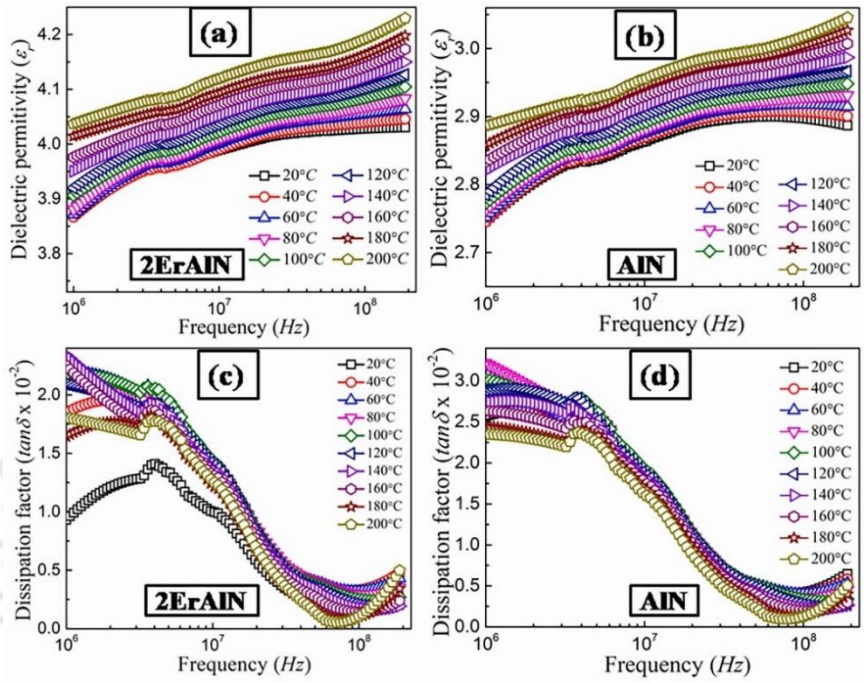

***Figure 4. 18*: The variation in dielectric properties concerning the frequency at a positive temperature from 20 ℃ to 200 ℃ (a) 2ErAlN; (b)AlN; (c) 2ErAlN and (d) AlN samples.**

In both samples, the dielectric permittivity displayed a constant response in the entire temperature range, except it is slightly raised at high temperatures. In contrast, the $\tan\delta$ exhibited a slight dispersion up to 5 MHz above that it decreased, but a minor enhancement is observed at higher temperatures. At higher temperatures, the variation of dielectric permittivity with frequency increasing from 1 MHz to 100 MHz of the best additive 2ErAlN sample (see Figure 4.18 (a)) and of pure AlN (see Figure 4.18 (b)) is studied.

This result (Figure 4.18) reveals that the Er_2O_3 added sample displayed a higher dielectric permittivity than the pure AlN sample and is constant with frequency variation. The variation of dissipation factor by the increasing frequency at higher temperatures of the best additive 2ErAlN sample (Figure 4.18 (c)) and of pure AlN (Figure 4.18 (d)) seems to be slightly

decreasing with frequency but not much. This constant dielectric permittivity and slight variation in dissipation factor in the order of 10^{-2} by varying frequencies from 1 MHz to 100 MHz at high temperatures represent the sample's purity and stability at high temperatures.

4.6.5 Microwave-dielectric properties

The estimated microwave dielectric properties (dielectric permittivity (ε_r) and dissipation factor $(\tan\delta)$) at 12 GHz resonant frequency, of AlN ceramics with Er_2O_3 additive sintered at 1700 ℃, for 3 h are listed in Table 4.10.

Table 4. 10: The dielectric permittivity and dissipation factor values of AlN ceramics with additive sintered at 1700 ℃ for 3 h.

Sample	ε_r	tan δ
0.5 ErAlN	7.20	4.3×10^{-3}
1 ErAlN	7.56	4.4×10^{-3}
2 ErAlN	7.81	5.0×10^{-4}
3 ErAlN	7.65	4.3×10^{-3}

The samples' dielectric constant and dissipation factor improved with an increase in additive concentration from 0.5-2 wt%. But beyond 2 wt%, both of them are degraded. The best dielectric permittivity (ε_r) 7.81 and low dissipation factor $(\tan\delta)$ 5 x 10^{-4}obtained for the sample 2ErAlN sintered in a two-stage sintering process (1600 ℃ for 3 h and then at 1700 ℃ for 3 h). This low dissipation factor can be due to maximum density, suppression of the secondary phase, and uniform microstructure. Dielectric losses are classified into two types. They are intrinsic and extrinsic [157]. Inherent losses are due to the composition and crystal structure of the material. Extrinsic losses are due to dislocations, porosity, grain boundaries, vacancies [158], secondary phases, impurities, etc. [157]. In these samples, the extrinsic factors (secondary phases, porosity, and abnormal grain growth) are negligible due to the obtained

pure phase AlN for AlN-ZnO composite ceramics. Smaller particle sizes eliminated the porosity (ball milling) and liquid phase sintering, promoting density and uniform grain growth. Therefore, high dielectric permittivity and low dissipation factors are promising materials for RF-window applications.

4.6.6 Microwave analysis of the dielectric window

The window consists of a circular dielectric disc of the required thickness brazed on its periphery to a circular waveguide section sandwiched between two flanges having rectangular openings. Dimensions such as the circular waveguide's length on either side, the diameter, and the dielectric disc's thickness are chosen to make the window transparent to the RF power. The flange on the high-pressure side is a standard waveguide flange, whereas the one on the vacuum side is a UHV conflate flange. In the S-band at an operating frequency of 3.7 GHz, the WR 284 waveguide is used in which the broader and narrower sides are 72.14 mm and 34.04 mm, respectively; hence the diagonal of the waveguide should be 79.76 mm. Therefore, the diameter of the dielectric disc should be kept at 79.76 mm. But for high-power handling, it is better to keep the dielectric disc's diameter more than the computed diameter of the dielectric disc. In the present investigation, dielectric discs of 86 mm and 100 mm diameters are considered for this study. The selection of proper dielectric material is essential for the design of a dielectric window. The dielectric should have the following properties (a) low value of loss tangent to reduce dielectric loss, (b) high thermal conductivity to avoid local heating due to dielectric loss, (c) high mechanical strength to withstand the differential pressure, (d) good joining ability with the metals. Considering the unique properties of AlN into account, aluminium nitride is selected as a dielectric material for the present dielectric window.

The AlN-based pillbox-type dielectric window is studied in the CST microwave studio. The window consists of a circular dielectric disc of the required thickness brazed on its

periphery to a circular waveguide section between two flanges having rectangular openings. The rectangular opening is matched with the WR 284 rectangular waveguide. The broader and narrower sides are 72.14 mm and 34.04 mm, respectively; hence, the waveguide's diagonal should be 79.76 mm. Therefore, the dielectric disc's diameter should be greater or equal to that dimension. The circular waveguide's length, diameter, and thickness of the dielectric disc are optimized to make the window transparent to the RF power. Two designs are considered and optimized. Design 1: window diameter and thickness value of 86 mm and 3 mm, respectively. Design-2: window diameter and thickness value of 100 mm and 6.7 mm, respectively. The experimentally derived dielectric properties are considered in the simulation. The specifications of the dielectric window are given in Table 4.11. The window's three-dimensional model and section view are shown in Figure 4.19 and Figure 4.20, respectively. The dimensions of the dielectric window are computed in the frequency domain solver in CST software, which is given in Table 4.12. The parametric analysis is performed. The length and thickness of the dielectric material's circular waveguide section vary to study the window's electrical response concerning dimensional variation.

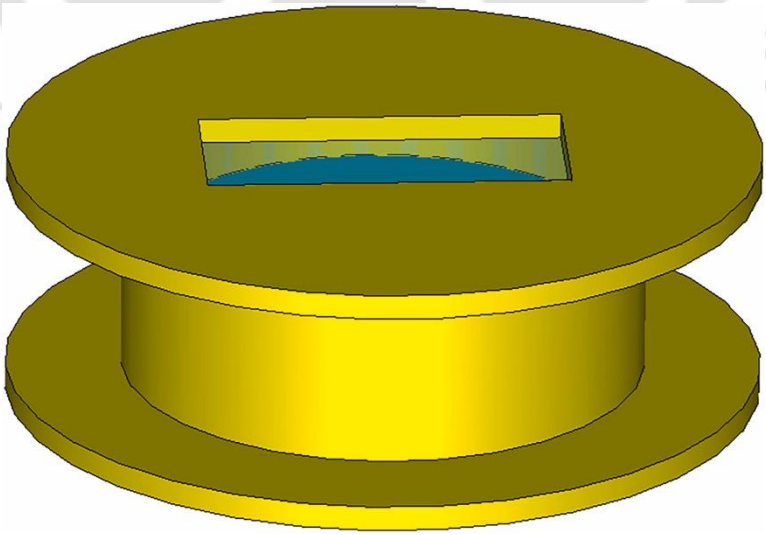

***Figure 4. 19*: Three-dimensional view of the window model.**

In the case of 86.00 mm dielectric diameter, the optimized thickness of the dielectric and length of the window are found to be 3.00 mm and 34.91 mm, respectively, and the corresponding value of return loss and insertion loss are found to be 46 dB and 0.009 dB at spot frequency 3.7 GHz.

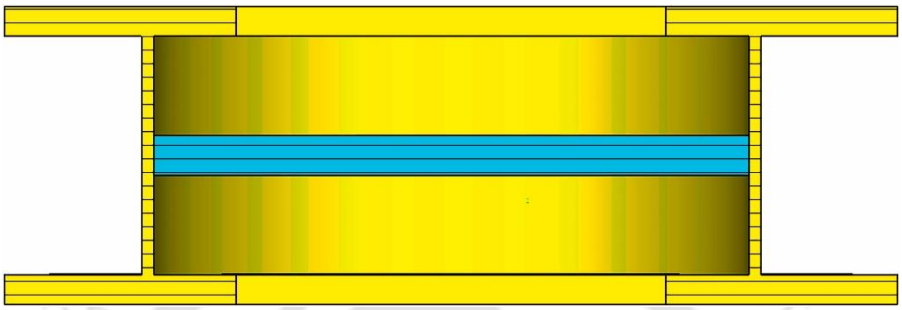

***Figure 4. 20*: Section view of the window.**

On the other hand, in the case of dielectric of the diameter of 100.00 mm, the optimized thickness and length of the window are found to be 6.7 mm and 40.00 mm with corresponding values of return loss and insertion loss of 64 dB and 0.0076 dB. The output parameters of the window are given in Table 4.12.

***Table 4. 11*: Input parameters used for simulation.**

Parameter	Value
Operating frequency	3.17 GHz
Peak power	6.0 MW
Average power	6.0 KW
Return loss	≤30 dB
Insertion loss	≤0.1 dB
The dielectric constant of the material	7.8
Loss tangent	5×10^{-4}
Pressure difference	3bar

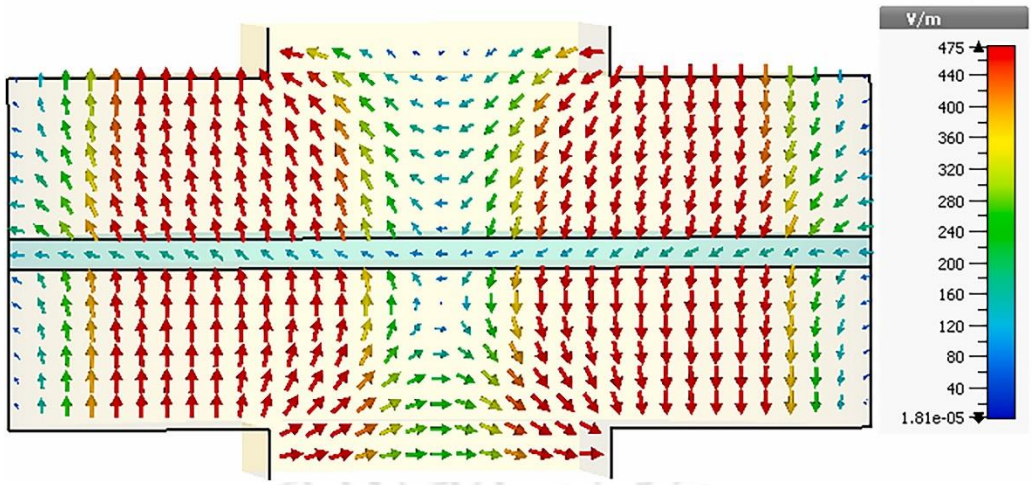

***Figure 4. 21*: Electric field pattern inside the window.**

***Table 4. 12*: Output parameters obtained from the simulation.**

Parameter	Design 1	Design 2
Dielectric diameter	100 mm	86 mm
Dielectric thickness	6.7 mm	3 mm
Length of the circular waveguide	40 mm	34.91 mm
Thickness of flange	5 mm	5 mm
Return loss	60.11 dB	61.2 dB
Insertion loss	0.007 dB	0.009 dB

The window draws all assumed parameters for designing a dielectric window using CST software. The electric field pattern inside the window is shown in Figure 4.21. The return loss (S_{11} in dB) for both designs is provided in Figure 4.24 and Figure 4.25, respectively. The preparation of pure and Er_2O_3 doped AlN ceramics sintered using a sintering bed (layers of carbon and AlN powders) revealed the phase pure ceramics without the presence of the Al_2O_3 phase crucial for the input parameters of the simulation studies. Further, the sintered samples exhibited good relative density and excellent microwave dielectric properties. The theoretical design of the dielectric window is carried out using CST software. The window's return loss and insertion loss are computed for a spot frequency of 3.7 GHz for two aluminium nitride

discs of 86 mm and 100 mm diameters. The return loss and insertion loss are optimized for the window of length 40 mm; the thickness and diameter of the AlN are 6.7 mm and 100 mm, respectively.

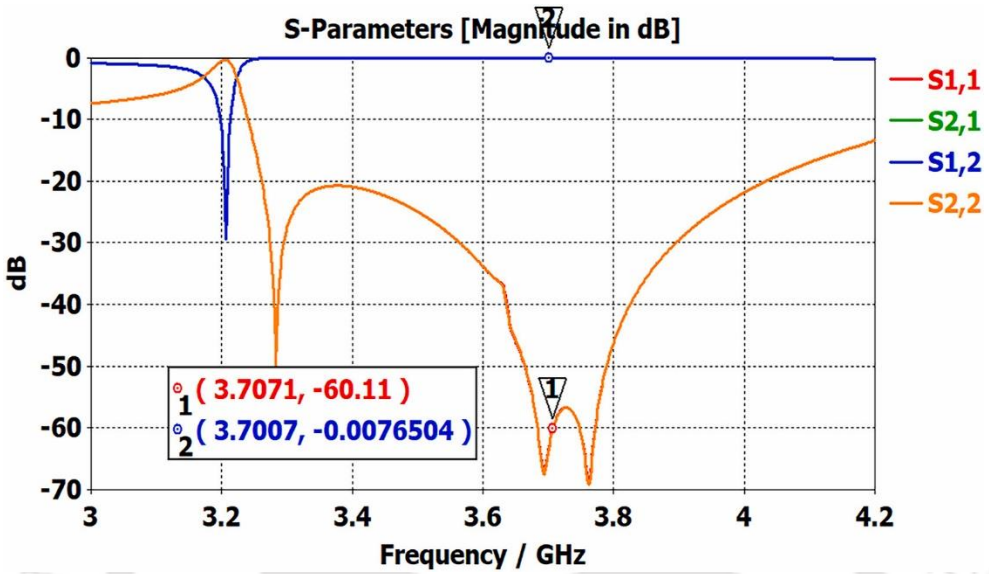

Figure 4. 22: S-parameters of design-1 of the window.

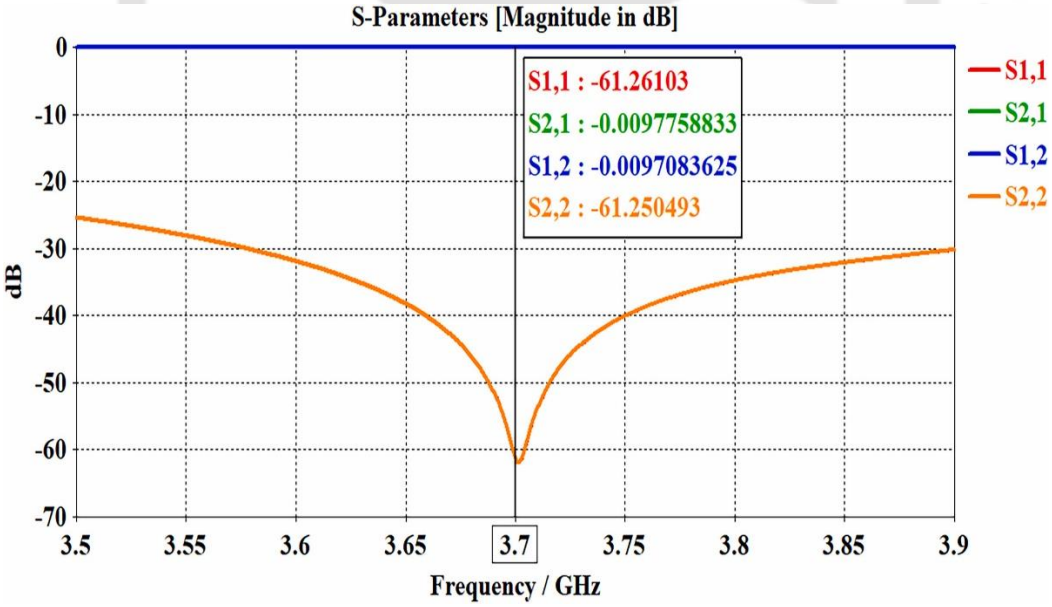

Figure 4. 23: S-parameters of design-2 of the window.

The computed return loss and insertion loss are found to be 60.11 dB and 0.0076, respectively, shown in Figure 4.22. The return loss and insertion loss are also optimized for the

window of length 34.91 mm; the thickness and diameter of the AlN are 3 mm and 86 mm, respectively.

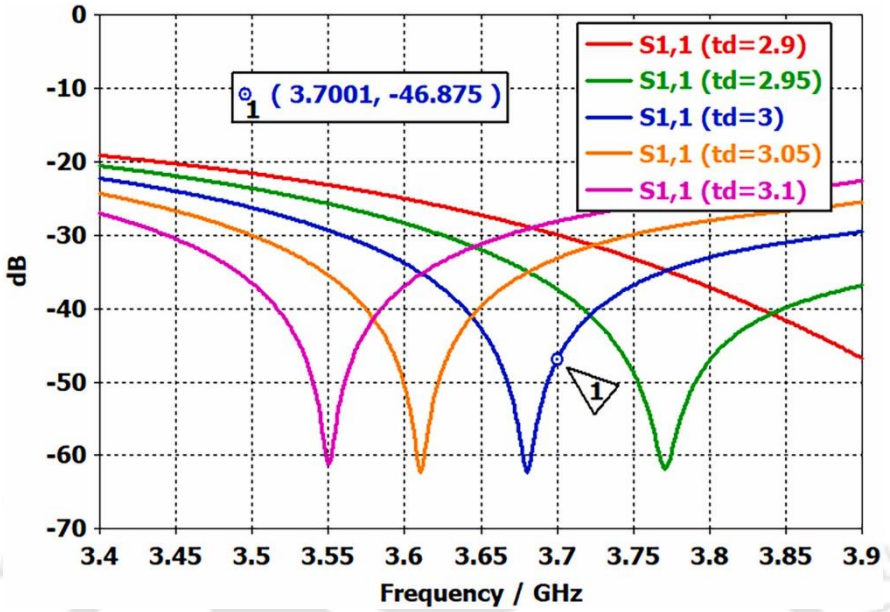

Figure 4. 24: S_{11} of the design-1 of the window.

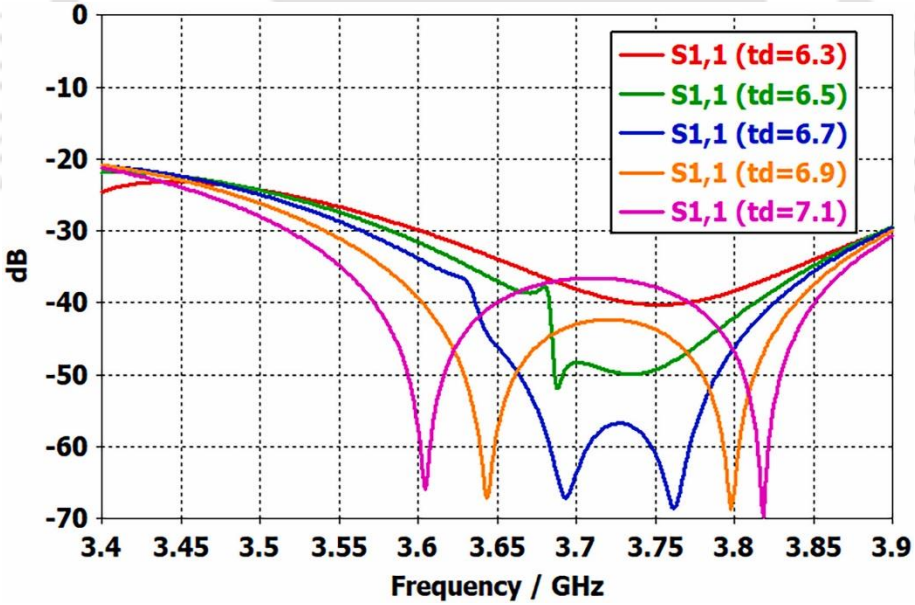

Figure 4. 25: $S_{11}$of design-2 of the window.

The computed return loss and insertion losses are 61.25 dB and 0.009 dB, respectively, shown in Figure 4.23. It is evident from the S-parameters results that both design-1 and design-2 are acceptable. However, design-2 has a relatively smaller diameter of the dielectric disc and

dielectric thickness also, so economical point of view, design-2 is better. Hence, design-2 should be adopted for the fabrication of the window. Although both the designs provide excellent transmission of RF power, in view of ease of fabrication, Design1 is chosen for the window's future development.

4.6 Conclusions

- AlN-ZnO composite ceramics are prepared using a powder bed in conventional sintering. The powder bed comprises AlN (aluminum nitride) and C (carbon). The pure AlN and AlN-ZnO composite ceramics are obtained with pure wurtzite structure AlN phase without any secondary oxide (Al_2O_3).
- The obtained XRD pattern of all sintered pure and AlN-ZnO composite ceramics appropriately matched with the JCPDS of card number 01-077-9871 of the wurtzite AlN phase with the $P6_3mc$ space group. This structure is confirmed from the Raman spectrum with six vibrational modes of the wurtzite AlN phase.
- AlN-15ZnO composite ceramic shows good dielectric properties ($5.1 \leq \varepsilon_r \leq 8.0$ and $0.02 \times 10^{-2} \leq \tan\delta \leq 38 \times 10^{-2}$) in the temperature range 30-500 ℃, at the lower frequencies ranging from 1kHz to 1MHz.
- AlN-15ZnO composite ceramic shows the best dielectric permittivity ($\varepsilon_r = 7.20$) with dissipation factor ($\tan\delta = 4.90 \times 10^{-3}$) at microwave frequencies.
- The present study also investigated the structural and dielectric properties of pure and Er_2O_3-doped AlN ceramics. The obtained experimental values are considered as input parameters to design a dielectric window for S-band frequency.
- The preparation of pristine and Er_2O_3 doped AlN ceramics sintered using a sintering bed (layers of carbon and AlN powders) revealed the phase pure ceramics without the Al_2O_3 phase are crucial for the input parameters of the simulation studies. Further, the

samples sintered exhibited good relative density and excellent microwave dielectric properties.

- The theoretical design of the dielectric window is carried out using CST software. The window's return loss and insertion loss are computed for spot frequency 3.7 GHz for two aluminium nitride discs of 86 mm and 100 mm.
- The return loss and insertion loss are optimized for the window of length 40 mm; the thickness and diameter of the AlN are 6.7 mm and 100 mm, respectively. The computed return loss and insertion loss are found to be 60.11 dB and 0.0076, respectively.
- The return loss and insertion loss are also optimized for the window of length 34.91 mm; the thickness and diameter of the AlN are 3 mm and 86 mm, respectively. The computed return loss and insertion loss are 61.25 dB and 0.009 dB, respectively.
- It is evident from the S-parameters results that both design-1 and design-2 are acceptable. However, design-2 has a relatively smaller diameter of the dielectric disc and dielectric thickness, so from an economical point of view, design-2 is better. Hence, design-2 will be adopted for the fabrication of the window.
- The best microwave dielectric constant and loss tangent values are input parameters to design the window dimensions and other parameters. The window parts will be designed based on the design, and finally, the window can be developed.

Chapter 5

Effect of BN on Structural and Dielectric Properties of AlN Ceramics

5.1 Graphical abstract:

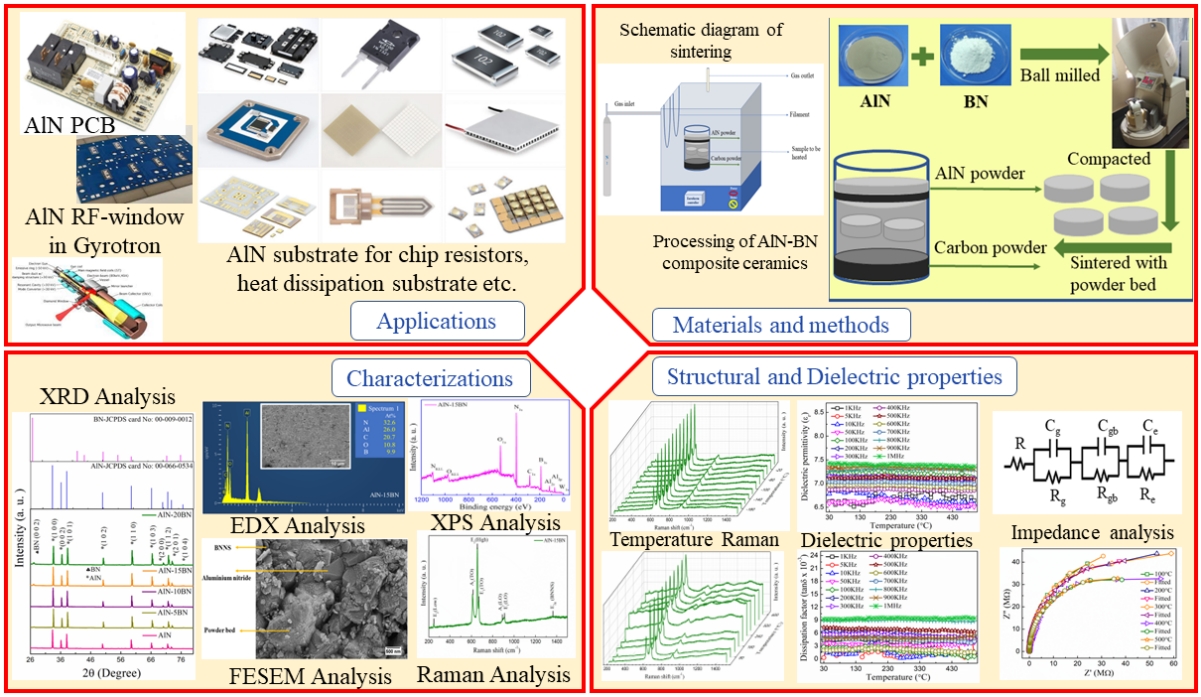

5.2 Abstract

In this study, AlN-BN composite ceramics have been sintered with a powder bed sintered at 1700 ℃ in the presence of nitrogen. The structure of the sintered composite ceramics obtained in this process is confirmed as wurtzite AlN and h-BN from XRD and confirmed by the Raman vibrational modes. The temperature dependent Raman spectra show six vibrational modes of wurtzite structure at every temperature. The XPS studies reveal the pure nitride phase formation of the AlN-BN composite, and the presence of oxygen is only at the sample's surface. The obtained composites exhibit pure wurtzite AlN phase without any oxide phases as secondary phases. The best dielectric properties ($\varepsilon_r = 6.50$ - 7.48) with ($\tan\delta = 0.2$ x 10^{-3} -

9.8 x 10^{-3}) are achieved for AlN-15BN composite ceramics by varying temperatures from 30-500 ℃, with frequency variation from 1 kHz to 1 MHz. Impedance spectra of AlN-BN composite ceramics are appropriately fitted with the equivalent circuit consisting of RCRCRC for all the sintered samples. The best microwave dielectric properties as $\varepsilon_r = 7.38$ and $\tan\delta =$ 2.60 x 10^{-3} achieved are appropriate for RF-window and electronic applications.

5.3 Introduction

AlN has unique properties such as high thermal conductivity [112], low thermal expansion coefficient, low dielectric permittivity, low dissipation factor, high mechanical strength, high-temperature resistance, and chemically inert. AlN is considered an ideal material for a new generation of highly integrated semiconductor substrates, electronic packaging, and other applications that require heat dissipation and high mechanical strength. Also, AlN has melt metal corrosion resistance and is an excellent crucible material for casting pure aluminium or aluminium alloy and iron [159]. Aluminium nitride has numerous applications, such as deep ultraviolet light emitters, high-frequency filters, photodetectors, and laser diode applications.

Boron nitride (BN) resembles graphite, having a layered structure with a hexagonal phase. BN's planar networks of boron (B) and nitrogen (N) atoms stack with weak van der wall interactions and dipole moment force between boron and nitrogen. BN also displays excellent properties such as high thermal conductivity, low thermal expansion coefficient, high-temperature resistance, excellent mechanical properties, and good dielectric properties. Based on the requirements of the applications discussed above, it is necessary to prepare AlN-BN composite ceramics in the pure phase with maximum density at lower sintering temperatures. Also, the formation of Al_2O_3 is inevitable. This study addresses the above problems by using the ball mill to reduce the initial particle size and the powder bed to address the process challenges involved in AlN-BN composites. Thus, preparing AlN-BN composite ceramics will

give good thermal conductivity, low dielectric constant, low dissipation factor, good temperature resistance, good machinability, and excellent insulation materials. Thus, these AlN-BN materials are appropriate for the substrate [160] and electronic packaging materials in a large-scale integrated circuit [161, 162]. However, AlN and BN are compounds containing covalent bonds; hence, sintering is difficult at low temperatures in conventional sintering. There are different sintering methods, such as conventional sintering [30, 163], spark plasma sintering [164, 165], hot isostatic pressing sintering [111, 166], and microwave sintering [167, 168]. Spark plasma sintering, hot isostatic pressing sintering, and microwave sintering require costly special equipment and difficult-to-process ceramics with the application of pressure in a short duration. Conventional sintering is cost-effective but takes a long time and is easy to process, large number of samples can be sintered while in other techniques only one sample can be sintered at a time. Many researchers used special techniques and sintering aids to sinter AlN-BN composite ceramics. Kanai. et. al., [169] considered 75% BN and 25% AlN ball milled and placed in a graphite mold and pressed with 40 MPa. Then, sintered BN-AlN composite ceramics using hot pressing at 1800 ℃, for 2 h with CaC_2 as a sintering aid from 0-2 wt%. obtained ceramics contains crystallographic phase of AlN, BN, AlON, $Ca_5Al_6O_{14}$ and $CaAl_2O_4$. The obtained composite ceramics with 0.8 wt% CaC_2 shows high thermal conductivity ~247 W/mK. Zhao et. al., [170] sintered AlN-BN composite ceramics in hot pressing sintered at 1750-1900 ℃, for 3 h with the heating rate 10 ℃/min by pressing 30 MPa pressure and using 0-4 wt% CaF_2 as a sintering aid. The obtained composite had AlN, BN, and CaF_2 phases, and reaches thermal conductivity 110 W/mK, with dielectric permittivity between 7.29 and 7.64. Jin et al., [171] studied machinability of the AlN-BN composite by coating AlN particles with BN using solution-based method. Boric acid, urea used a source for BN and alcohol as a milling media. Dried the composites at 850 ℃ for 15 h in nitrogen gas. Hot pressed the composites 1850 ℃, for 1 h with 30 MPa. The obtained composite is having AlN, BN

phases with $Al_5 Y_3O_{12}$ phase. Li. Yong-Li. et. al., [172] fabricated AlN-BN composite ceramics using spark plasma sintering technique with Y_2O_3 as a sintering aid. The AlN-BN composite ceramics with Y_2O_3 sintered at 1600-1800 ℃ for 10 min with a heating and cooling rate 100-200 ℃/min, and a pressure of 30 MPa applied. The obtained ceramics contains AlN, BN crystalline phases with $Al_5 Y_3O_{12}$, Y_2O_3. Achieved thermal conductivity 110-140 W/mK for 15 vol% BN composites. Spark plasma sintering is chosen to sinter AlN ceramics with sintering aids as rare earth oxides, fluorides etc., achieved densified composite ceramics by sintering high temperatures above 1700 ℃, with other phases and studied thermal and dielectric properties at room temperature [24, 25].

However, studies on temperature-dependent structural and dielectric properties are lacking. Sintering of AlN-BN ceramics with pure phase in the conventional sintering method is also challenging. Using a conventional sintering technique motivated us to study the AlN-BN composite ceramics' structural and dielectric properties at different temperatures.

5.4 Materials and methods:

AlN-BN composite ceramics are prepared using the conventional sintering method using a powder bed. Initially, the commercially available AlN powder and BN (boron nitride) powder (purity > 98%, average particle size 1 μm) are chosen for preparing AlN-BN composite ceramics. These chemicals are weighed according to different wt% shown in Table 5.1; then ball milled in propanol as a liquid medium with 500 rpm for 12 h by a planetary ball mill. The mixed slurry is further dried in an oven at 90 ℃ for 18 h. The dried sample is ground to get fine powder using an agate mortar and mixed with 5 mol% PVA as a binder. The AlN powder ball is milled in dry condition with 150 rpm for 10 h with relaxation and hand mixing for every 2 h interval for pure AlN ceramics. The fine powder is compacted into a cylindrical shape of dimension 10 mm diameter, 1 mm, and 5 mm thickness. The compacted discs are sintered using

the conventional sintering method with the help of a powder bed in a furnace in the presence of nitrogen flow. The powder bed consists of a combination of AlN and C (carbon) powder layers. The discs are immersed in the powder bed AlN layer to control the ceramics' secondary phase and pores. The AlN-BN composite ceramics are sintered at a high temperature of 1700 ℃ with a dwelling time of 20 h.

Table 5. 1: Specification of the AlN-BN composites.

Sample	AlN (wt %)	BN (wt %)	Relative density (%)
AlN	100	0	94.67
AlN-5BN	95	5	94.58
AlN-10BN	90	10	94.54
AlN-15BN	85	15	94.45
AlN-20BN	80	20	94.23

5.5 Results and discussions:

5.5.1 Structural and density analysis:

AlN-BN composite ceramics are sintered using a powder bed at 1700 ℃ for 20 h in the presence of nitrogen. The sintered composite ceramics are polished finely, and the density of the samples is measured using the Archimedes principle using distilled water as a liquid media, as listed in Table 5.1. These results convey that all samples are densified, and the AlN-BN composite ceramics achieve ~ 95% relative density. By increasing BN content in the composite, the relative density showed little decreasing nature due to the poor sinterability nature of BN but formed a pure nitride phase without any secondary and intermediate phases. AlN-xBN composite ceramics have an AlN phase with JCPDS card no: 00-066-0534 and a BN phase with JCPDS card no: 00-009-0012. All the sintered AlN-xBN composite ceramics are

sintered by adopting a powder bed at 1700 ℃ for 20 h in the presence of nitrogen with different weight percentages of BN from (x = 5-20). All composite XRD patterns are shown in Figure 5.1.

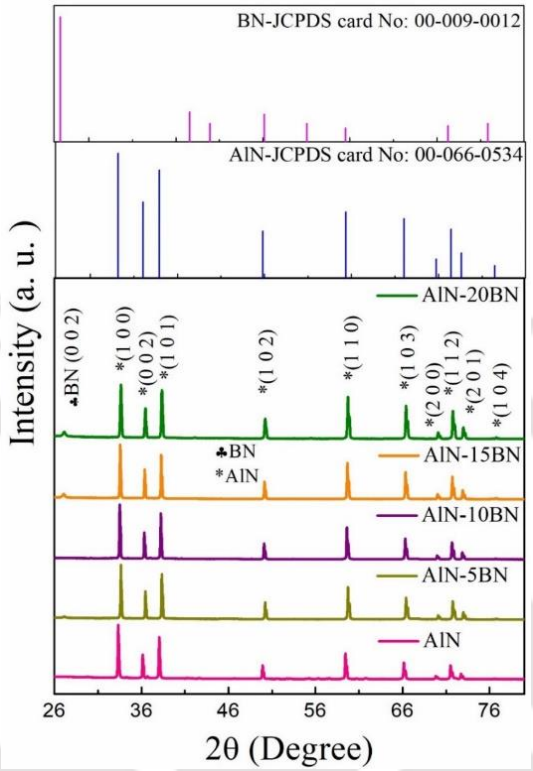

***Figure 5. 1**: The XRD pattern of AlN-xBN composite ceramics, sintered at 1700 ℃ for 20 h.*

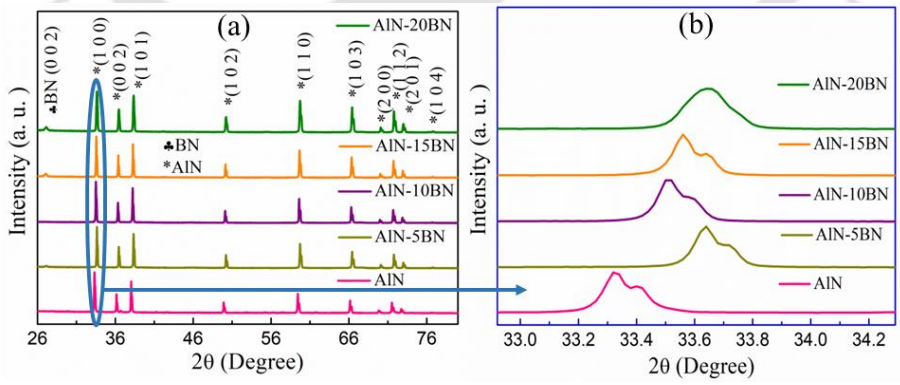

***Figure 5. 2**: (a) The XRD pattern of AlN-xBN composite ceramics, sintered at 1700 ℃ for 20 h. (b) Enlarged image of (1 0 0) peak.*

These results reveal that all the AlN-BN composite ceramics show wurtzite AlN with a small BN (low intensity) (0 0 2) peak. The pure AlN ceramic and other composite ceramics

show a wurtzite AlN phase without any oxidized phase. Commonly, Al_2O_3 is observed in AlN ceramics as a secondary phase in conventional sintering. However, in the current study, the sintered samples' XRD pattern reveals no oxidation phase as a secondary phase. The powder bed adopted for conventional sintering of AlN-xBN composite ceramics helps to avoid the oxidation phase, evident from the obtained XRD pattern.

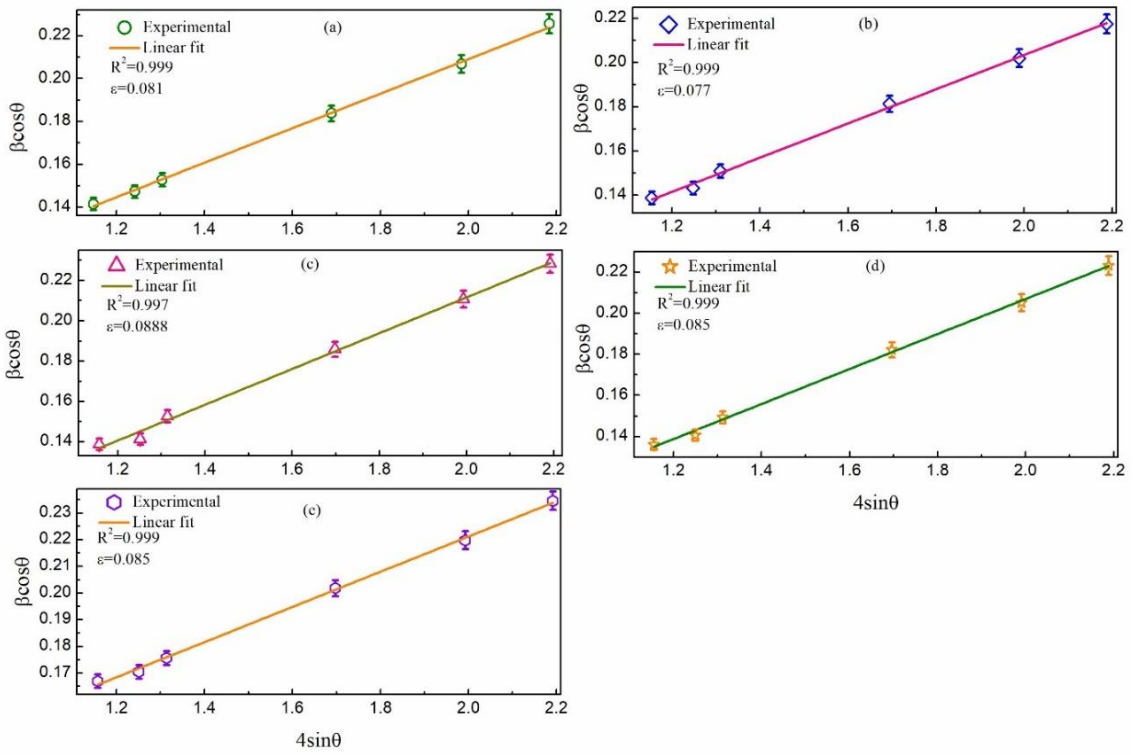

***Figure 5. 3*: The W-H plots of (a) AlN, (b) AlN-5BN (c) AlN-10BN, (d) AlN-15BN (e) AlN-20BN composite ceramics, sintered at 1700 ℃ for 20 h.**

The enlarged image of the (1 0 0) peak of the XRD pattern of AlN-xBN ceramics (see Figure 5.2) shown in Figure 5.2(b) reveals that all additive AlN ceramics (1 0 0) diffraction peak shifts towards higher 2θ angle in comparing with pure AlN ceramics. The diffraction peak of the AlN-BN composite ceramics is fitted using the Gaussian function and plotted the W-H plot for each composite to study structural properties, as shown in Figure 5.3. This shift results in increasing lattice volume (see Table 5.2).

The AlN-10BN peak shifts towards a lower 2θ angle in comparison with the AlN-5BN composite resulting in increasing stress (see Figure 5.3(b) and (c)) and increases lattice volume (Table 5.2). XRD peaks' peak shifts and broadening are attributed to lattice strain in composite ceramics [175]. The lattice strain induced by adding BN in the composite ceramics, Williamson Hall (W-H) plots are linearly fitted and shown in Figure 5.3. The XRD peak broadening is the result of both crystallite size and strain as follows [176, 177];

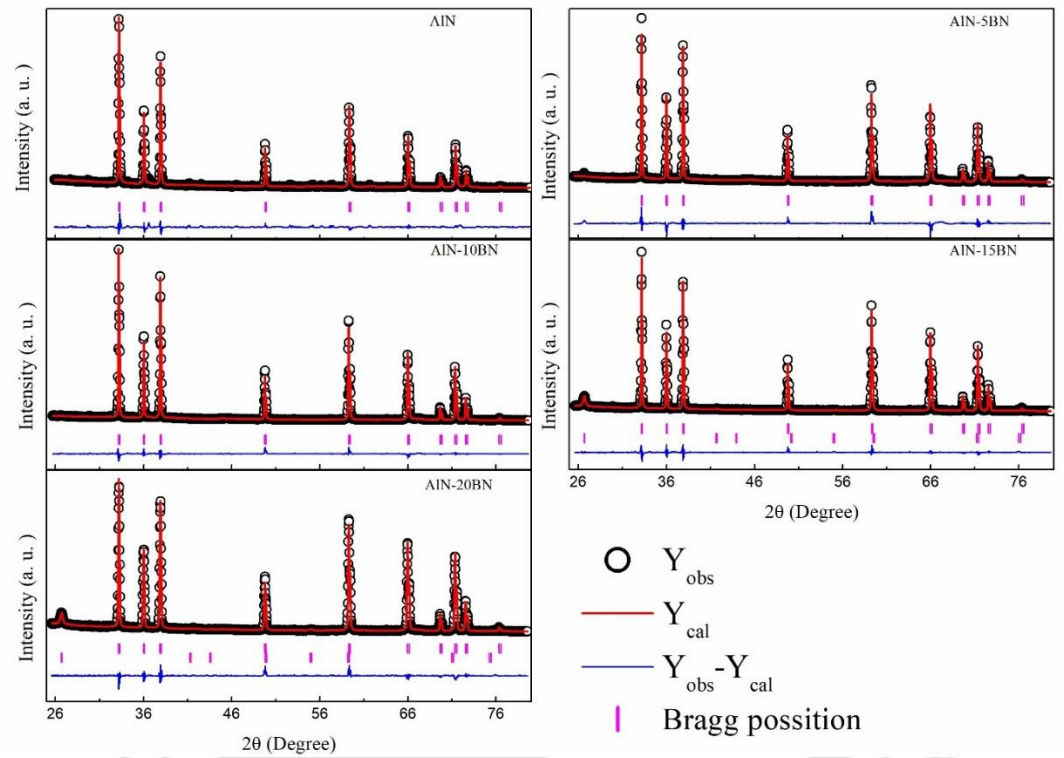

Figure 5. 4: The Rietveld refinement of AlN-xBN (x = 0-20) composite ceramics, sintered at 1700 ℃ for 20 h.

$$\beta_{hkl} = \beta_{cs} + \beta_s \tag{5.1}$$

here, $\beta_{cs} = \frac{k\lambda}{D\cos\theta}$, where k is a constant (~0.94), λ is the wavelength of the incident ray, D is the crystallite size, θ is the Bragg angle. Peak broadening from strain is $\beta_s = 4\varepsilon\frac{\sin\theta}{\cos\theta}$, ε is strain. The obtained XRD patterns are refined using the Rietveld refinement software using the Pseudo Voigt function. Refined XRD patterns of all the AlN-xBN composites are shown in Figure 5.4, and refined parameters are shown in Table 5.2. It reveals that all composite

ceramics shows wurtzite AlN with $P6_3mc$ space group of space group number 186. The quality of fitting given by χ^2 values. The obtained χ^2 values, lattice volume, lattice constants, Rf-factor, and the Bragg Rf-factor for all sintered AlN-xBN composite ceramics are listed in Table 5.2. It is observed that lattice constants and lattice volume are enhanced by adding BN.

Table 5. 2: The refined parameters of AlN-xBN composite ceramics.

Composite	χ^2	a (AlN) (Å)	c (AlN) (Å)	a (BN) (Å)	c (BN) (Å)
AlN	1.12	3.113 (28)	4.981 (76)	-	-
AlN-5BN	1.78	3.115 (42)	4.985 (75)	-	-
AlN-10BN	1.43	3.115 (29)	4.984 (52)	-	-
AlN-15BN	1.26	3.115 (29)	4.986 (53)	2.524 (10)	6.679 (08)
AlN-20BN	1.34	3.116 (47)	4.987 (85)	2.502 (13)	6.680 (07)

5.5.2 Raman spectroscopy:

Aluninium nitrides (III nitrides) normally crystallize in two forms, such as zinc blend and wurtzite structures [178]. In AlN ceramics, the frequencies related to $A_1\ (TO)$ and $E_1\ (TO)$ grouped with the frequency gap ~ 60 cm^{-1}, $E_1(LO)$ and $A_1(LO)$ Modes are grouped in the frequency range of ~ 20 cm^{-1}, and LO-TO group splitting is in the ~ 200 cm^{-1} frequency range [179]. This result reveals that the dominant interaction in AlN ceramics is long-range electrostatic field interaction. The obtained spectrum of all AlN-xBN composite ceramics conveys the dominant interaction as long-range electrostatic force (see Figure 5.5).

The Raman spectra of all sintered AlN-xBN composite ceramics are observed at room temperature by exciting the sample with a 514 nm laser, with a 5 sec acquisition time, and shown in Figure 5.5. All samples show 6 phonon modes of wurtzite AlN [180], with one BNNS (boron nitride nanosheets) phonon mode for BN-added ceramics except for pure samples. The

pure AlN shows 6 phonon modes of AlN [181]. The phonon modes of each sample fitted using the Lorentzian function to extract the exact value are listed in Table 5.3.

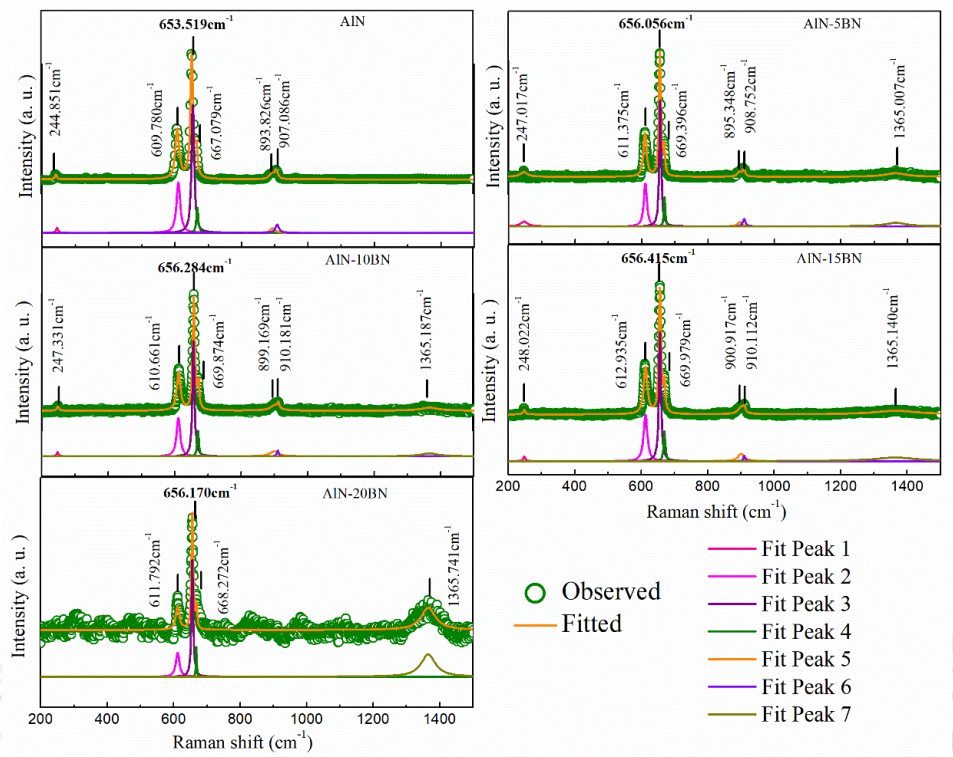

Figure 5. 5: The Raman spectra of AlN-xBN (x = 0-20) composite ceramics sintered at 1700 ℃ for 20 h.

These results reveal that all sintered AlN-xBN composite ceramics contains only aluminium nitride and boron nitride phases. No alumina phase or any other oxide compound is present in the sintered AlN-xBN composite ceramics sintered at 1700 ℃ for 20 h using a powder bed in the presence of nitrogen. The powder bed used in this method helped prevent oxygen from entering the AlN lattice. All AlN-BN composites show the blue shift (shifting towards higher frequency) compared with pure AlN ceramic vibrational modes (see Table 5.3) with an extra BN peak at ~ 1365 cm^{-1} corresponding to the E_{2g} phonon mode of h-BN. E_2 (High) and E_1 (TO) modes show a blue shift up to AlN-15BN, and the other shows a redshift (shifting towards lower frequency) with the increase of BN additive. A_1 (LO) mode shows a blue shift up to 15 wt% addition of BN; for further, this mode is not visible. E_1 (LO) and E_2

(Low) modes show a blue shift up to AlN-10BN, the other AlN-15BN shows a redshift, and for AlN-20BN, this mode is not clear. E_{2g} phonon mode corresponds to phonon mode of h-BN in composite ceramics, showing blue shift up to 10 wt% addition for other 15 wt% shows red shift and for 20 wt% shows blue shift.

Table 5. 3: The fitted values for the Raman spectra of AlN-xBN composite ceramics

Sample/Phonon mode		E_2 (Low)	A_1 (TO)	E_2 (High)	E_1 (TO)	A_1 (LO)	E_1 (LO)	E_{2g} (BNNS)
AlN	γ (Cm^{-1})	244.85	609.78	653.52	667.08	893.83	907.09	
	β (Cm^{-1})	7.519	13.695	9.403	6.919	17.863	13.209	
AlN-5BN	γ (Cm^{-1})	247.02	611.37	656.05	669.40	895.35	908.75	1365.01
	β (Cm^{-1})	26.601	10.886	6.664	4.916	15.978	9.382	79.885
AlN-10BN	γ (Cm^{-1})	247.33	610.66	656.28	669.87	899.17	910.18	1365.19
	β (Cm^{-1})	7.973	13.056	7.313	6.113	32.873	7.100	66.174
AlN-15BN	γ (Cm^{-1})	248.02	612.93	656.41	669.98	900.92	910.11	1365.14
	β (Cm^{-1})	7.813	13.296	7.469	6.152	22.905	6.275	156.542
AlN-20BN	γ (Cm^{-1})	-	611.792	656.17	668.27	-	-	1365.74
	β (Cm^{-1})	-	13.031	6.226	2.874	-	-	53.085

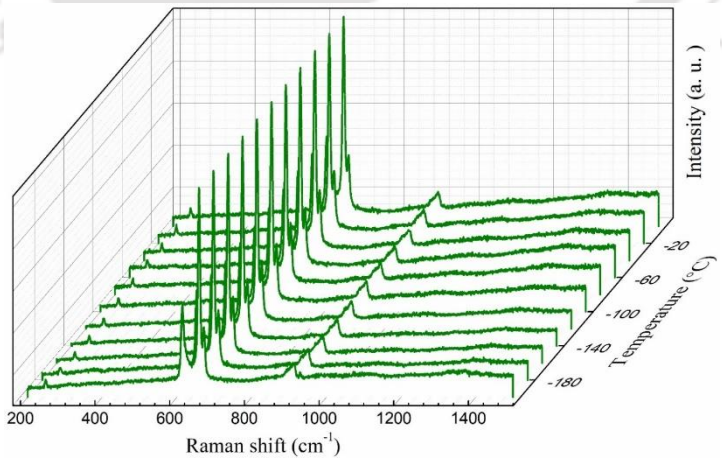

Figure 5. 6: The Raman spectra of AlN-15BN composite ceramics, sintered at 1700 ℃ for 20 h recorded at low temperatures from 0 ℃ to -196 ℃.

The Raman spectra of AlN-15BN composite ceramics are observed at different temperatures ranging from -196 ℃ to 400 ℃ to study the stability and purity of the sample with temperature variation using liquid nitrogen. The Raman spectrum of AlN-15BN composite ceramics by varying temperatures from -196 ℃ to 0 ℃ are shown in Figure 5.6. At higher temperatures, to observe the Raman spectrum of AlN-15BN composite ceramics, liquid nitrogen is removed, heated the sample is from 20 to 400 ℃, and Raman spectra are recorded by increasing temperature, as shown in Figure 5.7. These Raman spectra are fitted using the Lorentz function and observed the Raman shift and FWHM of each phonon mode at every temperature. This result shows that the Raman spectrum of AlN-15BN composite ceramics shows 6 vibrational modes of wurtzite AlN at each temperature and maintains purity and stability at low temperatures.

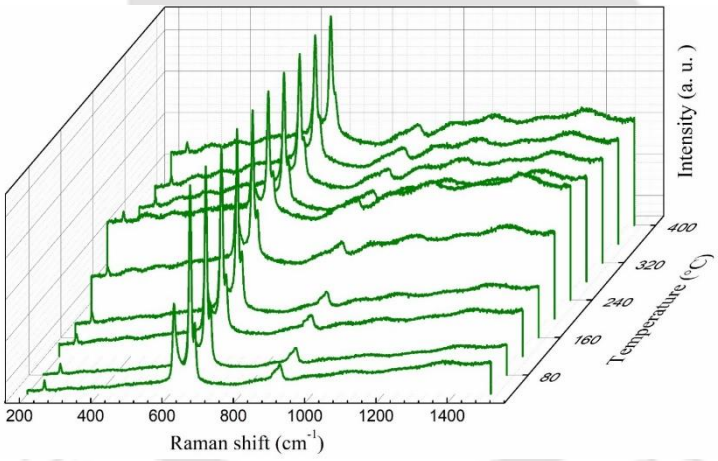

Figure 5. 7: The Raman spectra of AlN-15BN composite ceramics, sintered at 1700 ℃ for 20 h recorded at high temperatures from 10 ℃ to 400 ℃.

No new phonon modes appear, and no phonon modes of AlN and BN are missing while increasing the temperature in the obtained spectra. The observed changes are only in FWHM, Raman shift, and intensities of phonon modes. These changes are due to the absence of phase transition. These Raman spectra at each temperature are fitted using the Lorentz function, and fitted values of Raman shift and FWHM of each phonon mode collected and plotted with

temperature and shown in Figure 5.8. Every mode shows a linear nature with temperature. Each mode shows a redshift (shifting towards lower frequency) by increasing temperature from -196 ℃ to 0 ℃ (see Figure 5.8). These Raman shifts and FWHM at positive temperatures are plotted with temperature and shown in Figure 5.9. This result reveals that the phonon modes also show a redshift at higher temperatures while increasing temperature from 20 to 400 ℃.

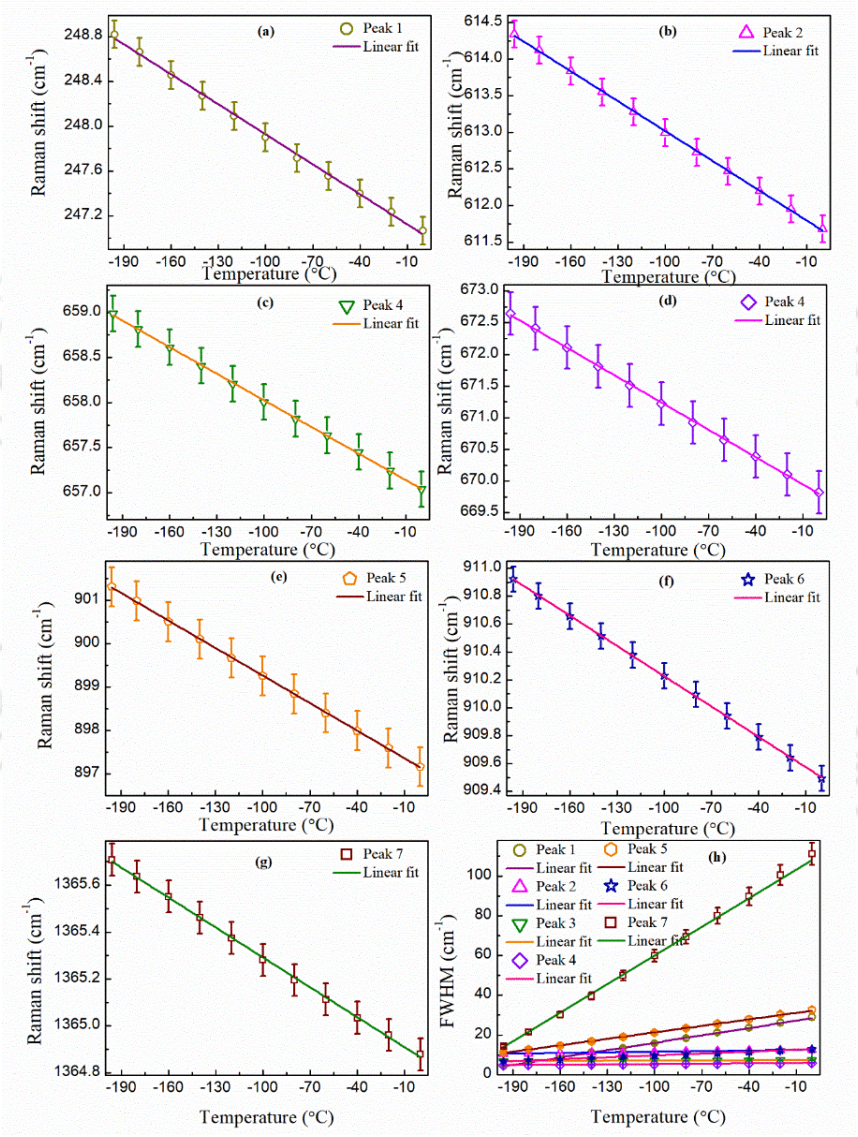

Figure 5. 8: The behavior of Raman shifts and FWHM of each vibration mode with temperature variation (0 ℃ to -196 ℃) for AlN-15BN composite ceramics.

At higher temperatures, the composite shows six vibrational modes of wurtzite AlN with one E_{2g} phonon mode corresponding to h-BN, indicating that the composite maintains purity and stability at higher temperatures.

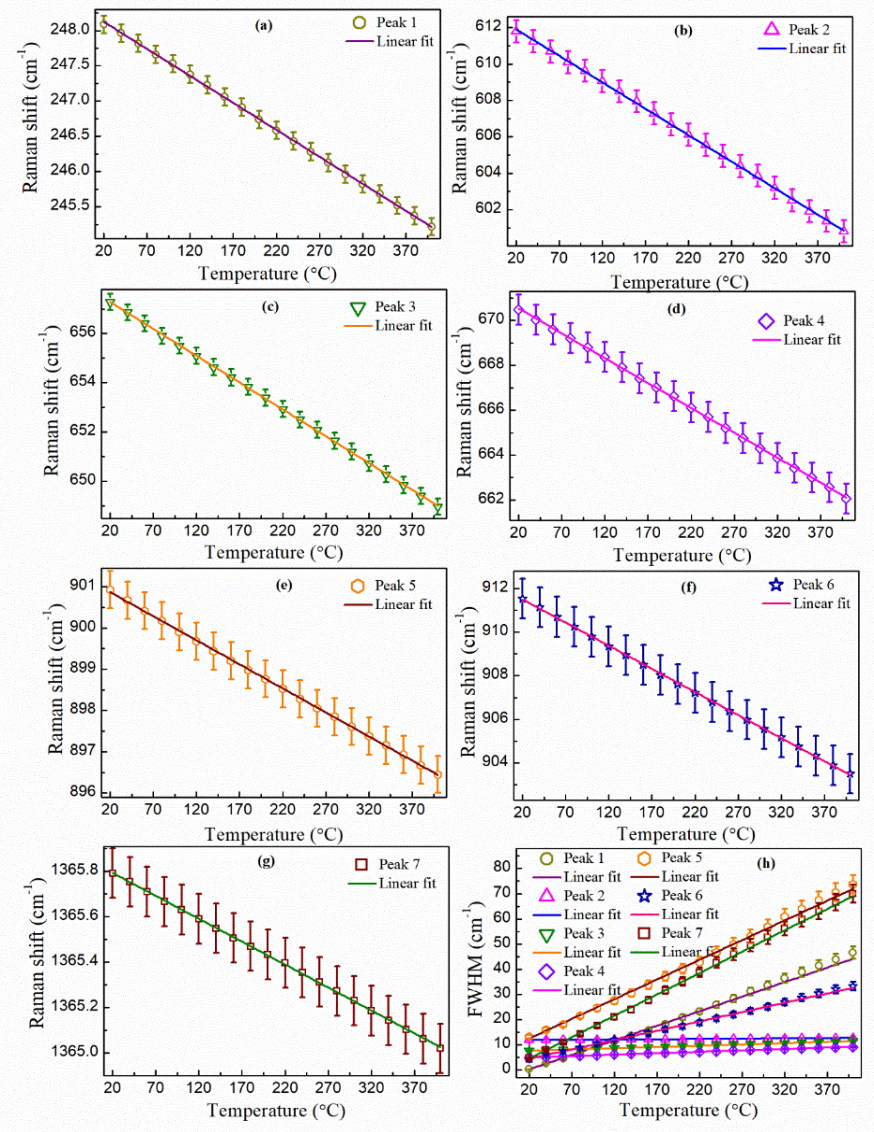

***Figure 5. 9*: The change in Raman shifts and FWHM by varying temperature from 20 ℃ to 400 ℃ for AlN-15BN composite ceramics related to each phonon mode.**

The temperature dependence of the Raman shift fitted linearly with the best-suited equation as follows;

$$\omega(T) = \omega_0 + \chi\, T \tag{5.3}$$

where ω_0 is the extrapolated peak position at absolute zero temperature, and χ is the first-order temperature coefficient.

5.5.3 EDAX analysis

The elemental analysis of AlN-15BN composite ceramics sintered at 1700 ℃ for 20 h in the presence of nitrogen using a powder bed is observed from EDS spectra shown in Figure 5.10.

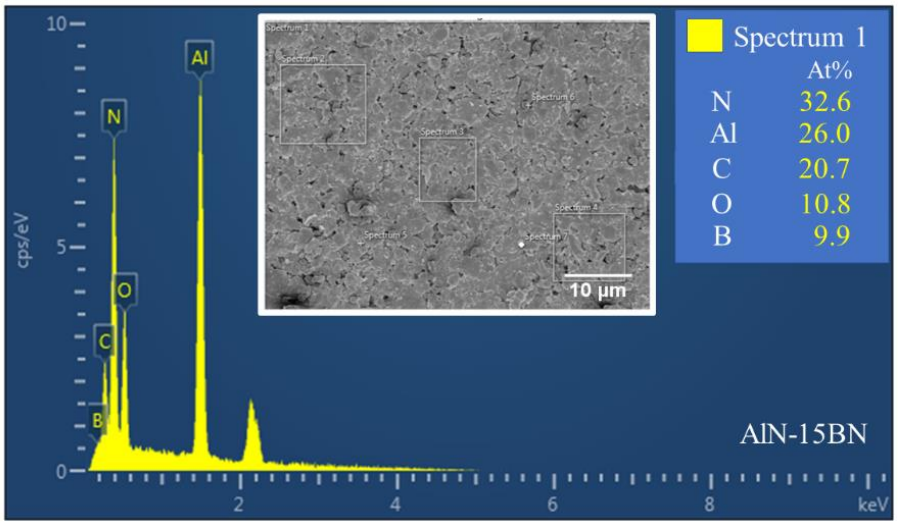

***Figure 5. 10*: The EDS spectra of AlN-15BN composite ceramics, sintered at 1700 ℃ for 20 h using a powder bed.**

It is observed that there are no other elements except carbon and oxygen in the composite ceramics. The initial raw AlN powder contains some amount of carbon and some amount of carbon on the surface of the composite due to the contribution of the powder bed used for sintering. The raw material consists oxygen in it by default hence, a meager atomic percentage is present in the AlN-15BN composite ceramics. The disc of AlN-15BN composite embedded in a powder bed of AlN surrounded by carbon powder up and down. Hence, there is less chance of oxidation evident from XRD and Raman spectra. The amount of each element present in the AlN-15BN composite ceramics is given in atomics percentages in Figure 5.10.

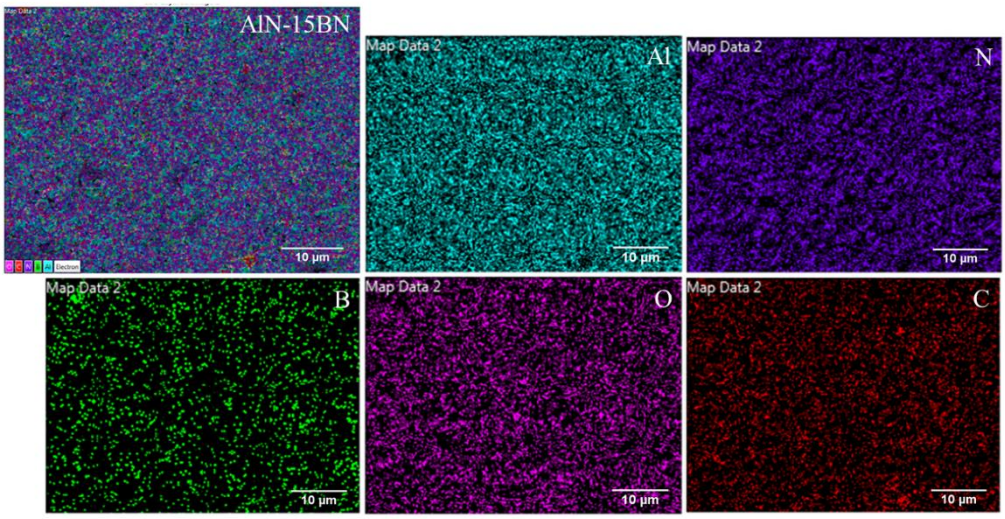

***Figure 5. 11*: The elemental mapping of AlN-15BN composite ceramics, sintered using a powder bed at 1700 ℃ for 20 h.**

The elemental mapping of AlN-15BN composite ceramics is shown in Figure 5.11. This result reveals that all elements are uniformly distributed in the composite. The common problem in conventional sintering of AlN ceramics is oxidation and secondary phase. The carbon powder in the powder bed helps avoid oxidation while sintering at high temperatures, ~1700 ℃, for 20 h. The carbon is not in direct contact with the AlN-BN disc; hence, it does not create any pores or distortions in the microstructure.

5.5.4 Microstructural analysis

The microstructure of the AlN-15BN composite ceramics sintered at 1700 ℃ for 20 h using a powder bed, observed by FESEM, is shown in Figure 5.12. The surface morphology is obtained as a sintered sample to show the powder bed and the AlN-BN composite. This result conveys that AlN-15BN composite ceramics sintered using powder bed contain hexagonal AlN grains and circular BNNS grains, as shown in Figure 5.12. The powder bed is also evident on the surface of the microstructure of composite ceramics. No other grains are observed in the microstructure. This result confirms the purity of sintered composite in the conventional sintering method using a powder bed.

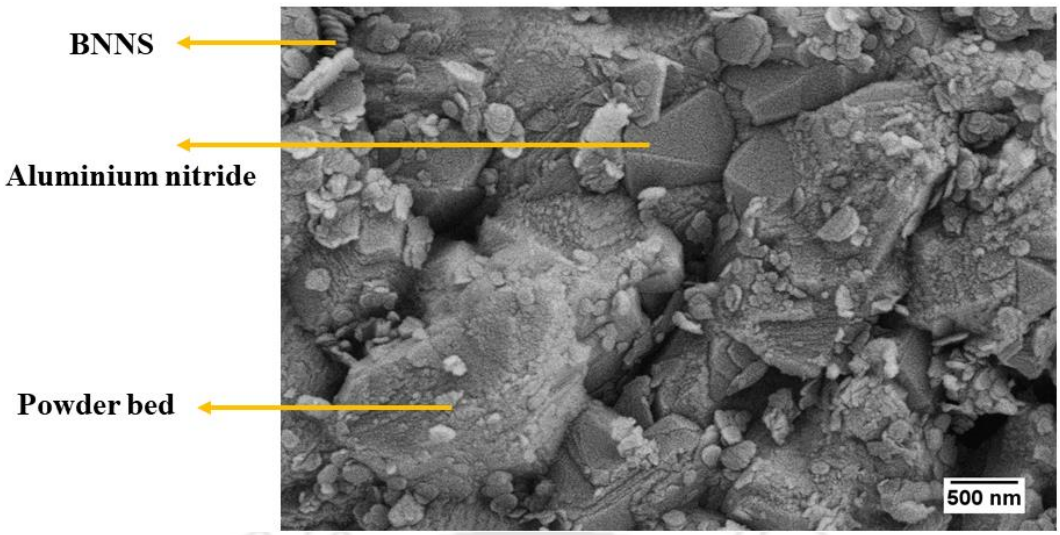

***Figure 5. 12*: The Microstructure of AlN-15BN composite ceramics, sintered at 1700 ℃ for 20 h using a powder bed.**

5.5.5 XPS analysis

Figure 5.13 shows the XPS survey spectra of AlN-15BN composite ceramics sintered at 1700 ℃ for 20 h using a powder bed in the presence of nitrogen.

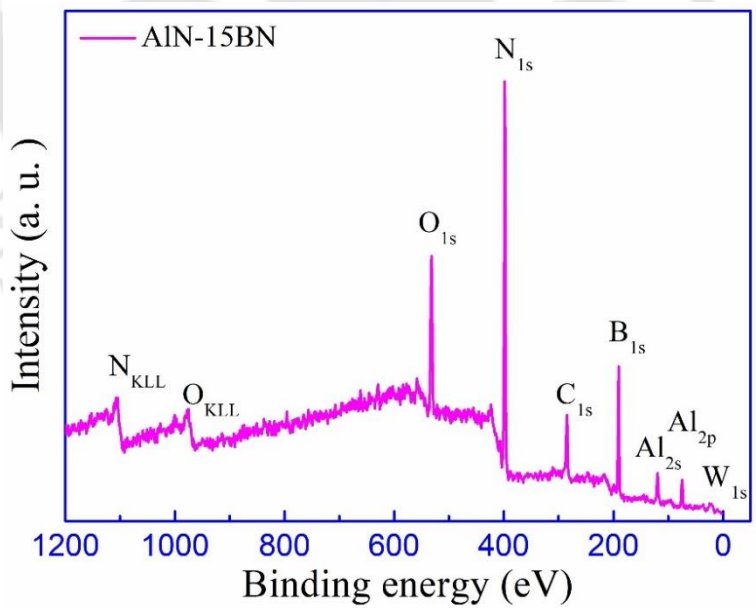

***Figure 5. 13*: The XPS survey spectra of AlN-15BN composite ceramics, sintered at 1700 ℃ for 20 h.**

This spectrum reveals the presence of elements in the obtained composites as Al (aluminium), B (boron), N (nitrogen), O (oxygen), and C (carbon) atoms. The peaks with a

high intensity related to 1s and low-intensity auger KLL peaks are observed corresponding to both N and O atoms, including Al 2s, Al 2p, B 1s, and C 1s peaks. In Figure 5.13, the peak located at 284.74 eV corresponding to C 1s presents; this shows that the peak calibration is carried out as a reference to C 1s peak. The peaks corresponding to Al and N atoms in the obtained spectrum for AlN-15BN composite ceramics agree with Rosenberger. L. [182]. The peaks corresponding to B and N atoms in Figure 5.13 agree with Pakdel. [183].

Table 5. 4: The deconvoluted bonds and their binding energy values of each element present in AlN-15BN composite ceramics.

Sub shell	Chemical bond	Binding energy (eV)
Al 2p	Al-N	74.484
	Al-O	74.733
B 1s	B-N	190.203
	O-B-N	190.494
	B-OH	191.488
	B-O	192.326
N 1s	N-Al	397.627
	N-B	398.108
	N-Al-O	398.438
	N-O	399.416
O 1s	O-H	531.485
	Os	532.413

Wang. et al. [184] studied the XPS spectra of commercially available AlN ceramics and reported as Al 2p sub shell deconvoluted into Al-N (73.55 eV), Al-O (74.64 eV) at alumina domains and grain boundaries O1s deconvoluted into O-Al (530.53 eV) grain boundaries, O-Al (532.04 eV) alumina domains, N 1s deconvoluted as N-N (395.65 eV), N-Al (396.9 eV), N-Al-O (398 eV) alumina domains and grain boundaries, N-Al-O (399.6 eV) at the surface

only, C 1s as C-C (284.8 eV). Zhao. et al. [185] reported the deconvolution of B 1s as B-O at 192.3 eV. Achour. et al. [186] reported the deconvolution of B 1s spectra 190 eV attributed to B-N, 190.8 eV for the bond as N-B-O, at 191.9 eV for B-OH, and 192.3 eV for B-O, 190.7 eV for O-B-N, 191.7 eV assigned for B-OH. N 1s peak deconvoluted as N-B at 397.7 eV for turbostratic structure (t-BN) for the contribution of N-O / N-OH at 398.7 eV and N-H at 400 eV.

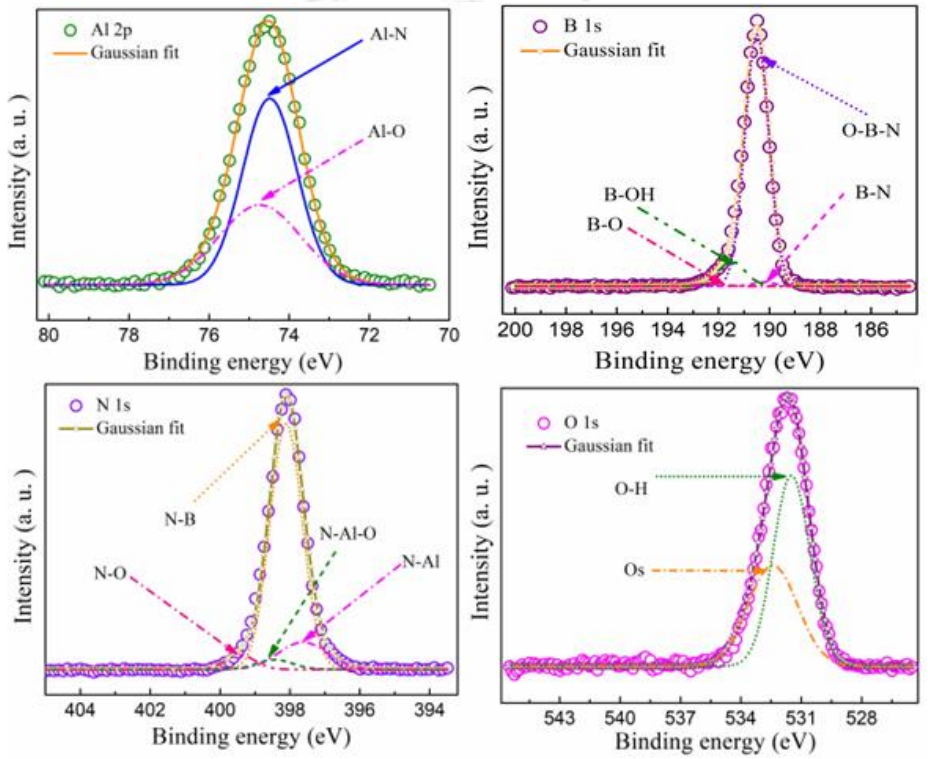

***Figure 5. 14*: The XPS high-resolution spectra of Al 2p, B 1s, N 1s, and O 1s for AlN-15BN composite ceramics, sintered at 1700 ℃ for 20 h using a powder bed.**

The binding energy of Al 2p depends upon the chemical state of the Al cation; hence, for detecting different binding states of the aluminium atom, Al 2p XPS high-resolution spectra are fitted. High-resolution spectra of Al 2p fitted using the Gaussian function deconvoluted into two peaks. Peak values are identified using the values listed in the National Institute of Standards and Technology (NIST) database. Figure 5.14(a) shows the evolution of high-resolution spectra of the Al 2p signal for the AlN-15BN composite ceramic. This Al 2p peak deconvoluted into two peaks, one at 74.48 eV and another at 74.73 eV, are attributed to the

contribution of Al-N for the aluminium bonded to nitrogen in wurtzite AlN and Al-O bonds, respectively. These deconvoluted peaks of each element with their binding energies are listed in Table 5.4. B 1s peak deconvoluted into four peaks at 190.203 eV, 190.494 eV, 191.488 eV, and 192.326 eV attributed to B-N, O-B-N, B-OH, and B-O, respectively. High-resolution spectra with fitted deconvoluted peaks of B 1s are shown in Figure 5.14(b). N 1s peak corresponding to nitrogen atom deconvoluted into 4 peaks at 397.627 eV, 398.108 eV, 398.438 eV, and 399.416 eV (see Figure 5.14(c)) corresponding to the contribution of N-Al, N-B, N-Al-O, and N-O respectively. N-Al-O (399.438) value is similar to the previously reported values [184] due to surface oxygen only. This result confirms that no oxygen presents in grains and grain boundaries. O 1s peak deconvoluted into two peaks, O-H at 531.485 eV and other as Os (surface oxygen) at 532.413 eV.

5.5.6 Dielectric studies:

The dielectric properties of AlN-xBN composite ceramics, sintered at 1700 ℃ for 20 h, are studied at different frequencies ranging from 1 kHz to 1 MHz by varying temperatures from 30 to 500 ℃ and shown in Figure 5.15. The dielectric permittivity of pure AlN ceramics is shown in Figure 5.15(a). This result reveals that pure AlN ceramics dielectric permittivity ranges from 5.60 to 8.00 by varying temperatures from 30-500 ℃. The dielectric permittivity of AlN-5BN composite ceramics is in the range 4.23 to 5.68 (see Figure 5.15(b)), for AlN-10BN composite ceramics is in the range 4.23 to 6.98 (see Figure 5.15(c)). At lower frequencies, the value extends up to 8; for AlN-15BN composite ceramics is between 6.50 to 7.48 (see Figure 5.15(d)), and for AlN-20BN composite ceramics is in the range of 4.46 to 6.98 (see Figure 5.15(e)). All pure and AlN-BN composite ceramics show minor increasing nature by increasing frequency from 1 kHz to 1 MHz, constant nature with increasing temperature 30-500℃. This increment is due to interfacial and dipolar polarization. In pure AlN ceramics, the

dielectric permittivity shows a disordered nature at lower frequencies from 1 kHz to 50 kHz. At higher frequencies, the dielectric permittivity shows constant nature with temperature increment from 30 to 380 ℃ and then slightly increases nature at high temperatures from 380 to 500 ℃. The AlN-5BN composite ceramic shows constant dielectric permittivity at each frequency with temperature variation. It is slightly disordered at low frequencies from 1 kHz to 10 kHz, with increasing temperature from 380 to 500 ℃ as dielectric permittivity with a little growing nature.

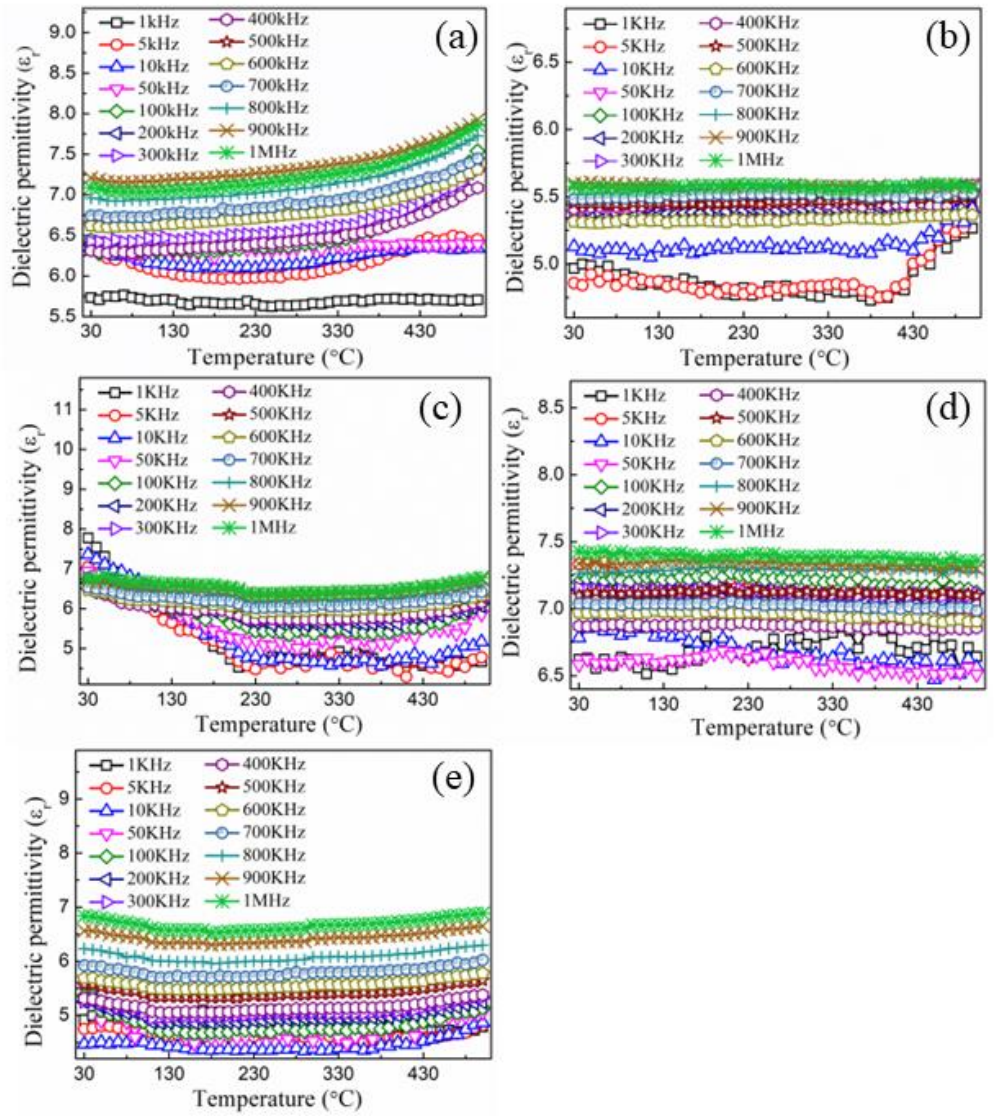

***Figure 5. 15*: The variation in the dielectric permittivity of (a) AlN, (b) AlN-5BN, (c) AlN-10BN, (d) AlN-15BN (e) AlN-20BN composite ceramics, sintered at 1700 ℃ for 20 h, at different frequencies ranging from 1 kHz to 1 MHz.**

AlN-10BN composite ceramics also show constant dielectric permittivity value by increasing the temperature from 30-500 ℃, but at lower frequencies ranging from 1 kHz to 50 kHz, show little decreasing value by increasing the temperature from 30-220 ℃, then show constant value up to 440 ℃, and then shows the increasing value from 440-500 ℃.

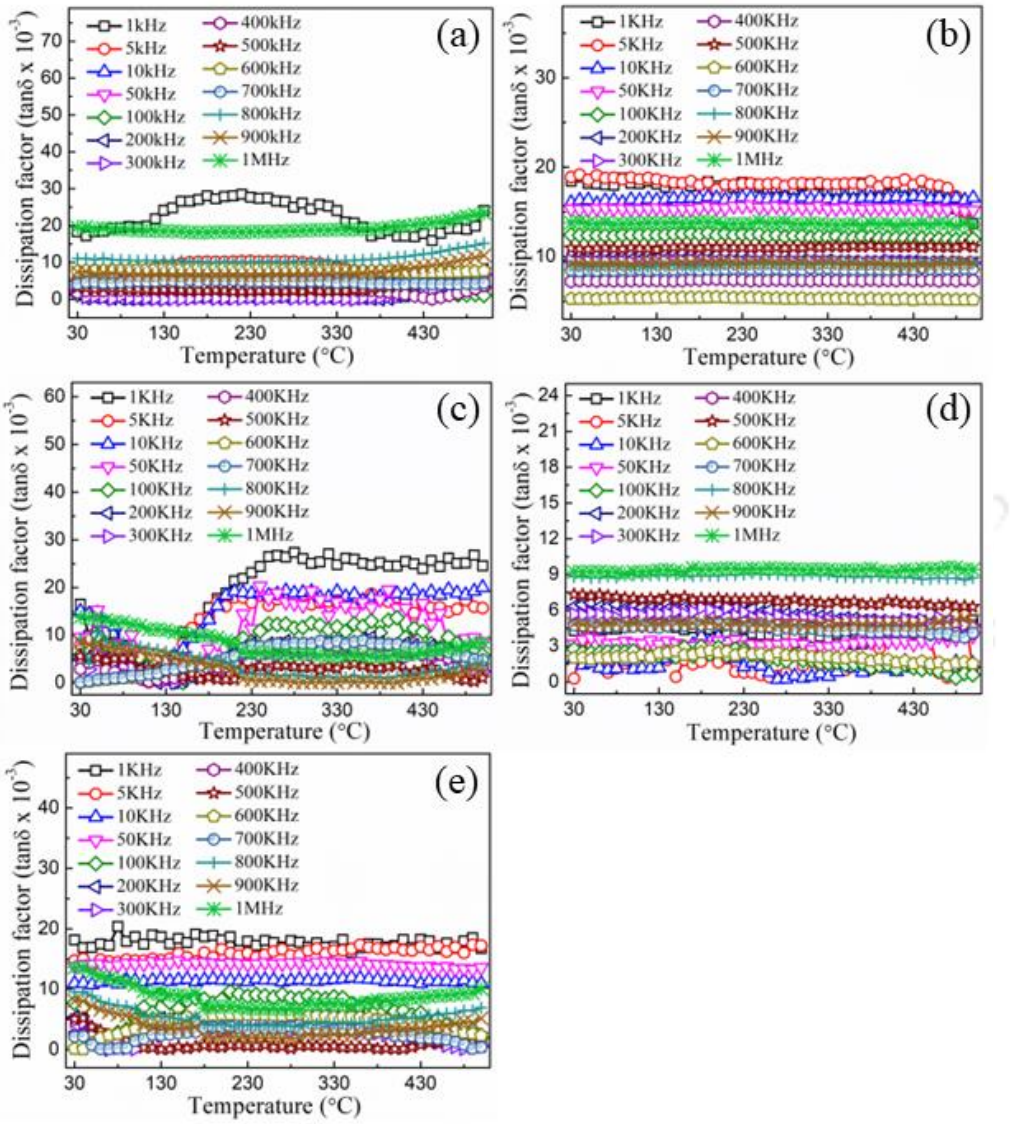

***Figure 5. 16*: The variation in the dielectric permittivity of (a) AlN, (b) AlN-5BN, (c) AlN-10BN, (d) AlN-15BN (e) AlN-20BN composite ceramics, sintered at 1700 ℃ for 20 h, at different frequencies ranging from 1 kHz to 1 MHz.**

For AlN-15BN, composite ceramics show the constant value at each frequency by increasing the temperature to 30-500 ℃, at lower frequencies from 1 kHz to 50 kHz, showing little fluctuations. AlN-20BN composite shows almost constant value with temperature

variation at each frequency ranging from 100 kHz to 1 MHz, with minor fluctuations at lower frequencies from 1 kHz to 50 kHz (see Figure 5.15(e)).

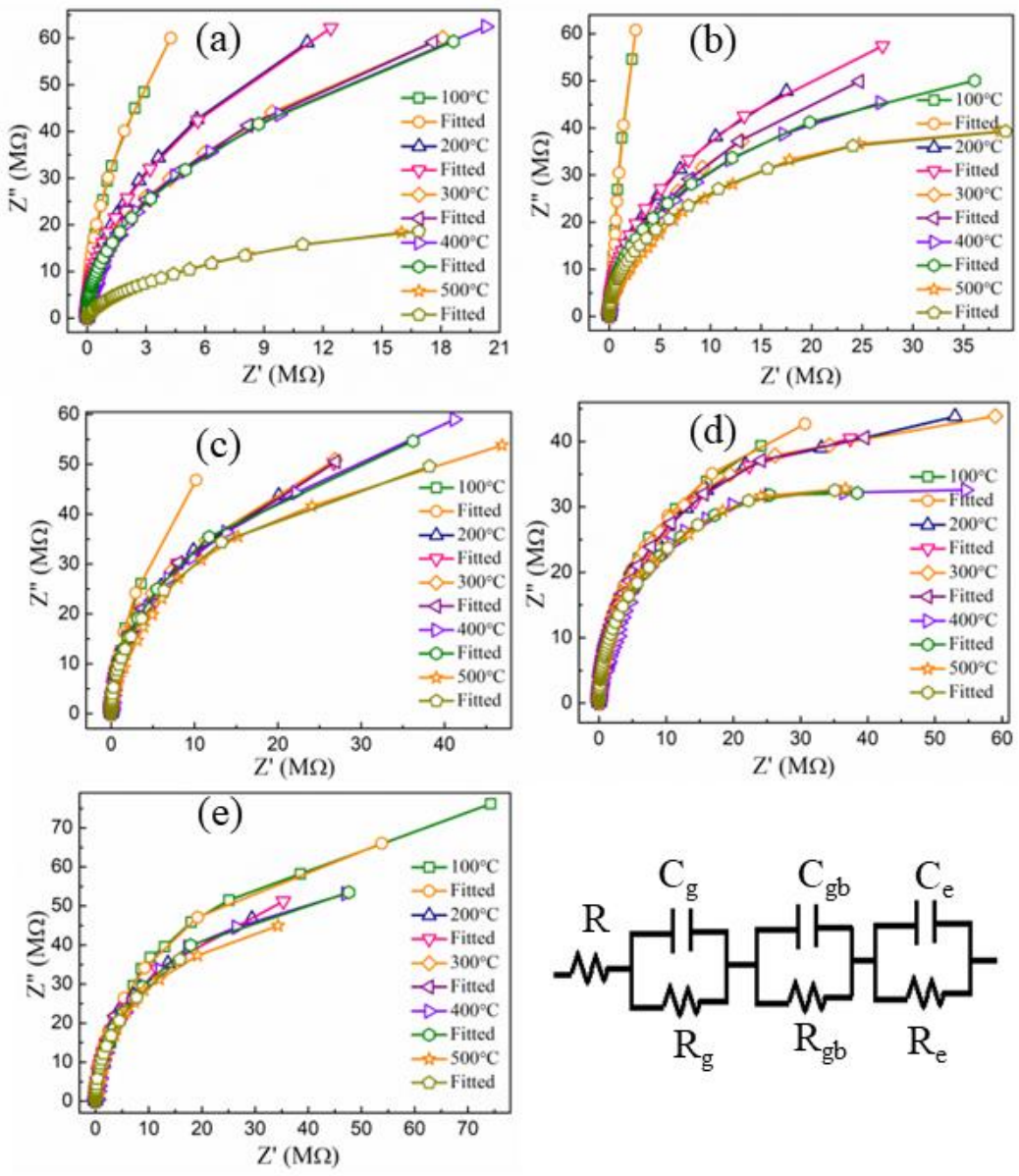

***Figure 5. 17*: The Cole-Cole plot for the ceramics (a) AlN, (b) AlN-5BN, (c) AlN-10BN, (d) AlN-15BN, (e) AlN-20BN.**

Among all AlN-BN composite ceramics, AlN-15BN composite ceramic shows the best dielectric permittivity with good behavior by varying temperatures from 30-500 ℃. The dissipation factor of each composite ceramic is measured and shown in Figure 5.16. In the dissipation factor, each composite shows fluctuations similarly at the same frequencies as in

dielectric permittivity fluctuations. At other frequencies, it offers constant behavior with a low dissipation factor in the order of 10^{-3}. The Best dielectric permittivity (6.50-7.48) with low dissipation factor (0.2×10^{-3}-9.8×10^{-3}) obtained for AlN-15BN composite ceramics. This result reveals that AlN-15BN composite ceramics are suitable for RF-window and electronic applications. The obtained dielectric properties indicate pure phase formation of AlN-BN composites without the secondary phase.

A secondary phase would enhance the loss tangent, and the obtained values are better than the reported values. The slight change in the electric properties of the material can be detected from impedance spectroscopy [187]. This spectroscopy is an essential and easy tool for a wide range of materials to detect small changes in their electrical properties. This impedance spectroscopy is necessary to develop and improve the material since it separates its electrical properties into components [188]. The Impedance (Z) can be expressed as real (Z') and imaginary (Z'') parts and can be calculated from the following relations;

$$Z' = |Z| + \cos\varphi = R \tag{5.4}$$

$$Z'' = |Z| + \sin\varphi = X_c = \frac{-1}{\omega C} \tag{5.5}$$

$$\varepsilon' = \frac{Ct}{\varepsilon_0 A} = \frac{t}{\omega Z'' A \varepsilon_0} \tag{5.6}$$

$$\varepsilon'' = \frac{\sigma(\omega)}{\varepsilon_0 \omega} = \frac{t}{\omega Z' A \varepsilon_0} \tag{5.7}$$

$$\tan\delta = \frac{\varepsilon' \sigma(\omega)}{\varepsilon''} = \frac{t}{RA} \tag{5.8}$$

where R is the resistance, φ is the phase angle, X is the reactance, C is the capacitance, ε_0 is the permittivity of the free space, $\sigma(\omega)$ conductivity, ω is the angular frequency, and A and t are the area and thickness of the samples, respectively.

The measured impedance as real and imaginary from the following relations are fitted with an equivalent circuit comprising 3 parallel connected resistance and capacitance. The fitted impedance spectra are shown in Figure 5.17. This result reveals that one resistor and

capacitor is a contribution of grain, another resistor and capacitor are the contributions of grain boundary, and the last one is the contribution of the electrode. All AlN-BN composite ceramics are appropriately fitted with the same equivalent circuit. All samples show decreasing impedance with an increase in frequency. All composite AlN-BN ceramics' impedance merges at higher frequencies above 2.4 kHz. The obtained results are in good agreement with previously reported values [189].

5.5.7 Microwave dielectric studies:

The calculated dielectric values of all AlN-BN composite ceramics at 12 GHz are listed in Table 5.5. This result reveals that the dielectric permittivity of AlN-BN composite ceramics is lower than pure AlN ceramics since the dielectric permittivity of pure BN ($\varepsilon_r = 5$) is less than AlN. Thus, the low dielectric permittivity ($\varepsilon_r = 7.38$) and low dissipation factor ($\tan\delta = 2.60 \times 10^{-3}$) was achieved for AlN-15BN composite ceramics with pure nitride phase without any oxide phase are best suitable for RF window and electronic applications.

Table 5. 5: The Microwave dielectric properties of AlN-15BN composite ceramics.

Sample	Dielectric Permittivity	Loss tangent ($\tan\delta \times 10^{-3}$)
AlN	8.44	2.64
AlN-5BN	6.86	5.16
AlN-10BN	7.35	2.98
AlN-15BN	7.38	2.60
AlN-20BN	6.85	4.13

5.6 Conclusions:

- AlN-BN composite ceramics are prepared in conventional sintering by adopting a powder bed. The AlN-BN composite ceramics are sintered at a low temperature of 1700 ℃ using

a powder bed and obtained pure nitride ceramics with AlN and BN phases without any oxide phase as a secondary phase.

- The XRD and Raman spectrum of obtained AlN-BN composite ceramics confirms that the obtained ceramics are of wurtzite crystal structure with $P6_3mc$ and space group number 186. The temperature Raman demonstrates the stability of vibrational modes at low and high temperatures.
- The XPS spectrum of AlN-15BN composite ceramics shows that the sintered samples do not contain any Al-O-N peak, indicating that the sintered sample was not oxidized. The oxygen present in the XPS spectrum is surface oxygen due to the adsorbed gas used in XPS as oxygen.
- The obtained dielectric properties of AlN-15BN composite ceramic show the best dielectric permittivity (6.50-7.48) and low dissipations factor (0.2×10^{-3}-9.8×10^{-3}). This result reveals that the obtained AlN-BN composite ceramics are appropriate for electronic applications.
- The Cole-Cole plots of impedance spectra of all AlN-BN composite ceramics show non-Debye type relaxations. They are fitted with RCRCRC circuits corresponding to three parallelly connected R and C circuits connected in series corresponding to grain, grain boundary, and electrode.
- The best microwave dielectric properties at 12GHz, such as low dielectric permittivity ($\varepsilon_r = 7.38$) and low dissipation factor ($\tan\delta = 2.60 \times 10^{-3}$) is obtained for AlN-15BN composite ceramics with pure nitride phase without any alumina or intermediate phases are appropriate for RF-window and electronic applications.

Chapter 6

The Effect of the Sintering Method on Structural and Dielectric Properties of AlN Ceramics with Additives $CaZrO_3$ and Y_2O_3

6.1 Graphical abstract:

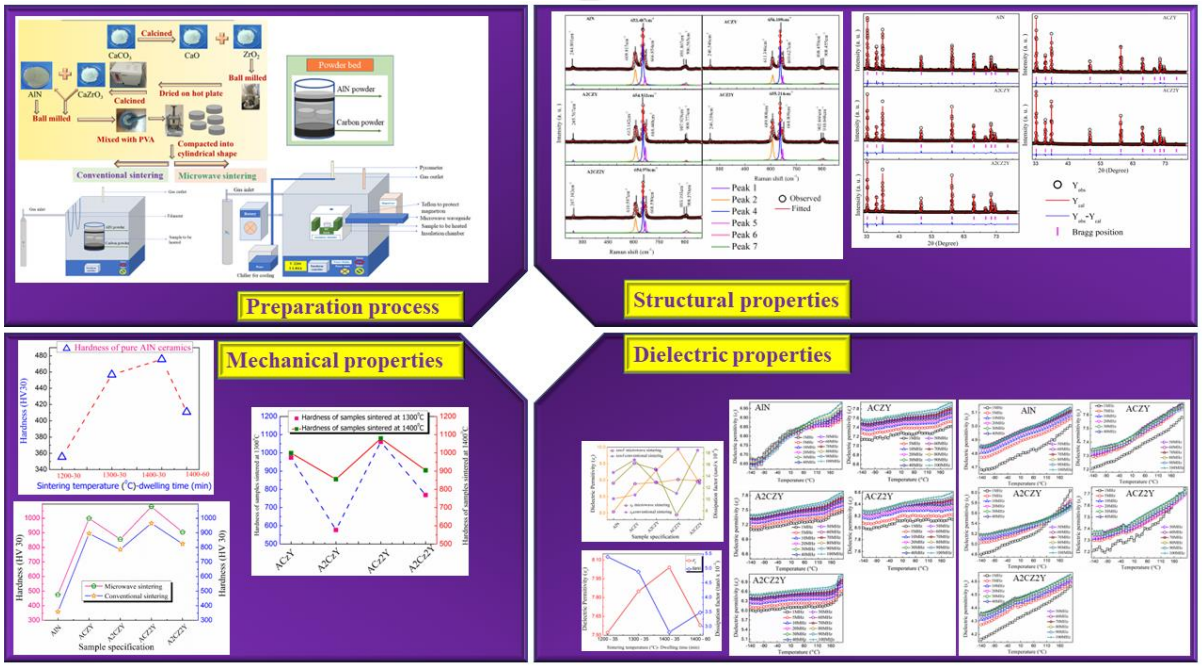

6.2 Abstract:

This investigation demonstrates the effect of the sintering method on AlN composite ceramic's properties. In the conventional sintering method, a powder bed is adopted to sinter at a low temperature of ~1700 ℃. In contrast, the microwave sintering method adopts a susceptor bed to sinter at 1400 ℃. High relative density for additive ACZ2Y sample, 97.68% in microwave sintering and 98.87% in conventional sintering are achieved. Pure wurtzite structure without any secondary phase with space group $P6_3mc$ is obtained for all pure and additive ceramics in both sintering methods. The Raman spectrum of all sintered samples confirms the wurtzite structure by exhibiting six vibrational modes in both sintering methods.

The best composite ACZ2Y ceramic sintered in conventional sintering shows dielectric permittivity $7.99 \leq \varepsilon_r \leq 8.61$ and $0.12 \times 10^{-2} \leq \tan\delta \leq 5.21 \times 10^{-2}$ and for the composite sintered in microwave sintering exhibited as $7.20 \leq \varepsilon_r \leq 7.96$ and $0.31 \times 10^{-2} \leq \tan\delta \leq 1.37 \times 10^{-2}$. The microwave dielectric properties of the best composite ACZ2Y ceramic $\varepsilon_r = 9.94$, $\tan\delta = 11.05 \times 10^{-4}$, and $\varepsilon_r = 9.02$, $\tan\delta = 7.34 \times 10^{-4}$ achieved in conventional sintering and microwave sintering respectively. Conventional sintered composite ceramics achieve good dielectric properties with higher relative density than the sample sintered in the microwave sintering method, but a time-consuming process. Microwave sintered composite ceramics also exhibit good dielectric permittivity with a lower dissipation factor than that obtained in the conventional sintering method with appropriate relative density and achieved in less time duration at lower sintering temperature.

6.3 Introduction:

Aluminium nitride (AlN) has good mechanical strength and non-toxicity compared to BeO (beryllium oxide) as a competing material [70, 132]. AlN is a promising non-oxide material for thermomechanical and electronic ceramic applications [190]. The required properties for packaging materials are high thermal conductivity, high electrical resistivity, and low thermal expansion coefficient, similar to silicon [191–193]. The required properties for electronic chips are low dielectric constant, low dissipation factor, high mechanical strength, high stability, non-toxicity, ease of cutting and polishing full filled by AlN ceramics [194–196]. The covalent bond present in AlN makes it a compound with limited atomic mobility. Hence, the Sintering of AlN at low temperatures with pure phase without oxidation is challenging.

Cheng. Jiping et al. [63] sintered pure AlN ceramics using the microwave sintering method at 1850 ℃ for 30-60 min. Here, a BN (boron nitride) crucible was used with the powder

bed containing 50% AlN and 50% BN to separate pellets and to reduce decomposition or evaporation of AlN while sintering at high temperatures. Some researchers used additives such as oxide composites, rare earth oxides, fluorides, and nitrides. Yu. Yind-Da et al. [197] sintered AlN ceramics using rare earth oxide (Y_2O_3) as an additive with AlN powder as a powder bed in a BN crucible covered by its lid and graphite crucible in a graphite furnace at 1880 ℃ for 2 h in a nitrogen atmosphere. The yttrium aluminate garnet (YAG) formed as a secondary phase. Quao L et al. [136] and Du Xueli et al. [198] sintered pure AlN ceramics using spark plasma sintering at lower sintering temperatures of 1600 ℃ and 1470 ℃, respectively. He. Xiualn et al. [174] sintered AlN-BN composite ceramics using Sm_2O_3 and CaF_2 as sintering additives in spark plasma sintering method at a temperature of 1800 ℃ for 10 min with 40 MPa uniaxial pressure in the presence of nitrogen. $SmAlO_3$ and $Ca_3Al_2O_6$ are formed as secondary phases in the obtained AlN-BN composite ceramics. Geng fu Xu et al., [199] AlN is prepared by combustion reaction method, with Y_2O_3 additive sintered from 1600 ℃-2000 ℃.

Very few studies are available on the dielectric and structural properties of AlN ceramics with pure phase and comparing both microwave and conventional Sintering of AlN ceramics. Hence, this study aims to prepare pure AlN ceramics, sintering AlN at low temperatures with high-density achievement, and compare the structural and dielectric properties of AlN ceramics sintered in both methods.

6.4 Experimental procedure:

The pure and additive AlN ceramics are prepared in conventional sintering and microwave sintering methods, and the effect of sintering on the properties of AlN and additive AlN ceramics are compared. Additives are considered as $CaZrO_3$ and Y_2O_3 to densify AlN ceramics at low sintering temperatures. The additives are taken in different wt%, as shown in Table 6.1. Pure AlN powder ball milled in dry condition with 150 rpm for 10 h. AlN, $CaZrO_3$,

and Y_2O_3 are taken per the sample specification (Table 6.1) and ball milled using iso-propanol as a liquid media with 150 rpm for 12 h to prepare composite. The ball-milled suspension is dried on a hot plate and ground using agate mortar to get a fine powder. The fine powder is mixed with 2 mol% PVA (polyvinyl alcohol) and then compacted into a cylindrical shape by applying 2 MPa pressure. The compacted sample is inserted in a powder bed (see Figure 6.1), consisting of AlN powder and C (carbon) powder as a layer in a crucible to prevent oxidation. This arrangement is placed in a chamber and sintered in the conventional sintering method at 1700 ℃ for 20 h dwelling time with a 15 ℃/min rate of heating in the presence of nitrogen flow. The sample is inserted in the susceptor bed consisting of AlN and carbon powders as layers, placed in between SiC (silicon carbide bricks) shown in Figure 6.1, and sintered at 1400 ℃ for 30 min.

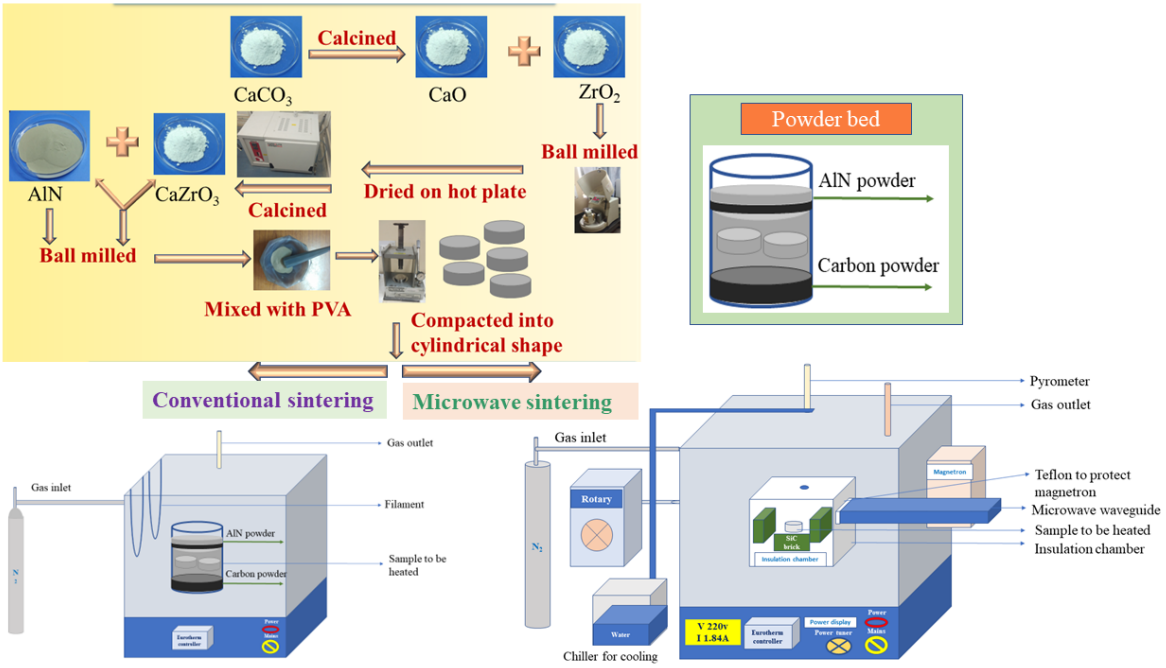

Figure 6. 1: The schematic diagram of preparing pure and additive AlN ceramics using different sintering methods.

6.5 Results and discussions:

6.5.1 Sintering and relative density:

The pure AlN powders are ball milled for 10 h and, compacted into cylindrical shapes, are sintered at different temperatures from 1200 ℃ to 1400 ℃ with a dwelling time of 35 min. One pure AlN sample is sintered at 1400 ℃ with a dwelling time 60 min for checking the variation of properties by varying the dwelling time. The relative densities of sintered pure AlN ceramics are shown in Figure 6.2. This result conveys that the density of AlN ceramics is improving by increasing the sintering temperature from 1200 ℃ to 1400 ℃ with a constant dwelling time of 35 min, further increasing dwelling time to 60 min, the density decreases. The increase in the density with sintering temperature is due to the increase in grain size and decrease in porosity. The density of the ceramics decreased with a rise in the dwelling time at 1400 ℃ from 30 min to 60 min.

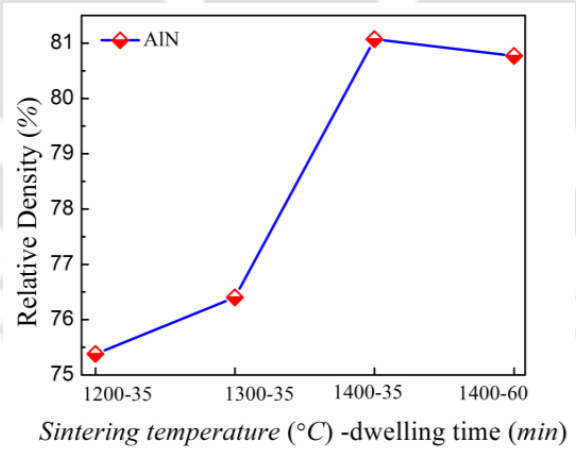

Figure 6. 2: Variation in relative density of pure AlN ceramics as a function of sintering temperature and dwelling time.

The reduction in density is due to the escalation of the grain growth over the nucleation, causing an increase in porosity [200]. The maximum density obtained for pure AlN ceramics, sintered at 1400 ℃ with a dwelling time of 35 min, is 2.70 g/cm^3 (81.07%). To improve the

density of AlN ceramics $CaZrO_3$ and Y_2O_3 are chosen as sintering additives. These samples are sintered at different temperatures from 1200 ℃ to 1400 ℃ with a soaking time of 35 min. The densities of these samples are shown in Figure 6.3. This result reveals that the density of AlN composite ceramics improved with a rise in the sintering temperature from 1200 ℃ to 1400 ℃.

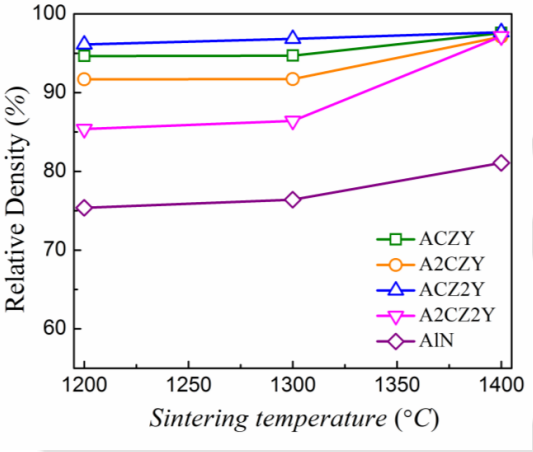

***Figure 6. 3*: The variation in relative density as a function of sintering temperature for different concentrations of additives.**

***Table 6. 1*: The sample specification of additives used to prepare additive AlN ceramics.**

S. No	Specification of AlN ceramics with Additives			
	Sample name	AlN (wt.%)	$CaZrO_3$ (wt.%)	Y_2O_3 (wt.%)
1	AlN	100	0	0
2	ACZY	98	1	1
3	A2CZY	97	2	1
4	ACZ2Y	97	1	2
5	A2CZ2Y	96	2	2

This density improvement could be due to the smaller initial particle sizes, which facilitate the nucleation over grain growth, reduced porosity, and uniform microstructure. The maximum densities among all the prepared samples are shown by 1 wt% $CaZrO_3$ and 2 wt%

of Y_2O_3 additive AlN (ACZ2Y) ceramics, sintered at 1400 ℃ with dwelling time 35 min is 3.25 g/cm^3 reached 97.68% of the theoretical density. AlN ceramics added with additives exhibited higher densities than pure ceramics. It is a combined effect of smaller initial particles, filling vacancies by additives while sintering, uniform grain growth, and also due to the formation of liquid phase effect.

AlN ceramics sintered with $CaZrO_3$ and Y_2O_3 additives using conventional sintering at 1700 ℃ for 20 h. In microwave sintering at 1400 ℃ for 30 min in the presence of nitrogen using powder bed. The density of the sintered ceramics is measured using Archimedes' principle and shown in Figure 6.4. The relative density of AlN and ACZ2Y samples sintered in conventional Sintering is higher than in the microwave sintering method. ACZY and A2CZ2Y samples sintered in the microwave sintering method show higher relative density than conventional Sintering, and A2CZY samples show almost equal relative density in both sintering techniques.

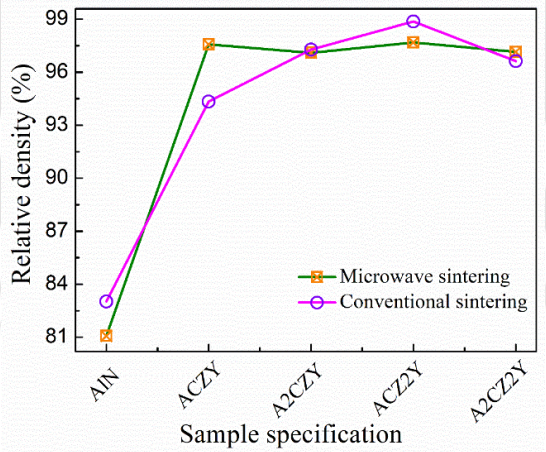

Figure 6. 4: The relative density of pure and additive AlN ceramics sintered, using different methods.

These results convey that using a powder bed helps densify AlN ceramics with additives at low temperatures in both conventional and microwave sintering methods. Still, the time

consumption is different in both methods. The highest relative density (98.87%) is achieved by conventionally sintered ACZ2Y samples among all additive AlN ceramics. AlN ceramics sintered with $CaZrO_3$ and Y_2O_3 additives using conventional Sintering at 1700 ℃ for 20 h. In microwave sintering at 1400 ℃ for 30 min in the presence of nitrogen using powder bed. The density of the sintered ceramics is measured using Archimedes' principle and shown in Figure 6.4. The relative density of AlN and ACZ2Y samples sintered in conventional Sintering is higher than in the microwave sintering method. ACZY and A2CZ2Y samples sintered in the microwave sintering method show higher relative density than conventional Sintering, and A2CZY samples show almost equal relative density in both sintering techniques. These results convey that using a powder bed helps densify AlN ceramics with additives at low temperatures in both conventional and microwave sintering methods. Still, the time consumption is different in both methods. The highest relative density (98.87%) was achieved by conventionally sintered ACZ2Y samples among all additive AlN ceramics.

6.5.2 Structural analysis:

The crystal structure and phase purity of sintered additive AlN ceramics is identified from the XRD diffraction spectrum and shown in Figure 6.5. The additive AlN ceramics sintered in the conventional sintering method at 1700 ℃ for 20 h is shown in Figure 6.5(a) and sintered in the microwave sintering method shown in Figure 6.5(b). This result reveals that all sintered samples showed wurtzite AlN with pure phase AlN without any secondary phase formation. The structure of sintered AlN ceramics is confirmed as wurtzite phase with space group $P6_3mc$ by matching appropriately with standard JCPDS data with card no: 00-003-1144. The Rietveld refinement of the obtained XRD pattern of all samples is carried out using the Pseudo Voigt function shown in Figure 6.6 for conventionally sintered samples and Figure 6.7 for the samples sintered in the microwave sintering method. The Rietveld refined parameters

for the samples sintered in the conventional sintering method are listed in Table 6.2, and the samples sintered in the microwave sintering method are listed in Table 6.3.

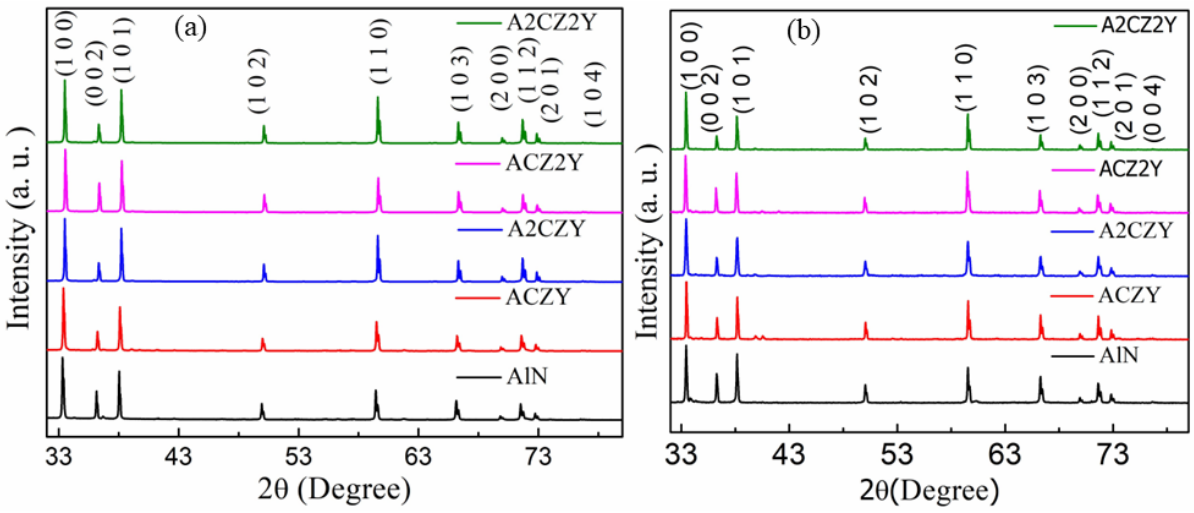

***Figure 6. 5*: The XRD pattern of pure and additive AlN ceramics, sintered in (a) Conventional and (b) Microwave sintering methods.**

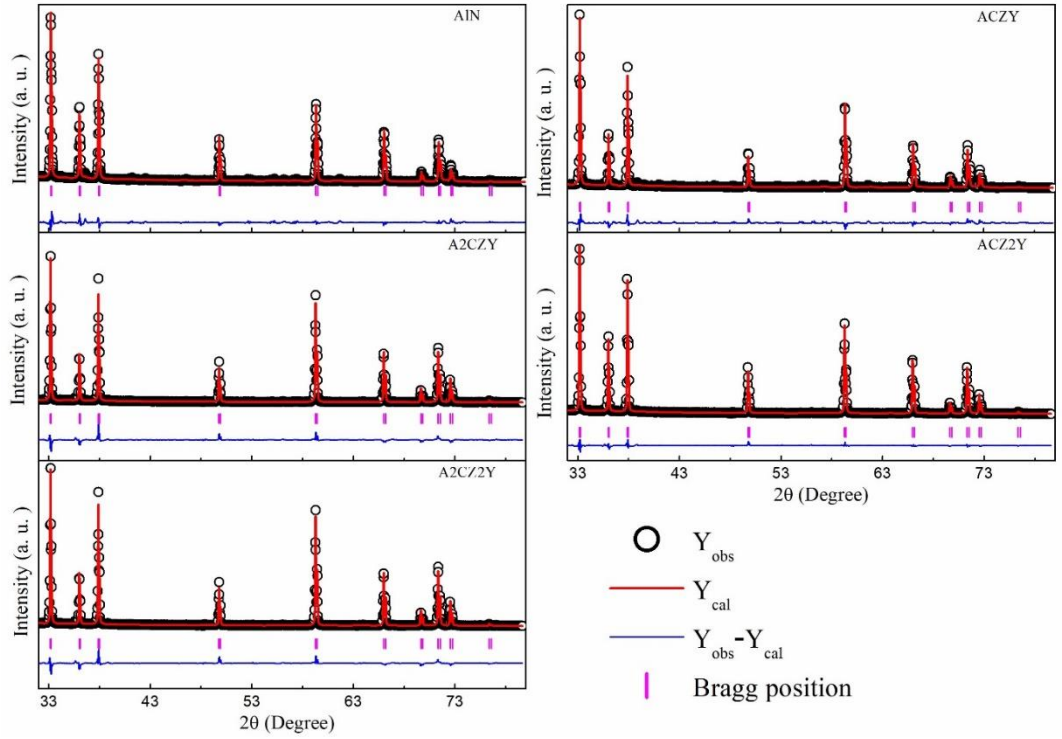

***Figure 6. 6*: The Rietveld refinement of XRD pattern of pure and additive AlN ceramics, sintered in conventional sintering.**

Table 6. 2: The Rietveld refined parameters of pure and additive AlN ceramics, sintered in conventional sintering.

Conventional sintered composite	χ^2	Rf-factor	Bragg Rf-factor	a (Å)	c (Å)	Volume $(Å)^3$
AlN	1.12	3.08	3.59	3.113 (28)	4.981 (76)	41.793 (1)
ACZY	2.15	4.55	3.51	3.113 (67)	4.981 (14)	41.809 (2)
A2CZY	1.86	4.57	3.63	3.115 (61)	4.983 (16)	41.873 (1)
ACZ2Y	1.52	1.16	1.82	3.116 (28)	4.985 (53)	41.912 (1)
A2CZ2Y	2.32	7.03	4.24	3.115 (49)	4.983 (98)	41.873 (1)

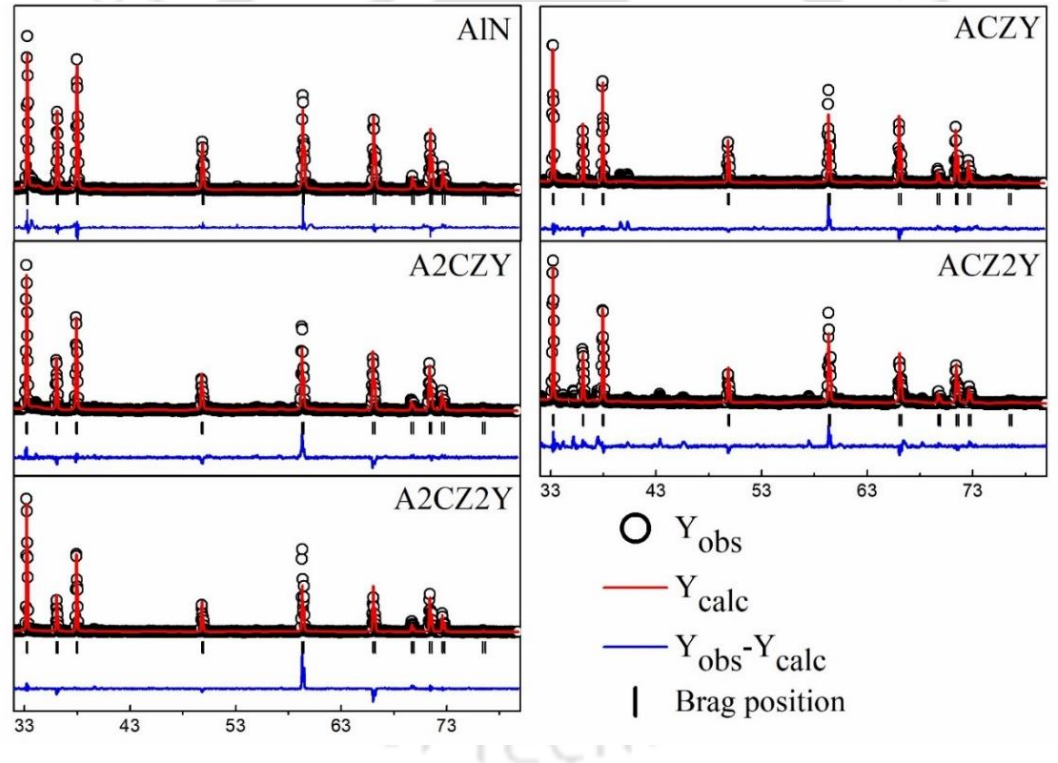

Figure 6. 7: The Rietveld refinement of XRD pattern of pure and additive AlN ceramics sintered using microwave sintering technique.

These results reveal that both the method's XRD pattern fitted properly and the lattice parameters of all the samples are in good agreement with each other such as the lattice volume of all the samples are ~ 41.80 $Å^3$ and lattice parameters are a ~ 3.113 Å, c ~ 4.981 Å. The value

of good fit χ^2 obtains little higher values in the microwave sintering method than in conventional sintered samples. This result shows that the XRD pattern of AlN ceramics sintered in the conventional sintering method fitted very nicely than that of microwave sintered samples. These results agree with previously reported AlN ceramics [200, 201].

Secondary phase such as alumina in AlN ceramics will deteriorate it's properties and thus effects applications. Since, (alumina) secondary phase creates thermal conductivity and lattice mismatch with AlN at their interface leads to crack or stress. The powder bed helps avoid alumina (Al_2O_3) phase formation in both methods, and the additives are taken in very small amounts; hence it is not formed any secondary phase is confirmed from the XRD pattern. ACZ2Y composite ceramics are better fitted than all other composites sintered in conventional sintering.

Table 6. 3: The Rietveld refined parameters of pure and additive AlN ceramics sintered in microwave sintering technique.

Microwave sintered composite	χ^2	Brag R factor	Rf -factor	*a* = *b* (Å)	*c* (Å)	Volume (Å^3)
AlN	3.88	6.03	4.56	3.113 (15)	4.980 (27)	41.805 (4)
ACZY	4.67	8.87	6.62	3.115 (12)	4.983 (15)	41.859 (2)
A2CZY	3.54	9.40	6.96	3.114 (11)	4.981 (19)	41.828 (3)
ACZ2Y	4.23	11.6	7.76	3.113 (11)	4.981 (16)	41.807 (3)
A2CZ2Y	5.14	13.1	9.43	3.113 (12)	4.981(17)	41.812 (2)

6.5.3 Raman spectroscopy:

The Raman Spectra of all pure and composite AlN ceramics sintered in conventional and microwave sintering methods is recorded by exciting the sample with a 514 nm laser with

30 mW power. The obtained Raman spectra of all samples is fitted using the Lorentz function and shown in Figure 6.8 and Figure 6.9 for the samples sintered in conventional and microwave sintering, respectively.

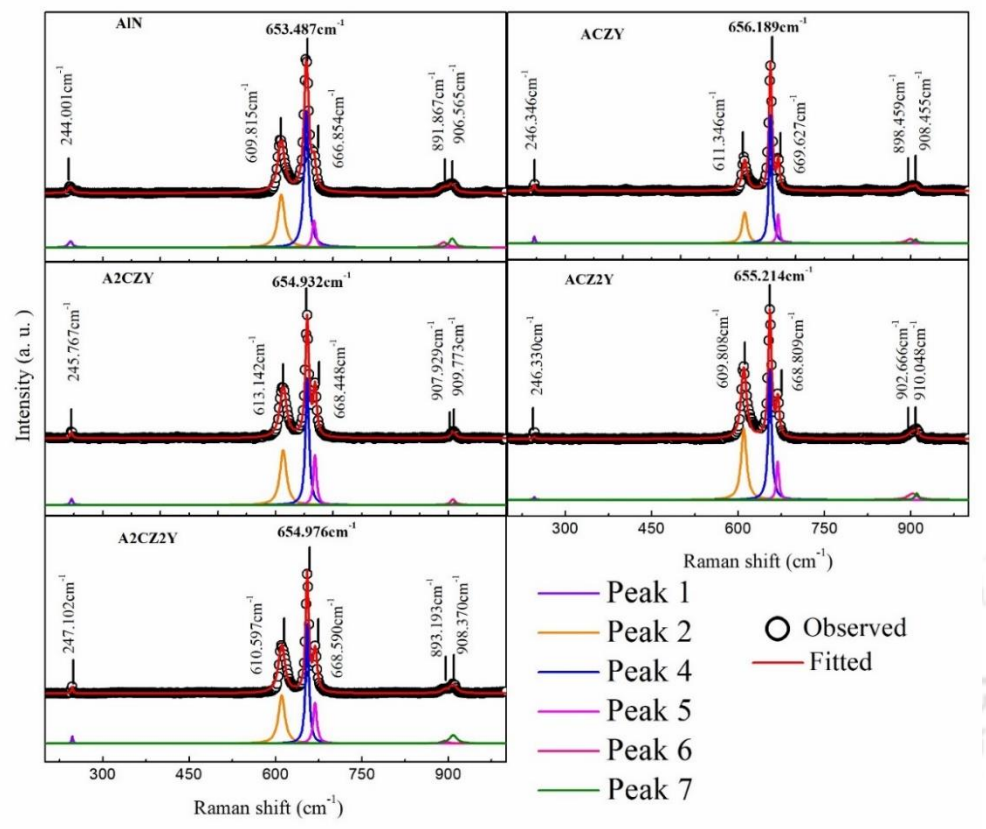

***Figure 6. 8*: The Raman spectrum of pure and additive AlN ceramics sintered by conventional sintering.**

All the fitted Raman spectra reveal six vibrational modes of the wurtzite structure AlN pure phase without any secondary phases such as alumina (commonly existing secondary phase) or any other additive composites such as $CaZrO_3$ and Y_2O_3 or their composites. Those six vibrational modes are E_2 (Low), A_1 (TO), E_2 (High), E_1 (TO), A_1 (LO), and E_1 (LO). The best composition ACZ2Y sample sintered in conventional sintering method exhibited phonon modes are 246.33 cm^{-1} (E_2 (Low)), 609.81 cm^{-1} (A_1 (TO)), 655.21 cm^{-1} (E_2 (High)), 668.81 cm^{-1} (E_1 (TO)), 902.67 cm^{-1} (A_1 (LO)) and 910.05 cm^{-1} (E_1 (LO)).

***Table 6. 4*: The Raman spectrum pure and additive AlN ceramics fitted parameters sintered in the conventional sintering method.**

Sample/Phonon mode		E_2 (Low)	A_1 (TO)	E_2 (High)	E_1 (TO)	A_1 (LO)	E_1 (LO)
AlN	γ (Cm^{-1})	244.00	609.81	653.49	666.85	891.87	906.57
	β (Cm^{-1})	9.371	13.952	9.312	7.237	17.080	12.583
ACZY	γ (Cm^{-1})	246.35	611.35	656.19	669.63	898.46	908.45
	β (Cm^{-1})	3.323	10.326	6.093	4.986	18.284	7.825
A2CZY	γ (Cm^{-1})	245.77	613.14	654.93	668.45	907.93	909.77
	β (Cm^{-1})	5.235	13.325	7.292	6.494	10.586	6.116
ACZ2Y	γ (Cm^{-1})	246.33	609.81	655.21	668.81	902.67	910.05
	β (Cm^{-1})	4.074	11.106	6.937	5.481	20.143	7.621
A2CZ2Y	γ (Cm^{-1})	247.10	610.60	654.98	668.59	893.19	908.37
	β (Cm^{-1})	3.083	13.294	6.502	7.625	13.555	16.312

***Table 6. 5*: The Raman spectrum pure and additive AlN ceramics fitted parameters sintered in microwave sintering method.**

Sample/Phonon mode		E_2 (Low)	A_1 (TO)	E_2 (High)	E_1 (TO)	A_1 (LO)	E_1 (LO)
AlN	γ (Cm^{-1})	247.67	610.65	656.27	670.07	895.37	909.77
	β (Cm^{-1})	3.433	13.464	8.163	8.717	18.694	12.224
ACZY	γ (Cm^{-1})	247.41	612.23	656.5	669.7	892.65	909.29
	β (Cm^{-1})	3.573	11.36	8.742	8.428	12.631	15.703
A2CZY	γ (Cm^{-1})	247.44	612.99	656.55	670.04	891.94	911.1
	β (Cm^{-1})	3.662	11.65	7.741	9.118	16.449	12.915
ACZ2Y	γ (Cm^{-1})	247.48	613.53	657.69	671.05	900.31	909.98
	β (Cm^{-1})	3.217	13.62	8.29	7.163	11.227	9.592
A2CZ2Y	γ (Cm^{-1})	247.71	610.12	656.22	670.01	895.54	910.87
	β (Cm^{-1})	3.37	9.374	8.832	6.315	20.137	11.775

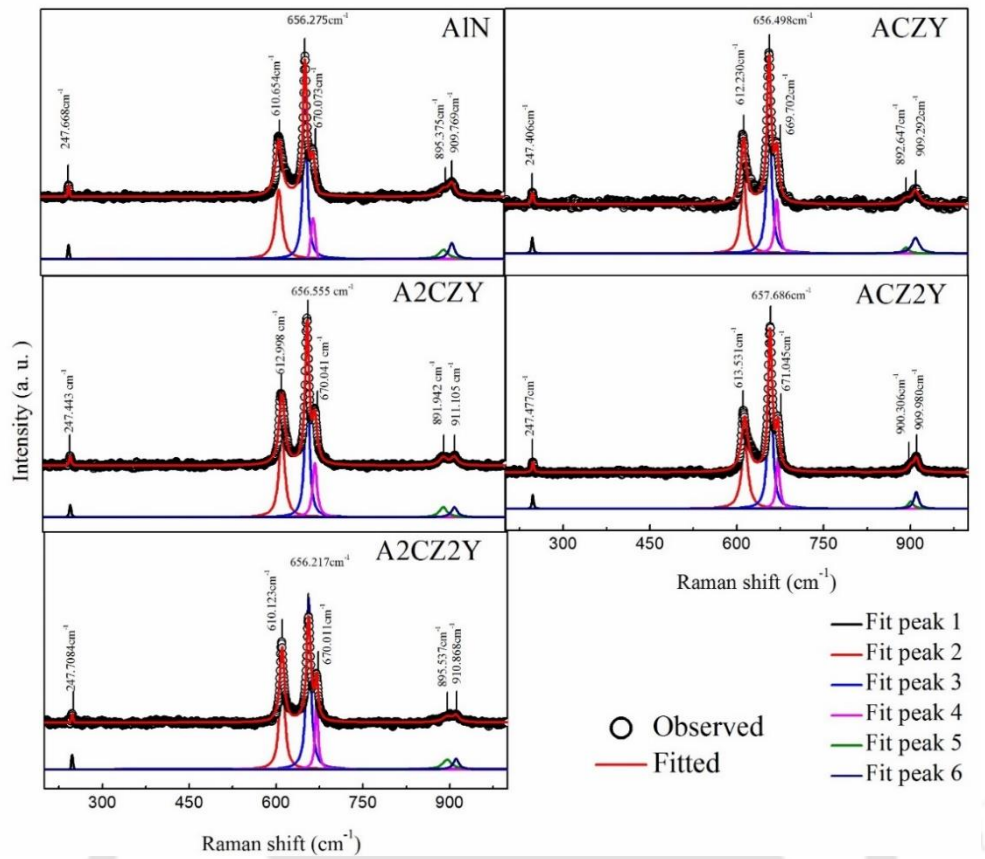

***Figure 6. 9*: The Raman spectrum of pure and additive AlN ceramics sintered in microwave sintering.**

The composite ceramics ACZ2Y sintered in microwave sintering method exhibited six vibrational modes as 247.48 cm^{-1}, 613.53 cm^{-1}, 657.69 cm^{-1}, 671.05 cm^{-1}, 900.31 cm^{-1}, and 909.98 cm^{-1} respectively. The Raman shift and full-width half maximum of all vibrational modes for each sample sintered in conventional and microwave sintering are observed and shown in Tables 6.4 and 6.5, respectively. Thus, the obtained six vibrational modes of all sintered AlN composites in both methods agree with the previous literature [202, 203]. Raman spectra fit nicely and complement the XRD studies. The fitted result gives us exact FWHM (β) values (see Table 6.4 and Table 6.5), revealing that the phonon modes frequencies (γ) for each sample is in agreement with pure AlN wrutzite structure. The Raman spectra shows with slight increment and decrement in FWHM values by increasing the additive concentration tells us that the additive elements are filled the V_{Al}^{3-} (aluminum vacancy) and V_N (nitrogen vacancy)

as stated in the previous literature [180]. Hence, no secondary phase is observed in the synthesized/densified sample in this process.

6.5.4 EDAX analysis:

The elemental analysis of the pure AlN and ACZ2Y (AlN composite) samples is obtained by EDS spectra and is shown in Figures 6.10(a) and 6.10(b), respectively. The EDS spectra of the best AlN composite ceramics sintered in the conventional sintering method are shown in Figure 6.10(c).

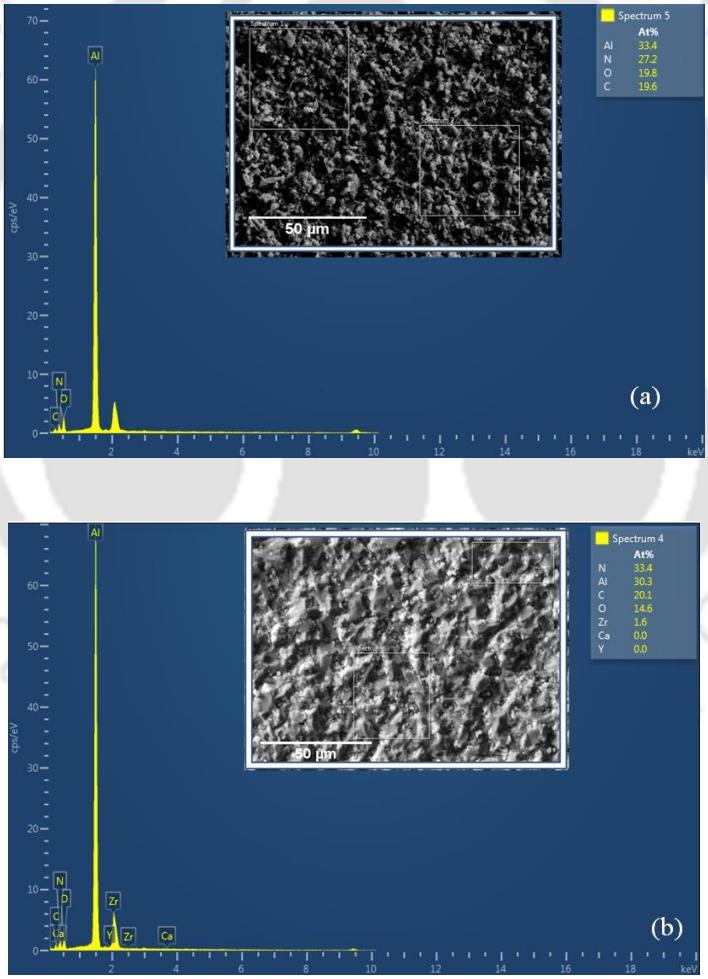

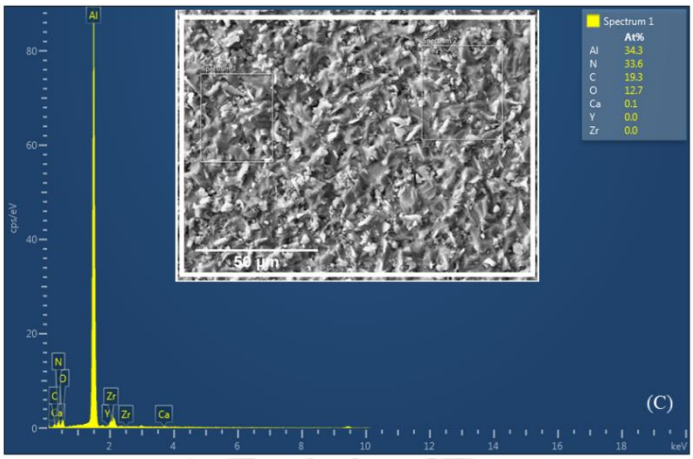

***Figure 6. 10*: EDS spectra of (a) the pure AlN and (b) ACZ2Y (AlN composite) sintered in microwave sintering method (c) EDS spectra of the ACZ2Y (AlN composite) sintered in conventional sintering method.**

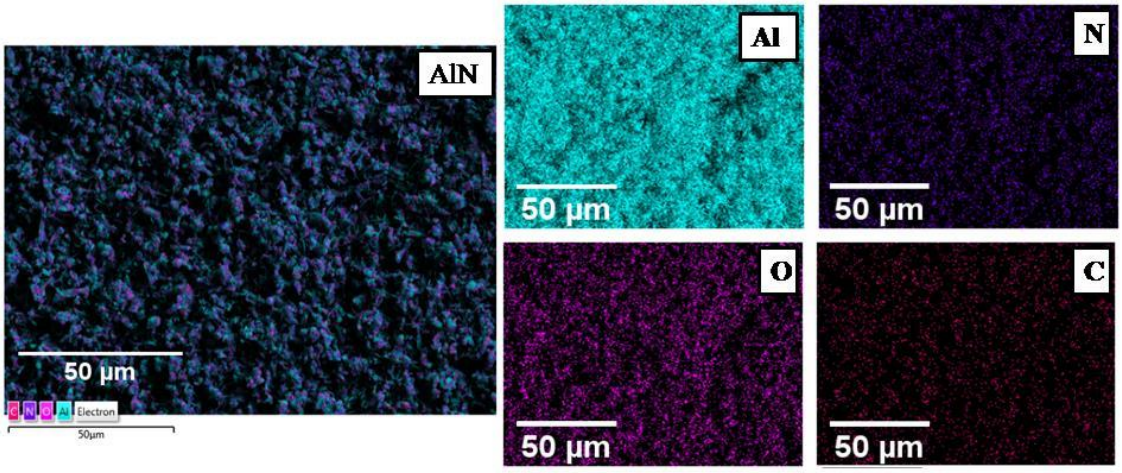

***Figure 6. 11*: Elemental mapping of the elements in the pure AlN ceramics, sintered at 1400 ℃.**

It is observed that no trace of other elements is detected except some amount of carbon present with the additive elements. Because of the higher temperature and high microwave power, densification occurs fast. The unique arrangement helps to avoid the direct contact of carbon with samples protected from porosity and yields good density at a lower sintering temperature than in conventional sintering. This study shows that the maximum density and phase of pure ceramics can be obtained from this technique.

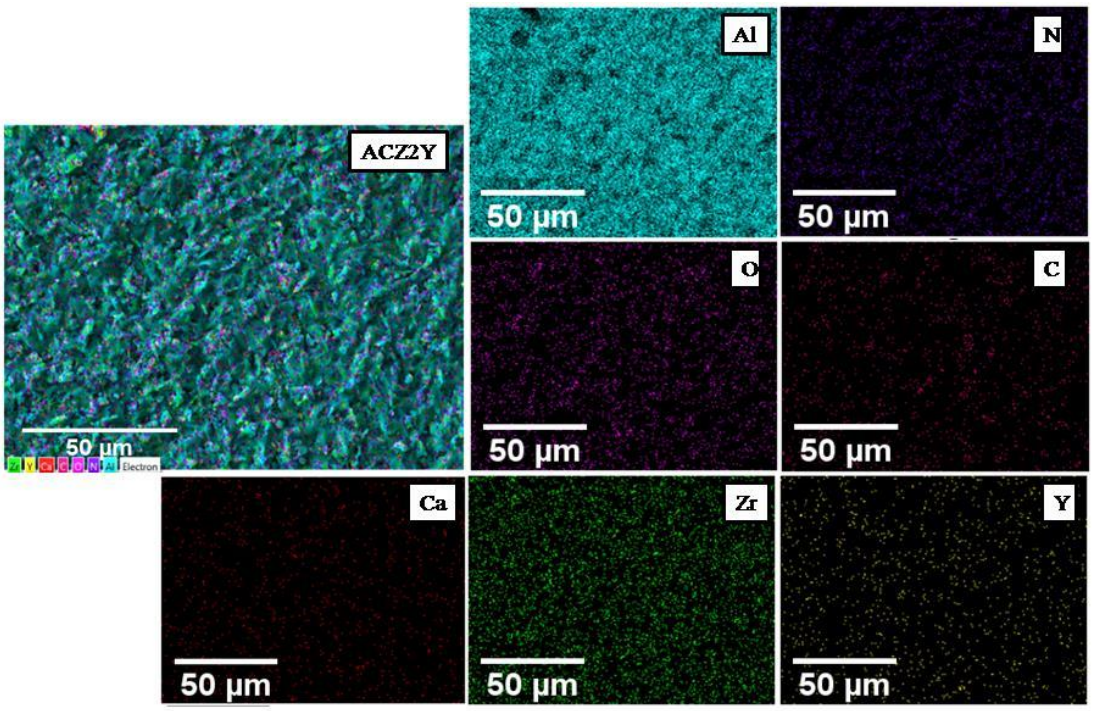

***Figure 6. 12*: Elemental mapping of the best additive AlN ceramics (ACZ2Y) sintered at 1400 ℃.**

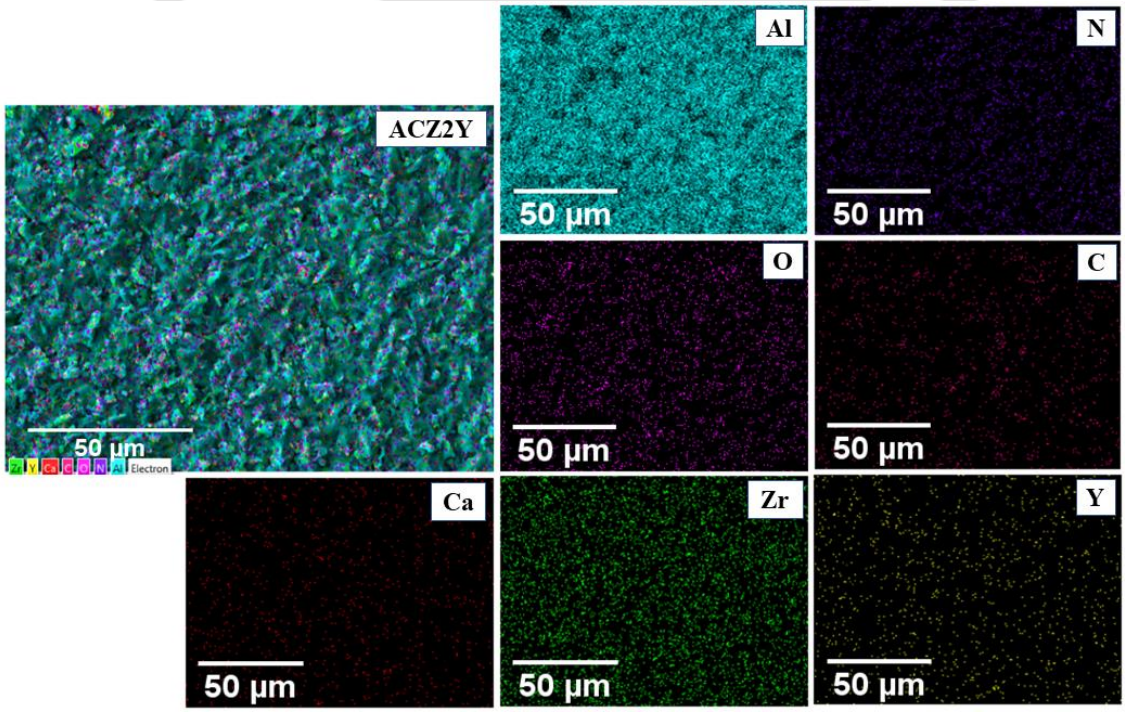

***Figure 6. 13*: Elemental mapping of the additive AlN ceramics (ACZ2Y) sintered at 1700 ℃ in conventional sintering method.**

Further, the initial powder contained little oxygen and carbon atoms on the AlN surface due to the preparation process of the powder sample. Hence, the sintered samples did not show any abnormal behavior in this process. In addition, carbon in the susceptor bed did not promote porosity and oxidation during the sintering process. In this process, carbon is not in direct contact with the sample. Further, to confirm the distribution of the elements over the sample, the elemental mapping of these two samples performed and are depicted in Figures 6.11 and 6.12, accordingly. The elements distribution present in the best AlN composite ACZ2Y sintered in the conventional sintering method at 1700 ℃ is shown in Figure 6.13. It is observed that the elements present in all the samples are distributed uniformly.

6.5.5 Dielectric properties:

Pure and additive AlN samples of dimension 10 mm diameter and 1 mm thickness sintered at 1700 ℃ for 20 h are considered for dielectric properties analysis. The sintered samples are polished and coated with silver as an electrode on the top and bottom surfaces and then carried out for dielectric analysis. All conventional and microwave-sintered samples' dielectric permittivity is shown in Figure 6.14 and Figure 6.15, respectively, and the dissipation factor is shown in Figures 6.16 and 6.17, respectively. Dielectric permittivity for pure AlN ceramics sintered in conventional sintering ranges from 6.60 to 6.97; ACZ2Y ranges from 7.99 to 8.61 for best composition. ACZ2Y exhibits higher dielectric permittivity values than other composites and pure AlN ceramics. The pure AlN sample shows a slightly increased rate of increasing dielectric permittivity from 6.60 to 6.97 with a minimum 0.37 difference between the minimum and maximum. Other additive composite shows constant dielectric permittivity approximately with a low rate of increase with a 0.5-1.0 difference between the minimum and maximum for the temperature variation from -140 ℃ to 200 ℃ due to grain and grain boundaries (see Figure 6.11).

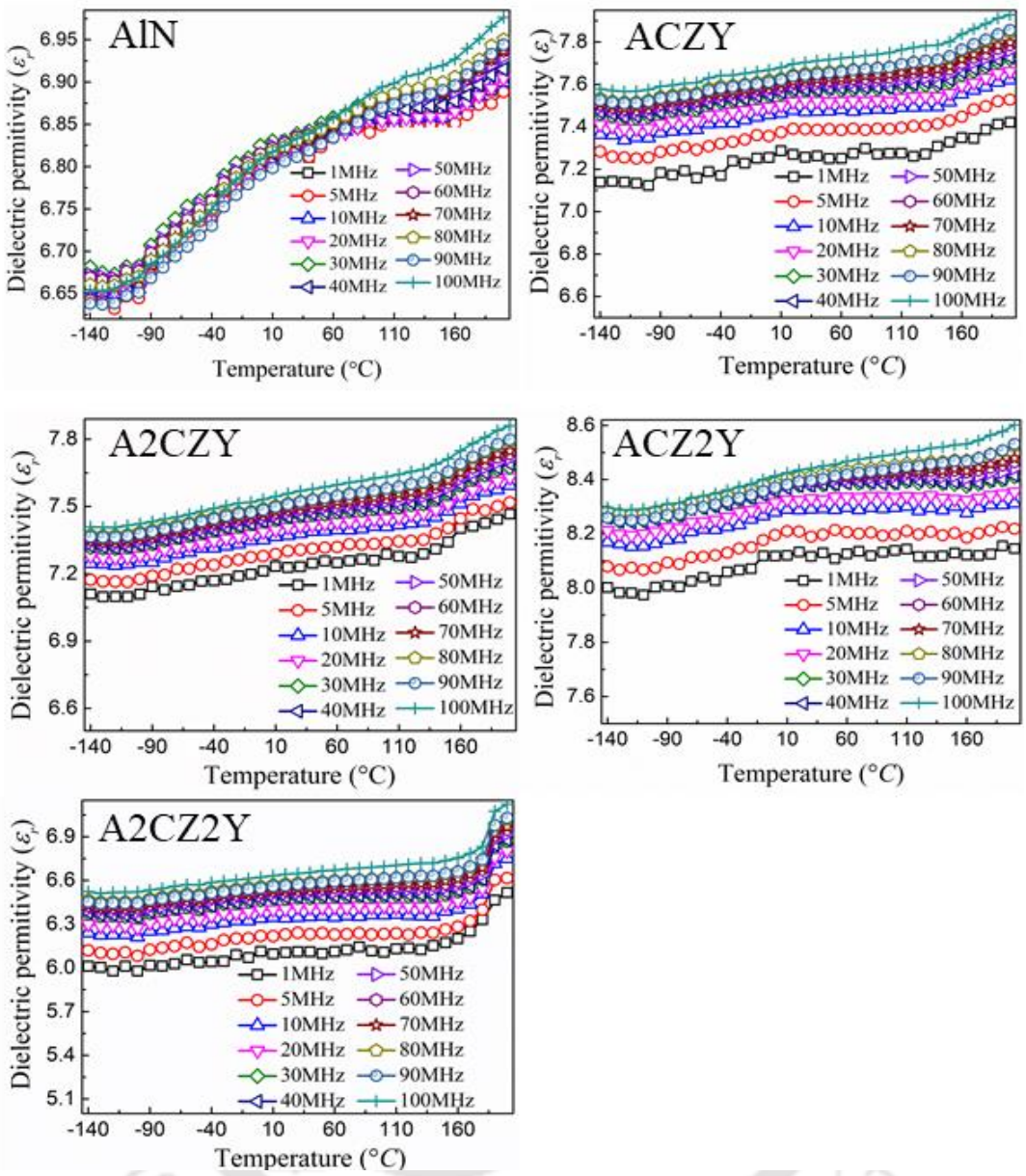

***Figure 6. 14*: Dielectric permittivity of pure and additive AlN ceramics sintered conventional sintering as a function of temperature (-140 to 200 ℃) measured at various frequencies (1 MHz to 100 MHz).**

The dissipation factor of the best sample ACZ2Y sample shows lower values from (0.12 – 5.21) x 10^{-2} than all other composites. The dissipation factor of all sintered samples showed very low values in the order of 10^{-2} and is almost constant without drastic changes by varying temperatures from -140 ℃ to 200 ℃.

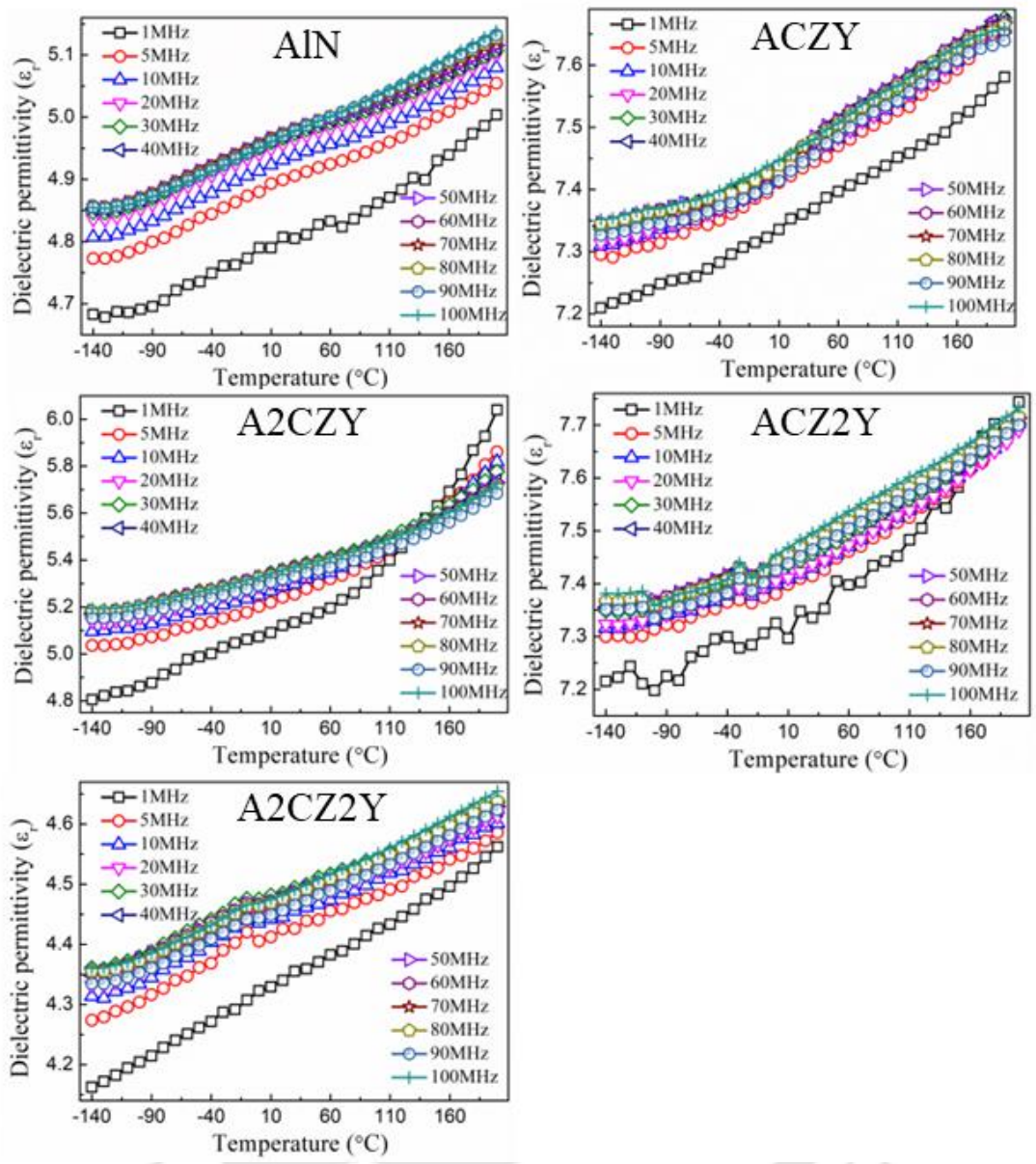

***Figure 6. 15*: The Dielectric permittivity of pure and additive-added AlN microwave sintered ceramics measured as a function of temperatures from -140 to 200 ℃ at various frequencies (1 MHz to 100 MHz).**

Pure and additive AlN composite ceramics sintered in microwave sintering method at 1400 ℃ for 30 min considered for dielectric measurements by varying temperatures from -140 ℃ to 200 ℃. The dielectric permittivity and dissipation factor changing the temperature at various frequencies from 1 MHz to 100 MHz are measured for all sintered pure and additive AlN ceramics sintered in microwave sintering method are shown in Figure 6.15 and Figure

6.17. The dielectric permittivity of pure AlN ceramics sintered in the microwave sintering method is 4.67 - 5.15 by varying temperature range -140 to 200 ℃ at various frequencies from 1 MHz to 100 MHz. The dielectric permittivity for ACZY composite ceramic is 7.22-7.69, and for A2CZY composite is 4.80-6.09.

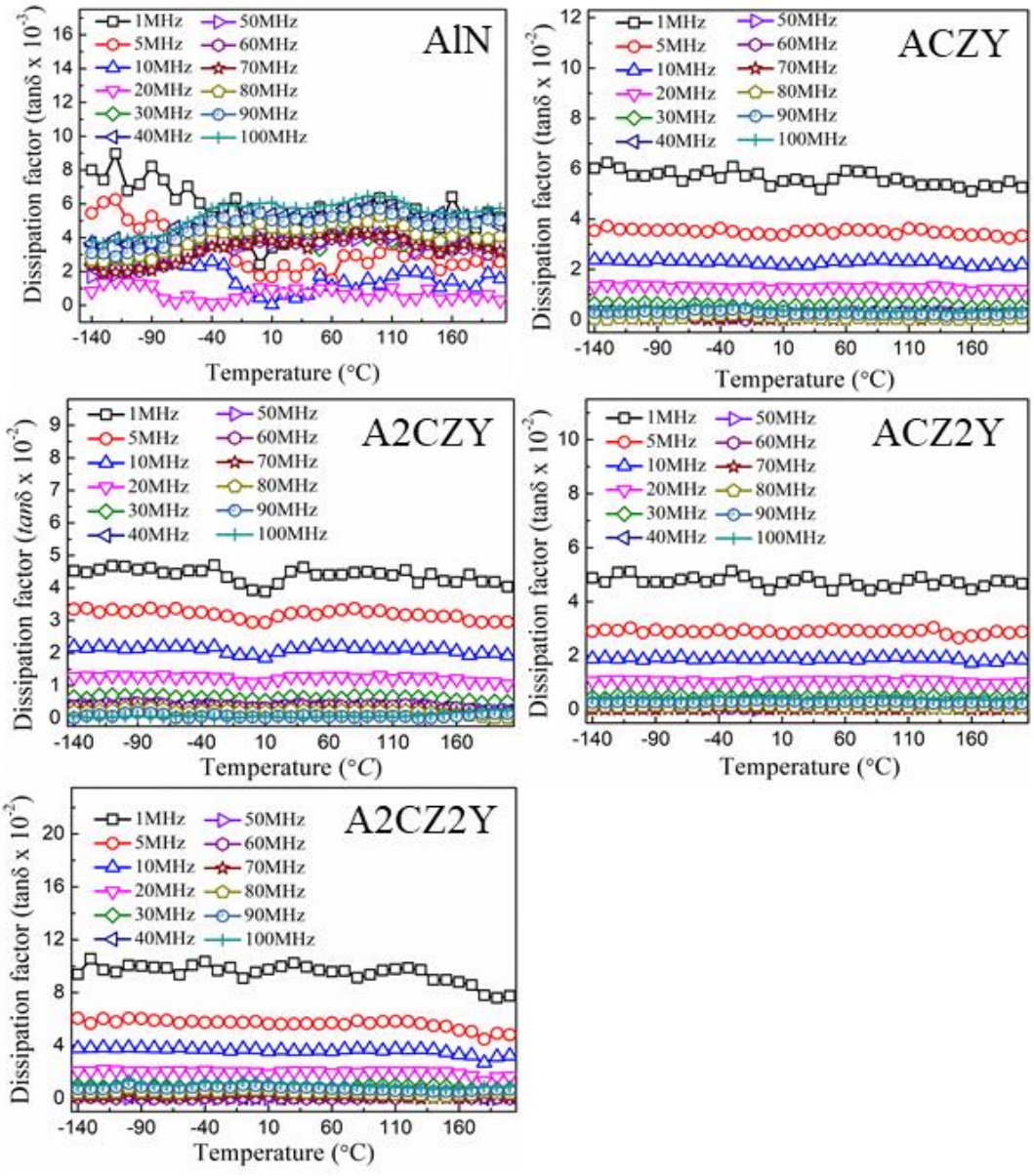

***Figure 6. 16*: The dissipation factor of pure and additive added AlN conventionally sintered ceramics with varying temperatures (-140 to 200 ℃) measured at various frequencies (1 MHz to 100 MHz).**

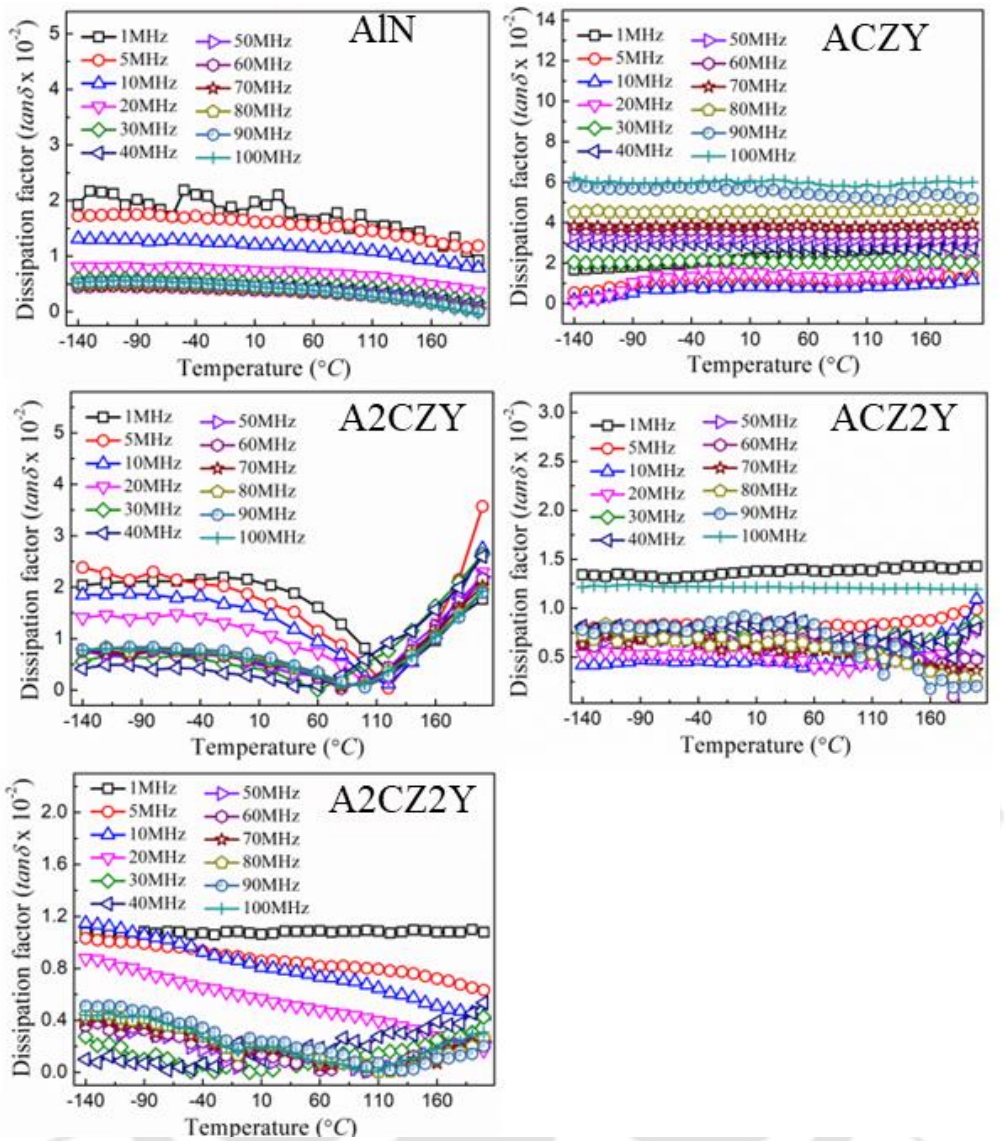

***Figure 6. 17*: The dissipation factor of pure and additive added AlN microwave sintered ceramics with varying temperatures (-140 to 200 ℃) measured at various frequencies (1 MHz to 100 MHz).**

The dielectric permittivity of ACZ2Y is in the range 7.20-7.96; for A2CZ2Y, ceramic dielectric permittivity is in the range 4.11-4.67 (see Figure 6.15) respectively by varying temperature -140 to 200 ℃ at various frequencies from 1 MHz to 100 MHz. All the sample exhibited constant dielectric permittivity with a minimal increasing value of 0.4-1.2 by increasing temperature. This increment in dielectric permittivity by increasing temperature is due to thermally activated charges. The dielectric permittivity of all the sintered samples shows

approximately relative values with a small increment by varying frequency from 1 MHz to 100 MHz due to the sample's space charge and dipolar polarization. The dissipation factor for pure AlN ceramics is $0.11 \times 10^{-2} \leq \tan\delta \leq 2.23 \times 10^{-2}$, ACZY composite ceramic is $0.03 \times 10^{-2} \leq \tan\delta \leq 6.12 \times 10^{-2}$, A2CZY composite $0.02 \times 10^{-2} \leq \tan\delta \leq 3.71 \times 10^{-2}$, ACZ2Y $0.31 \times 10^{-2} \leq \tan\delta \leq 1.37 \times 10^{-2}$, and for A2CZ2Y $0.21 \times 10^{-2} \leq \tan\delta \leq 1.19 \times 10^{-2}$ (see Figure 6.17) respectively by varying temperature -140 to 200 ℃ at various frequencies from 1 MHz to 100 MHz. The A2CZY sample shows a small fluctuation in the temperature range of 60-120 ℃ (see Figure 6.17) might be due to polarization relaxations; consequently, at a similar temperature range, the dielectric permittivity also fluctuates (see Figure 6.15). The best composite ACZ2Y ceramic sintered in conventional sintering shows a dielectric permittivity of $7.99 \leq \varepsilon_r \leq 8.61$ and $0.12 \times 10^{-2} \leq \tan\delta \leq 5.21 \times 10^{-2}$ and for the composite sintered in microwave sintering exhibited as $7.20 \leq \varepsilon_r \leq 7.96$ and $0.31 \times 10^{-2} \leq \tan\delta \leq 1.37 \times 10^{-2}$. The obtained dielectric properties are in good agreement with the previously reported values [205]. Due to the compactness, the dielectric permittivity of the samples sintered in conventional sintering is higher than that of the samples sintered in microwave sintering. The microwave-sintered sample exhibits lower dielectric permittivity with a lower dissipation factor than the sample sintered in conventional Sintering.

6.5.6 Microwave dielectric properties:

The microwave dielectric properties of sintered pure and additives added AlN ceramics are studied by using a vector network analyzer (VNA) using the Krupka resonator cavity at 12 GHz, RT. The dielectric constant and loss tangent values calculated for pure AlN ceramics are shown in Figure 6.18. The high dielectric constant ($\varepsilon_r = 8.04$) and low loss tangent ($\tan\delta = 2.804 \times 10^{-3}$) are obtained for AlN ceramics, sintered at 1400 ℃ with dwelling time 35 min. It is found that the dielectric constant of AlN ceramics is improved by the rise in sintering

temperature from 1200 ℃ to 1400 ℃ with a dwelling time of 35 min, and decreasing further increase in dwelling time to 60 min at 1400 ℃. The dielectric constant and loss tangent values of AlN ceramics added with different additives are shown in Figure 6.19. This result reveals that additive AlN ceramics show the best dielectric properties compared to pure AlN ceramics due to enhanced density by adding the additive.

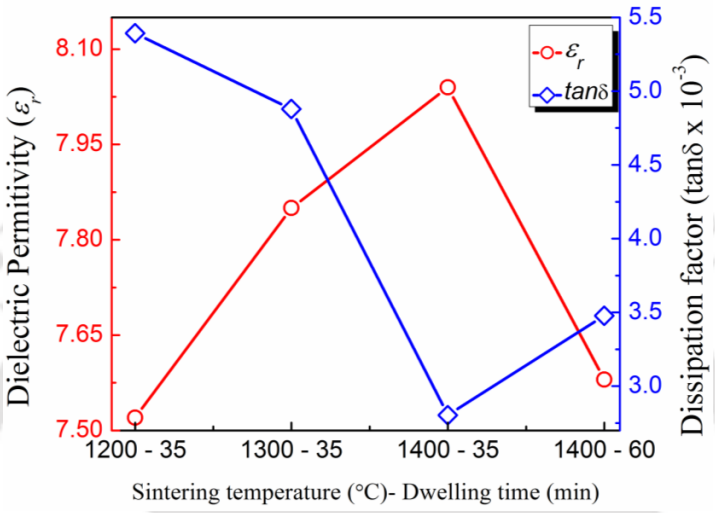

Figure 6. 18: The dielectric permittivity and dissipation factor variation of pure AlN ceramics sintered at different temperatures and dwelling times.

Surprisingly, the best dielectric permittivity ($\varepsilon_r = 9.02$) and low dissipation factor ($\tan\delta = 7.340 \times 10^{-4}$) is achieved by the 1 wt% of $CaZrO_3$, and 2 wt% of Y_2O_3 additive AlN ceramics and these values are in good agreement with the previously reported values [206]. This process achieved a low dielectric constant and low loss tangent, are enhanced as compared to the earlier studies [207]. The microwave dielectric properties are measured for conventionally sintered pure and additive AlN composites with $CaZrO_3$ and Y_2O_3. These measured values are compared with the microwave dielectric properties of the same composites sintered in the microwave sintering method and shown in Figure 6.20. The high ε_r with low $\tan\delta$ achieved in both methods by the same composite ACZ2Y ceramic (see Figure 6.20).

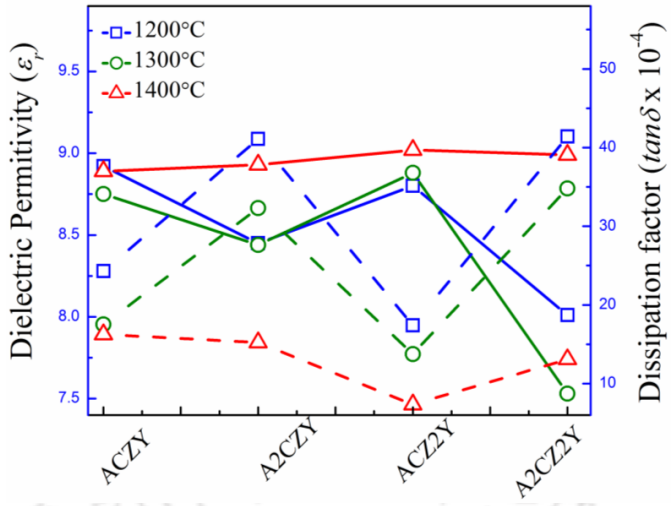

***Figure 6. 19*: Variation in dielectric constant and loss tangent value of additive added AlN ceramics, sintered at different sintering temperatures.**

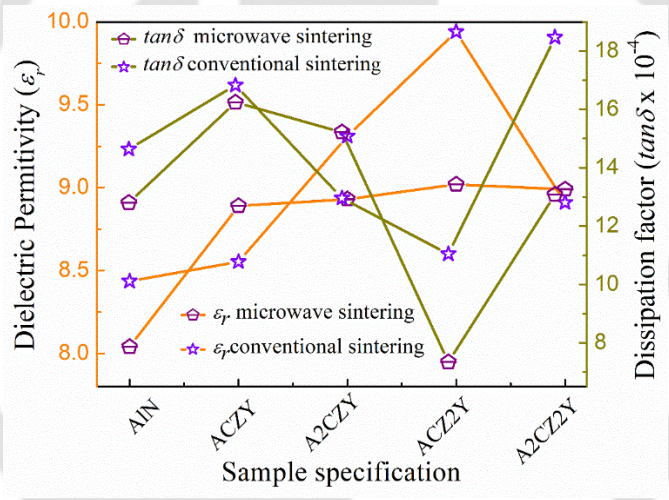

***Figure 6. 20*: Variation in dielectric constant and loss tangent value of additive added AlN ceramics, sintered using different sintering methods.**

The microwave dielectric properties of the best composite ACZ2Y ceramic, sintered in the conventional sintering method achieved a dielectric permittivity of 9.94 and a low dissipation factor of 11.05 x 10^{-4}. The ACZ2Y composite ceramic sintered in microwave sintering method with a dielectric permittivity of 9.02 and a low dissipation factor of 7.34 x 10^{-4} is better than the previously reported values [158, 208]. The dielectric losses are of two types: intrinsic and extrinsic; intrinsic losses are associated with the crystal structure of ceramics, and

extrinsic losses are due to dislocations, porosity, vacancies, and impurities [209]. In this study, the interaction with surroundings is less due to microwave sintering with a shorter duration. Hence, porosity and vacancies are decreased. Microwave susceptor bed prevents dislocations and impurities [210] (oxide form due to oxidation). Therefore, the obtained high dielectric constant and low loss tangent ACZ2Y (additive AlN ceramics) are suitable for RF-window applications.

6.5.7 Hardness measurement:

Vicker's hardness tester is used to measure the hardness of the sintered ceramics. In this hardness test, the indent is formed on the surface of the ceramics after applying the load by the right pyramid with a square base. The pyramid has an angle of 136° between opposite faces subjected to load. The two diagonals of the indentation are measured after removing the load using a microscope.

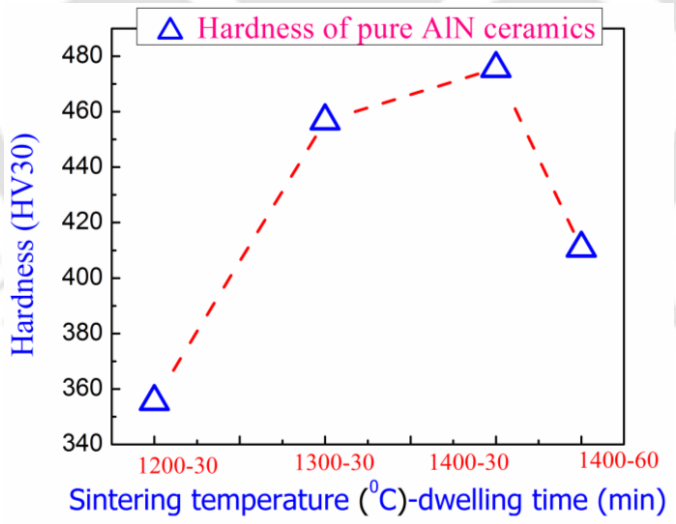

Figure 6. 21: Variation of hardness values of pure AlN ceramics measured as a function of sintering temperature and dwelling time.

The hardness value of the sintered AlN and additive AlN ceramics are calculated using the following relation [211];

$$HV = \frac{2F\ sin\frac{136^\circ}{2}}{d^2} = (1.8542)(\frac{F}{d^2}) \quad (6.6)$$

where HV is Vickers hardness, *F* is the load in kg *f*, and d is the average of two diagonals. The Vickers hardness values of pure AlN ceramics, sintered at different temperatures and dwelling times, are shown in Figure 6.21.

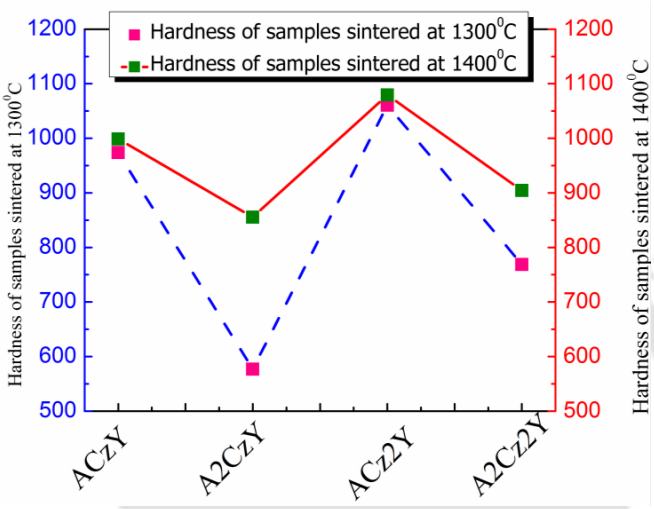

***Figure 6. 22*: Comparison of varying hardness values of AlN ceramics added with additives at two sintering temperatures.**

It conveys that the hardness of the ceramics improved by increasing the sintering temperature from 1200 ℃ to 1400 ℃ with a dwelling time 35 min, further increasing the dwelling time to 60 min at 1400 ℃ the hardness value is decreased (see Figure 6.21) and followed the similar response as density which shows its dependency on the relative density. The hardness (475.58 HV30) is obtained for pure AlN ceramics sintered at 1400 ℃ with 35 min dwelling time. The hardness of the additive-added AlN ceramics is shown in Figure 6.22. These values reveal that the hardness of additive AlN ceramics enhanced with an increase in the sintering temperature. It also shows that hardness varies by the additives' concentration. Surprisingly, the maximum hardness (1079.51 HV30) is achieved among all the additives AlN ceramics with 1 wt% $CaZrO_3$ and 2 wt% of Y_2O_3, sintered at 1400 ℃. The hardness of the

samples sintered in the conventional sintering method are measured and compared with that of the samples sintered in the microwave sintering method, as shown in Figure 6.23. The composite ACZ2Y exhibited high hardness (965.63 HV30) among all other composites and pure AlN ceramics.

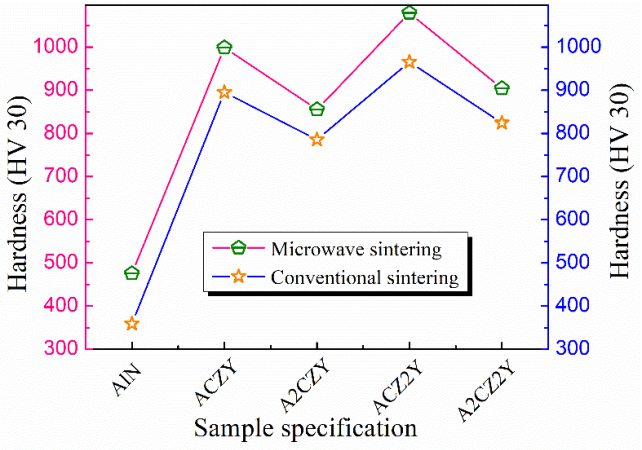

Figure 6. 23: Variation in hardness of pure and additive-added AlN ceramics, sintered using different sintering methods.

The hardness achieved by conventional sintering is lesser than that of the hardness values achieved by microwave sintering. The reason for decreasing the hardness in the samples sintered in conventional sintering might be due to grains and grain boundaries. These values reveal that the hardness of additive AlN ceramics enhanced with an increase in the sintering temperature. It also shows hardness variation by the additives' concentration. This increase in hardness by adding additives is due to an enhancement in density and occupying vacancies with additive elements.

6.6 Conclusion:

AIN ceramic comprises 1 wt% $CaZrO_3$ and 2 wt% of Y_2O_3 additive AlN (ACZ2Y) ceramics, sintered at 1400 ℃ with a dwelling time of 35 min having a relative density of 97.68% of the theoretical density. The same composite achieves a maximum density of 98.87%

sintered in conventional sintering, approximately similar with little more value than the sintered in microwave sintering method.

❖ Composite AlN ceramics achieved good dielectric properties with pure wurtzite AlN phase without any secondary phase such as alumina or other composites with additives. XRD spectra and Raman vibrational modes of all obtained composite AlN ceramics with $CaZrO_3$ and Y_2O_3 approve the resultant composite's purity.

❖ EDS spectra of best composite (ACZ2Y) AlN with $CaZrO_3$ and Y_2O_3 additive sintered in both methods show that pure AlN phase with minimal amount presented related to negligible additives does not affect the structural and dielectric properties of AlN ceramics.

❖ The microwave dielectric properties of the best composite ACZ2Y ceramic sintered in the conventional sintering method achieved dielectric properties as (ε_r) 9.94 and ($\tan\delta$) of 11.05 x 10^{-4}. ACZ2Y composite ceramic sintered in microwave sintering method as (ε_r) 9.02 and ($\tan\delta$) 7.34 x 10^{-4} at 12 GHz. The ceramics sintered in microwave sintered achieved a low dissipation factor with appropriate dielectric permittivity due to smaller grains and highly compacted densified structure with direct heating of microwave power.

❖ The maximum hardness (1079.51 HV30) is achieved by ACZ2Y composite AlN ceramic sintered in microwave sintering method higher than that of hardness 965.63 HV30 achieved by the same composite ceramic sintered in conventional sintering method. The low value of hardness in conventional sintering is due to grain size and compactness.

Chapter 7

Summary and Future Scope of Work

7.1 Summary

This chapter summarizes exciting results and highlights the present thesis work with conclusions. This thesis primarily focuses on nitride (AlN) ceramics preparation to achieve pure phase, discussion on structural and dielectric properties, which are highly interesting from the point of view of scientific research, microwave, and electronic industries. The fundamental aspects of RF-window with its requirements and basics of dielectrics with applications of nitride materials are presented in Chapter 1. The preparation of nitride ceramics in different methods, and characterization techniques are discussed in Chapter 2. In summary, the dielectric resonator (DR) of pure phase AlN ceramics have been prepared by conventional and studied the dielectric properties presented in Chapter 3. The effect of various additives such as oxides (rare earth oxides Er_2O_3, other oxides ZnO), nitride additives such as BN, some composites as $CaZrO_3$, Y_2O_3 their concentrations, processing parameters and its effect on crystal structure, microstructure, and microwave dielectric properties are studied systematically in chapter 4, 5, 6 respectively. Successful efforts are made to reduce the sintering temperature from 1900 to 1700 ℃ and to obtain pure-phase AlN ceramics without any secondary phases, such as alumina, without affecting microwave dielectric and dielectric properties. In the conventional sintering method, the powder bed with a combination of AlN powder and carbon powder plays an essential role in densifying AlN ceramics at low sintering temperatures and obtaining a pure phase. Summary of all results for optimized AlN and composite ceramics are listed in **Table 7.1**. A summary of the key results and significant findings are as follows;

***Table 7. 1*: The summary of all results for optimized AlN and its composite ceramics.**

Sample	χ^2	Relative density (%)	Sintering temperature / method	a=b (Å)	c (Å)	Dielectric permittivity (ε_r) at 12 GHz	Dissipation factor (tan δ) 12 GHz
AlN	2.32	95	1700 ℃ - 30h / conventional	3.113(2)	4.982(9)	8.83	21.69 x 10^{-4}
AlN-15ZnO	1.28	94.43	1700 ℃ - 20h / conventional	3.115(23)	4.986(65)	7.195	4.90 x 10^{-3}
AlN - 2Er_2O_3	2.52	94	1600 ℃ - 3h + 1700 ℃ - 3h / conventional	3.113 (18)	4.983 (27)	7.81	5.00 x 10^{-4}
AlN-15BN - 20h	1.26	94.45	1700 ℃ 20h / conventional	3.115(29) BN(2.524(10))	4.986(53) BN(6.679(08))	7.38	2.60 x 10^{-3}
AlN 2$CaZrO_3$ Y_2O_3	1.52	98.87	1700 ℃ - 20h / conventional	3.116 (28)	4.985 (53)	9.94	11.05 x 10^{-4}
	4.23	97.68	1400 ℃ - 30min – 35min / Microwave	3.113 (11)	4.981 (16)	8.04	2.80 x 10^{-3}

7.1.1 Pure AlN ceramics:

- AlN compacted Disks were immersed in a powder bed containing AlN powder surrounded by carbon powder to avoid oxidation. The powder bed has 70% AlN with 30% Carbon powder at the bottom and top as two layers. The compacted samples sintered at 1700 ℃ for 20 h show good density and structure. The sintering time and dwelling time are optimized from 1400-1700 ℃ and 5 h to 30 h dwelling time, respectively.
- This research obtained a new method to prepare AlN ceramics at low sintering temperatures by optimizing the sintering environment and conditions, such as in the presence of nitrogen, without a powder bed, and with a powder bed. The powder bed composition is also optimized in this process, such as with only AlN powder oxidation not

able to be avoided entirely and only with carbon powder bed; carbon powder enters into the grains of AlN and in the combination of AlN and carbon powder.

- In the optimized condition of powder bed used to sinter AlN ceramics with different dwelling periods and studied the effect of powder bed with the variation of dwelling time on structural, microstructural, dielectric, and microwave dielectric properties of AlN ceramics.
- The Rietveld refinement of the obtained XRD pattern of sintered samples confirms crystal structure as wurtzite with $P6_3mc$ space group and confirmed from the Raman spectrum by exhibiting the well-known six vibrational modes of wurtzite AlN.
- The temperature-dependent Raman spectrum shows that the obtained ceramics are highly stable in structure without any phase transformations at temperatures ranging from -196 ℃ to 400 ℃ by exhibiting six vibrational modes of wurtzite AlN at each temperature.
- The obtained AlN ceramics sintered at 1700 ℃ for 20 h achieved the best dielectric permittivity ($\varepsilon_r = 8.83$) with a low dissipation factor ($\tan\delta = 21.686 \times 10^{-4}$) at microwave frequencies. The obtained ceramics show good dielectric behavior at low frequencies (1 kHz to 1 MHz) at different temperatures ranging from 30-200 ℃. The broadband dielectric properties were also studied at temperatures ranging from -140 ℃ to 200 ℃ using liquid nitrogen.

7.1.2 Oxide additive AlN ceramics with Er_2O_3 and ZnO as additives:

- In this study, the effect of oxide additives on structural and dielectric properties of AlN ceramics was investigated systematically for transmitting a signal with high speed in electronic applications. Here, one rare earth oxide (Er_2O_3) and ZnO with a structure similar to AlN have been chosen as oxide additives.

- The obtained composite ceramics crystalline structure was identified by refinement of the XRD pattern and matches appropriately with JCPDS of card number 01-077-9871 of the wurtzite AlN phase. This result confirms that the AlN pure and composites (AlN-ZnO and AlN- Er_2O_3) form pure wurtzite structure without any secondary oxide phases such as ZnO, Er_2O_3, and typical secondary phase Al_2O_3 (alumina forms due to oxidation while sintering at high temperatures). The Raman spectrum of all sintered samples also confirms the wurtzite phase by exhibiting the known six vibrational modes of wurtzite AlN.

- The powder bed prevented the oxidation process due to the immersion of compacted samples in AlN powder, and the surroundings at the top and bottom covered with carbon powder and then at the top covered with AlN again. This powder bed arrangement doesn't allow the oxygen to enter the composites while sintering at high temperatures, and the environment flowing with nitrogen also helps control entering oxygen from outside.

- Both oxide composites (AlN-ZnO and AlN-Er_2O_3) show good dielectric properties with temperature variation at low frequencies. These oxide composites show the best dielectric properties at microwave frequencies as $\varepsilon_r = 7.810$ and $\tan\delta = 5.00 \times 10^{-4}$ for 2ErAlN composite ceramic, $\varepsilon_r = 7.195$ and $\tan\delta = 4.90 \times 10^{-3}$ for AlN-15ZnO composite ceramic.

- Considering these microwave dielectric properties of AlN-Er_2O_3 composite ceramics as input, the theoretical design was carried out for designing RF windows using CST software for spot frequency 3.7 GHz. The return loss and insertion loss are also optimized for the window of length 34.91 mm; the thickness and diameter of the AlN are 3 mm and 86 mm, respectively. The computed return loss and insertion loss are 61.25 dB and 0.009 dB, respectively.

7.1.3 Effect of nitride additives (BN) on structural and dielectric properties of AlN ceramics:

- In this study, an attempt has been made to synthesize AlN-BN composite ceramics in a conventional sintering method using a powder bed to understand the effect of nitride additives on the structural and dielectric properties of AlN ceramics.
- The AlN-BN composite ceramics are sintered at a low temperature of 1700 ℃ using a powder bed and obtained pure nitride ceramics with AlN and BN phases without any oxide phase as a secondary phase. AlN-xBN composite ceramics have an AlN phase matched with JCPDS card no: 00-066-0534 and a BN phase with JCPDS card no: 00-009-0012.
- The Rietveld refinement of the obtained XRD pattern of all composite ceramics confirms that the AlN present in the composite is a wurtzite crystal structure with $P6_3mc$ and space group number 186. The temperature Raman demonstrates vibrational modes at low and high temperatures stability of obtained AlN-15BN composite ceramic.
- The oxygen in the composite AlN-15BN ceramic is due to the contribution of surface oxygen and oxidized powder bed confirmed by the fitting of high-resolution XPS spectra of AlN-15BN composite ceramic.
- The dielectric properties of AlN-15BN composite ceramic were studied at different temperatures from 30-500 ℃, by varying frequencies from 1 kHz to 1 MHz and obtained as (ε_r = 6.50 - 7.48) and low dissipations factor ($\tan\delta$ = 0.2 x 10^{-3} - 9.8 x 10^{-3}). These obtained dielectric properties convey that AlN-BN composite ceramics are appropriate for electronic applications.
- The Cole-Cole plots of impedance spectra of all AlN-BN composite ceramics show non-Debye type relaxations. They are fitted with RCRCRC circuits corresponding to three parallelly connected R and C circuits connected in series corresponding to grain, grain boundary, and electrode.

- The obtained best microwave dielectric properties at 12GHz, such as ($\varepsilon_r = 7.381$) and ($\tan\delta = 2.603 \times 10^{-3}$) for AlN-15BN composite ceramics with pure nitride phase without any alumina or intermediate phases are appropriate for RF-window and electronic applications.

7.1.4 The Effect of the sintering method on structural and dielectric properties of AlN ceramics with additives $CaZrO_3$ and Y_2O_3:

- This study investigated the effect of the sintering method on the structural and dielectric properties of AIN ceramics by preparing AlN composites with $CaZrO_3$ and Y_2O_3 additives using conventional and microwave sintering methods. ACZ2Y (AIN ceramic comprises 1 wt% $CaZrO_3$ and 2 wt% of Y_2O_3 additive) ceramics, sintered at 1400 ℃ with a dwelling time of 35 min in microwave sintering method, achieved a relative density of 97.68% of the theoretical density. The same composite achieves a maximum density of 98.87% sintered in conventional Sintering at 1700 ℃ for 20 h. The achieved relative density is approximately similar with little more value than the composite relative density sintered in the microwave sintering method.
- The structure of sintered all composite ceramics in both methods is confirmed as wurtzite phase AlN with space group $P6_3mc$ by matching appropriately with standard JCPDS data with card no: 00-003-1144.
- The best composition ACZ2Y sample sintered in conventional sintering method exhibited phonon modes are 246.33 cm^{-1} (E_2 (Low)), 609.81 cm^{-1} (A_1 (TO)), 655.21 cm^{-1} (E_2 (High)), 668.81 cm^{-1} (E_1 (TO)), 902.67 cm^{-1} (A_1 (LO)) and 910.05 cm^{-1} (E_1 (LO)). The composite ceramic ACZ2Y sintered in microwave sintering method exhibited six vibrational modes as 247.48 cm^{-1}, 613.53 cm^{-1}, 657.69 cm^{-1}, 671.05 cm^{-1}, 900.31 cm^{-1}, and 909.98 cm^{-1} respectively.

- The best composite (ACZ2Y) AlN with $CaZrO_3$ and Y_2O_3 additive sintered in both methods show that pure AlN phase with minimal amount presented related to negligible additives revealed by EDS spectra. These minimal additive elements in the composite do not affect structural properties evident from XRD and Raman spectra.
- The conventional sintering method achieved dielectric properties as (ε_r) 9.94 and ($\tan\delta$) of 11.05 x 10^{-4} at 12 GHZ for ACZ2Y composite ceramic. The microwave dielectric properties as (ε_r) 9.02 and ($\tan\delta$) 7.34 x 10^{-4} at 12 GHz achieved the same composite sintered in the microwave sintering method.
- The maximum hardness (1079.51 HV30) is achieved by ACZ2Y composite AlN ceramic sintered in microwave sintering method higher than that of hardness 965.63 HV30 achieved by the same composite ceramic sintered in conventional sintering method. The low value of hardness in conventional Sintering is due to grain size and compactness.

7.2 Future scope of the work

In the present study, it has been observed that the powder bed method helped to obtain phase pure AlN ceramics with high density at lower sintering temperatures. These prepared pure AlN and its composites showed better structural, microstructural, dielectric, and microwave dielectric properties for pure and composite AlN ceramics. However, further studies are essential for the complete analysis of pure and additive AlN ceramics. Here, we proposed future work of the present study as follows;

- AlN ceramics, composite systems will be prepared with lower sintering temperatures, such as $BaZrO_3$, $BaSrTiO_3$, $CaTiO_3$, and KNN with rare earth oxides to minimize the sintering temperature and dwelling time while sintering for densifying. The effect of these additives makes AlN sinter at low temperatures with high density.

- The sintering method and parameters with the amount of additive to mix with AlN for suitable composite need to be optimized for obtaining phase pure AlN ceramics with good dielectric and thermal properties. AlN-KNN composite ceramics must be studied to improve piezoelectric properties with other properties of AlN ceramics.
- The composite ceramics with nitride additives such as GaN (Gallium nitride) and (Si_3N_4) silicon nitride need to be studied to obtain phase pure AlN ceramics with high thermal conductivity and improved dielectric properties. GaN has the same wurtzite structure; it may form good compatibility with the AlN structure to enhance the properties of AlN ceramics. AlN with carbide additives must be studied to avoid the alumina phase formation while sintering and obtain microwave-absorbing materials.
- We have focused on reducing sintering temperature and obtaining phase pure AlN ceramics with improved dielectric properties of pure and additive AlN ceramics with high density. The thermal conductivity of the AlN ceramics plays a vital role with its other properties in AlN applications, such as heat sinks, RF windows, and electronic applications. Hence, Thermal conductivity measurements of the prepared phase pure AlN ceramics will be helpful. The thermal conductivity of AlN ceramics with nitride additives compared with other oxide composites and corresponding dielectric properties at broadband frequencies will provide a complete study of AlN ceramics.
- Metallization of AlN ceramics is also essential to study for applications since it is used in RF windows, heat sinks, PCBs, etc., where metal contact is necessary. Metallization of AlN ceramics is essential to study the boning strength, the effect of thermal conductivity at the interface of ceramic and metal, and stresses induced at the interface of metal and ceramics with its impact on structural and thermal properties of AlN ceramics.
- AlN disc as RF window application in specified dimensions for magnetron applications needs to be fabricated. It is necessary to optimize the dimensions shape of RF window

effects in thermal and mechanical management of AlN in the magnetron or other devices theoretically and experimentally.

References

[1] Y. Saito, Surface Breakdown Phenomena in Alumina rf windows, IEEE Fiansactions Dielectr. Electr. Insul. 2 (1995).

[2] R.J. Bartkowski, E. Pekrul, M.F. Kirshner, High power aluminum nitride RF vacuum window, 5Th IEEE Int. Vac. Electron. Conf. IVEC 2004. (2004) 42. https://doi.org/10.1109/ivelec.2004.1316188.

[3] E. Savrun, V. Nguyen, D.K. Abe, High thermal conductivity aluminum nitride ceramics for high power microwave tubes, in: Third IEEE Int. Vac. Electron., 2002: pp. 34–35. https://doi.org/10.1109/IVELEC.2002.999246.

[4] R.J. Bartkowski, E. Pekrul, M.F. Kirshner, High power aluminum nitride RF vacuum window, in: IEEE Int. Vac. Electron Sources, 2006: pp. 33–34. https://doi.org/10.1109/ivelec.2004.1316188.

[5] J. Hillairet, J. Kim, N. Faure, J. Achard, Y.S. Bae, J.M. Bernard, L. Delpech, M. Goniche, S. Larroque, R. Magne, L. Marfisi, S. Park, S. Poli, N. Dechambre, K. Vulliez, Design and tests of 500 kW RF windows for the ITER LHCD system, Fusion Eng. Des. 94 (2015) 22–30. https://doi.org/10.1016/j.fusengdes.2015.02.065.

[6] Y.M. Jain, P.K. Sharma, H. V. Dixit, A. Jadhav, P. Parmar, Design and multiphysics analysis of a high power RF window for lhcd system of tokamaks, Prog. Electromagn. Res. Symp. 2017-Novem (2017) 2888–2894. https://doi.org/10.1109/PIERS-FALL.2017.8293626.

[7] T. Yunying, L. Fukun, W. Xiaojie, Design of 3.7GHz BeO Ceramic Window, Proc. 2nd Int. Conf. Model. Identif. Control. 119 (2015) 216–218. https://doi.org/10.2991/mic-

15.2015.49.

[8] V.E. Myasnikov, M. V Agapova, V.O. Nichiporenko, L.G. Popov, S. V Usachev, V.N. Iljin, V.A. Khmara, A.G. Litvak, G.G. Denisov, V.E. Zapevalov, V.A. Flyagin, A.S. Fix, V. V Alikaev, V.I. Iljin, IN 110- 170 GHz FREQUENCY RANGE, in: Electron. Radiophys. Ultra-High Freq., 1999: pp. 138–141.

[9] L. Hu, G. Ma, D. Sun, Q. Huang, T. Zhuo, S. Gong, Y. Jiang, Z. Zeng, Q. Ma, W. Lei, R. Song, P. Hu, X. Hu, Z. Guo, X. Ku, Z. Tan, C. Hongbin, F. Meng, System for Fusion Application, IEEE Trans. PLASMA Sci. 49 (2021) 1468–1474.

[10] M.R. Namordi, D.J. Coleman, Design Windows for Low-High-Low GaAs IMPATT's, IEEE Trans. Electron Devices. 27 (1980) 282–286. https://doi.org/10.1109/T-ED.1980.19851.

[11] M.M. and S.P.P. P.R. Tripathy, Dynamic properties and avalanche noise analysis of 4H-SiC over wz-GaN based IMPATTs at mm-wave window frequency, Semicond. Phys. Quantum Electron. Optoelectron. 14 (2011) 137–144. https://doi.org/10.15407/spqeo14.02.137.

[12] M. Thumm, A. Arnold, E. Borie, O. Braz, G. Dammertz, O. Dumbrajs, K. Koppenburg, M. Kuntze, G. Michel, B. Piosczyk, Frequency step-tunable (114-170 GHz) megawatt gyrotrons for plasma physics applications, Fusion Eng. Des. 53 (2001) 407–421. https://doi.org/10.1016/S0920-3796(00)00519-6.

[13] O. Braz, G. Dammertz, M. Kuntze, M. Thumm, D-band frequency step-tuning of a 1 MW gyrotron using a brewster output window, Int. J. Infrared Millimeter Waves. 18 (1997) 1465–1477. https://doi.org/10.1007/BF02678305.

[14] P. Anilkumar, D. Pamu, T. Tiwari, EM-Thermo-Mechanical Investigations on Pillbox

RF Window for 5 kW S-Band Microwave Tubes, IEEE Trans. Electron Devices. 69 (2022) 7046–7052. https://doi.org/10.1109/TED.2022.3215618.

[15] K.A. Korolev, S. Chen, M.N. Afsar, Complex magnetic permeability and dielectric permittivity of ferrites in millimeter waves, IEEE Trans. Magn. 44 (2008) 435–437. https://doi.org/10.1109/TMAG.2008.916033.

[16] R.W. McMillan, Near-Millimeter-Wave Sources of Radiation, Proc. IEEE. 73 (1985) 86–108. https://doi.org/10.1109/PROC.1985.13112.

[17] M.K. Alaria, N. Singh, A. Bera, RF characterization of Cavity and Window for Gyro-devices, 2021 IEEE MTT-S Int. Microw. RF Conf. IMARC 2021. (2021) 1–3. https://doi.org/10.1109/IMaRC49196.2021.9714614.

[18] G. Gantenbein, A. Samartsev, G. Aiello, G. Dammertz, J. Jelonnek, M. Losert, A. Schlaich, T.A. Scherer, D. Strauss, M. Thumm, D. Wagner, First operation of a step-frequency tunable 1-MW gyrotron with a diamond brewster angle output window, IEEE Trans. Electron Devices. 61 (2014) 1806–1811. https://doi.org/10.1109/TED.2013.2294739.

[19] S. Kesari, V; Singh, A; Seshadri, R; Kamath, Boron Nitride and Sapphire Windows for, IEEE Trans. Electron Devices. 63 (2016) 1–5.

[20] J.M. Dutta, G. Yu, C.R. Jones, Loss properties of SiC at millimeter wavelengths, Jt. 30th Int. Conf. Infrared Millim. Waves 13th Int. Conf. Terahertz Electron. 2005. IRMMW-THz 2005. 1 (2005) 213–214. https://doi.org/10.1109/icimw.2005.1572484.

[21] C.H. Du, T.H. Chang, P.K. Liu, Y.C. Huang, P.X. Jiang, S.X. Xu, Z.H. Geng, B.L. Hao, L. Xiao, G.F. Liu, Z. Di Li, S.H. Shi, Design of a W-band gyro-TWT amplifier with a lossy ceramic-loaded circuit, IEEE Trans. Electron Devices. 60 (2013) 2388–2394.

https://doi.org/10.1109/TED.2013.2264100.

[22] S.A. S. Michizono, Y. Saito, S. Yamaguchi, Dielectric Materials for Use as Output Window in High-power Klystrons, IEEE Trans. Electr. Insul. 28 (1993) 692–699. https://doi.org/10.1109/14.231552.

[23] M.K. Alaria, S. Das, A. Sinha, M.T. Area, Design of RF Window for 42 GHz, 200kW Gyrotron, Int. J. Microw. Opt. Technol. 5 (2010) 66–68.

[24] T. Terai, T. Kobayashi, T. Mitsuyama, T. Yoneoka, S. Tanaka, Fabrication and properties of Al2O3 and AlN coatings for fusion reactor blanket by sputtering method, Surf. Coatings Technol. 106 (1998) 18–22. https://doi.org/10.1016/S0257-8972(98)00486-1.

[25] U. Singh, N. Kumar, H. Khatun, N. Kumar, V. Yadav, A. Kumar, M. Sharma, M. Alaria, A. Bera, P.K. Jain, A.K. Sinha, Design of 42 GHz gyrotron for Indian fusion tokamak system, Fusion Eng. Des. 88 (2013) 2898–2906. https://doi.org/10.1016/j.fusengdes.2013.06.001.

[26] J. Xi, B. Liu, Y. Zhang, W.J. Weber, Ab initio molecular dynamics simulations of AlN responding to low energy particle radiation, J. Appl. Phys. 123 (2018). https://doi.org/10.1063/1.5009750.

[27] B. Reinhardt, J. Daw, B.R. Tittmann, Irradiation Testing of Piezoelectric (Aluminum Nitride, Zinc Oxide, and Bismuth Titanate) and Magnetostrictive Sensors (Remendur and Galfenol), IEEE Trans. Nucl. Sci. 65 (2018) 533–538. https://doi.org/10.1109/TNS.2017.2775163.

[28] S. Yin, K.J. Tseng, J. Zhao, Design of AlN-based micro-channel heat sink in direct bond copper for power electronics packaging, Appl. Therm. Eng. 52 (2013) 120–129.

https://doi.org/10.1016/j.applthermaleng.2012.11.014.

[29] S.D. Ekpe, F.J. Jimenez, S.K. Dew, Effect of process conditions on the microstructural formation of dc reactively sputter deposited AlN, J. Vac. Sci. Technol. A Vacuum, Surfaces, Film. 28 (2010) 1210–1214. https://doi.org/10.1116/1.3478670.

[30] X.L. Li, H.A. Ma, Y.J. Zheng, Y. Liu, G.H. Zuo, W.Q. Liu, J.G. Li, X. Jia, AlN ceramics prepared by high-pressure sintering with La2O3 as a sintering aid, J. Alloys Compd. 463 (2008) 412–416. https://doi.org/10.1016/j.jallcom.2007.09.050.

[31] N. Kietipaisalsophon, W. Bunjongpru, W. Techitdheera, J. Nukeaw, Structure properties of cubic-AIN grown by reactive gas-timing RF magnetron sputtering, Proc. IEEE Int. Conf. Ind. Technol. 2 (2002) 1365–1367. https://doi.org/10.1109/ICIT.2002.1189378.

[32] S. Mohri, T. Yoshitake, T. Hara, K. Nagayama, Growth of metastable cubic AlN by reactive pulsed laser deposition, Diam. Relat. Mater. 17 (2008) 1796–1799. https://doi.org/10.1016/j.diamond.2008.01.073.

[33] J. Kuang, C. Zhang, X. Zhou, Q. Liu, C. Ye, Formation and characterization of cubic AlN crystalline in a carbothermal reduction reaction, Mater. Lett. 59 (2005) 2006–2010. https://doi.org/10.1016/j.matlet.2005.02.039.

[34] Y. Ueda, T. Daio, T. Yoshida, H. Akamine, A. Tominaga, T. Okajima, T. Yoshitake, Crystalline-structural evaluations of cubic AlN thin films heteroepitaxially grown on sapphire (0001) by pulsed laser deposition, Jpn. J. Appl. Phys. 52 (2013). https://doi.org/10.7567/JJAP.52.08JE03.

[35] Y. Fu, X. Li, Y. Wang, H. He, X. Shen, Structural, optical and electrical properties of cubic AlN films deposited by laser molecular beam epitaxy, Appl. Phys. A Mater. Sci. Process. 106 (2012) 937–940. https://doi.org/10.1007/s00339-011-6713-5.

[36] G.F. Iriarte, J. Bjurström, J. Westlinder, F. Engelmark, I. V. Katardjiev, Synthesis of C-axis-oriented AlN thin films on high-conducting layers: Al, Mo, Ti, TiN, and Ni, IEEE Trans. Ultrason. Ferroelectr. Freq. Control. 52 (2005) 1170–1174. https://doi.org/10.1109/TUFFC.2005.1504003.

[37] R.D. Richtmyer, Dielectric resonators, J. Appl. Phys. 10 (1939) 391–398. https://doi.org/10.1063/1.1707320.

[38] I.M. Reane, D. Iddles, Microwave dielectric ceramics for resonators and filters in mobile phone networks, J. Am. Ceram. Soc. 89 (2006) 2063–2072. https://doi.org/10.1111/j.1551-2916.2006.01025.X.

[39] V.Q. Nguyen, J.S. Sanghera, I.K. Lloyd, I.D. Aggarwal, D. Gershon, Room temperature dielectric properties of the As40S(60-x)Sex glass system, J. Non. Cryst. Solids. 276 (2000) 151–158. https://doi.org/10.1016/S0022-3093(00)00278-7.

[40] T.W. Dakin, Conduction and polarization mechanisms and trends in dielectric, IEEE Electr. Insul. Mag. 22 (2006) 11–28. https://doi.org/10.1109/MEI.2006.1705854.

[41] M. Rinaldi, C. Zuniga, C. Zuo, G. Piazza, Super-High-Frequency Two-Port AlN Applications, IEEE Trans. Ultrason. Ferroelectr. Freq. Control. 57 (2010) 38–45.

[42] H.P. Loebl, M. Klee, C. Metzmacher, W. Brand, R. Milsom, P. Lok, Piezoelectric thin AlN films for bulk acoustic wave (BAW) resonators, Mater. Chem. Phys. 79 (2003) 143–146. https://doi.org/10.1016/S0254-0584(02)00252-3.

[43] J. Zou, C.M. Lin, C.S. Lam, A.P. Pisano, Transducer design for AlN Lamb wave resonators, J. Appl. Phys. 121 (2017). https://doi.org/10.1063/1.4979914.

[44] J.G. Rodríguez-Madrid, G.F. Iriaróte, J. Pedros, O.A. Williams, D. Brink, F. Calle,

Super-high-frequency SAW resonators on AlN/diamond, IEEE Electron Device Lett. 33 (2012) 495–497. https://doi.org/10.1109/LED.2012.2183851.

[45] C. Zuo, N. Sinha, G. Piazza, Very high frequency channel-select MEMS filters based on self-coupled piezoelectric AlN contour-mode resonators, Sensors Actuators, A Phys. 160 (2010) 132–140. https://doi.org/10.1016/j.sna.2010.04.011.

[46] M.B. Assouar, M. El Hakiki, O. Elmazria, P. Alnot, C. Tiusan, Synthesis and microstructural characterisation of reactive RF magnetron sputtering AlN films for surface acoustic wave filters, Diam. Relat. Mater. 13 (2004) 1111–1115. https://doi.org/10.1016/j.diamond.2003.11.064.

[47] R. Lanz, P. Muralt, Solidly mounted BAW filters for 8 GHz based on AlN thin films, Proc. IEEE Ultrason. Symp. 1 (2003) 178–181. https://doi.org/10.1109/ultsym.2003.1293383.

[48] M.I. Den Hertog, F. González-Posada, R. Songmuang, J.L. Rouviere, T. Fournier, B. Fernandez, E. Monroy, Correlation of polarity and crystal structure with optoelectronic and transport properties of GaN/AlN/GaN nanowire sensors, Nano Lett. 12 (2012) 5691–5696. https://doi.org/10.1021/nl302890f.

[49] C. Giordano, I. Ingrosso, M.T. Todaro, G. Maruccio, S. De Guido, R. Cingolani, A. Passaseo, M. De Vittorio, AlN on polysilicon piezoelectric cantilevers for sensors/actuators, Microelectron. Eng. 86 (2009) 1204–1207. https://doi.org/10.1016/j.mee.2008.12.075.

[50] X. Le, L. Peng, J. Pang, Z. Xu, C. Gao, J. Xie, Humidity sensors based on AlN microcantilevers excited at high-order resonant modes and sensing layers of uniform graphene oxide, Sensors Actuators, B Chem. 283 (2019) 198–206.

https://doi.org/10.1016/j.snb.2018.12.021.

[51] X.H. Wang, X.L. Wang, C. Feng, C.B. Yang, B.Z. Wang, J.X. Ran, H.L. Xiao, C.M. Wang, J.X. Wang, Hydrogen sensors based on AlGaN/AlN/GaN HEMT, Microelectronics J. 39 (2008) 20–23. https://doi.org/10.1016/j.mejo.2007.10.022.

[52] E.F. McCullen, H.E. Prakasam, W. Mo, R. Naik, K.Y.S. Ng, L. Rimai, G.W. Auner, Electrical characterization of metal/AlN/Si thin film hydrogen sensors with Pd and Al gates, J. Appl. Phys. 93 (2003) 5757–5762. https://doi.org/10.1063/1.1563312.

[53] L. Trinkler, B. Berzina, Localised transitions in luminescence of AlN ceramics, Radiat. Meas. 71 (2014) 232–236. https://doi.org/10.1016/j.radmeas.2014.02.016.

[54] I.D. Breev, A.N. Anisimov, A.A. Wolfson, O.P. Kazarova, E.N. Mokhov, Raman Scattering in AlN Crystals Grown by Sublimation on SiC and AlN Seeds, Semiconductors. 53 (2019) 1558–1561. https://doi.org/10.1134/S1063782619110034.

[55] V.S. Kudyakova, V. V. Bannikov, A.A. Elagin, R.A. Shishkin, M. V. Baranov, A.R. Beketov, Gas-phase synthesis of hexagonal and cubic phases of aluminum nitride: A method and its advantages, Tech. Phys. Lett. 42 (2016) 260–262. https://doi.org/10.1134/S106378501603010X.

[56] C.S.C. and A.P. Agrawal, Fine Line Thin Dielectric Circuit Board Characterization, in: 44th Electron. Components Technol. Conf. IEEE, 1994: pp. 564–569.

[57] H. Tian, J. Zheng, L. Liu, H. Wu, H. Kimura, Y. Lu, Z. Yue, Structure characteristics and microwave dielectric properties of Pr2(Zr1−xTix)3(MoO4)9 solid solution ceramic with a stable temperature coefficient, J. Mater. Sci. Technol. 116 (2022) 121–129. https://doi.org/10.1016/j.jmst.2021.10.051.

[58] C. Feng, X. Zhou, B. Tao, H. Wu, S. Huang, Crystal structure and enhanced microwave dielectric properties of the Ce2[Zr1−x(Al1/2Ta1/2)x]3(MoO4)9 ceramics at microwave frequency, J. Adv. Ceram. 11 (2022) 392–402. https://doi.org/10.1007/s40145-021-0541-7.

[59] X. Zhou, L. Liu, J. Sun, N. Zhang, H. Sun, H. Wu, W. Tao, Effects of (Mg1/3Sb2/3)4+ substitution on the structure and microwave dielectric properties of Ce2Zr3(MoO4)9 ceramics, J. Adv. Ceram. 10 (2021) 778–789. https://doi.org/10.1007/s40145-021-0472-3.

[60] J. Katsutoshi Komeya, Oiso; Akihiko Tsuge, Yokohama; Hiroshi Inoue, Kawasaki, SINTERED BODIES OF ALUMINUM NTRIDE United States Patent (19) 4,435,513, 1984.

[61] H. Fritz Aldinger, Rodenbach; Richard Keilberth, Kleinheubach; Waltraud Werdecker, LOW-CONTAMINATION ALN CRUCIBLE FOR MONOCRYSTAL PULLING AND METHOD, 1985.

[62] C.Y. Hsieh, C.N. Lin, S.L. Chung, J. Cheng, D.K. Agrawal, Microwave sintering of AlN powder synthesized by a SHS method, J. Eur. Ceram. Soc. 27 (2007) 343–350. https://doi.org/10.1016/j.jeurceramsoc.2006.03.003.

[63] J. Cheng, D. Agrawal, Y. Zhang, R. Roy, Development of translucent aluminum nitride (AIN) using microwave sintering process, J. Electroceramics. 9 (2002) 67–71. https://doi.org/10.1023/A:1021646219797.

[64] F. Masahiro Uda, Tokyo; Katsuhisa Ohsaki, Matsudo; Yoshikazu Morita, United States Patent (19), Patent number: 5,167,944_METHOD FOR THE PRODUCTION OF ALUMINUM NITRIDE-BASED SINTERED PRODUCTS, 1992.

[65] J. Wang, X. Jia, C. Jia, G. Dong, Y. Zhang, L. Jia, Dielectric properties of spark plasma sintering AlN-W composite ceramics, Rare Met. 30 (2011) 633–638. https://doi.org/10.1007/s12598-011-0441-z.

[66] T. Belin, F. Epron, Characterization methods of carbon nanotubes: A review, Mater. Sci. Eng. B Solid-State Mater. Adv. Technol. 119 (2005) 105–118. https://doi.org/10.1016/j.mseb.2005.02.046.

[67] M.J. Li, L.M. Zhang, Q. Shen, T. Li, M.Q. Yu, Microstructure and properties of spark plasma sintered AlN ceramics, J. Mater. Sci. 41 (2006) 7934–7938. https://doi.org/10.1007/s10853-006-0862-5.

[68] H.M. Lee, D.K. Kim, High-strength AlN ceramics by low-temperature sintering with CaZrO3-Y2O3 co-additives, J. Eur. Ceram. Soc. 34 (2014) 3627–3633. https://doi.org/10.1016/j.jeurceramsoc.2014.05.008.

[69] Y. Xiong, Z.Y. Fu, H. Wang, Y.C. Wang, Q.J. Zhang, Microstructure and IR transmittance of spark plasma sintering translucent AlN ceramics with CaF2 additive, Mater. Sci. Eng. B. 123 (2005) 57–62. https://doi.org/10.1016/j.mseb.2005.06.023.

[70] J.H. Harris, Sintered aluminum nitride ceramics for high-power electronic applications, Jom. 50 (1998) 56–60. https://doi.org/10.1007/s11837-998-0130-z.

[71] G.A. Slack, R.A. Tanzilli, R.O. Pohl, J.W. Vandersande, The intrinsic thermal conductivity of AIN, J. Phys. Chem. Solids. 48 (1987) 641–647. https://doi.org/10.1016/0022-3697(87)90153-3.

[72] P. Li, L. Teng, M. Guo, M. Zhang, S. Seetharaman, Oxidation kinetics of AlN under CO 2 atmosphere, Metall. Mater. Trans. B. 43 (2012) 406–412. https://doi.org/10.1007/s11663-011-9611-5.

[73] X. mei Hou, C. sheng Yue, A. Kumar Singh, M. Zhang, K.C. Chou, Morphological development and oxidation mechanisms of aluminum nitride whiskers, J. Solid State Chem. 183 (2010) 963–968. https://doi.org/10.1016/j.jssc.2010.02.022.

[74] H.J. Lee, S.W. Kim, S.S. Ryu, Sintering behavior of aluminum nitride ceramics with MgO-CaO-Al2O3-SiO2 glass additive, Int. J. Refract. Met. Hard Mater. 53 (2015) 46–50. https://doi.org/10.1016/j.ijrmhm.2015.04.013.

[75] Y. Liu, H. Zhou, Y. Wu, L. Qiao, Improving thermal conductivity of aluminum nitride ceramics by refining microstructure, Mater. Lett. 43 (2000) 114–117. https://doi.org/10.1016/S0167-577X(99)00241-4.

[76] A. V. Virkar, T.B. Jackson, R.A. Cutler, Thermodynamic and Kinetic Effects of Oxygen Removal on the Thermal Conductivity of Aluminum Nitride, J. Am. Ceram. Soc. 72 (1989) 2031–2042. https://doi.org/10.1111/j.1151-2916.1989.tb06027.x.

[77] T.B. Jackson, A. V. Virkar, K.L. More, R.B. Dinwiddie, R.A. Cutler, High-thermal-conductivity aluminum nitride ceramics: The effect of thermodynamic, kinetic, and microstructural factors, J. Am. Ceram. Soc. 80 (1997) 1421–1435. https://doi.org/10.1111/j.1151-2916.1997.tb03000.x.

[78] R. Terao, J. Tatami, T. Meguro, K. Komeya, Fracture behavior of AlN ceramics with rare earth oxides, J. Eur. Ceram. Soc. 22 (2002) 1051–1059. https://doi.org/10.1016/S0955-2219(01)00422-8.

[79] Y. Yao, L. Wang, C. Li, X. Jiang, T. Qiu, Effects of rare earth oxide additives on the thermal behaviors of aluminum nitride ceramics, Rare Met. 28 (2009) 596–599. https://doi.org/10.1007/s12598-009-0114-3.

[80] M. Kazan, B. Ruffí, C. Zgheib, P. Masri, Oxygen behavior in aluminum nitride, J. Appl.

Phys. 98 (2005). https://doi.org/10.1063/1.2137461.

[81] M. Zhu, N. Zhang, H. Wang, Y.D. Li, S.G. Huang, Q.J. Li, Y. Yu, Y.M. Guo, X.L. Liu, C.C. Wang, Point-defect-induced colossal dielectric behavior in GaAs single crystals, RSC Adv. 7 (2017) 26130–26135. https://doi.org/10.1039/c7ra00058h.

[82] H. Jiang, X.H. Wang, W. Lei, G.F. Fan, W.Z. Lu, Effects of two-step sintering on thermal and mechanical properties of aluminum nitride ceramics by impedance spectroscopy analysis, J. Eur. Ceram. Soc. 39 (2019) 249–254. https://doi.org/10.1016/j.jeurceramsoc.2018.09.026.

[83] L. Qiao, H. Zhou, R. Fu, Thermal conductivity of AlN ceramics sintered with CaF2 and YF3, Ceram. Int. 29 (2003) 893–896. https://doi.org/10.1016/S0272-8842(03)00033-6.

[84] X. Du, M. Qin, A. Farid, I.S. Humail, X. Qu, Study of rare-earth oxide sintering aid systems for AlN ceramics, Mater. Sci. Eng. A. 460–461 (2007) 471–474. https://doi.org/10.1016/j.msea.2007.01.137.

[85] M. Liu, S. Wang, S. Li, C. Liu, S. Luo, D. Wang, Preparation of nano-AlN powder by sol–gel foaming and its sintering properties, Int. J. Appl. Ceram. Technol. 20 (2023) 2261–2270. https://doi.org/10.1111/ijac.14330.

[86] Q. He, M. Qin, M. Huang, H. Wu, H. Lu, H. Wang, X. Mu, Y. Wang, X. Qu, Synthesis of highly sinterable AlN nanopowders through sol-gel route by reduction-nitridation in ammonia, Ceram. Int. 45 (2019) 14568–14575. https://doi.org/10.1016/j.ceramint.2019.04.174.

[87] J. Cheng, D. Agrawal, Y. Zhang, R. Roy, Microwave reactive sintering to fully transparent aluminum oxynitride (ALON) ceramics, J. Mater. Sci. Lett. 20 (2001) 77–79. https://doi.org/10.1023/A:1006731218817.

[88] G.F. Xu, Y. Carmel, T. Olorunyolemi, I.K. Lloyd, O.C. Wilson, Microwave sintering and properties of AlN/TiB2 composites, J. Mater. Res. 18 (2003) 66–76. https://doi.org/10.1557/JMR.2003.0010.

[89] X. He, F. Ye, H. Zhang, L. Liu, Effect of Sm2O3 content on microstructure and thermal conductivity of Spark Plasma Sintered AlN ceramics, J. Alloys Compd. 482 (2009) 345–348. https://doi.org/10.1016/j.jallcom.2009.04.013.

[90] C. Suryanarayana, E. Ivanov, V. V. Boldyrev, The science and technology of mechanical alloying, Mater. Sci. Eng. A. 304–306 (2001) 151–158. https://doi.org/10.1016/S0921-5093(00)01465-9.

[91] C. Suryanarayana, Recent developments in mechanical alloying, Rev. Adv. Mater. Sci. 18 (2008) 203–211. https://doi.org/10.1080/10667857.1994.11785013.

[92] R.K. Bordia, S.J.L. Kang, E.A. Olevsky, Current understanding and future research directions at the onset of the next century of sintering science and technology, J. Am. Ceram. Soc. 100 (2017) 2314–2352. https://doi.org/10.1111/jace.14919.

[93] J. Ryu, J.J. Choi, H.E. Kim, Effect of Heating Rate on the Sintering Behavior and the Piezoelectric Properties of Lead Zirconate Titanate Ceramics, J. Am. Ceram. Soc. 84 (2001) 902–904. https://doi.org/10.1111/j.1151-2916.2001.tb00766.x.

[94] E.T. Thostenson, T.W. Chou, Microwave processing: fundamentals and applications, Compos. Part A Appl. Sci. Manuf. 30 (1999) 1055–1071. https://doi.org/10.1016/S1359-835X(99)00020-2.

[95] K.E. Haque, Microwave energy for mineral treatment processes - A brief review, Int. J. Miner. Process. 57 (1999) 1–24. https://doi.org/10.1016/s0301-7516(99)00009-5.

[96] A. Goldstein, N. Travitzky, A. Singurindy, M. Kravchik, Direct microwave sintering of yttria-stabilized zirconia at 2·45 GHz, J. Eur. Ceram. Soc. 19 (1999) 2067–2072. https://doi.org/10.1016/s0955-2219(99)00020-5.

[97] C. Leonelli, P. Veronesi, L. Denti, A. Gatto, L. Iuliano, Microwave assisted sintering of green metal parts, J. Mater. Process. Technol. 205 (2008) 489–496. https://doi.org/10.1016/j.jmatprotec.2007.11.263.

[98] J. Sun, W. Wang, Q. Yue, Review on microwave-matter interaction fundamentals and efficient microwave-associated heating strategies, Materials (Basel). 9 (2016). https://doi.org/10.3390/ma9040231.

[99] R. Castro, K. van Benthem, Sintering, 2012. https://doi.org/10.1007/978-3-642-31009-6.

[100] R. de Oro Calderon, C. Gierl-Mayer, H. Danninger, Fundamentals of Sintering: Liquid Phase Sintering, Encycl. Mater. Met. Alloy. (2021) 481–492. https://doi.org/10.1016/B978-0-12-819726-4.00127-7.

[101] Z. Razavi Hesabi, H.R. Hafizpour, A. Simchi, An investigation on the compressibility of aluminum/nano-alumina composite powder prepared by blending and mechanical milling, Mater. Sci. Eng. A. 454–455 (2007) 89–98. https://doi.org/10.1016/j.msea.2006.11.129.

[102] W.J. Bartels, Characterization of Thin Layers on Perfect Crystals With a Multipurpose High Resolution X-Ray Diffractometer., J. Vac. Sci. Technol. B Microelectron. Nanom. Struct. 1 (1982) 338–345. https://doi.org/10.1116/1.582553.

[103] M. L. B., V.D. R. B., C. D. E., L. D., P. Scardi, Reitveld Refinement Guidelines, J. Appl. Crystallogr. 32 (1999) 36–50. https://doi.org/10.1107/S0021889898009856.

[104] S. Vitali, S. Aliaksandra, L. Igor K., Multidimensional Raman Spectroscopic Signatures as a Tool for Forensic Identification of Body Fluid Traces : A Review, Appl. Spectrosc. 65 (2011) 1223–1232. https://doi.org/10.1366/11-06455.

[105] G. Dent, E. Smith, Modern Raman Spectroscopy – A Practical Approach, 2019.

[106] R. R. D., Dielectric Resonators □, J. Appl. Phys. 6 (1939) 391–398.

[107] P. James K., R. Chung-Li, Application of Dielectric Resonators Microwave Components, IEE Trans. Microw. Theory Tech. MTT-29 (1981) 754–770.

[108] J. Sheen, A dielectric resonator method of measuring dielectric properties of low loss materials in the microwave region, Meas. Sci. Technol. 19 (2008). https://doi.org/10.1088/0957-0233/19/5/055701.

[109] H. B. W., C. Paul D., A dielectric resonator method of measuring inductive capacities in the millimeter range., IRE Trans. Microw. Theory Tech. 8 (1960) 402–410.

[110] R. Bachelard, P. Joubert, Aluminium nitride by carbothermal nitridation, Mater. Sci. Eng. A. 109 (1989) 247–251. https://doi.org/10.1016/0921-5093(89)90595-9.

[111] B. Feng, Y. Zhou, C. Peng, X. Li, J. Liu, Y. Wang, P. Rao, J. Wu, Vibration assisted hot-press sintering of AlN ceramics, J. Am. Ceram. Soc. 98 (2015) 1711–1713. https://doi.org/10.1111/jace.13591.

[112] A. Franco Júnior, D.J. Shanafield, Thermal conductivity of polycrystalline aluminum nitride (AlN) ceramics, Cerâmica. 50 (2004) 247–253. https://doi.org/10.1590/s0366-69132004000300012.

[113] T.B. Jackson, A. V Virkar, High-Thermal-Conductivity Aluminum Nitride Ceramics :, J. Am. Ceram. Soc. 80 (1997) 1421–1435.

[114] H.M. Lee, K. Bharathi, D.K. Kim, Processing and characterization of aluminum nitride ceramics for high thermal conductivity, Adv. Eng. Mater. 16 (2014) 655–669. https://doi.org/10.1002/adem.201400078.

[115] X. He, F. Ye, H. Zhang, Z. Zhou, Study on microstructure and thermal conductivity of Spark Plasma Sintering AlN ceramics, Mater. Des. 31 (2010) 4110–4115. https://doi.org/10.1016/j.matdes.2010.04.046.

[116] R. Kobayashi, J. Tatami, T. Wakihara, T. Meguro, K. Komeya, Temperature dependence of the electrical properties and seebeck coefficient of AlN-SiC ceramics, J. Am. Ceram. Soc. 89 (2006) 1295–1299. https://doi.org/10.1111/j.1551-2916.2005.00837.x.

[117] X. Fang, L. Pan, J. Yao, S. Yin, Y. Wang, Q. Li, J. Yang, Controllable dielectric properties and strong electromagnetic wave absorption properties of SiC/spherical graphite-AlN microwave-attenuating composite ceramics, Ceram. Int. 47 (2021) 22636–22645. https://doi.org/10.1016/j.ceramint.2021.04.277.

[118] Heryanto, B. Abdullah, D. Tahir, Mahdalia, Quantitative analysis of X-Ray diffraction spectra for determine structural properties and deformation energy of Al, Cu and Si, J. Phys. Conf. Ser. 1317 (2019). https://doi.org/10.1088/1742-6596/1317/1/012052.

[119] I.W. Chen, Mobility control of ceramic grain boundaries and interfaces, Mater. Sci. Eng. A. 166 (1993) 51–58. https://doi.org/10.1016/0921-5093(93)90309-3.

[120] H. Siegle, G. Kaczmarczyk, L. Filippidis, A. Litvinchuk, A. Hoffmann, C. Thomsen, Zone-boundary phonons in hexagonal and cubic GaN, Phys. Rev. B - Condens. Matter Mater. Phys. 55 (1997) 7000–7004. https://doi.org/10.1103/PhysRevB.55.7000.

[121] A.R. Goñi, H. Siegle, C. Thomsen, K. Syassen, J.M. Wagner, Effect of pressure on optical phonon modes and transverse effective charges in (formula presented) and

(formula presented), Phys. Rev. B - Condens. Matter Mater. Phys. 64 (2001) 1–6. https://doi.org/10.1103/PhysRevB.64.035205.

[122] V.Y. Davydov, Y.E. Kitaev, I.N. Goncharuk, A.M. Tsaregorodtsev, A.N. Smirnov, A.O. Lebedev, V.M. Botnaryk, Y. V. Zhilyaev, M.B. Smirnov, A.P. Mirgorodsky, O.K. Semchinova, Phonon spectrum of wurtzite GaN and AlN Experiment and theory, J. Cryst. Growth. 189–190 (1998) 656–660. https://doi.org/10.1016/S0022-0248(98)00239-5.

[123] D.H. Wang, S.R. Xu, Y. Hao, J.C. Zhang, T.H. Xu, Z.Y. Lin, H. Zhou, X.Y. Xue, Study on the relationships between Raman shifts and temperature range for a-plane GaN using temperature-dependent Raman scattering, Chinese Phys. B. 22 (2013). https://doi.org/10.1088/1674-1056/22/2/028101.

[124] Z. Su, J. Sha, G. Pan, J. Liu, D. Yang, C. Dickinson, W. Zhou, Temperature-dependent raman scattering of silicon nanowires, J. Phys. Chem. B. 110 (2006) 1229–1234. https://doi.org/10.1021/jp055869o.

[125] E. Talebian, M. Talebian, A general review on the derivation of Clausius-Mossotti relation, Optik (Stuttg). 124 (2013) 2324–2326. https://doi.org/10.1016/j.ijleo.2012.06.090.

[126] V.K. Veerapandiyan, Inducing Diffuse Phase Transitions in Barium Titanate, (2017).

[127] I.P. Fesenko, M.A. Kuzenkova, LOW DIELECTRIC LOSS CERAMICS OF AlN FINE AND NANOPOWDERS, Powder Metall. Met. Ceram. 41 (2002) 567–569.

[128] A. Satapathy, E. Sinha, B.K. Sonu, S.K. Rout, Conduction and relaxation phenomena in barium zirconate ceramic in wet N2 environment, J. Alloys Compd. 811 (2019) 152042. https://doi.org/10.1016/j.jallcom.2019.152042.

[129] W. Yang, S. Yu, R. Sun, R. Du, Nano- and microsize effect of CCTO fillers on the dielectric behavior of CCTO/PVDF composites, Acta Mater. 59 (2011) 5593–5602. https://doi.org/10.1016/j.actamat.2011.05.034.

[130] D.C. Dube, R. Zurmuhlen, A. Bell, N. Setter, W. Wersing, Dielectric measurements on high-Q ceramics in the microwave region, J. Am. Ceram. Soc. 80 (1997) 1095–1100. https://doi.org/10.1111/j.1151-2916.1997.tb02951.x.

[131] M. González, A. Ibarra, The Dielectric behaviour of commercial polycrystalline aluminum nitride, Diam. Relat. Mater. 9 (2000) 467–471. https://doi.org/10.1016/S0925-9635(99)00200-9.

[132] X. Zang, Y. Lu, Preparation and dielectric properties at high frequency of AlN-based composited ceramic, J. Mater. Sci. Mater. Electron. 31 (2020) 2826–2832. https://doi.org/10.1007/s10854-019-02826-4.

[133] A. Bellosi, L. Esposito, E. Scafè, L. Fabbri, The influence of microstructure on the thermal conductivity of aluminium nitride, J. Mater. Sci. 29 (1994) 5014–5022. https://doi.org/10.1007/BF01151092.

[134] K. Watari, K. Ishizaki, T. Fujikawa, Thermal conduction mechanism of aluminium nitride ceramics, J. Mater. Sci. 27 (1992) 2627–2630. https://doi.org/10.1007/BF00540680.

[135] 1 Giuseppe Pezzottia,*, Atsushi Nakahiraa, Masahiko Tajikab, Effect of extended annealing cycles on the thermal conductivity of AlN/Y2O3 ceramics, J. Eur. Ceram. Soc. 20 (2000) 1319–1325. https://doi.org/S0955221999002861.

[136] L. Liang, Qiao*, Heping, Zhou, Cuiwei, Microstructure and thermal conductivity of spark plasma sintering AlN ceramics, Mater. Sci. Eng. B. 99 (2013) 102–105.

https://doi.org/10.1179/026708309X12506933873666.

[137] K.A. Khor, K.H. Cheng, L.G. Yu, F. Boey, Thermal conductivity and dielectric constant of spark plasma sintered aluminum nitride, Mater. Sci. Eng. A. 347 (2003) 300–305. https://doi.org/10.1016/S0921-5093(02)00601-9.

[138] T. Yoshioka, Y. Makino, S. Miyake, Low temperature sintering of aluminum nitride with millimeter-wave heating, J. Mater. Sci. 38 (2003) 101–106. https://doi.org/10.1023/A:1021118000721.

[139] T. Honma, Y. Kuroki, T. Okamoto, M. Takata, Y. Kanechika, M. Azuma, H. Taniguchi, Transmittance and cathodoluminescence of AlN ceramics sintered with Ca3Al2O6 as sintering additive, Ceram. Int. 34 (2008) 943–946. https://doi.org/10.1016/j.ceramint.2007.09.062.

[140] Y. Saito, S. Michizono, S. Anami, Surface Flashover on Alumina rf Windows for High-power Use, IEEE Trans. Electr. Insul. 28 (1993) 566–573. https://doi.org/10.1109/14.231539.

[141] T. Tiwari, Study of RF window for X-band linac at frequency 9.3 GHz, in: 2008 IEEE Int. Vac. Electron. Conf. IVEC with 9th IEEE Int. Vac. Electron Sources Conf. IVESC, IEEE, 2008: pp. 374–375. https://doi.org/10.1109/IVELEC.2008.4556540.

[142] T. Tiwari, Study of dielectric window for X-band linac, in: 2008 Int. Conf. Recent Adv. Microw. Theory Appl. Microw. 2008, IEEE, 2008: pp. 132–134. https://doi.org/10.1109/AMTA.2008.4763032.

[143] Y. Joo, B.J. Lee, S.H. Kim, H.S. Kong, W. Hwang, S. Roh, J. Ryu, Development of new S-band RF window for stable high-power operation in linear accelerator RF system, Nucl. Instruments Methods Phys. Res. Sect. A Accel. Spectrometers, Detect. Assoc.

Equip. 866 (2017) 1–8. https://doi.org/10.1016/j.nima.2017.05.031.

[144] H. Kim, J. Verboncoeur, Y. Lau, Invited Paper - Modeling RF Window Breakdown: from Vacuum Multipactor to RF Plasma, IEEE Trans. Dielectr. Electr. Insul. 14 (2007) 774–782. https://doi.org/10.1109/tdei.2007.4286505.

[145] B. V Prokofiev, M.A. Martynenko, A simple pillbox-type mixed-mode window for high power microwave devices, in: IVEC 2017 - 18th Int. Vac. Electron. Conf., IEEE, 2018: pp. 1–2. https://doi.org/10.1109/IVEC.2017.8289511.

[146] M.K. Joshi, N. Nayek, T. Tiwari, R. Bhattacharjee, Design and Analysis of Overmoded RF Window for High-Power Applications in X -Band, IEEE Trans. Plasma Sci. 48 (2020) 127–132. https://doi.org/10.1109/TPS.2019.2956763.

[147] T. Tiwari, C.S. Nainwad, A.B. Shah, Study of window for s-band linear accelerator, in: 4th IEEE Int. Vac. Electron. Conf. IVEC 2003 - Proc., IEEE, 2003: pp. 60–61. https://doi.org/10.1109/IVEC.2003.1286053.

[148] S. Watari, K., Valecillos, M. C., Brito, M. E., Toriyama, M., & Kanzaki, Densification and Thermal Conductivity of AlN Doped with Y2O3, CaO, and Li2O, J. Am. Ceram. Soc. 79 (1996) 3103–3108.

[149] L.D. Merkle, A.C. Sutorik, T. Sanamyan, L.K. Hussey, G. Gilde, C. Cooper, M. Dubinskii, Fluorescence of Er^3+:AlN polycrystalline ceramic, Opt. Mater. Express. 2 (2012) 78. https://doi.org/10.1364/ome.2.000078.

[150] Y.C. Lan, X.L. Chen, Y.G. Cao, Y.P. Xu, L.D. Xun, T. Xu, J.K. Liang, Low-temperature synthesis and photoluminescence of AlN, J. Cryst. Growth. 207 (1999) 247–250. https://doi.org/10.1016/S0022-0248(99)00448-0.

[151] J. Das, S.K. Pradhan, D.R. Sahu, D.K. Mishra, S.N. Sarangi, B.B. Nayak, S. Verma, B.K. Roul, Micro-Raman and XPS studies of pure ZnO ceramics, Phys. B Condens. Matter. 405 (2010) 2492–2497. https://doi.org/10.1016/j.physb.2010.03.020.

[152] J.C. Goldsby, Micro-mechanical and electrical properties of monolithic aluminum nitride at high temperatures, J. Alloys Compd. 321 (2001) 67–71. https://doi.org/10.1016/S0925-8388(01)00953-7.

[153] T. Yagi, K. Shinozaki, N. Mizutani, M. Kato, A. Tsuge, Thermal diffusivity of SiO2 and Y2O3 added AIN ceramics, J. Mater. Sci. 24 (1989) 1332–1336. https://doi.org/10.1007/PL00020217.

[154] T. Kallel, M. Dammak, J. Wang, W.M. Jadwisienczak, Raman characterization and stress analysis of AlN:Er3+ epilayers grown on sapphire and silicon substrates, Mater. Sci. Eng. B Solid-State Mater. Adv. Technol. 187 (2014) 46–52. https://doi.org/10.1016/j.mseb.2014.04.003.

[155] P. Gao, C. Jia, W. Cao, C. Wang, D. Liang, G. Xu, Dielectric properties of spark plasma sintered AlN / SiC composite ceramics, Int. J. Miner. Metall. Mater. 21 (2014) 589–594. https://doi.org/10.1007/s12613-014-0946-1.

[156] S. Kume, M. Yasuoka, N. Omura, K. Watari, Effects of annealing on dielectric loss and microstructure of aluminum nitride ceramics, J. Am. Ceram. Soc. 88 (2005) 3229–3231. https://doi.org/10.1111/j.1551-2916.2005.00556.x.

[157] S.J. Penn, N.M.N. Alford, A. Templeton, X. Wang, M. Xu, M. Reece, K. Schrapel, Effect of porosity and grain size on the microwave dielectric properties of sintered alumina, J. Am. Ceram. Soc. 80 (1997) 1885–1888. https://doi.org/10.1111/j.1151-2916.1997.tb03066.x.

[158] S. Kume, M. Yasuoka, S.K. Lee, A. Kan, H. Ogawa, K. Watari, Dielectric and thermal properties of AlN ceramics, J. Eur. Ceram. Soc. 27 (2007) 2967–2971. https://doi.org/10.1016/j.jeurceramsoc.2006.11.023.

[159] C. Amy, D. Budenstein, M. Bagepalli, D. England, F. Deangelis, G. Wilk, C. Jarrett, C. Kelsall, J. Hirschey, H. Wen, A. Chavan, B. Gilleland, C. Yuan, W.C. Chueh, K.H. Sandhage, Y. Kawajiri, A. Henry, Pumping liquid metal at high temperatures up to 1,673 kelvin, Nature. 550 (2017) 199–203. https://doi.org/10.1038/nature24054.

[160] E.S. Dettmer, B.M. Romenesko, H.K. Charles, B.G. Carkhuff, D.J. Merrill, Steady state thermal conductivity measurements of AlN and SiC substrate materials, Proc. - Electron. Components Technol. Conf. 12 (1989) 551–556. https://doi.org/10.1109/ecc.1989.77804.

[161] K. Kuang, R. Sturdivant, RF and microwave microelectronics packaging II, 2017. https://doi.org/10.1007/978-3-319-51697-4.

[162] G. Piazza, V. Felmetsger, P. Muralt, R.H. Olsson, R. Ruby, Piezoelectric aluminum nitride thin fi lms for microelectromechanical systems, MRS Bull. 37 (2012) 1051–1061. https://doi.org/10.1557/mrs.2012.268.

[163] L. Qiao, H. Zhou, H. Xue, S. Wang, Effect of Y2O3 on low temperature sintering and thermal conductivity of AIN ceramics, J. Eur. Ceram. Soc. 23 (2003) 61–67. https://doi.org/10.1016/S0955-2219(02)00079-1.

[164] M. Coëffe-Desvaux, N. Pradeilles, P. Marchet, M. Vandenhende, M. Joinet, A. Maître, Comparative Study on Electrical Conductivity of CeO2-Doped AlN Ceramics Sintered by Hot-Pressing and Spark Plasma Sintering, Materials (Basel). 15 (2022). https://doi.org/10.3390/ma15072399.

[165] T.P. Nguyen, M. Dashti Germi, Z. Hamidzadeh Mahaseni, S.A. Delbari, Q. Van Le, Z. Ahmadi, M. Shokouhimehr, A. Sabahi Namini, M. Shahedi Asl, Enhanced densification of spark plasma sintered TiB2 ceramics with low content AlN additive, Ceram. Int. 46 (2020) 22127–22133. https://doi.org/10.1016/j.ceramint.2020.05.278.

[166] P. Yang, L. Wang, W. Zhao, L. Cai, Y. Feng, Hot-pressing sintered AlN-BN ceramics with high thermal conductivity and low dielectric loss, Ceram. Int. 46 (2020) 8431–8437. https://doi.org/10.1016/j.ceramint.2019.12.077.

[167] S. Zhao, Z. Yang, X. Zhou, Z. Liu, Properties and microstructure of pressureless sintered and microwave sintered SIC-ALN ceramics, ICCM Int. Conf. Compos. Mater. 2017-Augus (2017) 20–25.

[168] S.L. Chung, T.I. Tsai, S.C. Huang, High thermal conductivity ceramics from combustion synthesized AlN powder through microwave sintering and reheating, Int. J. Self-Propagating High-Temperature Synth. 21 (2012) 45–50. https://doi.org/10.3103/S1061386212010049.

[169] T. Kanai, K. Tanemoto, H. Kubo, Hot-pressed bn–aln ceramic composites of high thermal conductivity, Jpn. J. Appl. Phys. 29 (1990) 683–687. https://doi.org/10.1143/JJAP.29.683.

[170] H. Zhao, W. Wang, Z. Fu, H. Wang, Thermal conductivity and dielectric property of hot-pressing sintered AlN-BN ceramic composites, Ceram. Int. 35 (2009) 105–109. https://doi.org/10.1016/j.ceramint.2007.09.111.

[171] H.Y. Jin, W. Wang, J.Q. Gao, G.J. Qiao, Z.H. Jin, Study of machinable AlN/BN ceramic composites, Mater. Lett. 60 (2006) 190–193. https://doi.org/10.1016/j.matlet.2005.08.029.

[172] Y.L. Li, J. Zhang, J.X. Zhang, Fabrication and thermal conductivity of AlN/BN ceramics by spark plasma sintering, Ceram. Int. 35 (2009) 2219–2224. https://doi.org/10.1016/j.ceramint.2008.12.003.

[173] H. Zhao, W. Wang, H. Wang, Z. Fu, Spark plasma sintered AlN-BN composites and its thermal conductivity, J. Wuhan Univ. Technol. Mater. Sci. Ed. 23 (2008) 866–869. https://doi.org/10.1007/s11595-007-6866-4.

[174] X. He, Q. Gong, Y. Guo, J. Liu, Microstructure and properties of AlN-BN composites prepared by sparking plasma sintering method, J. Alloys Compd. 675 (2016) 168–173. https://doi.org/10.1016/j.jallcom.2016.03.058.

[175] P. Bindu, S. Thomas, Estimation of lattice strain in ZnO nanoparticles: X-ray peak profile analysis, J. Theor. Appl. Phys. 8 (2014) 123–134. https://doi.org/10.1007/s40094-014-0141-9.

[176] B.D. Cullity, PRELIMINARY AND CONTENT.pdf, (2014). http://lib.hpu.edu.vn/handle/123456789/29008.

[177] J. Tientong, S. Garcia, C.R. Thurber, T.D. Golden, Synthesis of nickel and nickel hydroxide nanopowders by simplified chemical reduction, J. Nanotechnol. 2014 (2014). https://doi.org/10.1155/2014/193162.

[178] B. Ahmed, B.I. Sharma, Structural and electronic properties of aln in rocksalt, zinc blende and wurtzite phase: A dft study, Dig. J. Nanomater. Biostructures. 16 (2021) 125–133. https://doi.org/10.15251/djnb.2021.161.125.

[179] L.E. McNeil, M. Grimsditch, R.H. French, Vibrational Spectroscopy of Aluminum Nitride, J. Am. Ceram. Soc. 76 (1993) 1132–1136. https://doi.org/10.1111/j.1151-2916.1993.tb03730.x.

[180] H.K. Lee, D.K. Kim, Investigation on thermal conductivity of aluminum nitride ceramics by FT-Raman spectroscopy, J. Am. Ceram. Soc. 93 (2010) 2167–2170. https://doi.org/10.1111/j.1551-2916.2010.03704.x.

[181] Y. Guojun, C. Guangde, L. Huiming, Solid-state metasynthesis and characterization of AlN nanocrystals, Int. J. Refract. Met. Hard Mater. 26 (2008) 5–8. https://doi.org/10.1016/j.ijrmhm.2007.03.003.

[182] L. Rosenberger, R. Baird, E. McCullen, G. Auner, G. Shreve, XPS analysis of aluminum nitride films deposited by plasma source molecular beam epitaxy, Surf. Interface Anal. 40 (2008) 1254–1261. https://doi.org/10.1002/sia.2874.

[183] A. Pakdel, Y. Bando, D. Golberg, Plasma-assisted interface engineering of boron nitride nanostructure films, ACS Nano. 8 (2014) 10631–10639. https://doi.org/10.1021/nn5041729.

[184] K. Wang, C. Wang, Aluminum-vacancy-related dielectric relaxations in AlN ceramics, J. Am. Ceram. Soc. 101 (2018) 2009–2016. https://doi.org/10.1111/jace.15370.

[185] G. Zhao, A. Wang, W. He, Y. Xing, X. Xu, 2D New Nonmetal Photocatalyst of Sulfur-Doped h-BN Nanosheeets with High Photocatalytic Activity, Adv. Mater. Interfaces. 6 (2019) 2–8. https://doi.org/10.1002/admi.201900062.

[186] H. Achour, A. Achour, S. Solaymani, M. Islam, S. Vizireanu, A. Arman, A. Ahmadpourian, G. Dinescu, Plasma surface functionalization of boron nitride nano-sheets, Diam. Relat. Mater. 77 (2017) 110–115. https://doi.org/10.1016/j.diamond.2017.06.012.

[187] R. Sharma, C. Henderson, G.W. Warren, S.L. Burkett, Study of electrical properties of polymeric materials using electrochemical impedance spectroscopy, J. Appl. Polym.

Sci. 68 (1998) 553–560. https://doi.org/10.1002/(SICI)1097-4628(19980425)68:4<553::AID-APP6>3.0.CO;2-L.

[188] M.K.E.-M. F.E. Salman, N.H. Shash, H. Abou El-Haded, Electrical conduction and dielectric properties of vanadium phosphate glasses doped with lithium, J. Phys. Chem. Solids. 63 (2002) 1957–1966. https://doi.org/10.1016/j.jnoncrysol.2009.07.028.

[189] H. Jiang, X.H. Wang, G.F. Fan, M. Fu, W. Lei, X.C. Wang, F. Liang, W.Z. Lu, Effect of oxidation on flexural strength and thermal properties of AlN ceramics with residual stress and impedance spectroscopy analysis of defects and impurities, Ceram. Int. 45 (2019) 13019–13023. https://doi.org/10.1016/j.ceramint.2019.03.232.

[190] R.J. Ji, Y.H. Liu, Y.Z. Zhang, H.F. Zhang, X.P. Li, X. Dong, An experimental research on single discharge machining of insulating ceramics efficiently with high energy capacitor, Sci. China Technol. Sci. 54 (2011) 1537–1545. https://doi.org/10.1007/s11431-011-4327-y.

[191] J. Zhu, R. An, C. Wang, W. Zhang, G. Wen, Characterization of the Microstructure of an AlN-Mullite-Al2O3 Ceramic Layer on WCu Composite Alloy for Microelectronic Application, J. Electron. Mater. 44 (2015) 4154–4160. https://doi.org/10.1007/s11664-015-3961-8.

[192] A. Agrawal, A. Satapathy, Epoxy composites filled with micro-sized AlN particles for microelectronic applications, Part. Sci. Technol. 33 (2015) 2–7. https://doi.org/10.1080/02726351.2014.919547.

[193] F.Y.C. Boey, L. Sun, X. Song, K.A. Khor, High dielectric AlN/Al2O3 composite powder using a plasma spray approach for microelectronics application, J. Mater. Sci. Mater. Electron. 10 (1999) 455–459. https://doi.org/10.1023/a:1008978314036.

[194] L. Yin, L. Yang, W. Yang, Y. Guo, K. Ma, S. Li, J. Zhang, Thermal design and analysis of multi-chip LED module with ceramic substrate, Solid. State. Electron. 54 (2010) 1520–1524. https://doi.org/10.1016/j.sse.2010.06.028.

[195] J. Hoople, J. Kuo, S. Ardanuc, A. Lal, Chip-scale sonic communication using AlN transducers, IEEE Int. Ultrason. Symp. IUS. (2013) 1934–1937. https://doi.org/10.1109/ULTSYM.2013.0493.

[196] A. Micol, A. Zeanh, T. Lhommeau, S. Azzopardi, E. Woirgard, O. Dalverny, M. Karama, An investigation into the reliability of power modules considering baseplate solders thermal fatigue in aeronautical applications, Microelectron. Reliab. 49 (2009) 1370–1374. https://doi.org/10.1016/j.microrel.2009.06.046.

[197] Y. Da Yu, A.M. Hundere, R. Hoier, R.E. Dunin-Borkowski, M.A. Einarsrud, Microstructural characterization and microstructural effects on the thermal conductivity of AIN(Y2O3) ceramics, J. Eur. Ceram. Soc. 22 (2002) 247–252. https://doi.org/10.1016/S0955-2219(01)00252-7.

[198] X. Du, M. Qin, A. Rauf, Z. Yuan, B. Yang, X. Qu, Structure and properties of AlN ceramics prepared with spark plasma sintering of ultra-fine powders, Mater. Sci. Eng. A. 496 (2008) 269–272. https://doi.org/10.1016/j.msea.2008.05.027.

[199] Y.C. Geng-fu Xu, Tayo Olorunyolemi, Otto C. Wilson and Isabel K. Lloyd, Microwave sintering of high thermal conductivity AlN, J. Mater. Res. Technol. 17 (2002).

[200] J.X. Xue, H.T. Liu, Y. Tang, C.M. Xu, G.J. Zhang, Effect of sintering atmosphere on the densification behavior of hot pressed TiN ceramics, Ceram. Int. 39 (2013) 8531–8535. https://doi.org/10.1016/j.ceramint.2013.03.062.

[201] W. Paszkowicz, S. Podsiadło, R. Minikayev, Rietveld-refinement study of aluminium

and gallium nitrides, J. Alloys Compd. 382 (2004) 100–106. https://doi.org/10.1016/j.jallcom.2004.05.036.

[202] H. Yu, F. Peng, H. Liang, S. Guan, L. Tan, Z. Xiong, X. Xiang, Q. Li, L. Lei, D. He, Pressure-Induced Structural Phase Transformation and Yield Strength of AlN, J. Phys. Chem. C. (2019) 1–6. https://doi.org/10.1021/acs.jpcc.9b07459.

[203] M. Kuball, J.M. Hayes, A.D. Prins, N.W.A. Van Uden, D.J. Dunstan, Y. Shi, J.H. Edgar, Raman scattering studies on single-crystalline bulk AIN under high pressures, Appl. Phys. Lett. 78 (2001) 724–726. https://doi.org/10.1063/1.1344567.

[204] L. Shen, T. Cheng, L. Wu, X. Li, Q. Cui, Synthesis and optical properties of aluminum nitride nanowires prepared by arc discharge method, J. Alloys Compd. 465 (2008) 562–566. https://doi.org/10.1016/j.jallcom.2007.11.007.

[205] D. Zientara, M.M. Bućko, J. Lis, Dielectric properties of aluminium nitride-γ-alon materials, J. Eur. Ceram. Soc. 27 (2007) 4051–4054. https://doi.org/10.1016/j.jeurceramsoc.2007.02.093.

[206] P. Yang, L. Wang, W. Zhao, L. Cai, Y. Feng, Hot-pressing sintered AlN-BN ceramics with high thermal conductivity and low dielectric loss, Ceram. Int. 46 (2020) 8431–8437. https://doi.org/10.1016/j.ceramint.2019.12.077.

[207] S. Kume, M. Yasuoka, N. Omura, K. Watari, Effect of zirconia addition on dielectric loss and microstructure of aluminum nitride ceramics, Ceram. Int. 33 (2007) 269–272. https://doi.org/10.1016/j.ceramint.2005.09.015.

[208] S. Kume, M. Yasuoka, N. Omura, K. Watari, Effects of MgO addition on the density and dielectric loss of AlN ceramics sintered in presence of Y2O3, J. Eur. Ceram. Soc. 25 (2005) 2791–2794. https://doi.org/10.1016/j.jeurceramsoc.2005.03.141.

[209] L. Nedelcu, C.D. Geambasu, M. Enculescu, M.G. Banciu, Intrinsic Dielectric Loss in Zr0.8Sn0.2TiO4 Ceramics Investigated by Terahertz Time Domain Spectroscopy, Materials (Basel). 14 (2021) 216.

[210] E. Ghasali, Y. Orooji, H. Niknam Germi, Investigation on in-situ formed Al 3 V-Al-VC nano composite through conventional , microwave and spark plasma sintering, Heliyon. 5 (2019) e01754. https://doi.org/10.1016/j.heliyon.2019.e01754.

[211] J. Schneider, M. Bigerelle, A. Iost, Statistical analysis of the Vickers hardness, Mater. Sci. Eng. A. 262 (1999) 256–263.